TRAJECTORY DESIGN IN THE SUN-EARTH-MOON FOUR BODY PROBLEM

A Thesis
Submitted to the Faculty

of

Purdue University

by

Roby S. Wilson

In Partial Fulfillment of the
Requirements for the Degree

of

Doctor of Philosophy

December 1998

To Kim

ACKNOWLEDGMENTS

First and foremost, I wish to thank my wife, Kim. Her encouragement and understanding through all the late nights and long weekends kept me sane over the past few years. She is one of the reasons I am glad that I stayed to pursue my doctorate. Next, of course, I need to thank my parents. Their love and concern for me helped me to mature as a person and they are always helpful and honest in their advice to me. Aside from my wife and parents, though, the person who has had the largest impact on my life is Dr. Howell. I have always admired her keen understanding of this research area and her respect for others in the field. Without her advice, encouragement, and guidance, this work would never have been completed. I am honored to have worked for her and hope to be able to work with her again in the future. I also wish to thank Brian Barden. We entered the research group at the same time and I have always enjoyed his company and sense of humor. He has contributed much to this work in terms of designs for manifolds and Lissajous trajectories and I am truly indebted to him for his help.

Finally, I wish to thank those institutions that have provided funding for my graduate studies. Over the years, I have been partially funded by the Purdue Department of Aeronautics and Astronautics, the Indiana Space Grant Consortium, the Purdue Research Foundation, as well as the National Aeronautics and Space Administration through the Advanced Concepts Research Projects (ACRP) Program, Award No. NCC7–5, and the Jet Propulsion Laboratory under Contract No. 960194.

PREFACE

I was only 10 days old when Neil Armstrong and Buzz Aldrin stepped out of The Eagle onto the Moon for the first time. Although I would be hard pressed to recall the event, it has always had a profound impact on my love for space. I sincerely hope that this work, while paling in comparison to the Apollo project, can make some small contribution to humanity's exploration of the universe.

TABLE OF CONTENTS

Page

Page

Page

LIST OF TABLES

LIST OF FIGURES

ABSTRACT

Wilson, Roby S., Ph.D., Purdue University, December, 1998. Trajectory Design in the Sun-Earth-Moon Four Body Problem. Major Professor: Dr. Kathleen C. Howell.

The objective of this work is the development of efficient techniques for the preliminary design of trajectories in the Sun-Earth-Moon four body problem that may involve lunar gravity assists and must satisfy specific trajectory requirements, such as apogee placement, launch constraints, or end state targeting. These types of trajectories are highly applicable to mission design in the restricted three and four body problems. The general solution approach proceeds in three steps. In the initial analysis, conic arcs and/or other types of trajectory segments are connected at patch points to construct a first approximation. Next, multi-conic methods are used to incorporate any additional force models that may have been neglected in the initial analysis. An optimization procedure is then employed to reduce the effective velocity discontinuities, while satisfying any constraints. Finally, a numerical differential corrections process results in a fully continuous trajectory that satisfies the design constraints, and includes appropriate lunar and solar gravitational models.

The methodology is applicable to a wide range of trajectory solutions. Examples are presented for multiple lunar swingby trajectories, transfers to libration point orbits, and achieving escape velocity using lunar gravity assists. Additionally, the specific application of the methodology to the GENESIS trajectory is detailed. The three step process is also presented as a method to perform error analysis, and for the determination of effective recoveries from injection or other maneuver errors. Finally, a parametric study and a targeting scheme are presented in a preliminary investigation into optimizing the cost of transfer trajectories to libration point orbits.

1. INTRODUCTION

If all goes according to plan, August 2003 should be remembered for the return of a well traveled spacecraft named GENESIS that will reenter the Earth's atmosphere over the desert of Utah carrying the first ever samples of solar wind particles from beyond the local Earth environment.[1] Throughout its two and a half year mission, GENESIS will be moving along a trajectory designed to take advantage of the complex dynamics in the Sun-Earth-Moon system in order to meet mission requirements and minimize fuel costs. GENESIS is just one of a series of new missions being proposed by NASA and other space agencies to exploit the dynamics in the gravitational problem of three and four bodies to meet mission design criteria. These missions require new and innovative design strategies to determine efficient and practical trajectories. This work details such a strategy for determining the motion of a spacecraft in a system defined in terms of four bodies, specifically, the Sun, Earth, Moon, and spacecraft. Although interest in the three and four body problems is currently high, detailed study of motion under the influence of multiple gravitational fields dates back hundreds of years.

1.1 History of Contributions

The motion of the Moon about the Earth has received intense study at various times since antiquity. However, not until Leonhard Euler in the mid 1700's were detailed measurements of the lunar motion actually determined. Euler sought a closed form solution for the Moon's motion, similar to the two body conic motion investigated by Johannes Kepler. Although he did not develop a workable theory to explain the lunar motion, his observations and calculations proved invaluable to others

investigating similar problems.[2] Joseph Lagrange used Euler's results to formulate equations that govern the motion of the Moon under the gravitational influence of the Sun and the Earth. This formulation appeared in the publication *Essai sur le Problème des Trois Corps* (Essay on the Problem of Three Bodies) in 1772.[3] By assuming that the mass of the third body is infinitesimal compared to the other two, Lagrange reduced the order of the problem; subsequently this reduced order problem has been given the name "Restricted Three Body Problem" (R3BP). A general closed form solution to this problem is still not known, but Lagrange did identify a set of particular solutions for the motion of the third mass. He noted that, under the proper assumptions, including circular motion of the massive bodies, the circular restricted three body problem yields five equilibrium points, also called libration points, or Lagrange points. However, Lagrange was not able to derive a closed form solution to the problem. Henri Poincaré later proved that no analytical solution for the n-body problem is, in fact, possible for $n > 2$, and thus, the three body problem in particular.[3] Poincaré's keen insights furthered research into the n-body problem and mathematics in general, but it was not until the advent of high speed computing and numerical analysis that additional particular solutions to the restricted three body problem have become available.

The focus of this current effort is the numerical determination of particular solutions in a restricted four body problem (R4BP), such as the Sun-Earth-Moon-spacecraft system. In this analysis, such solutions are frequently composed of a sequence of trajectory arcs and may include one or more lunar encounters. Since the 1960's, and the success of the Apollo program, there has been much investigation of trajectories that exploit an encounter with a secondary body (e.g., the Moon) perhaps multiple times. In his 1968 paper, Hénon[4] develops a series of periodic solutions in the planar, circular restricted three body problem that can be used to represent the motion of a spacecraft. His solution employs a "zero–sphere" approach such that the larger primary is the dominant gravity field, while the smaller primary's gravity is neglected. The motion of the smaller primary about the larger is, however, retained

in the model. By using this approximation, he is able to locate families of conic orbits about the larger primary that encounter the second primary repeatedly.

Hénon's approach has been extended and generalized by, among others, Hitzl,[5] Howell,[6] and Howell and Marsh,[7] to include eccentricity and arbitrary orientation of the spacecraft orbit relative to the orbit of the second primary. Once again, a series of conic solutions are determined that encounter (or more precisely – *collide with*) the smaller massless primary in a periodic fashion. This approximate solution to the restricted three body problem can be employed in the Earth-Moon-spacecraft system to determine a conic path that encounters the Moon in a periodic manner. These geocentric conic arcs are useful in determining an initial approximation to the four body problem that includes multiple lunar encounters.

In a related problem, Farquhar and Dunham[8] demonstrated in 1980, that a pair of orbits could be used to generate a "double lunar swingby" trajectory. Although the second primary (the Moon) is still assumed to be massless, its gravity is recognized as a source of discontinuities in the problem. The double lunar swingby combines two conic arcs with lunar encounters at the end point of each arc, such that the gravity of the "massless" primary shifts the spacecraft from one conic segment to the other, and then back periodically.

In designing the extended trajectory for the continuation of the ISEE–3/ICE mission (the first ever libration point mission, launched in 1978), Farquhar and Dunham[9] proposed using such trajectories to alternatively raise and lower the orbit apogee distances, while maintaining a specified orientation relative to the Sun–Earth line. Using various numerical and optimization techniques, it was possible to design a trajectory for the ISEE–3/ICE mission that used a series of lunar encounters to meet the mission goal of exploring the geomagnetic tail region of the Earth, and to take advantage of the post–mission opportunity to rendezvous with the comet Giacobini–Zinner. Both objectives were achieved within a limited fuel budget by exploiting the lunar gravity. Numerous other missions, for example WIND, GEOTAIL, and HITEN,[10,11] have been proposed and flown using similar concepts to achieve mission goals. However,

the solution process employed by Farquhar and Dunham, as well as others, such as Ishii and Matuo,[12] to obtain these trajectories involves much numerical integration of the equations of motion. It is very time consuming and requires extensive knowledge of the underlying problem, as well as very accurate initial estimates of the trajectory to obtain an acceptable solution.

1.2 Problem Definition

The ultimate goal of this work is the development of a quicker, more efficient methodology to determine trajectories in multi-body problems. The design strategy must be effective in various regimes, including regions of space in which two or more gravitational fields have comparable significance, and should allow modeling of non-gravitational perturbations. The resulting trajectories must meet various design requirements and constraints, while including the option for multiple lunar encounters. The trajectories sought through this process may be complete end-to-end solutions, or may be associated with some other predetermined solution, such as an orbit about a libration point. Furthermore, in contrast to standard trajectory design techniques in astrodynamics, it is assumed that the methodology will exploit rotating coordinate systems wherever applicable. Consistent with the approaches of Marsh,[13] Spencer,[14] and Wilson,[15] the current procedure is based on a three step process to determine a suitable solution. However, this process can be modified according to the accuracy of the initial approximation, especially when a solution to the four body problem is already available, for example, from dynamical systems theory.[1]

The first step in the methodology is the development of an initial approximation that meets mission design criteria. This initial approximation is sometimes conic in nature, as in the previously mentioned conic collision orbits, but allows the use of higher order models, such as numerical results from a restricted three body problem. Combinations of different kinds of solutions can also be utilized to generate a trajectory that meets design requirements. This analysis is useful for establishing general trajectory characteristics such as: orientation relative to the Sun-Earth line, apogee

and perigee distances, and approximate lunar encounter locations. The purpose of this first step is to provide a reasonable approximation to the trajectory that is efficient enough to allow numerous searches through the solution space, yet sufficiently accurate to serve as an initial estimate for the motion in the full model. The initial approximation is not, however, limited to "approximate" solutions such as conics, but can, in fact, be a previously determined solution to the four body problem. This is useful when analyzing transfers to and from libration point orbits using dynamical systems theory, as well as for modification of existing trajectories to meet different design criteria.

The ultimate goal of the process is an accurate representation of the motion in the four body problem, however, the errors associated with some initial approximations do not allow a numerically integrated trajectory to be directly determined that meets the design requirements. The second step of the process, then, is introduced to improve the initial approximation such that an acceptable solution to the restricted three or four body problem is obtained. Marsh[13] uses a series of semi-analytical approximations to improve an initial conic guess such that a numerically integrated solution is successfully determined. Although the technique is useful, it proves to be very labor intensive and requires much user interaction and knowledge of the problem. Instead, the approach suggested by Spencer[14] using multi-conic techniques during the intermediate step is further developed in this analysis.

Multi-conic analytical techniques were first formulated in the 1970's by S. Wilson,[16] Byrnes and Hooper,[17] D'Amario,[18] and others as a way of approximating solutions in the restricted three body problem. In a multi-conic procedure, the contributions of each gravity field are evaluated separately and then combined in a manner that yields an accurate approximation of the position and velocity of the spacecraft at discrete times along the trajectory. A series of approximations over a range of times can then be used to represent the motion of the vehicle. These multi-conic techniques are not limited to gravitational perturbations, but can also be used to include other types of forces, such as solar radiation pressure, so that all modeled forces can be represented in the approximation.

The second step of the process improves the initial estimate of the solution by incorporating, through multi-conic analysis, the effects of additional gravity fields and forces, such as solar radiation pressure, that may have been neglected in the initial analysis. This intermediate step also allows the design criteria and mission constraints to be fully incorporated into the trajectory solution. A differential corrections process is employed to ensure position and velocity continuity along the path, while satisfying any constraints placed on the solution.

The goal of the intermediate step is to preserve the general characteristics of the initial estimate, such that numerical integration of the solution produces a trajectory that accurately reflects the desired motion in the four body problem. The final step of the process, then, is numerical integration of the trajectory using a model in which the position and velocity states of all gravitational sources are determined from ephemeris data. In general, the numerical integration results in only minor changes to the trajectory obtained in the previous steps, and serves as confirmation of the overall design. Therefore, much of the design can be accomplished using simpler models with the knowledge that a viable numerically integrated solution can be obtained.

1.3 Outline

The discussion in this document begins with an overview of various aspects of the problem, including: reference frames, coordinate transformations, the equations of motion in the restricted three body, state transition matrices, development of the multi-conic approximations, and a brief synopsis of dynamical systems theory, as applied to the restricted three body problem. These topics are fundamental to the development of the three step solution process, and its application to trajectory design.

The next chapter provides a detailed discussion of the three step process that is employed to produce the trajectory solutions. An explanation of the procedures used to generate the initial approximation is presented, covering conic initial guesses, as well as approximations from the restricted three body problem. The basis for the

intermediate step is then derived, and the incorporation of trajectory constraints is introduced. The sensitivity matrix that is developed in this intermediate step is a key element in producing viable four body solutions from the initial approximation, as well as modifying existing solutions.

The application of the three step algorithm is detailed and then employed to generate a number of different types of trajectory solutions, including: multiple lunar swingbys, using lunar gravity assists to achieve escape velocity, transfers to libration point trajectories, and the GENESIS trajectory. Error analysis and recovery strategies are then presented for various types of solutions with an emphasis on using the procedure developed here to determine cost effective recoveries from injection and other maneuver errors. Finally, a parametric study and a targeting scheme are presented as a preliminary investigation into optimizing the cost of transfer trajectories to libration point orbits.

2. BACKGROUND

Investigation of the issues involved in obtaining specific solutions for the motion of a spacecraft in the restricted three and four body problems requires an initial discussion detailing some relevant background information. First, the different reference frames used in the analysis are presented, and state transformations are developed between the various frames. Each set of coordinate axes has its advantages that will become evident throughout the development of the solution process. Next, the restricted three body problem is introduced, and the differential equations governing the motion are developed. Based on these equations of motion, the multi-conic approximation to the motion is presented and discussed. Finally, an overview of dynamical systems theory and the development of state space manifolds based on the R3BP is discussed. Note that although it is possible to generalize this approach to other planetary systems, the methodology is applied here in the Sun-Earth-Moon-spacecraft system. Thus, all discussions throughout the text are based on application to this particular system.

2.1 Coordinate Systems

In the restricted n-body problem, coordinate systems and reference frames are crucial to a thorough understanding of the problem and aid in the successful development of the design strategy. The analysis in this work is accomplished using both inertial and rotating coordinate frames. The inertial frames have origins fixed in one of the primaries. Thus, the Earth Inertial (EI) frame $(\hat{X}_e, \hat{Y}_e, \hat{Z}_e)$ is an inertially fixed frame with origin at the Earth. This frame is defined consistent with some specified fundamental frame; the Earth Mean Equator and Equinox of J2000 is selected for

this analysis. (Throughout the text, a caret ($\hat{}$) will denote unit vectors, while an overbar ($\bar{}$) indicates a vector of variable length. Also note that uppercase letters will represent inertial reference frames, while lower case letters denote rotating coordinates.) The Moon Inertial (MI) frame $(\hat{X}_m, \hat{Y}_m, \hat{Z}_m)$ has its origin at the center of the Moon, and each axis remains parallel to the corresponding axis in the EI frame.

There are numerous rotating frames associated with analysis in the restricted problem. The Earth-Moon Barycentric Rotating (EMBR) frame $(\hat{x}_b, \hat{y}_b, \hat{z}_b)$ is, as its name indicates, a rotating frame with origin at the barycenter of the Earth-Moon system. The $\hat{x}_b$ axis is always directed from the Earth to the Moon as the primaries orbit their barycenter. The $\hat{z}_b$ axis is normal to the plane of motion of the primaries and $\hat{y}_b = \hat{z}_b \times \hat{x}_b$ completes the orthonormal triad. A similar frame (the SEBR) can be defined in the Sun-Earth system where the $\hat{x}$ axis is now directed from the Sun to the Earth, and the origin is the barycenter of the Sun-Earth system. The EI, MI, and EMBR frames appear in Figure 2.1. The position vector from the Earth-Moon barycenter (B) to the spacecraft (S/C) is written in terms of rotating coordinates as

$$\bar{r}_{bsc} = x\hat{x}_b + y\hat{y}_b + z\hat{z}_b \quad . \tag{2.1}$$

The location of the spacecraft could also be defined relative to the Earth in EI coordinates as

$$\bar{R}_{esc} = X_e\hat{X}_e + Y_e\hat{Y}_e + Z_e\hat{Z}_e \quad , \tag{2.2}$$

or relative to the Moon in MI coordinates as

$$\bar{R}_{msc} = X_m\hat{X}_m + Y_m\hat{Y}_m + Z_m\hat{Z}_m \quad . \tag{2.3}$$

Of course, each of these position vectors can also be written in terms of other reference frames without loss of generality. Note that the vector $\bar{R}_{em}$ describes the location of the Moon relative to the Earth in inertial coordinates.

Perhaps the most important frame employed in the analysis, from a trajectory design standpoint, is the Solar Rotating (SR) frame $(\hat{x}_s, \hat{y}_s, \hat{z}_s)$. Its origin is located at the center of the Earth, with the $\hat{x}_s$ axis directed along the vector from the Sun to

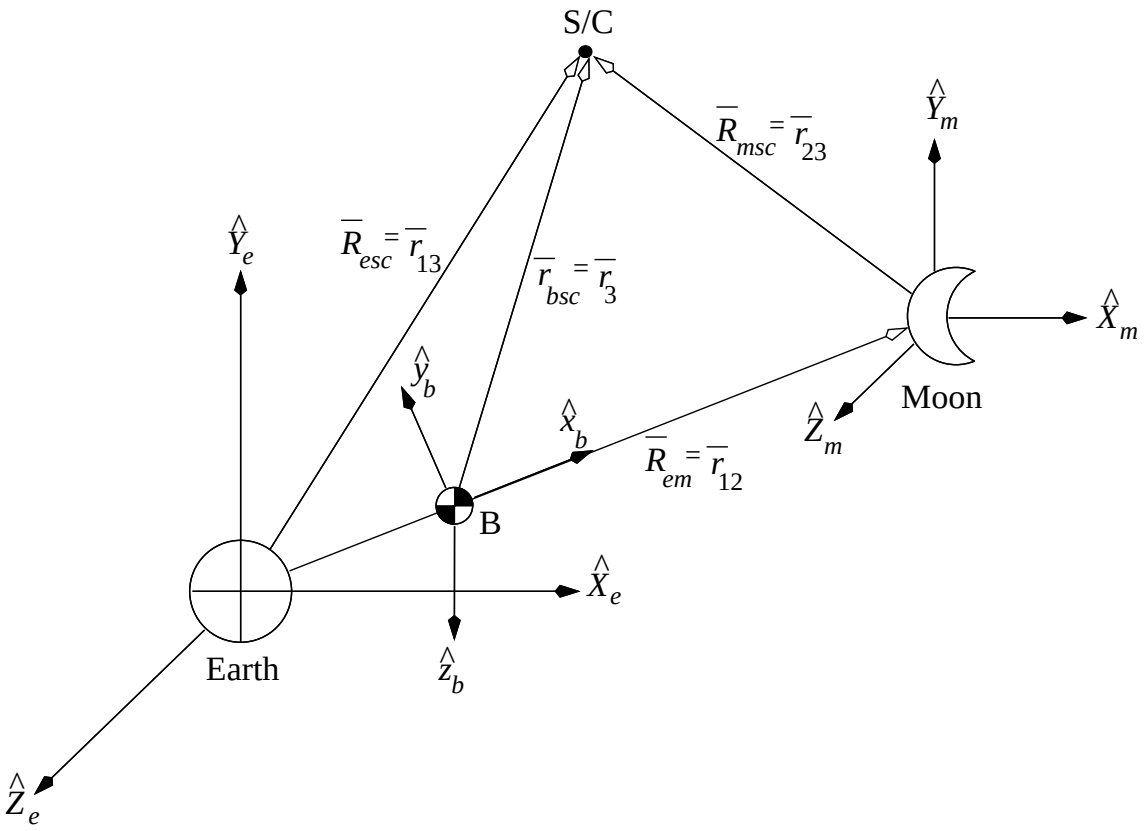

Figure 2.1. Earth Inertial, Moon Inertial, and Barycentric Rotating Frames

the Earth. The $\hat{z}_s$ axis is normal to the instantaneous plane of motion of the Earth about the Sun, and $\hat{y}_s = \hat{z}_s \times \hat{x}_s$. The Solar Rotating frame (see Figure 2.2) is critical in understanding the nature of the motion in the Sun-Earth-Moon system, as modeled in terms of the restricted three and four body problems. The angle ψ in Figure 2.2 is defined as the angle between the $+\hat{x}_s$ axis and the projection $\bar{P}$ of some position vector onto the $\hat{x}_s\hat{y}_s$ plane. This angle, sometimes called the elongation angle, ranges between $\pm\pi$, and is defined positive in a clockwise sense from the $+\hat{x}_s$ axis.

2.2 Coordinate Transformations

Throughout the process to determine particular solutions to the restricted four body problem, it is necessary to switch between various coordinate systems. State

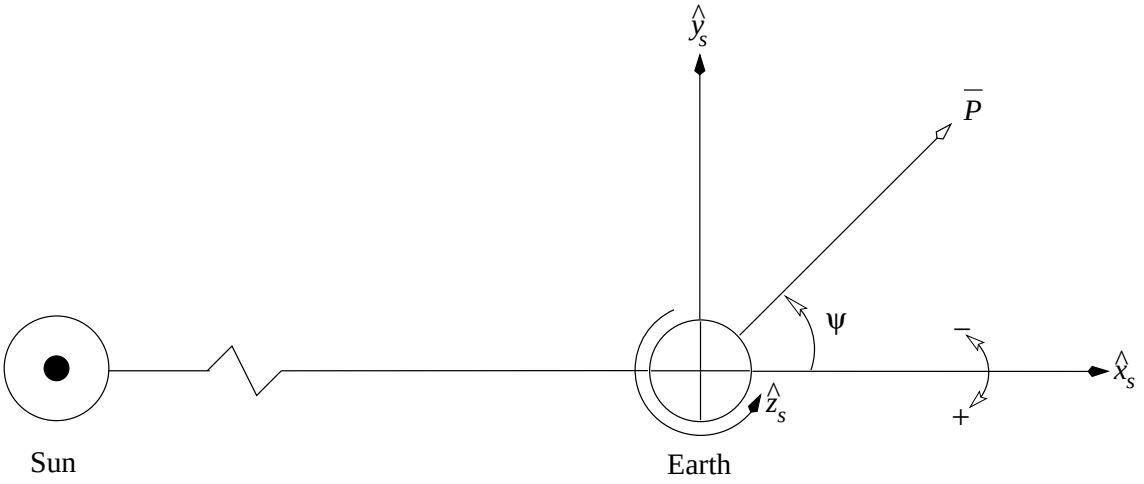

Figure 2.2. Solar Rotating Frame

space transformations exist between each of the reference frames presented in Section 2.1. Spencer[14] and Wilson[15] detail the steps required to transform between the inertial frames (EI and MI) and the barycentric rotating frames (EMBR and SEBR). However, in this analysis, the state transformation that is most frequently utilized is the one between the EI and SR frames. Since the origin defined for both of these frames is the Earth, a standard coordinate transformation can be performed to transform any given position/velocity state. Define, then, a direction cosine matrix relating the EI frame to the SR frame, i.e.,

$$ {}^{R}C^{I} = \begin{bmatrix} \hat{x}_s \bullet \hat{X}_e & \hat{x}_s \bullet \hat{Y}_e & \hat{x}_s \bullet \hat{Z}_e \\ \hat{y}_s \bullet \hat{X}_e & \hat{y}_s \bullet \hat{Y}_e & \hat{y}_s \bullet \hat{Z}_e \\ \hat{z}_s \bullet \hat{X}_e & \hat{z}_s \bullet \hat{Y}_e & \hat{z}_s \bullet \hat{Z}_e \end{bmatrix} \quad , \tag{2.4} $$

where superscript R denotes a rotating frame, superscript I denotes an inertial frame and '$\bullet$' represents the inner product. The position state in terms of EI coordinates ($\bar{R}_{esc}$) is transformed to SR coordinates ($\bar{r}_{esc}$) through the transformation relationship

$$ \bar{r}_{esc} = {}^{R}C^{I}\,\bar{R}_{esc} \quad . \tag{2.5} $$

This, then, transforms the three elements of the position state.

The transformation of the velocity state is complicated by the non-inertial nature of the rotating frame. If a vector $\bar{r}$ is assumed to be a position vector defined relative to

an inertial base point, but expressed in terms of a rotating frame, then the expression for the inertial derivative ($\frac{^I d}{dt}$) can be expanded in terms of the derivative relative to the rotating frame as follows,

$$\frac{^I d}{dt}(\bar{r}) = \frac{^R d}{dt}(\bar{r}) + {}^I\bar{\omega}^R \times \bar{r} \quad , \tag{2.6}$$

where ${}^I\bar{\omega}^R$ is the angular velocity of the rotating frame with respect to the inertial frame and $\frac{^R d}{dt}$ represents a rotating derivative with respect to time. The inertial velocity $\frac{^I d}{dt}(\bar{r})$ can, of course, also be expressed in terms of exactly the same position vector written in terms of inertial coordinates ($\bar{R}$), that is,

$$\frac{^I d}{dt}(\bar{r}) = \frac{^I d}{dt}({}^R C^I \bar{R}) \quad . \tag{2.7}$$

The transformation matrix ${}^R C^I$ does not depend on time, so using Equation (2.6) to rewrite Equation (2.7) produces

$${}^R C^I \; \frac{^I d}{dt}(\bar{R}) = \frac{^I d}{dt}(\bar{r}) = \frac{^R d}{dt}(\bar{r}) + {}^I\bar{\omega}^R \times \bar{r} \quad , \tag{2.8}$$

or

$${}^R C^I \; {}^I\bar{V} = {}^R\bar{v} + {}^I\bar{\omega}^R \times \bar{r} \quad , \tag{2.9}$$

where

$${}^I\bar{V} = \frac{^I d}{dt}(\bar{R}) \quad ; \quad {}^R\bar{v} = \frac{^R d}{dt}(\bar{r}) \quad . \tag{2.10}$$

The quantity ${}^I\bar{V}$ is the inertial velocity expressed in inertial coordinates, while ${}^R\bar{v}$ is a rotating velocity expressed in terms of rotating coordinates. Rearranging the terms in Equation (2.9) produces the desired transformation from EI to SR coordinates, i.e.,

$${}^R\bar{v}_{esc} = {}^R C^I \; {}^I\bar{V}_{esc} - {}^I\bar{\omega}^R \times \bar{r}_{esc} \quad . \tag{2.11}$$

In a similar manner, the state transformations from SR to EI frames are written

$$\bar{R}_{esc} = {}^I C^R \bar{r}_{esc} \quad , \tag{2.12}$$

$${}^I\bar{V}_{esc} = {}^I C^R \left[{}^R\bar{v}_{esc} + {}^I\bar{\omega}^R \times \bar{r}_{esc} \right] \quad , \tag{2.13}$$

where ${}^{I}C^{R} = \left[{}^{R}C^{I}\right]^{T}$. (Note that the superscripts I and R will be dropped from the velocity expressions throughout the remainder of the text. Unless otherwise stated, inertial velocities will be expressed in inertial coordinates and rotating velocities will be expressed in rotating coordinates.)

The SR coordinate frame is crucial in visualizing the solutions that are produced from the three step methodology. Since most of the computations in this work are performed in the inertial frame, the transformation between EI and SR frames is used extensively throughout the solution process, especially during input and output.

2.3 Equations of Motion for the Restricted Three Body Problem

Since the restricted three body equations of motion have no known analytical solution, various approaches have been developed to gain insight into the characteristics of the motion. By making certain assumptions that simplify the problem, analytical tools can be developed to to aid in the search for particular solutions. Two such approaches, multi-conic analysis and dynamical system theory (DST) as applied to the three body problem, are presented here. Application of both multi-conics and DST relies on particular forms of the restricted three body equations of motion.

The derivation of the governing differential equations begins by assuming that the mass of the third body (e.g., the spacecraft) is negligible as compared to the other two, and therefore, does not affect the motion of the two primaries. The time history for the motion of the primaries is then assumed known as a solution to a two body problem. (In practice, it is available from ephemeris data.) These two assumptions effectively reduce the number of degrees of freedom in the problem to three. That is, the problem is defined as the motion of the infinitesimal mass under the influence of two primaries, hence the name "restricted" three body problem.

The motion of the primaries can be modeled in a number of ways. The most coherent model results from the assumption of conic motion of the two primaries about their barycenter, since the third body has infinitesimal mass. If the relative motion of the primaries is modeled as elliptic, the resulting solution for the motion

of the spacecraft is termed a solution to the "elliptic" restricted three body problem (ER3BP); likewise, if the relative path of the two primaries is assumed to be circular, then the problem is labeled as the "circular" restricted three body problem (CR3BP). It might be desirable to use a more general model that incorporates the actual non-periodic nature of the primary motion. However, using ephemerides does not strictly satisfy the differential equations for the motion of three bodies; it is also unnecessary in preliminary analyses. Many useful analytical results are available under the assumption of conic motion for the primaries, thus a conic representation is selected for the derivation at this time. The equations of motion for the ER3BP will be developed here, since the CR3BP can be shown to be a subset of the ER3BP for a primary orbit eccentricity of zero.

The basic vector equation of motion relating the forces acting on the spacecraft (denoted with subscript 3) to its inertial acceleration can be written in the form,

$$\bar{F}_3 = m_3 \, {}^I\bar{r}_3'' \quad . \tag{2.14}$$

Here the prime represents differentiation with respect to dimensional time and superscript I denotes differentiation relative to an inertial observer. The position vector $\bar{r}_3$ is defined from the barycenter of the primary system to the spacecraft. (See Figure 2.1.) The resultant force vector $\bar{F}_3$ is the sum of all gravitational forces acting on the spacecraft with mass m_3. The force term on the left of Equation (2.14) can be evaluated from the inverse square law of gravity, that is,

$$\bar{F}_3 = -\frac{Gm_1m_3}{|\bar{r}_{13}|^3}\bar{r}_{13} - \frac{Gm_2m_3}{|\bar{r}_{23}|^3}\bar{r}_{23} \quad , \tag{2.15}$$

where G is the universal gravitational constant, m_1 and m_2 are the masses of the primaries, and $\bar{r}_{13}$ and $\bar{r}_{23}$ are the position vectors from the primaries to the spacecraft. (See Figure 2.1.) Combining Equations (2.14) and (2.15) produces

$${}^I\bar{r}_3'' = -\frac{Gm_1}{r_{13}^3}\bar{r}_{13} - \frac{Gm_2}{r_{23}^3}\bar{r}_{23} \quad . \tag{2.16}$$

For a solution process that is as general as possible, this equation is rewritten in a non-dimensional form. To do so, define the following characteristic quantities for

mass (M^*), length (L^*), and time (T^*),

$$M^* = m_1 + m_2 \;\; ; \;\; L^* = a_{12} \;\; ; \;\; T^* = \sqrt{\frac{L^{*^3}}{GM^*}} \quad , \tag{2.17}$$

where a_{12} is the semi–major axis associated with the relative motion of the primaries. Given these characteristic quantities, the non-dimensional gravitational constant becomes unity, that is

$$\tilde{G} = \frac{GM^*T^{*^2}}{L^{*^3}} = 1 \quad . \tag{2.18}$$

The non-dimensional form of Equation (2.16) can thus be written

$${}^I\ddot{\bar{\rho}} = -\frac{(1-\mu)}{d^3}\bar{d} - \frac{\mu}{f^3}\bar{f} \quad , \tag{2.19}$$

where dots denote differentiation with respect to non-dimensional time and

$$\bar{\rho} = \frac{\bar{r}_3}{L^*} \;\; ; \;\; \bar{d} = \frac{\bar{r}_{13}}{L^*} \quad ; \quad \bar{f} = \frac{\bar{r}_{23}}{L^*} \quad , \tag{2.20}$$

$$(1-\mu) = \frac{m_1}{M^*} \quad ; \;\; \mu = \frac{m_2}{M^*} \quad , \tag{2.21}$$

are the resulting non-dimensional variables.

Similar to the approach used by Pernicka,[19] a barycentric rotating frame (BR) having orthonormal unit vectors $\hat{x}_b$, $\hat{y}_b$, and $\hat{z}_b$ (as defined in Figure 2.1), is used to write the position vector $\bar{\rho}$. Inertially differentiating with respect to non-dimensional time produces the kinematic expressions for the velocity and acceleration of the spacecraft. The following kinematic vector equations represent the position, velocity, and acceleration of the spacecraft in terms of BR coordinates,

$$\bar{\rho} = x\hat{x}_b + y\hat{y}_b + z\hat{z}_b \quad , \tag{2.22}$$

$${}^I\dot{\bar{\rho}} = (\dot{x}_b - \dot{\theta}y)\hat{x}_b + (\dot{y} + \dot{\theta}x)\hat{y}_b + \dot{z}\hat{z}_b \quad , \tag{2.23}$$

$${}^I\ddot{\bar{\rho}} = [(\ddot{x} - \dot{\theta}^2 x) - (\ddot{\theta}y + 2\dot{\theta}\dot{y})]\hat{x}_b + [(\ddot{y} - \dot{\theta}^2 y) + (\ddot{\theta}x + 2\dot{\theta}\dot{x})]\hat{y}_b + \ddot{z}\hat{z}_b \quad , \tag{2.24}$$

where $\dot{\theta}$ and $\ddot{\theta}$ are the angular velocity and angular acceleration, respectively, of the BR frame with respect to the inertial frame. Using the orbital parameters: semi-major axis (a), eccentricity (e), as well as the eccentric anomaly (E) of the primaries,

the quantities $\dot{\theta}$ and $\ddot{\theta}$ can be written in non-dimensional form as

$$\dot{\theta} = \frac{\sqrt{1-e^2}}{(1-e\cos E)^2} \quad , \tag{2.25}$$

$$\ddot{\theta} = -2e\sin E\frac{\sqrt{1-e^2}}{(1-e\cos E)^4} \quad . \tag{2.26}$$

Note that, by definition, the semi-major axis of the orbit of the smaller primary relative to the larger is unity in non-dimensional units, and thus, does not appear explicitly in the above expressions. From the vector geometry (see Figure 2.1), the non-dimensional position vectors $\bar{d} = \bar{r}_{13}/L^*$ from the Earth to the spacecraft and also $\bar{f} = \bar{r}_{23}/L^*$ from the Moon to the spacecraft can be expressed in terms of BR coordinates as

$$\bar{d} = (x+\mu)\hat{x}_b + y\hat{y}_b + z\hat{z}_b \quad , \tag{2.27}$$

$$\bar{f} = (x-(1-\mu))\hat{x}_b + y\hat{y}_b + z\hat{z}_b \quad . \tag{2.28}$$

Combining Equations (2.24), (2.27), and (2.28) into (2.19) produces the desired equations of motion completely in terms of non-dimensional quantities,

$$(\ddot{x}-\dot{\theta}^2x)-(\ddot{\theta}y+2\dot{\theta}\dot{y}) = -\frac{(1-\mu)(x+\mu)}{d^3}-\frac{\mu(x-(1-\mu))}{f^3} \quad , \tag{2.29}$$

$$(\ddot{y}-\dot{\theta}^2y)+(\ddot{\theta}x+2\dot{\theta}\dot{x}) = -\frac{(1-\mu)y}{d^3}-\frac{\mu y}{f^3} \quad , \tag{2.30}$$

$$\ddot{z} = -\frac{(1-\mu)z}{d^3}-\frac{\mu z}{f^3} \quad . \tag{2.31}$$

When combined with Equations (2.25) and (2.26), these equations of motion yield three second–order scalar differential equations for the motion of the spacecraft in the ER3BP in terms of Barycentric Rotating coordinates. The CR3BP equations of motion are obtained from the model for the ER3BP by fixing the eccentricity of the primary motion to a constant value of zero in Equations (2.25) and (2.26). This eliminates θ from the equations of motion since for $e = 0$, it is apparent that $\ddot{\theta} = 0$, and $\dot{\theta} = 1$ in non-dimensional units. There is no known general closed–form solution to either form of these differential equations. Therefore, it is necessary to determine the spacecraft motion either through some type of analytical or semi–analytical

approximation process, or through direct numerical integration of the equations of motion.

2.3.1 State Transition Matrices for the Restricted Three Body Problem

The state transition matrix (STM) in this work represents a linear relationship between changes in the state at some time t_i and changes in the state at time t_f. Defined as such, the STM only has meaning relative to a specific reference solution. Equations governing the elements of the state transition matrix can be derived in the restricted three body problem. From the equations of motion in Section 2.3, the STM for certain types of arcs in the elliptic restricted three body problem are governed by a matrix differential equation of the form[19]

$$\frac{d}{d\tau}\left(\Phi(\tau, t_i)\right) = A(\tau)\Phi(\tau, t_i) \quad , \tag{2.32}$$

where $\Phi(\tau, t_i)$ is the STM from time t_i to time τ. The matrix $A(\tau)$ is a 6x6 matrix of time varying partial derivatives that is evaluated along the reference path. This matrix can be represented in terms of four 3x3 submatrices as

$$A(\tau) = \left[\begin{array}{c|c} \emptyset_3 & I_3 \\ \hline U_{QQ}(\tau) + \ddot{\theta}(\tau)\Omega & 2\dot{\theta}(\tau)\Omega \end{array}\right] \quad , \tag{2.33}$$

where the matrix $\emptyset_3$ is the 3x3 zero matrix, the matrix I_3 is the 3x3 identity matrix, and the matrix Ω is defined to be

$$\Omega \triangleq \left[\begin{array}{ccc} 0 & 1 & 0 \\ -1 & 0 & 0 \\ 0 & 0 & 0 \end{array}\right] \quad . \tag{2.34}$$

The quantities $\dot{\theta}(\tau)$ and $\ddot{\theta}(\tau)$ are the scalar non-dimensional expressions for angular velocity and angular acceleration defined in Equations (2.25) and (2.26) and evaluated at time τ. The matrix $U_{QQ}(\tau)$ is the symmetric matrix of second partial derivatives of the pseudo potential U with respect to x, y, and z, where U is defined as

$$U \triangleq \frac{1}{2}\dot{\theta}^2\left(x^2 + y^2\right) + \frac{(1-\mu)}{d} + \frac{\mu}{f} \quad , \tag{2.35}$$

and is also evaluated along the reference arc at time τ. Since $A(\tau)$ is a function of the state corresponding to the infinitesimal mass, it is necessary to integrate Equation (2.32) along with the equations of motion in Equations (2.29), (2.30), and (2.31) in order to obtain a numerical solution for the STM in the ER3BP (or CR3BP if $e = 0$). As a point of note, the STM obtained in this process is defined for a Barycentric Rotating coordinate frame and is associated with differential equations derived in terms of Barycentric Rotating state variables. It is necessary to transform this STM, along with the corresponding states, to an inertial frame in order to compare the results to those generated from analysis performed with inertial frames and states, such as two body conic solutions. See Wilson[15] for details on transforming state transition matrices between these rotating and inertial frames.

2.4 Multi-Conic Analysis

In the intermediate step between the initial approximation and a numerical solution that represents the motion under the influence of a complete and accurate force model, an approximation to the three body model, with perturbations, is frequently required. This intermediate result enables the initial "guess" to serve as the basis for an improved solution to the four body problem; in some cases this is a critical element in the design process. The solution approach employed in this intermediate step was developed in the late 1960's and early 1970's by S. Wilson,[16] Byrnes and Hooper,[17] and D'Amario,[18] among others, and is called multi-conic analysis.

When using multi-conics, the contributions of each primary to the motion of the spacecraft are evaluated separately as solutions to a two body problem, and then "overlapped" through the addition of a constant velocity segment. The result is a reasonably good approximation to motion in the R3BP. Multi-conic analysis also provides the capability to include other perturbing forces as well, for example: additional gravitational forces, such as solar gravity, or non-gravitational forces, such as solar radiation pressure. Through these perturbations, multi-conic analysis can be used to model the motion in the four body problem with all applicable forces

included. In contrast, the two body conic solution identifies only the contribution of the larger primary as the approximation to the motion, while all other influences are neglected. Since a solution generated with multi-conics can include all applicable forces, it should provide a more accurate method of representing the motion in the four body problem.

2.4.1 Approximations to the Restricted Three Body Equations of Motion

Consistent with the derivation in S. Wilson,[16] and using the non-dimensional notation in Section 2.3, it is noted from Figure 2.1 that the position of the spacecraft could be represented by the position vector relative to the larger primary ($\bar{r}_{13}$), or the position vector relative to the smaller primary ($\bar{r}_{23}$). These two position vectors are related geometrically by the vector sum

$$\bar{d} = \bar{r}_m + \bar{f} \quad , \tag{2.36}$$

where

$$\bar{d} = \frac{\bar{r}_{13}}{L^*} \;\; ; \;\; \bar{f} = \frac{\bar{r}_{23}}{L^*} \;\; ; \;\; \bar{r}_m = \frac{\bar{r}_{12}}{L^*} \quad . \tag{2.37}$$

The vectors $\bar{d}$ and $\bar{f}$ are the positions of the spacecraft with respect to the Earth and Moon, respectively, and $\bar{r}_m$ is the position vector of the Moon with respect to the Earth. Inertially differentiating this vector relationship twice yields

$${}^I\ddot{\bar{d}} = {}^I\ddot{\bar{r}}_m + {}^I\ddot{\bar{f}} \quad , \tag{2.38}$$

where, as before, superscript I denotes differentiation as viewed by an inertial observer and dot represents differentiation with respect to non-dimensional time. Incorporating the inverse square gravity field force model produces the standard vector equation for the relative motion of one particle with respect to another, while including the perturbing effects of a third particle. If the effect of the spacecraft mass on the motion of the primaries is neglected, two representative second order vector differential equations for the relative motion of the spacecraft result, i.e.,

$${}^I\ddot{\bar{d}} \;\; = \;\; -\frac{(1-\mu)}{d^3}\bar{d} - \frac{\mu}{f^3}\bar{f} - \frac{\mu}{r_m^3}\bar{r}_m \quad , \tag{2.39}$$

$$ {}^{I}\ddot{\bar{f}} = -\frac{(1-\mu)}{d^3}\bar{d} - \frac{\mu}{f^3}\bar{f} + \frac{(1-\mu)}{r_m^3}\bar{r}_m \quad , \tag{2.40} $$

as well as the classical differential equation governing the relative motion of the two primaries,

$$ {}^{I}\ddot{\bar{r}}_m = -\frac{\bar{r}_m}{r_m^3} \quad . \tag{2.41} $$

By integrating Equations (2.39), (2.40), and (2.41) from some initial time t_i to some final time t_f, the velocity states at time t_i can be related to the velocity states at time t_f through the following expressions,

$$ {}^{I}\dot{\bar{d}}_f - {}^{I}\dot{\bar{d}}_i = -(1-\mu)\int_{t_i}^{t_f}\frac{\bar{d}}{d^3}dt - \mu\int_{t_i}^{t_f}\frac{\bar{f}}{f^3}dt - \mu\int_{t_i}^{t_f}\frac{\bar{r}_m}{r_m^3}dt \quad , \tag{2.42} $$

$$ {}^{I}\dot{\bar{f}}_f - {}^{I}\dot{\bar{f}}_i = -(1-\mu)\int_{t_i}^{t_f}\frac{\bar{d}}{d^3}dt - \mu\int_{t_i}^{t_f}\frac{\bar{f}}{f^3}dt + (1-\mu)\int_{t_i}^{t_f}\frac{\bar{r}_m}{r_m^3}dt \quad , \tag{2.43} $$

$$ {}^{I}\dot{\bar{r}}_{m_f} - {}^{I}\dot{\bar{r}}_{m_i} = -\int_{t_i}^{t_f}\frac{\bar{r}_m}{r_m^3}dt \quad . \tag{2.44} $$

Integrating again from t_i to t_f yields the expressions for the position states,

$$ \begin{aligned} \bar{d}_f - \bar{d}_i = {} & (t_f - t_i)\,{}^{I}\dot{\bar{d}}_i - (1-\mu)\int_{t_i}^{t_f}\int_{t_i}^{t_f}\frac{\bar{d}}{d^3}dtdt - \mu\int_{t_i}^{t_f}\int_{t_i}^{t_f}\frac{\bar{f}}{f^3}dtdt \\ & -\mu\int_{t_i}^{t_f}\int_{t_i}^{t_f}\frac{\bar{r}_m}{r_m^3}dtdt \quad , \end{aligned} \tag{2.45} $$

$$ \begin{aligned} \bar{f}_f - \bar{f}_i = {} & (t_f - t_i)\,{}^{I}\dot{\bar{f}}_i - (1-\mu)\int_{t_i}^{t_f}\int_{t_i}^{t_f}\frac{\bar{d}}{d^3}dtdt - \mu\int_{t_i}^{t_f}\int_{t_i}^{t_f}\frac{\bar{f}}{f^3}dtdt \\ & +(1-\mu)\int_{t_i}^{t_f}\int_{t_i}^{t_f}\frac{\bar{r}_m}{r_m^3}dtdt \quad , \end{aligned} \tag{2.46} $$

$$ \bar{r}_{m_f} - \bar{r}_{m_i} = (t_f - t_i)\,{}^{I}\dot{\bar{r}}_{m_i} - \int_{t_i}^{t_f}\int_{t_i}^{t_f}\frac{\bar{r}_m}{r_m^3}dtdt \quad . \tag{2.47} $$

Equations (2.42), (2.43), (2.44), and (2.45), (2.46), (2.47) are exact representations of the motion in the R3BP. If the integrals in these expressions could be evaluated, the complete analytical solution to the R3BP would be available. As it is, only the integrals for the position and velocity states corresponding to the smaller primary $(\bar{r}_m, \dot{\bar{r}}_m)$ relative to the larger can be resolved analytically. Since the mass of the spacecraft is assumed to be infinitesimal with respect to the primaries, a solution to the two body problem can be used to evaluate the integral in the velocity expression

in Equation (2.44), that is,

$$\begin{aligned} {}^{I}\dot{\bar{r}}_{m_f} - {}^{I}\dot{\bar{r}}_{m_i} &= -\int_{t_i}^{t_f} \frac{\bar{r}_m}{r_m^3} dt \ , \\ &= {}^{I}\dot{\bar{r}}_{m_{i1f}} - {}^{I}\dot{\bar{r}}_{m_i} \quad = \quad {}^{I}\dot{\bar{r}}_{m_f} - {}^{I}\dot{\bar{r}}_{m_{f1i}} \quad . \end{aligned} \tag{2.48}$$

Similarly, the double integral in the position expression, Equation (2.47), can be rewritten as

$$\begin{aligned} \bar{r}_{m_f} - \bar{r}_{m_i} - (t_f - t_i)\,{}^{I}\dot{\bar{r}}_{m_i} &= -\int_{t_i}^{t_f} \int_{t_i}^{t_f} \frac{\bar{r}_m}{r_m^3} dt dt \ , \\ &= \bar{r}_{m_{i1f}} - \bar{r}_{m_i} \quad = \quad \bar{r}_{m_f} - \bar{r}_{m_{f1i}} \quad . \end{aligned} \tag{2.49}$$

The subscript notation $\bar{X}_{\alpha\beta\gamma}$, as defined by S. Wilson,[16] represents the two body propagation of the state $\bar{X}$ at time t_α to the state at time t_γ under the gravitational influence of body β. (Note that "body β" simply reflects the gravitational parameter Gm_β in the two body equations.) Thus, the states $(\bar{r}_{m_{f1i}}, {}^{I}\dot{\bar{r}}_{m_{f1i}})$ represent the backwards propagation of the state $(\bar{r}_{m_f}, {}^{I}\dot{\bar{r}}_{m_f})$ at t_f to the time t_i using the value 1 as the gravitational parameter. The value 1 is used as the parameter since the effects of the second primary are included, and by definition, the non-dimensional mass of the primary system is unity. Similarly, $(\bar{r}_{m_{i1f}}, {}^{I}\dot{\bar{r}}_{m_{i1f}})$ is the state of the smaller primary at the final time t_f due to forward propagation from the initial state at time t_i. It should be noted, however, that in this analysis, the state of any gravitational source (e.g., the Moon) is evaluated from ephemeris data. This is still consistent with the assumption that the motion of the primaries is known, a priori.

Since the remaining integrals in Equations (2.42), (2.43), (2.45), and (2.46) cannot be evaluated analytically, some approximations are required in order to obtain analytical expressions for the position and velocity of the spacecraft. Noting that, near the larger primary, the perturbation terms due to the smaller primary are negligible compared to the dominant gravity term, it is reasonable to neglect the integrals involving $\bar{f}$ and $\bar{r}_m$ in the expressions for ${}^{I}\dot{\bar{d}}$ and $\bar{d}$ (Equations (2.42) and (2.45)). Similarly, near the smaller primary, the integrals involving $\bar{d}$ and $\bar{r}_m$ can be neglected in the expressions for ${}^{I}\dot{\bar{f}}$ and $\bar{f}$ (Equations (2.43) and (2.46)).

The implication of these observations can be illustrated by an example. Suppose that a spacecraft trajectory originates in a region dominated by the Earth's gravity at some time t_i and the terminal point of the path is in a region dominated by the Moon's gravitational field at some time t_f. It is reasonably accurate to approximate the Earth relative position and velocity states $(\bar{d}_\tau, {}^I\dot{\bar{d}}_\tau)$ at some interior time τ as states associated with an Earth-centered conic that is propagated from the state at t_i (near the Earth) to the state at τ. This is a better estimate of the geocentric state than would be obtained by using an Earth-centered conic propagated backwards from t_f (near the Moon) to represent time τ. Employing the subscript notation, the geocentric position state at time τ is approximated as

$$\bar{d}_\tau \cong \bar{d}_{i(1-\mu)\tau} \quad , \tag{2.50}$$

and the geocentric velocity state is

$${}^I\dot{\bar{d}}_\tau \cong {}^I\dot{\bar{d}}_{i(1-\mu)\tau} \quad . \tag{2.51}$$

Similarly, it would be expected that a Moon-centered conic propagated backwards in time from the state at t_f to the state at τ would be a better approximation of the Moon relative position and velocity states $(\bar{f}_\tau, {}^I\dot{\bar{f}}_\tau)$ at time τ. Thus, the selenocentric position state is approximated as

$$\bar{f}_\tau \cong \bar{f}_{f\mu\tau} \quad , \tag{2.52}$$

and the selenocentric velocity state is

$${}^I\dot{\bar{f}}_\tau \cong {}^I\dot{\bar{f}}_{f\mu\tau} \quad , \tag{2.53}$$

both evaluated at time τ.

Recalling that the spacecraft is moving from an Earth dominated region at the initial time to a Moon dominated region at the final time, the final state $(\bar{f}, {}^I\dot{\bar{f}})$ is obtained in Moon relative coordinates. Thus, the original three body expressions for the selenocentric state, Equations (2.43) and (2.46), are approximated

by evaluating the necessary integrals using the previous approximations in Equations (2.50), (2.51), (2.52), and (2.53). This produces the following approximation for the Moon relative velocity state relationship from Equation (2.43),

$$\begin{aligned} {}^{I}\dot{\bar{f}}_f - {}^{I}\dot{\bar{f}}_i &\cong -\mu \int_{t_i}^{t_f} \frac{\bar{f}_{f\mu\tau}}{f^3_{f\mu\tau}} d\tau - (1-\mu)\int_{t_i}^{t_f} \frac{\bar{d}_{i(1-\mu)\tau}}{d^3_{i(1-\mu)\tau}} d\tau + (1-\mu)\int_{t_i}^{t_f} \frac{\bar{r}_m}{r^3_m} d\tau \quad , \\ &\cong {}^{I}\dot{\bar{f}}_f - {}^{I}\dot{\bar{f}}_{f\mu i} + {}^{I}\dot{\bar{d}}_{i(1-\mu)f} - {}^{I}\dot{\bar{d}}_i - (1-\mu)[{}^{I}\dot{\bar{r}}_{m_f} - {}^{I}\dot{\bar{r}}_{m_i}] \quad . \end{aligned} \tag{2.54}$$

Combining terms yields an expression for the Moon relative velocity state at the initial time t_i,

$${}^{I}\dot{\bar{f}}_{f\mu i} \cong [{}^{I}\dot{\bar{d}}_{i(1-\mu)f} - {}^{I}\dot{\bar{r}}_{m_f}] + \mu[{}^{I}\dot{\bar{r}}_{m_f} - {}^{I}\dot{\bar{r}}_{m_i}] \quad . \tag{2.55}$$

Similarly, the initial position state relative to the Moon at time t_i is approximated as

$$\bar{f}_{f\mu i} \cong [\bar{d}_{i(1-\mu)f} - \bar{r}_{m_f}] - (t_f - t_i)[{}^{I}\dot{\bar{d}}_{i(1-\mu)f} - {}^{I}\dot{\bar{r}}_{m_f}] + \mu[\bar{r}_{m_f} - \bar{r}_{m_i} - (t_f - t_i){}^{I}\dot{\bar{r}}_{m_f}] \quad . \tag{2.56}$$

The two expressions in Equations (2.55) and (2.56) are estimates of some initial state relative to the Moon $(\bar{f}_{f\mu i}, {}^{I}\dot{\bar{f}}_{f\mu i})$ at time t_i. When this initial state is propagated forward in time from t_i to t_f along a Moon-centered conic, a three body approximation to the final state of the spacecraft relative to the Moon is obtained. Employing the double subscript notation of Spencer,[14] Equations (2.55) and (2.56) can be used to evaluate the multi-conic approximation to the final state as

$${}^{I}\dot{\bar{f}}_f = \left[{}^{I}\dot{\bar{f}}_{f\mu i}\right]_{i\mu f} \quad , \tag{2.57}$$

$$\bar{f}_f = \left[\bar{f}_{f\mu i}\right]_{i\mu f} \quad , \tag{2.58}$$

See Wilson[15] for similar expressions for a trajectory that departs from a point located in a region dominated by the Moon's gravity field and terminates in a region where the Earth's influence is dominant.

2.4.2 Standard Multi-Conic Algorithm

The expressions in Equations (2.55) – (2.58) represent the multi-conic approximations for the motion in R3BP, yet the contribution of each term to the solution is

not readily apparent. In practice, implementation of these approximations in a multi-conic procedure is straightforward and highly intuitive. The steps in an algorithm developed by Byrnes and Hooper[17] (see Figure 2.3) for approximating the motion of a spacecraft moving, for example, from an Earth dominated gravity field towards a Moon dominated gravity field are:

Step 1. Propagate an Earth-centered conic forward in time from the geocentric position and velocity state at time t_i ($\bar{X}_i^{EI}$) to the geocentric state at the final time t_f ($\overset{*}{\bar{X}}_f^{EI}$), where $\bar{X}$ denotes position and velocity .

Step 2. Transform the Earth relative state at the final time ($\overset{*}{\bar{X}}_f^{EI}$) to a Moon relative state ($\overset{*}{\bar{X}}_f^{MI}$).

Step 3. Add any perturbations to the state at the end of Step 2. These perturbing terms are due to any additional forces modeled in the problem and to the motion of the primaries during propagation from t_i to t_f.

Step 4. Propagate backwards in time from t_f to t_i in the direction opposite to the selenocentric velocity at $\overset{*}{\bar{X}}_f^{MI}$. This is called the field free trajectory, since there is no active gravity field, only a constant velocity propagation backwards in time. This segment is thus a straight line path in the Moon Inertial frame.

Step 5. Propagate a Moon-centered conic forward in time from the Moon relative state at time t_i ($\overset{*}{\bar{X}}_i^{MI}$), at the end of Step 4, to obtain the approximation of the final state relative to the Moon at time t_f ($\bar{X}_f^{MI}$).

So, Step 1 essentially includes the effects of the Earth gravity on the spacecraft's motion, while Step 3 incorporates the perturbations due to such perturbing forces as solar gravity or solar radiation pressure. (Recall that if the solar gravity is included as a perturbation in Step 3, then the multi-conic analysis can be used as an approximation to the restricted four body problem.) Step 4, then, in essence, "resets" the time back to the initial time t_i, so that the Moon centered propagation in Step 5 can incorporate the lunar gravity effects on the motion of the spacecraft. The final state

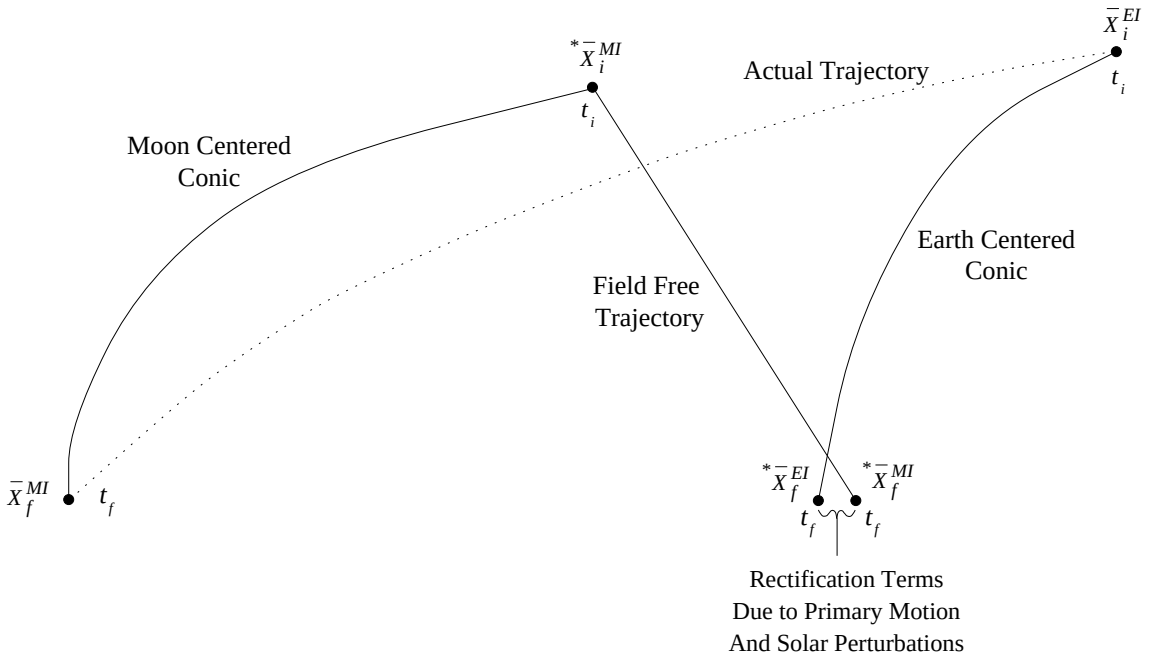

Figure 2.3. Diagram of a Single Multi-Conic Step

at time t_f ($\bar{X}_f^{MI}$), from Step 5, is the multi-conic estimate of the final selenocentric state in the R3BP given the initial geocentric state at t_i ($\bar{X}_i^{EI}$). Note that the algorithm estimates *only* the final state at time t_f given the initial state at time t_i; the algorithm is not an attempt to determine the path between the two states. Note also that the superscript (*) denotes an "interior pseudo state."[16] In actuality, these pseudo states do not exist in physical space; they are purely a result of the multi-conic algorithm. Multi-conics cannot accurately represent these interior states, and only yields an approximation of the final state of the trajectory, given some initial state. However, as the step size $\Delta t = t_f - t_i$ is reduced, a series of discrete states along the trajectory can be obtained. This discretized solution becomes increasingly accurate as Δt tends to zero.

2.4.3 Pseudostate Theory

Application of the multi-conic technique, as described above, is very successful at approximating specific state vectors in the restricted three and four body problems.

However, the algorithm becomes less effective if the trajectory includes a close passage of the second primary (in this case, the Moon). Since the modeling of the lunar flybys is one of the primary reasons for using multi-conics in the analysis of the restricted four body problem, a modified version of the multi-conic algorithm must be employed. This modified algorithm, developed by S. Wilson[16] in conjunction with the Byrnes and Hooper algorithm, is based on Pseudostate Theory. The basic approximations are the same as those associated with the previous multi-conic algorithms, however, Pseudostate Theory effectively models trajectories on hyperbolic orbits with respect to the second primary.

The approximations employed in the development of pseudostate theory are consistent with those discussed for the multi-conic algorithm in Section 2.4.1, but the pseudostate approach combines the two types of algorithms (Earth to Moon, and Moon to Earth) into a single sequence. That is, the pseudostate algorithm is an Earth to Moon series of multi-conic steps followed by a Moon to Earth multi-conic algorithm, overlapped at the lunar periapsis point. Similar to the procedures in S. Wilson[16] and Byrnes,[20] an algorithm (see Figure 2.4) to approximate a trajectory that includes a lunar encounter (periapsis) is represented in the following steps:

Step 1. Propagate an Earth-centered conic forward in time from the geocentric position and velocity state at time t_i ($\bar{X}_i^{EI}$) to the Earth relative state at the estimated lunar periapsis time t_p ($\overset{*}{\bar{X}}_1^{EI}$).

Step 2. Transform the geocentric state ($\overset{*}{\bar{X}}_1^{EI}$) at the end of Step 1 to a selenocentric state ($\overset{*}{\bar{X}}_1^{MI}$).

Step 3. Propagate a field free segment backwards in time, in the direction opposite to the selenocentric velocity at time t_p (point 1^*) until the trajectory punctures the "Pseudostate Transformation Sphere" at some time $t_p - \Delta t_{arr}$ with corresponding state $\overset{*}{\bar{X}}_a^{MI}$.

Step 4. Propagate a Moon-centered conic forward in time from the Moon relative state at time $t_p - \Delta t_{arr}$ (point a^*), at the end of Step 3, to lunar periapsis.

Step 5. Add effects due to perturbing forces such as solar gravity or solar radiation pressure to the lunar periapsis state.

Step 6. Propagate the perturbed lunar periapsis state forward until the trajectory again punctures the Pseudostate Transformation Sphere at a later time $t_p + \Delta t_{dep}$ corresponding to the state ${}^{*}\bar{X}_b^{MI}$.

Step 7. Propagate a second field free segment backwards in time, in the direction opposite to the selenocentric velocity at time $t_p + \Delta t_{dep}$ (point b^*) to the time t_p (from Step 1) to produces the state ${}^{*}\bar{X}_2^{MI}$.

Step 8. Transform the Moon relative state at the end of Step 7 (${}^{*}\bar{X}_2^{MI}$) to an Earth relative state (${}^{*}\bar{X}_2^{EI}$).

Step 9. Propagate an Earth-centered conic from the geocentric position and velocity state at time t_p (${}^{*}\bar{X}_2^{EI}$) forward in time to obtain the approximation to the final Earth relative state at time t_f (${}^{*}\bar{X}_f^{EI}$).

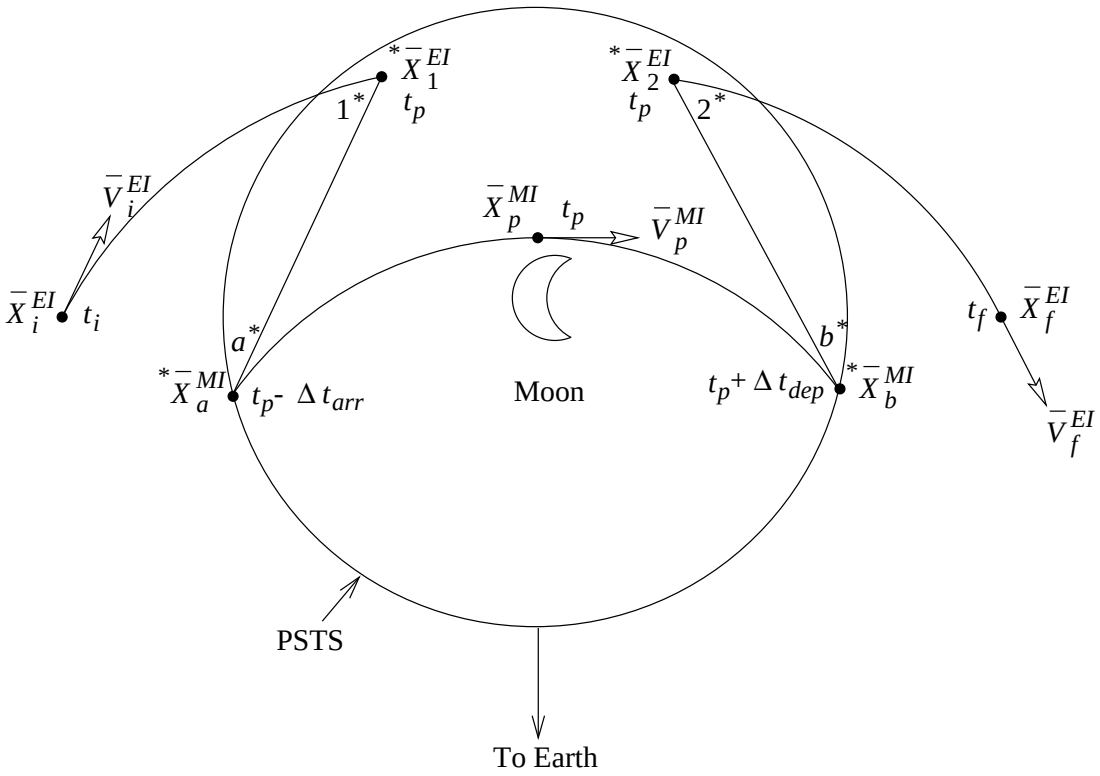

Figure 2.4. Diagram of the Pseudostate Theory (based on Byrnes,[20] Figure 1)

In the application of this algorithm, the Pseudostate Transformation Sphere (PSTS) is introduced. This is an arbitrary sphere about the Moon that is used by the pseudostate algorithm to enhance the solution process, as described in S. Wilson,[16] Byrnes,[20] and Sweetser.[21] Its size is commonly denoted either in units of radial distance from the Moon or in time from lunar periapsis. The determination of the size of the PSTS along with explicit definitions of Δt_{arr} and Δt_{dep} is discussed in detail in Sweetser[21] and Wilson.[15]

Note that the spacecraft may pass through perilune at a time that differs from the estimated perilune time t_p. However, the original estimate, t_p, is still used throughout the rest of the algorithm to insure consistency. This implies that any solution algorithm will generally be iterative to converge upon the "true" perilune state and time. Consistent with the discussion in Section 2.4.1, it should be noted that the interior states $(1^*, a^*, b^*, 2^*)$ do not physically exist. However, since pseudostate theory is, in fact, an overlapping of the two multi-conic algorithms at the lunar periapsis point, it does yield a good approximation of the perilune state, as well as the initial and final states. This will be useful later when the pseudostate algorithm is applied to restricted four body problems that include lunar swingbys.

For completeness, there are four degenerate cases to be considered. If the initial state $(\bar{X}_i^{EI})$ is inside the PSTS, the first three steps in the algorithm are bypassed and propagation begins with Step 4, that is, the initial state is transformed to selenocentric coordinates and propagated along a Moon-centered conic until the trajectory reaches the PSTS. In effect, this is simply a Moon to Earth type multi-conic algorithm. Likewise, if the final state is inside the PSTS, the pseudostate algorithm becomes an Earth to Moon type algorithm. Also note that if the time corresponding to the end of the first field free segment is prior to the initial time, the field free is terminated at the initial time and the Moon-centered conic begins at this point. Similarly, if the time that the Moon-centered conic pierces the PSTS at point b^* is beyond the final time, the conic is terminated at the final time and the second field free segment begins at this point.

Since this general approach effectively includes the influence of the second primary on the motion of the spacecraft, pseudostate theory will be used in addition to the standard multi-conic algorithm to improve the initial solution and provide better modeling of any lunar encounters.

2.4.4 State Transition Matrices in Multi-Conic Methods

The application of these methods to determine solutions in the four body problem necessitates the development of a method to compute state transition matrices for both single-direction multi-conic analysis and the pseudostate approximation. An added benefit, and what is eventually an integral component in the application of multi-conic methods to the motion in the four body problem, is the availability of analytical expressions for the state transition matrix. Although, in general, no analytical solution is available for the STM in the R3BP, the use of two body conics in the multi-conic approximations allows analytical representations for the elements of the STM to be developed from two body STM's. A number of authors, including Goodyear[22] and Hitzl,[23] have developed analytical representations for the partials in the STM for the two body problem. These partials are of two types, either elliptic or hyperbolic, corresponding to the conic reference orbit of interest. The expressions for the partials in each case are different, although very similar, and can be found in Hitzl[23] for the elliptic two body STM, and Spencer[14] for the STM in the hyperbolic case. Both conic cases are also summarized in Wilson.[15]

The STM for a single multi-conic step may be determined by sequentially multiplying the STM's corresponding to each propagation step in the algorithm. As an example, consider a spacecraft moving from the Earth to the Moon. The first step would yield an STM from propagation of the Earth-centered conic, using the appropriate two body solution. This matrix relates the initial geocentric state $\bar{X}_i^{EI}$ at time t_i to the final state ${}^{*}\bar{X}_f^{EI}$ of the Earth-centered conic at time t_f , and is denoted Φ_{fi}^{EC} (EC for Earth Conic). Next, the final geocentric state is transformed to a selenocentric state and the effects due to any perturbations are added. The transformation

and addition of the indirect effects due to primary motion do not affect the STM; however, the perturbing effects due to solar gravity, for instance, can be modeled in a state transition format.

Since the multi-conic step size is generally small (approximately 6 hours), the perturbation from the solar gravity can be approximated by assuming a constant acceleration over the given time step. This constant is taken to be the average acceleration on the spacecraft, that is

$$\bar{a}_{ave} = \frac{\bar{a}_f + \bar{a}_i}{2} \quad , \tag{2.59}$$

where $\bar{a}_i$ and $\bar{a}_f$ are the accelerations due to solar gravity at the initial and final times along the Earth conic segment. The acceleration on the spacecraft due to the Sun is written as

$$\bar{a} = -\mu_s \left[\frac{\bar{R}_{ssc}}{R_{ssc}^3} - \frac{\bar{R}_{se}}{R_{se}^3} \right] \quad , \tag{2.60}$$

where μ_s is the non-dimensional gravitational parameter of the Sun, $\bar{R}_{se}$ is the position vector of the Earth relative to the Sun, and $\bar{R}_{ssc}$ is the position vector of the spacecraft with respect to the Sun. This acceleration is written for a base point relative to the Earth so that,

$$\bar{R}_{ssc} = \bar{R}_{se} + \bar{R}_{esc} \quad , \tag{2.61}$$

evaluated at the specified time. (Note that $\bar{R}_{esc}$ is the position vector of the spacecraft with respect to the Earth.) Evaluating this constant average acceleration and integrating over the time interval produces the following perturbations for position and velocity

$$\bar{R}_{pert}(\tau) = \frac{1}{2}\bar{a}_{ave}\left(\tau - t_i\right)^2 \quad , \tag{2.62}$$

$$\bar{V}_{pert}(\tau) = \bar{a}_{ave}\left(\tau - t_i\right) \quad , \tag{2.63}$$

at some time τ.

Consider the states prior to any coordinate transformation, and denote $\bar{X}_1$ as the initial position and velocity state on the Earth centered conic, $\bar{X}_2$ as the final state

along the Earth conic, and $\bar{X}_3$ as the perturbed state due to the addition of the solar gravity. The change in state from $\bar{X}_2$ to $\bar{X}_3$ can be written as

$$\bar{R}_3 = \bar{R}_2 + \bar{R}_{pert}(\tau) \quad , \tag{2.64}$$

$$\bar{V}_3 = \bar{V}_2 + \bar{V}_{pert}(\tau) \quad . \tag{2.65}$$

The STM associated with this perturbation is expressed as a matrix of partial derivatives relating changes in $\bar{X}_3$ to changes in $\bar{X}_2$ (both at time t_f), and can be written

$$\Phi(t_f, t_f) = \Phi_{ff}^{pert} = \frac{\partial \bar{X}_3}{\partial \bar{X}_2} = \begin{bmatrix} \frac{\partial \bar{R}_3}{\partial \bar{R}_2} & \frac{\partial \bar{R}_3}{\partial \bar{V}_2} \\ \frac{\partial \bar{V}_3}{\partial \bar{R}_2} & \frac{\partial \bar{V}_3}{\partial \bar{V}_2} \end{bmatrix} \quad . \tag{2.66}$$

Since both $\bar{X}_2$ and $\bar{X}_3$ are associated with time t_f, the partials in this STM can be evaluated on the reference solution determined in Equations (2.64) and (2.65), keeping in mind that $\bar{a}_{ave}$ depends on $\bar{R}_2$ as well as $\bar{R}_1$ (the initial state on the Earth Conic segment). The partials are written explicitly as

$$\frac{\partial \bar{R}_3}{\partial \bar{R}_2} = I_3 + \frac{\partial \bar{R}_{pert}}{\partial \bar{R}_2} + \frac{\partial \bar{R}_{pert}}{\partial \bar{R}_1}\frac{\partial \bar{R}_1}{\partial \bar{R}_2} \quad , \tag{2.67}$$

$$\frac{\partial \bar{R}_3}{\partial \bar{V}_2} = \frac{\partial \bar{R}_{pert}}{\partial \bar{R}_1}\frac{\partial \bar{R}_1}{\partial \bar{V}_2} \quad , \tag{2.68}$$

$$\frac{\partial \bar{V}_3}{\partial \bar{R}_2} = \frac{\partial \bar{V}_{pert}}{\partial \bar{R}_2} + \frac{\partial \bar{V}_{pert}}{\partial \bar{R}_1}\frac{\partial \bar{R}_1}{\partial \bar{R}_2} \quad , \tag{2.69}$$

$$\frac{\partial \bar{V}_3}{\partial \bar{V}_2} = I_3 + \frac{\partial \bar{V}_{pert}}{\partial \bar{R}_1}\frac{\partial \bar{R}_1}{\partial \bar{V}_2} \quad . \tag{2.70}$$

The partials $\frac{\partial \bar{R}_1}{\partial \bar{R}_2}$ and $\frac{\partial \bar{R}_1}{\partial \bar{V}_2}$ are available from the inverse of the state transition matrix corresponding to the Earth Conic segment. It is convenient to express the 6x6 STM as four 3x3 sub-matrices, such that the STM for the EC segment is

$$\Phi_{21}^{-1} = \Phi_{12} = \Phi(t_1, t_2) = \begin{bmatrix} \frac{\partial \bar{R}_1}{\partial \bar{R}_2} & \frac{\partial \bar{R}_1}{\partial \bar{V}_2} \\ \frac{\partial \bar{V}_1}{\partial \bar{R}_2} & \frac{\partial \bar{V}_1}{\partial \bar{V}_2} \end{bmatrix} \quad , \tag{2.71}$$

$$= \begin{bmatrix} A_{12} & B_{12} \\ C_{12} & D_{12} \end{bmatrix} \quad , \tag{2.72}$$

and hence,

$$\frac{\partial \bar{R}_1}{\partial \bar{R}_2} = A_{12} \quad ; \quad \frac{\partial \bar{R}_1}{\partial \bar{V}_2} = B_{12} \quad . \tag{2.73}$$

This notation is used extensively throughout the text. The remaining partial derivatives from Equations (2.67) – (2.70) can be evaluated from the average acceleration, that is,

$$\frac{\partial \bar{R}_{pert}}{\partial \bar{R}_1} = \frac{\Delta t^2}{4}\frac{\partial \bar{a}_{ave}}{\partial \bar{R}_1} = \frac{\Delta t^2}{4}\frac{\partial \bar{a}_1}{\partial \bar{R}_1} \quad , \tag{2.74}$$

$$\frac{\partial \bar{R}_{pert}}{\partial \bar{R}_2} = \frac{\Delta t^2}{4}\frac{\partial \bar{a}_2}{\partial \bar{R}_2} \quad , \tag{2.75}$$

$$\frac{\partial \bar{V}_{pert}}{\partial \bar{R}_1} = \frac{\Delta t}{2}\frac{\partial \bar{a}_1}{\partial \bar{R}_1} \quad , \tag{2.76}$$

$$\frac{\partial \bar{V}_{pert}}{\partial \bar{R}_2} = \frac{\Delta t}{2}\frac{\partial \bar{a}_2}{\partial \bar{R}_2} \quad , \tag{2.77}$$

where

$$\frac{\partial \bar{a}_j}{\partial \bar{R}_j} = -\frac{\mu_s}{R_{ssc}^3}\left[I_3 - \frac{3\bar{R}_{ssc}\bar{R}_{ssc}^T}{R_{ssc}^2}\right] \quad , \tag{2.78}$$

evaluated at the specified time.

The next STM along the path is that associated with the field free trajectory (denoted by superscript FF). The field free STM relates ${}^*\bar{X}_f^{MI}$ to ${}^*\bar{X}_i^{MI}$ and is expressed simply as

$$\Phi_{if}^{FF} = \begin{bmatrix} I_3 & -\Delta t \cdot I_3 \\ \emptyset_3 & I_3 \end{bmatrix} \quad . \tag{2.79}$$

Since the field free segment is a constant velocity segment, the STM is just a linear function of the length of the propagation time $\Delta t = t_f - t_i$. In the final step of the algorithm, a Moon-centered conic (MC) is propagated forward in time to obtain the approximation to the final selenocentric state. The STM corresponding to this segment, denoted as Φ_{fi}^{MC}, therefore relates the state ${}^*\bar{X}_i^{MI}$ to the final state $\bar{X}_f^{MI}$. Because the multi-conic trajectory is continuous and since all the STM's are defined relative to the EI or MI coordinate frame, the determination of the complete STM that maps the initial state $\bar{X}_i^{EI}$ to the final state $\bar{X}_f^{MI}$ involves multiplying these four matrices sequentially to obtain

$$\Phi_{fi}^{step} = \Phi_{fi}^{MC}\ \Phi_{if}^{FF}\ \Phi_{ff}^{pert}\ \Phi_{fi}^{EC} \quad , \tag{2.80}$$

where

$$\delta \bar{X}_f^{MI} = \Phi_{fi}^{step} \, \delta \bar{X}_i^{EI} \quad . \tag{2.81}$$

A similar STM can be computed for each of the multi-conic steps along a given trajectory. The STM's from each multi-conic step are then sequentially multiplied together to create the state transition matrix for the entire trajectory. This complete matrix corresponding to the multi-conic approximation of the trajectory is employed in various differential corrections procedures to target desired endstates in the restricted four body problem.

A state transition matrix can also be computed for the pseudostate approximation using a similar sequential STM computation for each of the propagation steps in the pseudostate algorithm. This pseudostate STM is crucial in the determination of the lunar swingby, and is useful in determining a solution to the three body Lambert problem. Given two position vectors and a time of flight, it is often desired to determine a solution that passes through the two positions in the specified time. This problem is termed Lambert's problem, and its solution in the two body problem is well known. However, in the three body problem, no known solution exists for determining the path that passes through the two points in the given time.

Many different methods have been attempted to approximate the solution to this problem, but a particularly appropriate solution approach was proposed by Byrnes[20] to solve the three body Lambert problem (3BLP) using pseudostate theory to represent trajectories that pass close to the second primary, and can be modeled as hyperbolic with respect to that primary. Using pseudostate theory and the resulting state transition matrices in a differential corrections process, it is possible to determine a solution to the 3BLP that passes through both positions in the given flight time. This procedure forms the basis of the targeting scheme to identify a solution that passes through the patch points before and after the lunar flyby, or in other words, to bridge the "gaps" left by the poor modeling of the lunar encounter in the initial guess. The solution process, similar to the one used by Byrnes[20] to solve the 3BLP is discussed in Spencer[14] and Wilson.[15]

2.5 Dynamical Systems Theory

Multi-conic analysis and pseudostate theory constitute one type of approximation to the motion in the three body problem (or four body problem if solar perturbations are included). As will be demonstrated later, this approximation is an integral part of the intermediate step in the three step process, but multi-conic analysis is not the only method available to gain insight into the motion in the three body problem. A combination of analytical expressions and numerical techniques from dynamical systems theory (DST) can be used very effectively to determine specific types of trajectory arcs directly in the three body regime. Of course, since no analytical solution to this problem is available, extensive numerical analysis is still necessary. Dynamical systems theory is employed, then, to direct the numerical analysis in the determination of desired trajectories and trajectory arcs that reflect the natural dynamics of the system.

2.5.1 Libration Point Orbits

One motivation for investigating solution arcs in the three body problem is the existence of certain types of three body orbits. To briefly review these solutions and their significance, it is most convenient to present the solutions in the context of the CR3BP. Thus, at least initially, assume that the primaries are in circular orbits with respect to their barycenter. While various numerical solutions exist in the circular restricted three-body problem, two types that are of particular interest here are the collection of periodic halo and quasi-periodic Lissajous solutions near the collinear libration points. Various examples of such solutions are available in a number of three-body systems.[10,24–29]

Precisely periodic halo orbits do not actually exist in a complex model, e.g., one that employs ephemeris data for the states of the primaries. However, the quasi-periodic Lissajous trajectories do exist and can be exploited to obtain solutions that remain bounded over the time frames of interest. Using the Richardson and Cary

expansion[25] as an initial guess, the algorithm in Howell and Pernicka[29] is utilized to produce the trajectory that is plotted in Figure 2.5. This is an example of a Lissajous trajectory near the L_1 libration point (between the Earth and the Sun) in the Sun-Earth/Moon barycenter three-body system; it is determined using JPL ephemerides (DE202) for the states of the Sun, Earth, and Moon. The three planar projections in the figure have an origin at the L_1 libration point, and the three coordinate axes are defined consistent with the barycentric rotating frame, described previously. The

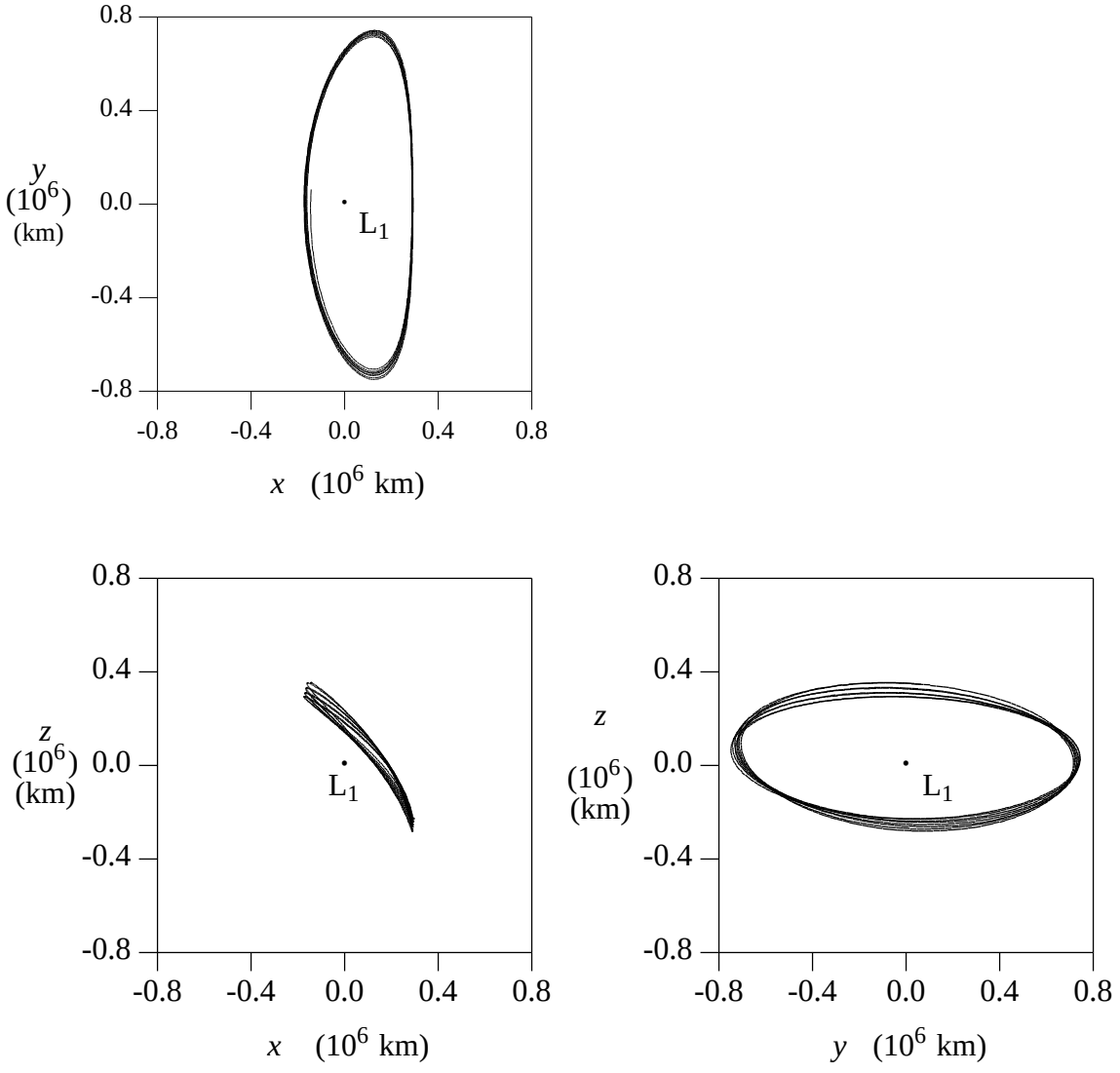

Figure 2.5. Lissajous Trajectory – Courtesy: Brian Barden[1]

Lissajous trajectory in the figure is characterized by an amplitude of motion in the $\hat{x}$ direction, denoted A_x, of approximately 230,000 km, while $A_y = 745{,}000$ km and $A_z = 320{,}000$ km. The portion of the Lissajous shown here originates on March 3, 2001 and has a total flight time of approximately 1399 days, corresponding to approximately 7.75 revolutions. Note that if this solution were perfectly periodic, (i.e., a halo orbit) the trajectory would close upon itself in all three projections; however, the Lissajous orbit, by definition, is not closed, as is evidenced in the figure.

2.5.2 Transfers to Libration Point Orbits

Determination of a nominal halo or Lissajous trajectory is the first part of the design process for a libration point mission. It is also necessary to determine transfer trajectories to and from the desired Libration Point Orbit (LPO). At this point, the introduction of DST as a means of dynamical analysis and design in the three-body problem is particularly appropriate. Prior to using this approach, a trial and error numerical search method was most frequently employed to design transfer trajectories. While this method has been successful for various missions, a more elegant and efficient procedure is available. Application of DST in the circular restricted three-body problem yields a relatively fast method of generating a number of different types of trajectories to and from libration point orbits.[28,30–34] This success has led to the development of a utility based on DST to produce a first guess that initiates the design process for transfer trajectories.[33] An additional benefit of DST is a better understanding of the geometry of the phase space that allows the mission designer to obtain valuable insight into the behavior of the solutions in this regime.

As discussed in detail in Barden, Howell, and Lo[34], investigations utilizing DST usually begin with special solutions, including the periodic orbits and quasi-periodic orbits described previously. Each of these solutions is an example of one of the fundamental models for the phase space, namely invariant manifolds. The concept of an invariant manifold can be simply described as follows: a collection of orbits that start on a surface and then stay on that surface for the duration of their dynamical

evolution. This basic definition can be used to characterize a variety of behaviors. In addition to the periodic and quasi-periodic solutions, there exist invariant manifolds that asymptotically approach or depart other invariant manifolds. These are called stable and unstable manifolds, respectively.[1]

In the circular three-body problem, the stable and unstable manifolds associated with periodic halo orbits are the basis for determining an initial guess for the transfer problem. The computation of the stable and unstable manifolds associated with a particular halo orbit is accomplished numerically in a procedure based on the monodromy matrix (the variational or state transition matrix after one period of the motion) associated with the halo orbit. The characteristics of the local geometry of the phase space associated with the halo orbit can be determined from the eigenvalues and eigenvectors of the monodromy matrix.

> "The local approximation of the stable (unstable) manifold involves calculating the eigenvector of the monodromy matrix that is associated with the stable (unstable) eigenvalue, and then using the state transition matrix to propagate the approximation to any point along the orbit. The eigenvalues are known to be of the following form:[27,28,30–34]
>
> $$\lambda_1 > 1 \ , \quad \lambda_2 = (1/\lambda_1) < 1 \ , \quad \lambda_3 = \lambda_4 = 1 \ ,$$
> $$\lambda_5 = \lambda_6^* \ , \quad \text{and } |\lambda_5| = |\lambda_6| = 1 \ ,$$
>
> where λ_5 and λ_6 are complex conjugates. Stable (and unstable) eigenspaces, E^s (E^u) are spanned by the eigenvectors whose eigenvalues have modulus less than one (modulus greater than one). There exist local stable and unstable manifolds, W^s_{loc} and W^u_{loc}, tangent to the eigenspaces at the fixed point and of the same dimension as the eigenspace.[35,36] Thus, for a fixed point $\bar{X}^H$ defined along the halo orbit, the one-dimensional stable (unstable) manifold is approximated by the eigenvector associated with the eigenvalue λ_2 (λ_1).
>
> First, consider the stable manifold. Let $\bar{Y}^{W^s}$ denote a six-dimensional vector that is coincident with the stable eigenvector and is scaled such that the elements corresponding to position in the phase space have been normalized. This vector serves as the local approximation to the stable manifold (W^s). Remove the fixed point $\bar{X}^H$ from the stable manifold to form two half-manifolds, W^{s^+} and W^{s^-}. Each half-manifold is itself a stable manifold consisting of a single trajectory. Now, consider some point $\bar{X}_o$ on W^{s^+}. Integrating both forward and backward in time from $\bar{X}_o$ produces W^{s^+}. Thus, conceptually, calculating a half-manifold can be

broken down into two steps: locating or approximating a point on W^{s+}, and numerically integrating from this point.

To generate the stable manifold, an algorithm has been employed that was developed to find both the stable and unstable manifolds of a second order system.[37] The algorithm, however, does not possess any inherent limit on the order of the system. Near the fixed point $\bar{X}^H$, the manifold W^{s+} is determined, to first order, by the stable eigenvector $\bar{Y}^{W^s}$. The next step is then to globalize this stable manifold. This is accomplished by numerically integrating backwards in time, such that when time is propagated forward, the resulting trajectory will asymptotically approach the reference orbit. This globalization requires an initial state that is on the stable manifold W^{s+} but displaced off of the halo orbit. To determine such an initial state, the position of the spacecraft is displaced from the halo in the direction of $\bar{Y}^{W^s}$ by some distance d_s, such that the new initial state, denoted as $\bar{X}_o^{W^s}$, is calculated as

$$\bar{X}_o^{W^s} = \bar{X}^H + d_s \, \bar{Y}^{W^s}.$$

Higher order expressions for $\bar{X}_o^{W^s}$ are available but not necessary. The magnitude of the scalar d_s should be small enough to avoid violating the linear estimate, yet not so small that the time of flight becomes too large due to the asymptotic nature of the stable manifold. A nominal value of $d_s = 200$ km is selected for the Sun-Earth/Moon barycenter system. Note that a similar procedure using the unstable eigenvalue associated with $\bar{X}^H$ can be used to approximate and generate the unstable manifold."†

This approach can be extended to determine manifold trajectories in the full four body model. The manifolds determined using this procedure are crucial in determining initial approximations for the transfer problem to and from desired halo and Lissajous orbits. For more on the application of dynamical systems theory to the n-body problem, see Barden,[33] Barden, Howell, and Lo,[34] and others.[29–32,35–37]

†Page 4, Reference [1]

3. THE THREE STEP METHODOLOGY

This chapter develops the methodology that serves as the basis for application of the three step process to determine solutions in the restricted four body problem. Each step in the process is examined in detail and the theoretical basis for the calculations is presented. First, a two body conic approximation is presented that can serve as an initial estimate for solutions involving one or more lunar gravity assists. A second type of initial estimate involving stable and unstable manifolds associated with periodic and quasi-periodic solutions in the R3BP is presented. These manifolds are useful, for example, in determining transfer trajectories to orbits about the collinear libration points. For any necessary intermediate step, the application of multi-conic techniques (as discussed in the previous chapter) to improve the initial estimate is then presented. In addition, a relationship is developed between the independent parameters that characterize a particular solution, namely the positions and times of various points along the trajectory, and the dependent variables associated with any velocity discontinuities, as well as any trajectory constraints. This linear relationship serves as the basis for improving the initial estimate sufficiently such that a fully continuous numerically integrated solution that meets the design criteria can be obtained. Lastly, a brief discussion of the equations of motion for the numerical integration process is presented, as well as the final integrated solutions for the two examples introduced in this chapter.

3.1 Initial Approximation: Conics

In order to develop a trajectory that may include one or more lunar gravity assists, an initial approximation that satisfies the specified design requirements is sought.

As a baseline, assume a solution such that all trajectory arcs can be approximated as geocentric two-body conics, thus neglecting the lunar and solar gravity effects. By specifying that each conic segment begin and/or end with a lunar encounter, an approximate multiple lunar swingby (MLS) trajectory can be created simply by "patching" these geocentric conic segments together at consecutive lunar encounter points. This type of analysis yields a useful initial approximation to the solution, and provides a basis of comparison for the final integrated trajectory.

The theoretical basis for determining lunar encounters at appropriate time intervals lies in the development of a timing condition relating the motion of the Sun, Earth, Moon, and spacecraft. The development of this timing condition and the theoretical basis for the initial conic approximation are presented in detail in Howell and Marsh,[7,38] and Marsh.[13] A brief summary of the details is presented here.

3.1.1 The Timing Condition

To construct a multiple lunar encounter trajectory, a method is required to design a series of Earth-centered conic segments that begin and/or end with lunar encounters, and are oriented in the desired direction relative to the SR frame. This approach ensures that the spacecraft and the Moon will be in the same vicinity at the appropriate times. From detailed discussions in Howell and Marsh,[7,38] and Marsh,[13] it is apparent that the determination of conic arcs that begin and end in lunar encounters can be reduced to the solution of a single algebraic equation, called the Timing Condition (TC). The functional form of this timing condition, from Howell and Marsh,[7] is an implicit algebraic function of the form

$$\mathrm{TC}(e_m,\ \phi,\ \sigma_{0,1,2},\ \xi,\ \eta\ ;\ a_c,\ e_c) = 0\ . \tag{3.1}$$

The variable e_m represents the eccentricity of the lunar orbit about the Earth with perigee at P_m. (See Figure 3.1.) The angle ϕ, also shown in the figure, describes the orientation of the spacecraft line of apsides with respect to the lunar line of apsides, measured clockwise from the $\hat{X}$ axis. (Note that the conic reference frame ($\hat{X}$,$\hat{Y}$) is

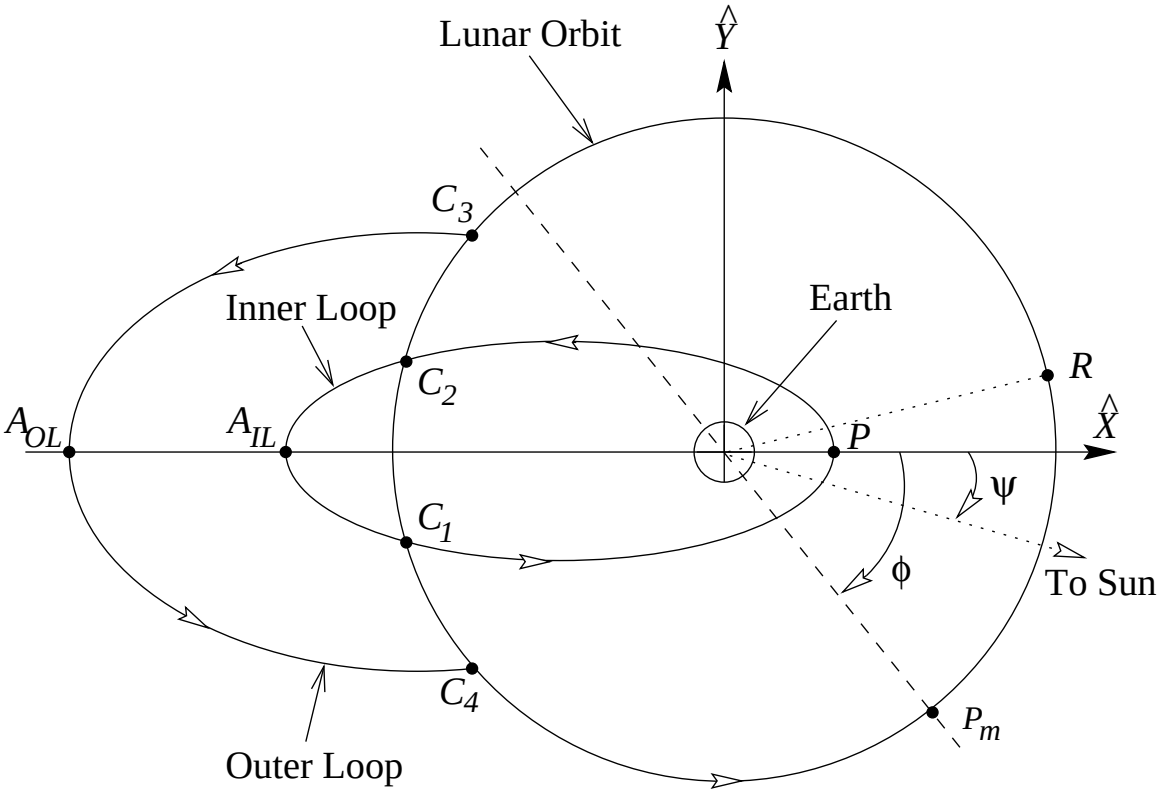

Figure 3.1. Conic Arc Definitions

defined such that $\hat{X}$ is coincident with the conic line of apsides in the general direction of the Moon at time $t = 0$, denoted as point R.) The parameters σ_i, ξ, and η are used to uniquely parameterize the Earth-centered orbit, as described in Howell and Marsh.[7]

The solution of this algebraic function yields two of the orbit parameters, a_c and e_c, associated with the conic segment. In addition, the true anomaly (θ_c) and the relative time (t_c) corresponding to the spacecraft location at the end points (C_i) are available. Note that in the conic reference frame, $t = 0$ is defined at a spacecraft crossing of the line of apsides (at perigee P, or apogee A_{OL} or A_{IL}) according to σ_2. Therefore, due to the near symmetry of the problem, the spacecraft, Earth, and Moon will be nearly collinear along the spacecraft line of apsides at $t = 0$.

3.1.2 Conic Arc Selection

Once the conic arc has been determined from the solution of the timing condition, it is necessary to orient this segment in the SR frame with respect to the Sun-Earth line (the $\hat{x}_s$ axis in the SR frame). It is assumed in the solution process that the conic orbit plane for each segment is coincident with the lunar orbit plane. (This requirement facilitates the conic selection process only and may be relaxed later.) Thus, it is possible to completely define the appropriate conic segment, as well as its orientation, in terms of the lunar orbit. The segment is represented by the orbit parameters ($a_c,\ e_c,\ \Omega_{moon},\ i_{moon},\ \theta_c,\ t_c$) at each endpoint C_i, where Ω_{moon} and i_{moon} are the argument of the ascending node and inclination of the Moon, respectively.

After the conic orbit plane is quantified, orientation of the spacecraft orbit is accomplished through identification of epochs corresponding to appropriate locations of the Sun and Moon relative to the Earth. Such epochs result from an iterative search through solar and lunar ephemerides. This process is aided by the inherent near symmetry of these consecutive collision orbits.[38] The angle ψ (see Figure 3.1) specifies the orientation of the spacecraft line of apsides with respect to the Sun-Earth line. This angle is ideally equal to 0 deg for a trajectory with anti-solar pointing apogees and equal to 180 deg for solar pointing apogees.

There are two types of solutions for the conic arcs generated by solution to the Timing Condition, as shown in Figure 3.1. The first type of conic arc is termed an "inner" loop.[13] For this type, an arc of the conic solution is selected that contains at least one perigee and some number of apogees during the time from one lunar encounter to the next. The other type of conic arc is called an "outer" loop,[13] and is characterized by conic segments that pass through at least one apogee and some number of perigees (perhaps zero) between lunar encounters.

For construction of a complete multiple lunar encounter path, a series of conic arc segments are patched together at the lunar encounters. The arcs must be properly sequenced using the conic arc selection process to ensure an orbit orientation

history consistent with the requirements. The entire process of creating a trajectory by patching these geocentric conic arc segments together is labeled Patched Conic Analysis (PCA).

This design process requires a set of input parameters that are determined from the design specifications for the mission. These parameters are used to solve for the orbital elements representing the conic arcs that comprise the initial estimate. The first input is the specification of the injection date for the MLS trajectory in Julian format (JD_1). In order to facilitate a solution, this date is frequently assumed to correspond to perigee on the first conic segment. The next inputs are the approximate lengths of the conic segments in an integer number of months (N_{mos}), and the expected number of apogees (N_{apo}) and perigees (N_{peri}). Note that if $N_{peri} > N_{apo}$ then the conic solution is the inner loop case. Conversely, if $N_{apo} > N_{peri}$ the desired conic is an outer loop.

The fifth required input parameter is an estimate of the angle ψ. Since the majority of the flight time is spent in the outer loops, it is desirable for these segments to match this specification as closely as possible. For inner loops, however, it is often desirable from a mission design standpoint to specify the perigee passage distance (R_p) in addition to ψ. This specification usually results in some loss of control over the orientation angle ψ for the segment, but since the inner loops are generally shorter in duration than the outer loops, this loss is not crucial to overall trajectory planning.

Given these inputs (JD_1, N_{mos}, N_{apo}, N_{peri}, ψ, and possibly R_p) that reflect the desirable characteristics for each Earth-centered conic, the conic arc selection algorithm solves the timing condition (TC) iteratively, as described in Marsh,[13] for the properly oriented conic arc segments that best match the mission specifications. From the solution to the TC, the orbit parameters representing the conic arcs and the dates of the lunar encounters are obtained. All conic segments are then patched together at lunar encounter points to create the two body approximation to the solution of the MLS problem.

3.1.3 Example: Multiple Lunar Swingby Trajectory

The motivation for incorporating multiple lunar swingbys into any trajectory may vary, but frequently the goal is to achieve certain orbital characteristics relative to the SR frame. The concept proposed by Farquhar and Dunham,[8] using lunar gravity assists to advance the line of apsides at the rate required to "fix" the orbit in the SR frame is one such example. To demonstrate this technique, a multiple lunar swingby trajectory has been constructed with three lunar encounters. The goal of this trajectory design is to utilize the Moon to perform orbital changes. Specifically, the lunar gravity is used to advance the line of apsides such that the apogees of the trajectory alternate from an anti-solar direction (towards L_2) to a solar pointing direction (towards L_1).

In this example, an initial date of July 17, 2009 is selected for the first perigee. For the first conic segment, a single phasing loop delivers the spacecraft to the first lunar encounter. This encounter shifts the orbit to an outer loop with apogee along the Sun-Earth line in the anti-solar direction. At the end of the second segment, another lunar encounter sets up a series of three large loops that align the trajectory to take advantage of the Moon a third time. This final encounter places the spacecraft on a conic arc with an apogee in the solar pointing direction. Table 3.1 contains a summary of the inputs to the conic arc selection algorithm. These inputs are used by the Timing Condition to determine a solution that meets the given design specifications. The table also contains the non-dimensional semi-major axis (a_c/L^*), eccentricity (e_c), and time of flight (Δt) corresponding to the conic arcs determined by the conic arc selection algorithm.

The trajectory produced by the algorithm appears in Figure 3.2 as projected onto the $\hat{X}\hat{Y}$ plane in the EI frame. This figure clearly illustrates the conic nature of the solution determined by the algorithm. It is seen that the lunar encounters are utilized to advance the line of apsides, while shifting the trajectory from one conic solution to the next. However, the key features of the solution are not evident

Table 3.1 Input/Output Parameters for Butterfly Example

Segment No.	1	2	3	4
		Inputs		
N_{mos}	1	2	6	2
N_{apo}	1	1	3	1
N_{peri}	2	0	4	0
R_p (km)	6578	–	80000	–
ψ (deg)	0.0	0.0	90.0	180.0
		Outputs		
a_c/L^*	0.55188	1.89157	1.49561	1.90476
e_c	0.96899	0.81352	0.86084	0.79041
Δt (days)	15.6917	64.6180	156.9156	65.2713

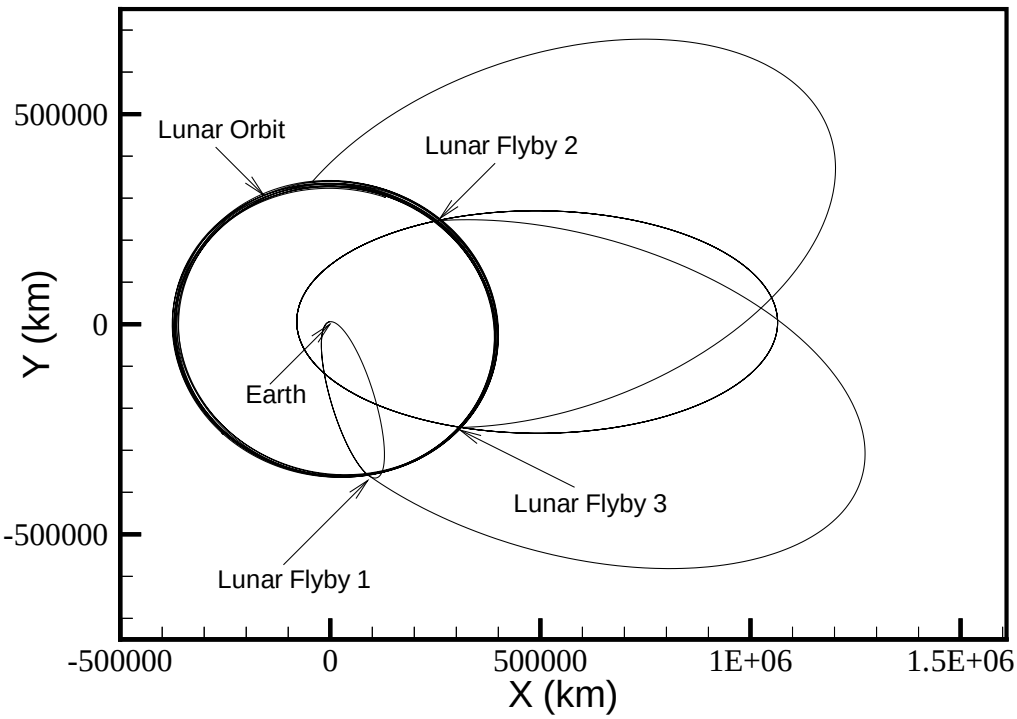

Figure 3.2. Butterfly Example – EI Projection onto $\hat{X}\hat{Y}$ plane

when the trajectory is viewed in the EI frame. If the same trajectory is now viewed as a projection onto the $\hat{x}\hat{y}$ plane in the SR frame (see Figure 3.3), the desired characteristics become evident. It is now seen that, from a single phasing loop, the first lunar encounter sets up a trajectory with an apogee in the direction of L_2 and then uses additional lunar gravity assists to alter the trajectory such that it is oriented toward L_1. This is a key distinguishing factor between this analysis and traditional patched conic methods. In this methodology, the SR frame is used as a basis for specifying trajectory characteristics. Once the "butterfly" trajectory is viewed in a more suitable frame, the given name becomes apparent.

3.2 Initial Approximation: R3BP

Another approach for construction of an initial approximation involves solutions to the restricted three body problem. One such example is a transfer from Earth to a Sun-Earth libration point orbit using zero, one, or more lunar gravity assists. In

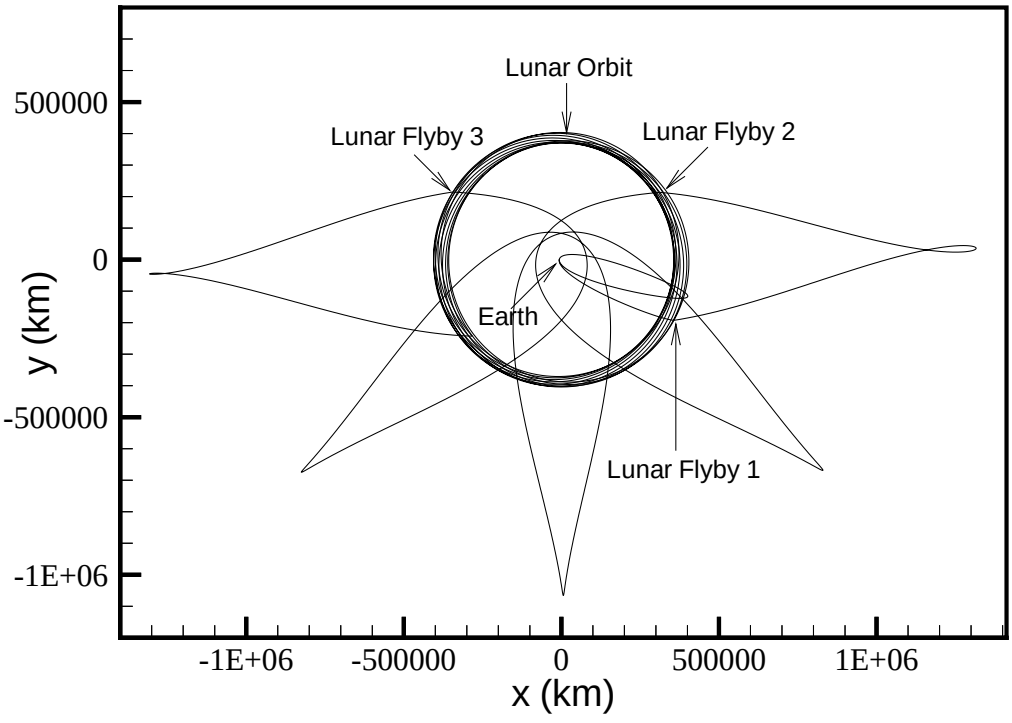

Figure 3.3. Butterfly Example – SR Projection onto $\hat{x}\hat{y}$ plane

this case, the final state that defines the trajectory is selected (somewhat arbitrarily) to coincide with a time and position state along a stable manifold associated with a pre-determined Libration Point Orbit (LPO).[34] This position/time state (obtained as a subset of the 7-dimensional state on the stable manifold) is then targeted by the trajectory arc selection algorithm to create a transfer from the Earth to the vicinity of the LPO. A deterministic injection maneuver at the selected position along the manifold completes the transfer. From this point, the vehicle asymptotically approaches the libration point orbit.

Targeting of the desired state along the given manifold is accomplished using two different methods, depending on the type of solution that is desired. In the first method, the conic arcs leading up to the final lunar encounter are determined as in the previous MLS example, and a two body Lambert solution is generated between the final lunar encounter and the desired final state to complete the transfer. This method is employed to obtain initial approximations for transfers that include one or more lunar gravity assists. Note that the entire approximation for the transfer is conic in nature, and is "patched" to a numerical solution in the four body problem. Hence, a velocity discontinuity will occur at the final state along the transfer, due, in part, to the differences in models used to compute the segments. In the second approach, an arc along the stable manifold (propagated backwards in time from the LPO to the Earth using a four body model) is employed as the approximation to represent the final segment in the trajectory. This type of initial approximation is especially relevant for those solutions with zero or possibly one lunar encounter. This is essential for trajectories such as GENESIS, where conic approximations are insufficient to properly model the dynamics.

3.2.1 Example: Transfer to a Libration Point Orbit

For an example that exploits this methodology, consider a transfer to a Lissajous orbit about the Sun-Earth L_2 point. The desired Lissajous orbit has A_y and A_z amplitudes of roughly 120,000 km each. Once the Lissajous has been designed, a

series of points along the Lissajous are then examined to generate a manifold that passes the Moon with an elongation angle of roughly 45 deg. (Elongation angle is simply the angle between a position vector and the Sun-Earth line; thus, it is the same angle as ψ, defined previously.) After the desired manifold is identified, a target state is selected along the manifold roughly 30 days after the lunar orbit crossing. Since this state is fixed in the present analysis, its selection will impact the cost of the Lissajous orbit insertion (LOI) maneuver that occurs at this fixed point. (This cost may be reduced by allowing this fixed state to move on the manifold surface.) After the LOI point is "fixed", an initial estimate of the solution is determined. In this example, the injection date onto the transfer trajectory is September 9, 2007, and a single phasing loop is employed to target the lunar flyby at the desired elongation angle. A two body Lambert solution about the Earth is used to complete the transfer between the Moon and the LOI point on October 26, 2007. The resulting trajectory is plotted in Figure 3.4 as a projection onto the $\hat{x}\hat{y}$ plane in the SR frame. The transfer up to LOI

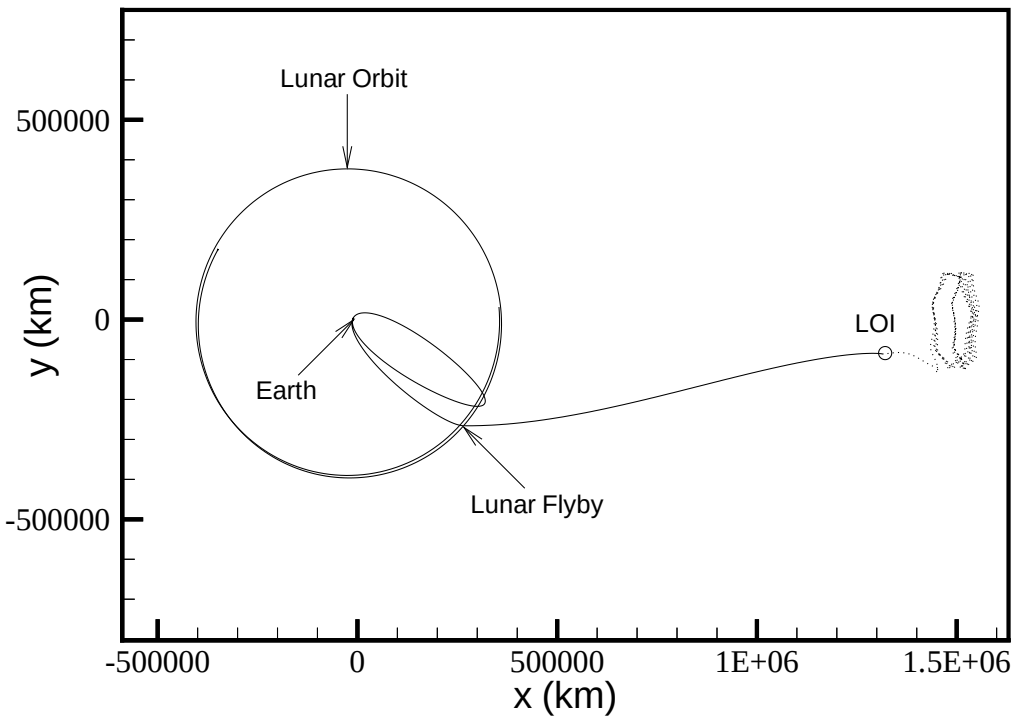

Figure 3.4. Earth-to-L_2 Transfer Example – SR Projection onto $\hat{x}\hat{y}$ plane

appears as a solid line, while the remainder of the manifold plus the Lissajous orbit are denoted with a dotted line. It is noted that the velocity discontinuity at the LOI point is 106 m/s. This large cost is due primarily to the patching together of a two body conic with a numerically integrated four body solution, and typically decreases substantially as the solution is improved.

3.3 Application of Multi-Conic Analysis to the Intermediate Step

The direct extension of the initial approximation to a fully integrated end-to-end solution in the four body problem is rarely possible in a single step. This is especially true when utilizing geocentric conics as the first guess, since the lunar and solar gravity are neglected in this type of approximation. In these instances, an intermediate step is introduced based on the multi-conic techniques described in Section 2.4. This intermediate step facilitates the transition to higher order models, and allows the determination of a numerically integrated solution that meets the given design constraints.

To apply the multi-conic approximations to the given problem, it is necessary that a discrete set of states (termed *patch points* or *target states*) be available to characterize the given trajectory. From the initial approximation, 7-dimensional state vectors (position, velocity, and time) are available, representing the initial and final states, the states before and after each lunar encounter, and other useful states, such as perigee and apogee locations. These target states essentially break the trajectory into a series of smaller segments that are bounded by successive patch points. Between the endpoints of all segments that do not include a lunar encounter, standard multi-conic theory, as described in Section 2.4.2, is applied to generate an updated trajectory arc for that segment.

To begin, the total flight time for the segment under consideration is subdivided to obtain a multi-conic step size (Δt) of roughly 6 hours. It has been determined that a multi-conic step of this size yields sufficient accuracy in the Sun-Earth-Moon system without sacrificing computational speed. The first multi-conic step along the

trajectory segment is propagated from the initial time t_i to the time $t_j = t_i + \Delta t$, and the state transition matrix, $\Phi_{j,i}^{\text{step}}$, for this step is computed using two body approximations. The endstate at the final time, t_j, then becomes the initial state for the next step, and the process is repeated until the final time for the given trajectory segment is reached.

The position state at the end of the final multi-conic step is compared to the desired final patch point state for the segment. If the difference in the position state is greater than a specified tolerance, the complete STM for the segment is used to differentially correct the velocity state at the initial point on the segment to eliminate the error. Note that in this differential corrections process, the initial position state and time of flight along the segment remain fixed. This entire propagation process is repeated until the final position state is within a prescribed tolerance. This algorithm, hereafter denoted Multi-Conic Analysis (MCA), is repeated for each of the segments along the trajectory that do *not* include a lunar flyby.

After MCA is applied to the non-swingby segments and the states at the patch points are updated, it is then necessary to model the lunar flybys to create a trajectory that is continuous in position and time. Pseudostate Analysis (PSA), as described in Section 2.4.3, is applied to alter the end states of the encounter segments that model the lunar flybys. (Note that the phrase "encounter segment" identifies an arc that includes a lunar flyby.) For use as input to the PSA procedure, the states corresponding to the patch points surrounding each lunar encounter are available from the MCA solution. Between the initial and final states defined for a given encounter segment (called *swingby states*), a two body Lambert problem relative to the Moon is solved to yield an estimate of the lunar periapsis state, and an estimate of the time of closest approach. After this initial estimate of the perilune state is computed, the lunar swingby is approximated by application of the Byrnes[20] pseudostate three body Lambert procedure to produce a trajectory arc between the initial and final swingby states. This procedure yields a more accurate estimate of the perilune state, as well as a second estimate of the velocity states at the swingby points.

At this stage, the trajectory has position and time continuity throughout. However, effective velocity discontinuities are introduced at each patch point across all the segments (excluding the initial and final states). The current estimate of the outgoing velocity state ($\bar{V}_n^+$) at any patch point n is compared with the incoming velocity state ($\bar{V}_n^-$) to compute the patch point velocity discontinuities, that is,

$$\Delta\bar{V}_n = \bar{V}_n^+ - \bar{V}_n^- \ . \tag{3.2}$$

These patch point $\Delta\bar{V}$'s are computed in EI coordinates. The reduction of these velocity discontinuities is the next step in producing a fully continuous solution.

3.3.1 Reduction of Velocity Discontinuities

The ultimate goal in the second step of the solution process is a trajectory that meets the design specifications and is continuous in both position and time, as well as velocity. In addition, any constraints placed upon the trajectory, such as launch/return conditions or trajectory end state requirements, must be satisfied. Thus, it is desired to develop an automated process to simultaneously reduce the patch point velocity discontinuities throughout the solution, while incorporating any constraints. This process is accomplished by varying the patch point state positions and times in a specified manner using a differential corrections scheme. The patch point $\Delta\bar{V}$'s can then be reduced significantly, if not eliminated altogether, while the desired characteristics of the solution are retained. This results in a numerically integrated trajectory that accurately reflects the design specifications.

The "cost" associated with the multi-conic estimate is defined as the sum of the magnitudes of all the velocity discontinuities along the trajectory, plus any constraint penalties. This cost must be minimized, while retaining the trajectory characteristics designed in the initial approximation. Define, then, a velocity discontinuity vector $\Delta\bar{V}_i$, expressed in EI coordinates, at each of the patch points, consistent with Equation (3.2). The subscript i will denote the patch point number ordered sequentially along the trajectory, beginning with the initial state. (Note that no effective velocity

discontinuities exist at the initial and final states of the trajectory.) The patch point states themselves (including the initial and final states) are also expressed using the i subscript convention.

3.3.2 Derivation of the State Relationship Matrix

To employ a differential corrections process to reduce the total cost, it is necessary to derive relationships between a given patch point $\Delta\bar{V}_i$ or constraint α_k and the independent variables in the problem. Since the trajectory is described in terms of discrete patch point positions and times, it is appropriate to choose these quantities as the independent parameters. Therefore, it is necessary to determine the variation of each $\Delta\bar{V}_i$ and each constraint α_k due to variations in the patch point positions and times, which have thus far been fixed at values determined during the initial approximation phase. A linear relationship between these states can be represented in matrix form as

$$\left\{ \begin{array}{c} \delta\Delta\bar{V}_i \\ \delta\alpha_k \end{array} \right\} = M \left\{ \begin{array}{c} \delta\bar{R}_j \\ \delta t_j \end{array} \right\} , \tag{3.3}$$

where

$$M = \left[\begin{array}{cc} \frac{\partial\Delta\bar{V}_i}{\partial\bar{R}_j} & \frac{\partial\Delta\bar{V}_i}{\partial t_j} \\ \frac{\partial\alpha_k}{\partial\bar{R}_j} & \frac{\partial\alpha_k}{\partial t_j} \end{array} \right] , \tag{3.4}$$

and $\bar{R}_j$ and t_j denote the position and time corresponding to the j^{th} patch point state. Notice that the matrix M (called the State Relationship Matrix or SRM) is generally not square, that is, there are more independent variables ($\bar{R}_j$ and t_j) than there are dependent variables ($\Delta\bar{V}_i$ and α_k). Since this system is underdetermined, there are infinitely many solutions, and it is therefore possible to estimate the changes in the values of the independent variables that are necessary to reduce $\Delta\bar{V}_i$ and α_k, and thus, the total cost. Note that if, through the addition of constraints, the system becomes overdetermined, it is still possible to add flexibility and maintain the underdetermined nature by including additional patch points in the analysis. Although the size of the SRM can be large, this disadvantage is offset by the fact that the STM's from the

MCA/PSA solution can be used to produce expressions for each partial derivative in the matrix.[15,39–41]

3.3.3 Variations of $\Delta\bar{V}_i$ with Positions

To determine analytical expressions for the elements in the SRM, begin by examining the general relationship between any velocity discontinuity $\Delta\bar{V}_n$ and changes in the independent position states. Split $\Delta\bar{V}_n$ into its component parts, as in Equation (3.2), and consider each partial derivative with respect to a patch point position vector $\bar{R}_j$. The corresponding elements in the SRM become

$$\frac{\partial\Delta\bar{V}_n}{\partial\bar{R}_j} = \frac{\partial\bar{V}_n^+}{\partial\bar{R}_j} - \frac{\partial\bar{V}_n^-}{\partial\bar{R}_j} \quad . \tag{3.5}$$

where $\delta\bar{R}_j$ can represent independent variations in each of the position vectors.

Since the trajectory segments between any consecutive patch point positions with a given flight time are solutions of a four body Lambert problem (4BLP), the Lambert partials discussed in D'Amario et al.[42] can be used to evaluate the partials in Equation (3.5). The elements of the state transition matrices that appear in these Lambert partials are already available from the MCA/PSA solution. From the three patch point position states that surround the velocity discontinuity ($\bar{R}_{n-1}$, $\bar{R}_n$, and $\bar{R}_{n+1}$), two trajectory arcs can be identified, that is one from $n-1$ to n, and one from n to $n+1$. The corresponding STM's, $\Phi_{n,n-1}$ and $\Phi_{n+1,n}$, can be written in terms of four 3×3 submatrices, for example,

$$\Phi_{n,n-1} = \begin{bmatrix} \frac{\partial\bar{R}_n}{\partial\bar{R}_{n-1}} & \frac{\partial\bar{R}_n}{\partial\bar{V}_{n-1}^+} \\ \frac{\partial\bar{V}_n^-}{\partial\bar{R}_{n-1}} & \frac{\partial\bar{V}_n^-}{\partial\bar{V}_{n-1}^+}. \end{bmatrix} = \begin{bmatrix} A_{n,n-1} & B_{n,n-1} \\ C_{n,n-1} & D_{n,n-1} \end{bmatrix} \quad . \tag{3.6}$$

From Wilson and Howell,[15,39–41] the non-zero variations of $\Delta\bar{V}_n$ with the positions $\bar{R}_j$ are written in terms of these submatrices as

$$\frac{\partial\Delta\bar{V}_n}{\partial\bar{R}_{n-1}} = -B_{n-1,n}^{-1} \ , \tag{3.7}$$

$$\frac{\partial\Delta\bar{V}_n}{\partial\bar{R}_n} = -B_{n+1,n}^{-1}A_{n+1,n} + B_{n-1,n}^{-1}A_{n-1,n} \ , \tag{3.8}$$

$$\frac{\partial\Delta\bar{V}_n}{\partial\bar{R}_{n+1}} = B_{n+1,n}^{-1} \ . \tag{3.9}$$

The partials of $\Delta\bar{V}_n$ with respect to all other patch point positions can be shown to be zero. This is true since, given the assumptions about the independent parameters, the velocities at any given patch point are related only to the solutions of the 4BLP that directly precede and follow the patch point n. The expressions in Equations (3.7)–(3.9) can be readily evaluated from the STM's determined during MCA/PSA. The results are used to form the partials that appear in the M matrix in Equation (3.3), that is, the partials relating $\Delta\bar{V}_i$ to changes in the patch point position states.

3.3.4 Variations of $\Delta\bar{V}_i$ with Times

It is also necessary to determine the partial derivatives of $\Delta\bar{V}_i$ with respect to the times associated with each patch point state. The process is similar to the one used to determine the partials with respect to the patch point positions. Now, however, it is necessary to include the effect of a differential change in time into the expression for the state differentials.

First, note that the change in state due to a differential change in time, δt, can be estimated by a first order approximation, that is,

$$\delta\bar{R}(t+\delta t) = \delta\bar{R}(t) + \bar{V}\delta t \ , \tag{3.10}$$

$$\delta\bar{V}(t+\delta t) = \delta\bar{V}(t) + \bar{a}(t)\delta t \ , \tag{3.11}$$

where $\bar{a}$ is the inertial acceleration of the spacecraft at the given instant, t.

Return again to the matrix M and write the expression relating the change in $\Delta\bar{V}_n$ to the change in time t_j as follows,

$$\frac{\partial\Delta\bar{V}_n}{\partial t_j} = \frac{\partial\bar{V}_n^+}{\partial t_j} - \frac{\partial\bar{V}_n^-}{\partial t_j} \ . \tag{3.12}$$

Consistent with the procedure for the position differentials, the non-zero variations of $\Delta\bar{V}_n$ with respect to the times t_j are evaluated as[15,39–41]

$$\frac{\partial\Delta\bar{V}_n}{\partial t_{n-1}} = B_{n-1,n}^{-1}\bar{V}_{n-1}^+ \ , \tag{3.13}$$

$$\frac{\partial\Delta\bar{V}_n}{\partial t_n} = B_{n+1,n}^{-1}A_{n+1,n}\bar{V}_n^+ - B_{n-1,n}^{-1}A_{n-1,n}\bar{V}_n^- \ , \tag{3.14}$$

$$\frac{\partial \Delta \bar{V}_n}{\partial t_{n+1}} = -B_{n+1,n}^{-1} \bar{V}_{n+1}^{-} \ . \tag{3.15}$$

The partials of $\Delta \bar{V}_n$ with respect to all other patch point times are zero by arguments similar to those stated previously. The expressions in Equations (3.13)–(3.15) are evaluated using the STM's computed in MCA/PSA, and from the velocity states at the patch points. These elements are appropriately placed in the M matrix in Equation (3.3) to complete the upper half of the SRM.

3.3.5 Constraint Variations

In order to incorporate any constraints into the solution process, it is necessary to determine the variations of the constraints with respect to variations in the independent parameters. The constraints that are examined in this study can be placed into two categories: either launch/return constraints or end state targeting constraints.

For launch or return constraints, a number of conditions are examined, including: altitude, date, inclination, perigee condition, flight path angle, declination, and right ascension. Each requires examination, beginning with altitude. Since altitude is directly related to the independent position variable $\bar{R}_1$, the constraint expression is written

$$\alpha_1 = \left| \bar{R}_1 \right| - R_{des} \ , \tag{3.16}$$

where R_{des} is the desired altitude. Thus, the variation is expressed as

$$\frac{\partial \alpha_1}{\partial \bar{R}_1} = \frac{\bar{R}_1^T}{\left| \bar{R}_1 \right|} \ . \tag{3.17}$$

Similarly, since the date is actually the independent parameter t_1, the functional form of the second constraint is

$$\alpha_2 = t_1 - t_{des} \ , \tag{3.18}$$

where t_{des} is the desired date. The variation is then

$$\frac{\partial \alpha_2}{\partial t_1} = 1 \quad , \tag{3.19}$$

and is thus constant.

From the definition of the inclination (i) in terms of the pole vector of the Earth ($\hat{Z}_{eq}$), the expression for inclination in terms of $\bar{R}_1$ and $\bar{V}_1$ is

$$\cos i = \frac{\bar{R}_1 \times \bar{V}_1}{\left|\bar{R}_1 \times \bar{V}_1\right|} \bullet \hat{Z}_{eq} \ , \tag{3.20}$$

where '$\bullet$' denotes the inner product and '$\times$' denotes the cross product. The functional form for the inclination constraint is expressed as

$$\alpha_3 = \cos i - \cos i_{des} \ , \tag{3.21}$$

where i_{des} is the desired inclination relative to the Earth equator and equinox of the date. So the total variation of the inclination can be written as

$$d\alpha_3 = \frac{\partial \alpha_3}{\partial \bar{R}_1} \delta \bar{R}_1 + \frac{\partial \alpha_3}{\partial \bar{V}_1} \delta \bar{V}_1 \ . \tag{3.22}$$

Now using Equation (3.17) and the trigonometric identities

$$(\bar{R}_1 \times \bar{V}_1) \bullet \hat{Z}_{eq} = (\hat{Z}_{eq} \times \bar{R}_1) \bullet \bar{V}_1 = (\bar{V}_1 \times \hat{Z}_{eq}) \bullet \bar{R}_1 \ , \tag{3.23}$$

$$\left|\bar{R}_1 \times \bar{V}_1\right| = \left[\left|\bar{R}_1\right|^2 \left|\bar{V}_1\right|^2 - (\bar{R} \bullet \bar{V}_1)^2\right]^{1/2} \ , \tag{3.24}$$

it follows that,

$$\frac{\partial \cos i}{\partial \bar{R}_1} = \frac{(\bar{V}_1 \times \hat{Z}_{eq})^T}{\left|\bar{R}_1 \times \bar{V}_1\right|} - \cos i \cdot \frac{\left|\bar{V}_1\right|^2 \bar{R}_1^T - (\bar{R}_1 \bullet \bar{V}_1) \bar{V}_1^T}{\left|\bar{R}_1 \times \bar{V}_1\right|^2} \ , \tag{3.25}$$

and

$$\frac{\partial \cos i}{\partial \bar{V}_1} = \frac{(\hat{Z}_{eq} \times \bar{R}_1)^T}{\left|\bar{R}_1 \times \bar{V}_1\right|} - \cos i \cdot \frac{\left|\bar{R}_1\right|^2 \bar{V}_1^T - (\bar{R}_1 \bullet \bar{V}_1) \bar{R}_1^T}{\left|\bar{R}_1 \times \bar{V}_1\right|^2} \ . \tag{3.26}$$

Return to Equation (3.22) and note that $\delta \bar{R}_1$ is one of the independent variables in the problem, but $\delta \bar{V}_1$ depends on the positions and times according to the relationship

$$\delta \bar{V}_1 = \frac{\partial \bar{V}_1}{\partial \bar{R}_1} \delta \bar{R}_1 + \frac{\partial \bar{V}_1}{\partial t_1} \delta t_1 + \frac{\partial \bar{V}_1}{\partial \bar{R}_2} \delta \bar{R}_2 + \frac{\partial \bar{V}_1}{\partial t_2} \delta t_2 \ . \tag{3.27}$$

Each of the partials in Equation (3.27) is a Lambert partial,[42] as described in the previous sections, so that from Equations (3.22), (3.25), and (3.26) the inclination

constraint variations are expressed in the following forms,

$$\frac{\partial \alpha_3}{\partial \bar{R}_1} = \frac{\partial \cos i}{\partial \bar{R}_1} - \frac{\partial \cos i}{\partial \bar{V}_1} \cdot B_{2,1}^{-1} A_{2,1} \ , \tag{3.28}$$

$$\frac{\partial \alpha_3}{\partial t_1} = \frac{\partial \cos i}{\partial \bar{V}_1} \cdot \left(\bar{a}_1 + B_{2,1}^{-1} A_{2,1} \bar{V}_1 \right) \ , \tag{3.29}$$

$$\frac{\partial \alpha_3}{\partial \bar{R}_2} = \frac{\partial \cos i}{\partial \bar{V}_1} \cdot B_{2,1}^{-1} \ , \tag{3.30}$$

$$\frac{\partial \alpha_3}{\partial t_2} = -\frac{\partial \cos i}{\partial \bar{V}_1} \cdot B_{2,1}^{-1} \bar{V}_2 \ , \tag{3.31}$$

where, as usual, the expressions are evaluated along the reference solution.

The functional form of the perigee constraint is expressed in terms of the apse condition, $\bar{R} \bullet \bar{V} = 0$, and is defined to be

$$\alpha_4 = \bar{R}_1 \bullet \bar{V}_1 \ . \tag{3.32}$$

The partials due to position and velocity are simply

$$\frac{\partial \left(\bar{R}_1 \bullet \bar{V}_1 \right)}{\partial \bar{R}_1} = \bar{V}_1^T \ , \tag{3.33}$$

$$\frac{\partial \left(\bar{R}_1 \bullet \bar{V}_1 \right)}{\partial \bar{V}_1} = \bar{R}_1^T \left[\frac{\partial \bar{V}_1}{\partial \bar{R}_1} + \frac{\partial \bar{V}_1}{\partial t_1} + \frac{\partial \bar{V}_1}{\partial \bar{R}_2} + \frac{\partial \bar{V}_1}{\partial t_1} \right] \ . \tag{3.34}$$

Thus, the variations of α_4 with respect to the independent variables can be written

$$\frac{\partial \alpha_4}{\partial \bar{R}_1} = \bar{V}_1^T - \bar{R}_1^T \cdot B_{2,1}^{-1} A_{2,1} \ , \tag{3.35}$$

$$\frac{\partial \alpha_4}{\partial t_1} = \bar{R}_1^T \cdot \left(\bar{a}_1 + B_{2,1}^{-1} A_{2,1} \bar{V}_1 \right) \ , \tag{3.36}$$

$$\frac{\partial \alpha_4}{\partial \bar{R}_2} = \bar{R}_1^T \cdot B_{2,1}^{-1} \ , \tag{3.37}$$

$$\frac{\partial \alpha_4}{\partial t_2} = -\bar{R}_1^T \cdot B_{2,1}^{-1} \bar{V}_2 \ . \tag{3.38}$$

A related extension of this apse constraint can be used to force given interior patch points to lie along the line of apsides, either at perigee or apogee. Note also that this constraint is *not* limited to simply enforcing the tangential apse condition (i.e. $\bar{R} \bullet \bar{V} = 0$). If a desired value for $\bar{R} \bullet \bar{V}$ is known, then the constraint can be modified to reflect this specification. Hence, Equation (3.32) could be rewritten as

$$\alpha_4 = (\bar{R}_1 \bullet \bar{V}_1) - (\bar{R} \bullet \bar{V})_{des} \ . \tag{3.39}$$

Note however, that the partials in Equations (3.35) – (3.38) are not affected by this modification.

A second extension related to this constraint is targeting of a specified flight path angle. The form of this type of constraint is

$$\alpha_5 = \sin\gamma - \sin\gamma_{des} = \frac{\bar{R}_1 \bullet \bar{V}_1}{\left|\bar{R}_1\right|\left|\bar{V}_1\right|} - \sin\gamma_{des} \quad , \tag{3.40}$$

where γ is the flight path angle defined from the local horizon (i.e., where $\bar{V}$ is tangent to $\bar{R}$). The partials due to changes in position and velocity are

$$\frac{\partial\alpha_5}{\partial\bar{R}_1} = \frac{\bar{V}_1^T}{\left|\bar{R}_1\right|\left|\bar{V}_1\right|} - \frac{\bar{R}_1 \bullet \bar{V}_1}{\left|\bar{R}_1\right|^2\left|\bar{V}_1\right|}\frac{\partial\left|\bar{R}_1\right|}{\partial\bar{R}_1} \quad , \tag{3.41}$$

$$\frac{\partial\alpha_5}{\partial\bar{V}_1} = \left[\frac{\bar{R}_1^T}{\left|\bar{R}_1\right|\left|\bar{V}_1\right|} - \frac{\bar{R}_1 \bullet \bar{V}_1}{\left|\bar{R}_1\right|\left|\bar{V}_1\right|^2}\right]\left[\frac{\partial\bar{V}_1}{\partial t_1} + \frac{\partial\bar{V}_1}{\partial\bar{R}_2} + \frac{\partial\bar{V}_1}{\partial t_2}\right] \quad . \tag{3.42}$$

Thus, the variations of flight path angle with respect to positions and times are

$$\frac{\partial\alpha_5}{\partial\bar{R}_1} = \frac{\bar{V}_1^T}{\left|\bar{R}_1\right|\left|\bar{V}_1\right|} - \frac{\bar{R}_1^T}{\left|\bar{R}_1\right|\left|\bar{V}_1\right|}B_{21}^{-1}A_{21} - \sin\gamma\left[\frac{\bar{R}_1^T}{\left|\bar{R}_1\right|^2} - \frac{\bar{V}^T}{\left|\bar{V}_1\right|^2}B_{21}^{-1}A_{21}\right] \quad , \tag{3.43}$$

$$\frac{\partial\alpha_5}{\partial t_1} = \left[\frac{\bar{R}_1^T}{\left|\bar{R}_1\right|\left|\bar{V}_1\right|} - \sin\gamma\frac{\bar{V}^T}{\left|\bar{V}_1\right|^2}\right]\left[\bar{a}_1 + B_{21}^{-1}A_{21}\bar{V}_1\right] \quad , \tag{3.44}$$

$$\frac{\partial\alpha_5}{\partial\bar{R}_2} = \left[\frac{\bar{R}_1^T}{\left|\bar{R}_1\right|\left|\bar{V}_1\right|} - \sin\gamma\frac{\bar{V}^T}{\left|\bar{V}_1\right|^2}\right]\left[B_{21}^{-1}\right] \quad , \tag{3.45}$$

$$\frac{\partial\alpha_5}{\partial t_2} = \left[\frac{\bar{R}_1^T}{\left|\bar{R}_1\right|\left|\bar{V}_1\right|} - \sin\gamma\frac{\bar{V}^T}{\left|\bar{V}_1\right|^2}\right]\left[-B_{21}^{-1}\bar{V}_2\right] \quad . \tag{3.46}$$

It is notable that the apse constraint or the flight path angle constraint can also be used to indirectly target true anomaly (θ), since θ is related to either of these conditions.

For declination and right ascension, it is desired to target a specific location on the rotating (non-inertial) Earth. Define then a set of Cartesian coordinates fixed in the Earth, such that $\hat{z}_{bf}$ is coincident at all times with the axis of rotation of the Earth

and is assumed constant. The $\hat{x}_{bf}$ unit vector is defined along the Greenwich meridian through the equator and $\hat{y}_{bf}$ completes the orthonormal triad. The declination can thus be evaluated as

$$\sin(dec) = \frac{\bar{R}_1 \bullet \hat{z}_{bf}}{\left|\bar{R}_1\right|} \quad , \tag{3.47}$$

and hence the constraint function is

$$\alpha_6 = \sin(dec) - \sin(dec)_{des} \quad . \tag{3.48}$$

As an approximation, ω_e, the rotation rate of the Earth about $\hat{z}_{bf}$, is assumed constant. Therefore, the expression for declination is only a function of the position vector $\bar{R}_1$, and the only non-zero partial in the SRM is

$$\frac{\partial \alpha_6}{\partial \bar{R}_1} = \frac{1}{\left|\bar{R}_1\right|}\left[\hat{z}_{bf}^T - \sin(dec)\,\frac{\bar{R}_1^T}{\left|\bar{R}_1\right|}\right] \quad . \tag{3.49}$$

In contrast, the right ascension with respect to the rotating Earth is computed as

$$rt.asc = \arctan\left(\frac{\bar{R}_1 \bullet \hat{y}_{bf}}{\bar{R}_1 \bullet \hat{x}_{bf}}\right) \quad , \tag{3.50}$$

so that

$$\alpha_7 = rt.asc - rt.asc_{des} \quad . \tag{3.51}$$

Although $\hat{z}_{bf}$ is assumed constant, the directions of $\hat{x}_{bf}$ and $\hat{y}_{bf}$ change with respect to the inertial frame as the Earth rotates, so right ascension is a function of position $\bar{R}_1$, as well as time t_1. The partial derivative of right ascension with respect to $\bar{R}_1$ is

$$\begin{aligned} \frac{\partial \alpha_7}{\partial \bar{R}_1} &= \frac{1}{\left[1 + \frac{\bar{R}_1 \bullet \hat{y}_{bf}}{\bar{R}_1 \bullet \hat{x}_{bf}}\right]^2} \frac{\partial}{\partial \bar{R}_1}\left(\frac{\bar{R}_1 \bullet \hat{y}_{bf}}{\bar{R}_1 \bullet \hat{x}_{bf}}\right) \quad , \\ &= \frac{\left(\bar{R}_1 \bullet \hat{x}_{bf}\right)\hat{y}_{bf}^T - \left(\bar{R}_1 \bullet \hat{y}_{bf}\right)\hat{x}_{bf}^T}{\left[\left(\bar{R}_1 \bullet \hat{x}_{bf}\right) + \left(\bar{R}_1 \bullet \hat{y}_{bf}\right)\right]^2} \quad . \end{aligned} \tag{3.52}$$

Similarly, the partial with respect to time is expressed

$$\frac{\partial \alpha_7}{\partial t_1} = \frac{1}{\left[1 + \frac{\bar{R}_1 \bullet \hat{y}_{bf}}{\bar{R}_1 \bullet \hat{x}_{bf}}\right]^2} \frac{\partial}{\partial t_1}\left(\frac{\bar{R}_1 \bullet \hat{y}_{bf}}{\bar{R}_1 \bullet \hat{x}_{bf}}\right) \quad . \tag{3.53}$$

From the previous assumption that ω_e is constant, the time derivatives of the unit vectors $\hat{x}_{bf}$ and $\hat{y}_{bf}$ can be written in the forms

$$\frac{\partial \hat{x}_{bf}}{\partial t_1} = \omega_e \hat{y}_{bf} \qquad \text{and} \qquad \frac{\partial \hat{y}_{bf}}{\partial t_1} = -\omega_e \hat{x}_{bf} \quad , \tag{3.54}$$

so that, ultimately, the partial of right ascension with respect to time reduces to

$$\frac{\partial \alpha_7}{\partial t_1} = \omega_e \frac{\left(\bar{R}_1 \bullet \hat{x}_{bf}\right)^2 + \left(\bar{R}_1 \bullet \hat{y}_{bf}\right)^2}{\left[\left(\bar{R}_1 \bullet \hat{x}_{bf}\right) + \left(\bar{R}_1 \bullet \hat{y}_{bf}\right)\right]^2} \quad . \tag{3.55}$$

Thus, the launch/return constraint variations are available. Other constraints of this form could also be derived in a similar manner.

A second type of constraint considered here is the end state ($\bar{R}_N,\ \bar{V}_N,\ t_N$) constraint. This constraint is used to target a desired final state ($\bar{R}_{des},\ \bar{V}_{des},\ t_{des}$) for the complete trajectory. The constraint functions are formally stated as

$$\alpha_{(8-10)} = \bar{R}_N - \bar{R}_{des}, \tag{3.56}$$

$$\alpha_{11} = t_N - t_{des}, \tag{3.57}$$

$$\alpha_{(12-14)} = \bar{V}_N - \bar{V}_{des}, \tag{3.58}$$

and the related variations with respect to the independent variables are

$$\frac{\partial \alpha_{(8-10)}}{\partial \bar{R}_N} = I_3 \ , \tag{3.59}$$

$$\frac{\partial \alpha_{11}}{\partial t_N} = 1 \ , \tag{3.60}$$

$$\frac{\partial \alpha_{(12-14)}}{\partial \bar{R}_N} = -B_{N-1,N}^{-1}\ A_{N-1,N} \quad , \tag{3.61}$$

$$\frac{\partial \alpha_{(12-14)}}{\partial t_N} = \bar{a}_N + B_{N-1,N}^{-1}\ A_{N-1,N}\ \bar{V}_N \quad , \tag{3.62}$$

$$\frac{\partial \alpha_{(12-14)}}{\partial \bar{R}_{N-1}} = B_{N-1,N}^{-1} \ , \tag{3.63}$$

$$\frac{\partial \alpha_{(12-14)}}{\partial t_{N-1}} = -B_{N-1,N}^{-1} \bar{V}_{N-1} \quad . \tag{3.64}$$

By appropriate choice of the independent parameters, any constraint functions active in the solution can be driven to zero (within an acceptable tolerance), thus enforcing the constraints.

3.3.6 Reduction Algorithm

The procedure for reduction of the velocity discontinuities and enforcement of the constraints is initiated from the discrete set of patch point states and times generated through the initial approximation. For each non-swingby segment, MCA is applied between the initial and final patch point states. The updated patch point states are then employed by PSA to generate a second estimate of the velocity states at the swingby points surrounding the flybys. The patch point $\Delta\bar{V}_i$ and constraint penalties are computed and the total cost is checked against a desired tolerance. The SRM in Equation (3.3) is then used in a differential corrections process to compute changes in the independent variables (positions and times) in an attempt to simultaneously reduce all the velocity discontinuities in the trajectory, as well as satisfy any constraints.

As noted, the system is underdetermined, and the SRM in Equation (3.3) is not invertible. Out of all possible changes in positions and times, choose the one with the smallest Euclidean norm, that is,

$$\left\{ \begin{array}{c} \delta\bar{R}_j \\ \delta t_j \end{array} \right\} = M^T \left(M M^T \right)^{-1} \left\{ \begin{array}{c} \delta\Delta\bar{V}_i \\ \delta\alpha_k \end{array} \right\} , \tag{3.65}$$

where the differential changes in $\Delta\bar{V}_i$ and α_k are selected to reduce the total cost. The differential changes in positions and times computed in Equation (3.65) are added to the patch point states. These new target states are then used to recompute an estimate of the trajectory with a cost that is lower than that of the previous solution. This process is repeated until the cost is minimized to within some tolerance. Note that, Equation (3.65) is a linear estimate of the changes, and thus, multiple iterations are required due to the nonlinear nature of the motion.

In practice, the jump from the initial approximation to MCA/PSA, including the solar perturbations, is often too great for the linear differential corrections process. In this case, MCA is applied to the PCA results using only the lunar gravity. After an acceptable convergence is achieved, the solar perturbations are added (sometimes

incrementally) and the four body approximation is obtained. The final trajectory approximated from this methodology is continuous in velocity and satisfies all constraints. These results are then input to a numerical propagation routine to achieve the final desired end-to-end solution.

3.3.7 Results

This intermediate step is applied to the two examples presented in Sections 3.1.3 and 3.2.1. These improved trajectories from MCA/PSA are viewed in the SR frame as projections onto the $\hat{x}_s\hat{y}_s$ plane (Figures 3.5 and 3.6). The trajectories include all of the propagation steps that comprise the MCA and PSA procedures. The "spikes" seen in the plot represent the various propagation steps, and are not representative of the "true" path. Although the MCA/PSA solution actually consists of a set of discrete solution states, plotting all of the various steps in the MCA/PSA algorithms shows the general characteristics of the trajectory quite well. It is seen that although significant changes in the trajectories have resulted from application of the intermediate step (especially in the MLS example), both solutions still retain the desired design characteristics.

The results for the butterfly trajectory include the following constraints at launch (or more specifically, injection onto the trajectory): altitude = 200 km, inclination = 28.5 deg, and trajectory insertion at perigee; the Earth-to-L_2 transfer trajectory has similar injection constraints. Additionally, constraints are placed on the end state position and date of the LPO transfer trajectory; these values are specified to be the same as those selected for the initial analysis. As mentioned, the end state is numerically generated using dynamical systems theory[34] to determine transfer characteristics to inject onto a path that asymptotically approaches a Lissajous orbit about the Sun-Earth L_2 libration point. In the MCA/PSA solution obtained here, the velocity at the end state was not constrained, so a velocity discontinuity equal to 18.9 m/s exists in "patching" these results to the Lissajous. Later a procedure is presented to reduce the Lissajous insertion cost by allowing the end state to vary along the one-dimensional manifold trajectory.

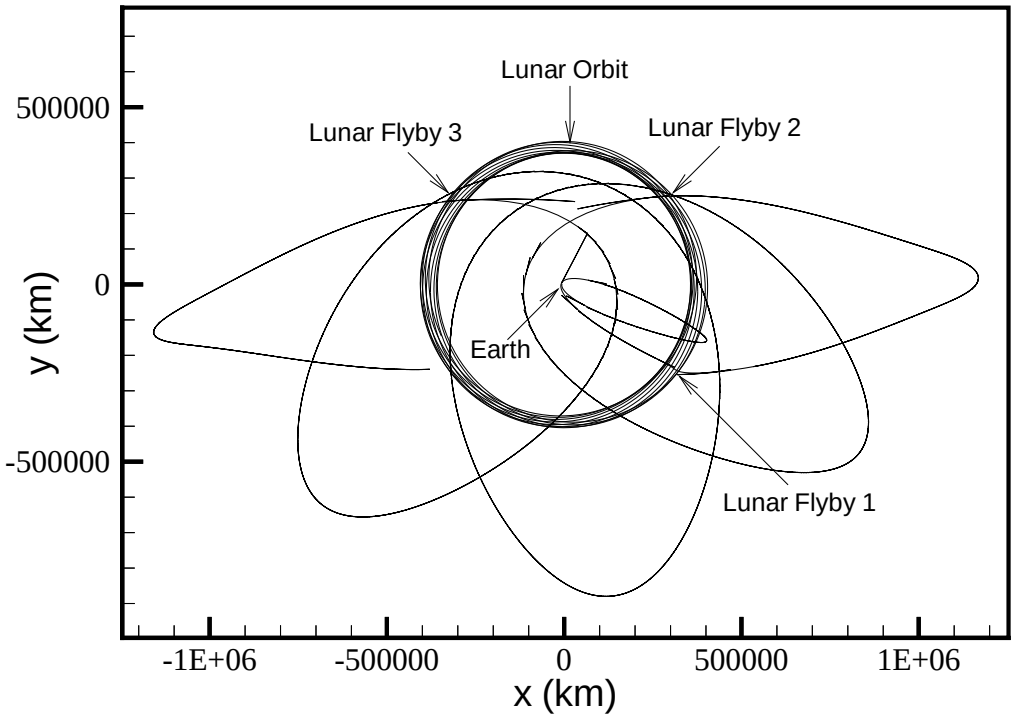

Figure 3.5. Butterfly Example – Multi-Conic Approximation

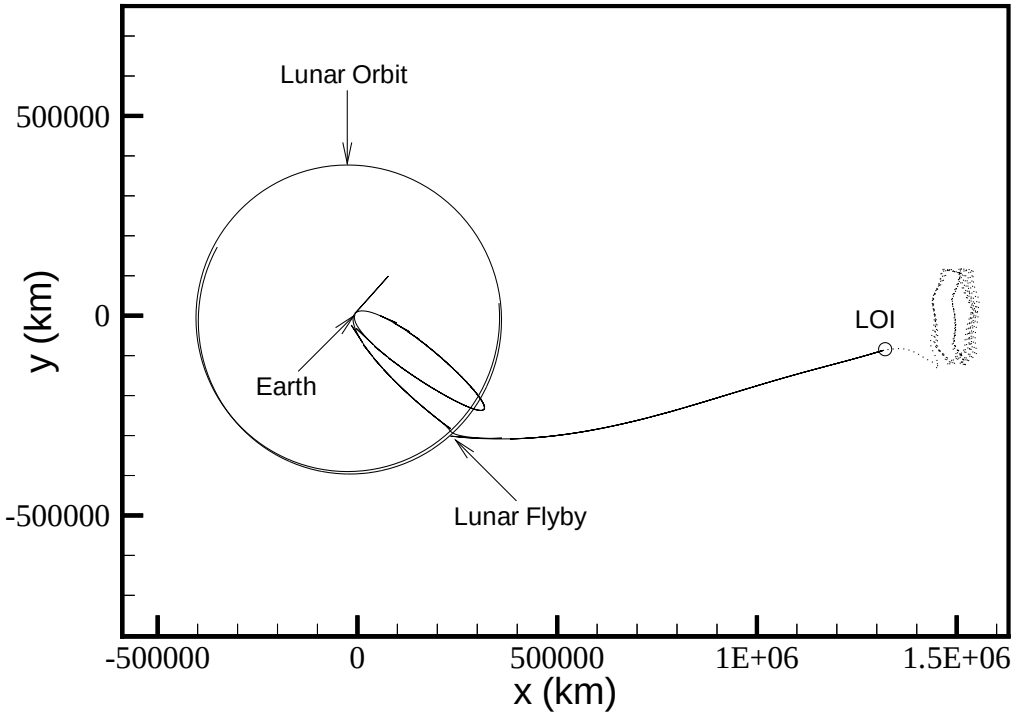

Figure 3.6. Earth-to-L_2 Transfer Example – Multi-Conic Approximation

3.4 Numerical Integration

For the final step, it is necessary to demonstrate that the trajectories obtained from the intermediate step are readily extensible to a numerically integrated solution. One approach might be to numerically integrate the equations of motion governing the restricted four body problem in a barycentric rotating frame. However, in this analysis, JPL DE405 ephemerides are employed to represent the states of the Sun, Earth, and Moon at the desired epochs. This ephemeris data is available in inertial coordinates; hence, coordinate transformations are required to integrate in the rotating frame. Thus, as an alternative, the relative equations of motion for four bodies are selected for this analysis. These equations of motion are derived relative to an inertial frame with no pre-determined model for the motion of the gravitational sources, and hence, represent a more consistent model for the numerical integration. The four body equations of motion relative to the Earth can be written in terms of the two standard vector differential equations,

$$\frac{{}^{I}d\bar{R}_{esc}}{dt} = \bar{V}_{esc} \quad , \tag{3.66}$$

$$\frac{{}^{I}d\bar{V}_{esc}}{dt} = \bar{a}_{sc} \quad , \tag{3.67}$$

where $\bar{R}_{esc}$ is the position vector of the spacecraft relative to the Earth, $\bar{V}_{esc}$ is an inertial velocity, and $\bar{a}_{sc}$ is computed from the contribution of each gravity field on the spacecraft based on the inverse square law of gravity. Given that there are three gravity fields, the terms in the force model appear in $\bar{a}_{sc}$ as follows,

$$\bar{a}_{sc} = -\mu_e \frac{\bar{R}_{esc}}{R^3_{esc}} - \mu_s \left[\frac{\bar{R}_{ssc}}{R^3_{ssc}} - \frac{\bar{R}_{se}}{R^3_{se}} \right] - \mu_m \left[\frac{\bar{R}_{msc}}{R^3_{msc}} - \frac{\bar{R}_{me}}{R^3_{me}} \right] \quad , \tag{3.68}$$

where $\bar{R}_{se}$ and $\bar{R}_{me}$ are the position vectors of the Sun and Moon, respectively, relative to the Earth. Equations (3.66) and (3.67) represent six first order differential equations governing the motion of the spacecraft under the influence of the Sun, Earth, and Moon.

Additionally, it is necessary to integrate the differential equations governing the state transition matrix, so that various differential corrections procedures can be

utilized. Similar to the discussion in Section 2.3.1, the differential equations for the STM are known to be of the form[19]

$$\frac{d\Phi}{dt} = A\ \Phi \quad , \tag{3.69}$$

where A is a 6x6 matrix of second partial derivatives of the gravitational potential function, U. This potential is written as

$$U = \frac{\mu_e}{R_{esc}} + \frac{\mu_s}{R_{ssc}} + \frac{\mu_m}{R_{msc}} \quad , \tag{3.70}$$

where now U takes on a more general form than the expression in terms of rotating coordinates from Equation (2.35). The partial derivatives of this potential function are taken with respect to the components of the position vector of the spacecraft relative to the Earth. When combined with the 6 state equations, these 42 differential equations can be numerically integrated to simulate the motion of the spacecraft in the four body problem.

For the numerical integration procedure, a process similar to the one employed in the intermediate step is used to compute the solution. The trajectory is again split into a series of smaller segments bounded by patch points that have been previously determined. For each segment, a differential corrections process is utilized to ensure position continuity over the entire trajectory. Differentially correcting each segment in this manner, however, reintroduces velocity discontinuities at the patch points due to the errors in the approximate MCA/PSA solution. These velocity discontinuities can again be eliminated by utilizing the SRM in a similar reduction process that is also used to enforce the constraints. Note that now, however, the expressions in the SRM are evaluated from numerically determined STM's instead of from the MCA/PSA approximations.

3.4.1 Final Integrated Results

The results of the numerical simulation for the two examples presented in Section 3.3.7 appear graphically in Figures 3.7 and 3.8. Both trajectories meet the design

criteria, as well as all constraints at insertion onto the transfer trajectory. Notice that no significant visual differences appear in the trajectories here as compared to those obtained from MCA/PSA in Figures 3.5 and 3.6. Also note that for the transfer trajectory, the LOI cost between the MCA/PSA and numerically integrated solutions increased by only 1.7 m/s to a cost of 20.6 m/s. A comparison of selected states along the trajectory for each of the three steps in the methodology is presented in Table 3.2. The first column lists the times (in Julian date) and positions (in km) generated from the conic approximation. The states examined are launch or insertion, apogee 2 (near L_2), apogee 4 (roughly at the mid-point of the trajectory), apogee 6 (near L_1), and the final state. The second column presents the differences between these states and those determined for the MCA/PSA solution. Notice that the procedure does produce large changes in the states, due to the addition of the lunar and solar gravity that are neglected in the conic approximation, however, as the figures demonstrate, the design characteristics are still maintained. The last column, then, presents the changes in the states between the final numerically integrated solution and the MCA/PSA solution. These changes are orders of magnitude smaller than the differences between the conic approximation and MCA/PSA. This confirms that the MCA/PSA intermediate step does incorporate the additional gravitational terms satisfactorily, and almost always allows the integrated trajectory to be determined without qualitative changes in the nature of the solution.

As a final comparison, the positions and times of the lunar periapse states for each flyby (in Moon Inertial coordinates) are presented in Table 3.3. Additionally the altitude of closest approach (in km) and the elongation angle (in deg) of the spacecraft at the lunar periapsis are tabulated. Notice first that the conic approximation does not model the lunar encounter, or more precisely, models it as a collision with the Moon; hence, the closest approach is reported as the location of the center of the Moon at the time of the collision, i.e., (0,0,0) in MI coordinates. The effects of the lunar gravity are incorporated through the use of the intermediate MCA/PSA step. The second column, then, presents the actual computed lunar periapsis states after

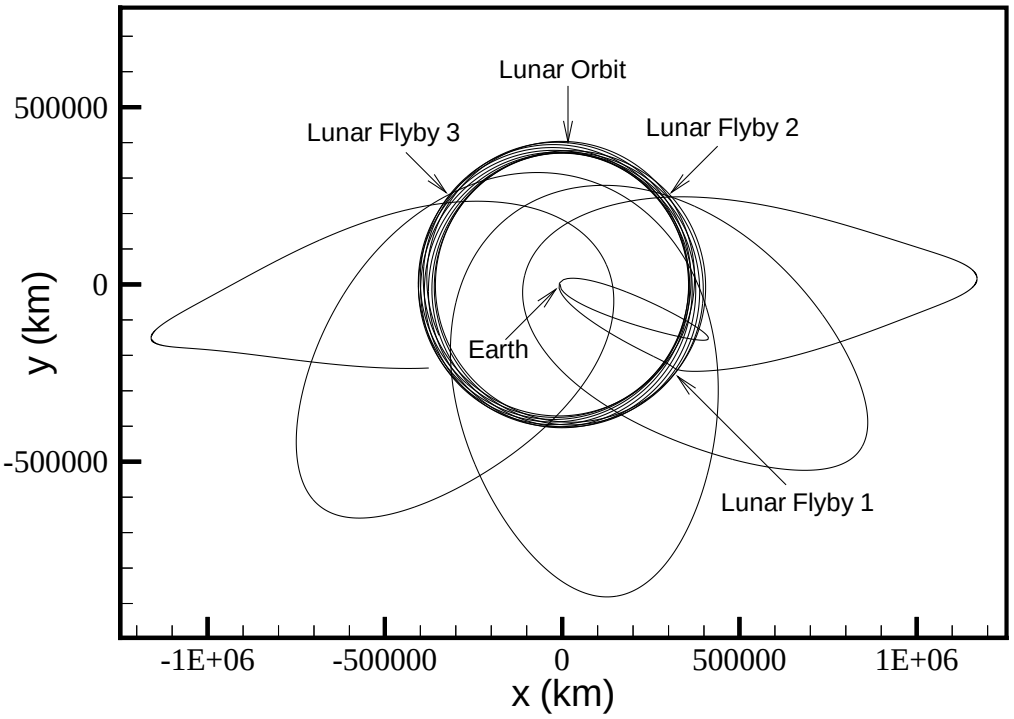

Figure 3.7. Butterfly Example – Integrated

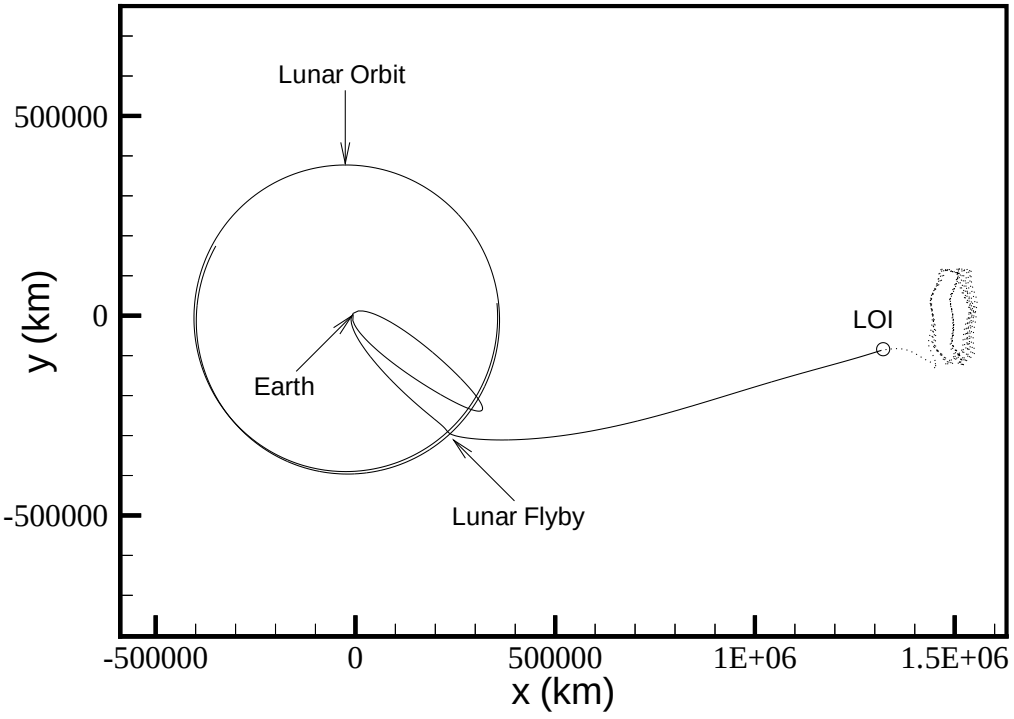

Figure 3.8. Earth-to-L_2 Transfer Example – Integrated

Table 3.2 Comparison of Results for Selected States – Butterfly Example

SR Coordinate Frame		Conic State Approximation	Change From Conic to MCA/PSA	Change From MCA/PSA to Integrated
Launch:	JD	2455031.2381	-0.5007	-0.0951
	x	-6457.73	81.96	-33.19
	y	1242.29	369.87	-137.72
	z	156.56	12.20	-14.97
Apogee 2:	JD	2455079.0722	-0.5067	0.0437
	x	1315974.31	-145711.42	1804.55
	y	35889.17	3866.51	-1664.15
	z	75020.00	41896.07	-652.45
Apogee 4:	JD	2455189.8486	0.3644	-0.1175
	x	6169.87	129447.99	9361.69
	y	-1065651.55	177361.82	-992.88
	z	93795.92	-46894.52	-2163.02
Apogee 6:	JD	2455300.8811	1.4258	-0.0371
	x	-1306424.47	139098.28	-1483.92
	y	-45260.81	-63743.34	-10919.44
	z	98076.44	-143658.10	-37395.72
Final:	JD	2455332.5724	-0.0124	-0.0233
	x	-394455.00	-427.82	2129.20
	y	-234208.03	9556.80	3019.03
	z	10865.06	-64773.72	2493.86

Table 3.3 Comparison of Results for Lunar Periapse States – Butterfly Example

MI Coordinate Frame		Conic State Approximation	MCA/PSA State Solution	Integrated State Solution
Flyby 1:	JD	2454339.4163	2454340.2200	2454340.2188
	X	0.00	-12043.60	-12464.24
	Y	0.00	-3071.81	-3173.66
	Z	0.00	-1885.69	-1953.68
	Altitude	–1737.40	10834.00	11272.07
	Elongation	20.00	11.12	11.19
Flyby 2:	JD	2454373.1916	2454372.9466	2454372.7672
	X	0.00	-35083.94	-33444.83
	Y	0.00	8256.26	9128.57
	Z	0.00	3721.79	4196.62
	Altitude	–1737.40	34496.57	33183.93
	Elongation	-40.29	-41.98	-39.26
Flyby 3:	JD	2454398.0940	2454398.3071	2454398.2136
	X	0.00	-6078.24	-6189.49
	Y	0.00	-20036.32	-18929.70
	Z	0.00	-511.38	-33.22
	Altitude	–1737.40	19206.83	18178.53
	Elongation	22.84	22.65	23.80

the convergence of the solution during the intermediate step. It is most important to note that the times of the lunar periapsis states change by up to 19 hours, for this trajectory, when the lunar gravity is introduced. This is one of the primary reasons that the conic approximation fails to allow a four body solution to be determined directly, and precipitates the inclusion of the second step in the methodology. The last

column reports the periapse states after convergence of the numerically integrated solution. As before, the changes are orders of magnitude smaller than the differences between the conic and MCA/PSA solutions. It is concluded then, that if a satisfactory solution is determined in the intermediate step, a similar numerically integrated solution is likely to be obtainable.

3.5 Supplemental Targeting Methodology

The methodology presented in the previous sections has proven to be a very effective tool to determine solutions in the four body problem. However, there are limitations to the procedure, based on some of the assumptions in the derivation of the intermediate step. Specifically, in the original three step algorithm developed in Section 3.3, the patch point positions and times are selected as the independent parameters in the problem. A linear relationship is then developed between these positions and times and the velocity discontinuities and constraints in the problem. This linear relationship is employed to alter the positions and times along the solution to eliminate any velocity discontinuities and enforce the design constraints for the problem. However, this effectively limits the number of constraints that can be placed on the initial or final states. This limitation is due to the necessity of forcing the solution through the positions and times of the patch points along the trajectory using four body Lambert solutions. This procedure, in turn, limits the available targets at the end states to a maximum of four constraints. The use of this algorithm to target the entire 7-dimensional end state (position, velocity, and time) is thus not possible.

As an alternative, the velocities and times at certain points along the nominal trajectory could be selected as the independent quantities in the solution. This new methodology does not employ Lambert type segments between patch points, but instead produces a solution that utilizes deterministic $\Delta\bar{V}$'s at the target states along the trajectory to meet the specified end state criteria. This approach is useful for any class of problems for which a nominal solution exists, but the initial or final

state is unacceptable (perhaps for operational or science reasons), or the end state requirements require targeting of the entire state vector. This methodology will be labeled the "supplemental targeting algorithm", since it is used to target a specific end state, or set of end state conditions based on some given nominal solution.

Consider then the problem of retargeting the end state of a *known* nominal solution from some fixed initial state (in position and time), using two or more deterministic maneuvers. Initially, a single interior state is selected between the initial state and the final state, such that the trajectory contains two deterministic $\Delta\bar{V}$'s, one at the initial state, and another at the interior point. The location of the interior maneuver is determined by forward propagation of the initial state at time t_1, including the first maneuver, to some time t_2, using the complete force model. The final state is then determined by propagation of the interior state, after the second deterministic maneuver is applied, to the final time t_f. Note that a multi-conic propagation could be utilized, however, since a nominal solution is given, it is further assumed that this nominal is a numerically computed solution in the four body problem; hence, numerical propagation is described here.

For this two maneuver solution, the procedure is initiated with the selection of the initial state $(\bar{R}_1, \bar{V}_1^-, t_1)$ from the nominal solution; this state is then fixed in position and time. A maneuver $\Delta\bar{V}_1$ is applied at this initial state to change the initial velocity to $\bar{V}_1^+ = \bar{V}_1^- + \Delta\bar{V}_1$. (Recall that superscript $(-)$ denotes an incoming or initial velocity at a state, while superscript $(+)$ denotes the outgoing or final velocity.) Numerical propagation in the full model yields the state at the interior point $(\bar{R}_2, \bar{V}_2^-, t_2)$. Another maneuver $\Delta\bar{V}_2$ is applied to alter the velocity at the interior state to $\bar{V}_2^+ = \bar{V}_2^- + \Delta\bar{V}_2$. This new state at t_2 is then propagated forward to t_f to produce the final state $(\bar{R}_f, \bar{V}_f, t_f)$. In this formulation, the independent parameters are the outgoing velocity states at each patch point $(\bar{V}_1^+, \bar{V}_2^+)$ and the time at the end of each propagation segment (t_2, t_f).

The goal of the targeter is to determine simultaneous changes in the free parameters $(\bar{V}_1^+, \bar{V}_2^+, t_2, t_f)$ to meet the desired final state $(\bar{R}_f, \bar{V}_f)$. This is represented by

the linear relationship

$$\left\{ \begin{array}{c} \delta\bar{R}_f \\ \delta\bar{V}_f \end{array} \right\} = S \left\{ \begin{array}{c} \delta\bar{V}_1^+ \\ \delta\bar{V}_2^+ \\ t_2 \\ t_f \end{array} \right\} \quad , \tag{3.71}$$

where $\delta\bar{R}_f$ and $\delta\bar{V}_f$ are the position and velocity errors between the actual and desired final states. The changes in the independent velocities and times are $\delta\bar{V}_1^+$, $\delta\bar{V}_2^+$, δt_2, and δt_f, and S is a matrix of partial derivatives, similar to the state relationship matrix derived in Section 3.3.2. For this two burn example, S can be written explicitly as

$$S = \left[\begin{array}{cccc} \frac{\partial\bar{R}_f}{\partial\bar{V}_1^+} & \frac{\partial\bar{R}_f}{\partial\bar{V}_2^+} & \frac{\partial\bar{R}_f}{\partial t_2} & \frac{\partial\bar{R}_f}{\partial t_f} \\ \frac{\partial\bar{V}_f}{\partial\bar{V}_1^+} & \frac{\partial\bar{V}_f}{\partial\bar{V}_2^+} & \frac{\partial\bar{V}_f}{\partial t_2} & \frac{\partial\bar{V}_f}{\partial t_f} \end{array} \right] \quad , \tag{3.72}$$

where each partial derivative can be derived in terms of the state variables and STM's associated with the trajectory.

Consider first the relationship between changes in the state at time t_1 to state changes at time t_2. Including the time variation at point 2, the linear relationship between the differentials can be written

$$\left\{ \begin{array}{c} \delta\bar{R}_2 \\ \delta\bar{V}_2^- \end{array} \right\} = \left[\begin{array}{cc} A_{21} & B_{21} \\ C_{21} & D_{21} \end{array} \right] \left\{ \begin{array}{c} \delta\bar{R}_1 \\ \delta\bar{V}_1^+ \end{array} \right\} + \left\{ \begin{array}{c} \bar{V}_2^- \\ \bar{a}_2 \end{array} \right\} \delta t_2 \quad , \tag{3.73}$$

where A_{21}, B_{21}, C_{21}, and D_{21} are 3x3 submatrices of the STM from state 1 to state 2, and $\bar{V}_2^-$ and $\bar{a}_2$ are the incoming velocity and acceleration at point 2. Note however, that $\delta\bar{R}_1$ (and δt_1) is zero since the initial state is assumed to be fixed. Thus, the changes in the state at time t_2 can be written in linear differential form as

$$\delta\bar{R}_2 = B_{21}\delta\bar{V}_1^+ + \bar{V}_2^-\delta t_2 \quad , \tag{3.74}$$

$$\delta\bar{V}_2^- = D_{21}\delta\bar{V}_1^+ + \bar{a}_2\delta t_2 \quad , \tag{3.75}$$

in terms of the independent parameters $\delta\bar{V}_1^+$ and δt_2.

Next, examine the relationship between changes in the state at time t_2 and changes in the final state. Again including the time variation of the final state, a linear

relationship between the differential changes can be written

$$\begin{Bmatrix} \delta\bar{R}_f \\ \delta\bar{V}_f \end{Bmatrix} = \begin{bmatrix} A_{f2} & B_{f2} \\ C_{f2} & D_{f2} \end{bmatrix} \begin{Bmatrix} \delta\bar{R}_2 \\ \delta\bar{V}_2^+ \end{Bmatrix} + \begin{Bmatrix} \bar{V}_f \\ \bar{a}_f \end{Bmatrix} \delta t_f \quad , \tag{3.76}$$

where A_{f2}, B_{f2}, C_{f2}, and D_{f2} are the submatrices of the STM from time t_2 to the final time t_f, and $\bar{V}_f$ and $\bar{a}_f$ are the final velocity and acceleration vectors. Substituting the expression for $\delta\bar{R}_2$ in Equation (3.74) into Equation (3.76) and collecting all terms into one matrix produces the desired relationship between the independent parameters and the final state, that is,

$$\begin{Bmatrix} \delta\bar{R}_f \\ \delta\bar{V}_f \end{Bmatrix} = \begin{bmatrix} A_{f2}B_{21} & B_{f2} & A_{f2}\bar{V}_2^- & \bar{V}_f \\ C_{f2}B_{21} & D_{f2} & C_{f2}\bar{V}_2^- & \bar{a}_f \end{bmatrix} \begin{Bmatrix} \delta\bar{V}_1^+ \\ \delta\bar{V}_2^+ \\ \delta t_2 \\ \delta t_f \end{Bmatrix} \quad . \tag{3.77}$$

Note that, as in the previous analysis, the system is underdetermined; that is, there are more independent parameters than dependent ones. The smallest Euclidean norm is thus used to determine the changes in velocities and times necessary to reduce the error in the final state, that is,

$$\begin{Bmatrix} \delta\bar{V}_i^+ \\ \delta t_j \end{Bmatrix} = S^T(SS^T)^{-1} \begin{Bmatrix} \delta\bar{R}_f \\ \delta\bar{V}_f \end{Bmatrix} \quad . \tag{3.78}$$

These changes are applied to the patch points and a new solution is computed that has a smaller error in the final state than the previous solution. Since the problem is highly nonlinear, an iterative process is required to meet the desired values at the final state.

This process can be generalized to include more than one interior maneuver. The general expression for the partials of $\delta\bar{R}_f$ with respect to the independent velocities is written,

$$\frac{\partial\bar{R}_f}{\partial\bar{V}_i^+} = A_{fm}\ A_{m(m-1)}\ \cdots A_{(i+2)(i+1)}\ B_{(i+1)i} \quad \text{for} \quad i = 1\ \text{ to }\ m-1 \quad , \tag{3.79}$$

where m is one less than the total number of states along the trajectory, for example, $m = 3$ for a three burn scheme with four states, including the initial and final states. Note that for $i = m$, the partial reduces to

$$\frac{\partial \bar{R}_f}{\partial \bar{V}_m^+} = B_{fm} \quad , \tag{3.80}$$

since $m+1$ is actually the final state f. Similarly, the partial derivatives of $\delta \bar{V}_f$ with respect to the velocities are, in general, expressed as

$$\frac{\partial \bar{V}_f}{\partial \bar{V}_i^+} = C_{fm}\, A_{m(m-1)}\, \cdots A_{(i+2)(i+1)}\, B_{(i+1)i} \quad \text{for} \quad i = 1 \;\text{ to }\; m-1 \quad , \tag{3.81}$$

except for the case when $i = m$, when the partial is simply

$$\frac{\partial \bar{V}_f}{\partial \bar{V}_m^+} = D_{fm} \quad . \tag{3.82}$$

Note that if a submatrix in any of the partials is undefined (e.g., $A_{(m+2)(m+1)}$) then that matrix is assumed to be the identity matrix I_3 to produce the proper expression for the partial derivative.

The partial of the final position vector with respect to the independent target times in the solution can be written

$$\frac{\partial \bar{R}_f}{\partial t_j} = A_{fm}\, A_{m(m-1)}\, \cdots A_{(j+1)j}\, \bar{V}_j^- \quad \text{for} \quad j = 2 \;\text{ to }\; m \quad , \tag{3.83}$$

and the partial with respect to the final time δt_f (when $j = m+1 = f$) is written

$$\frac{\partial \bar{R}_f}{\partial t_f} = \bar{V}_f \quad . \tag{3.84}$$

Similarly, the partials of the final velocity with respect to the time variations are

$$\frac{\partial \bar{V}_f}{\partial t_j} = C_{fm}\, A_{m(m-1)}\, \cdots A_{(j+1)j}\, \bar{V}_j^- \quad \text{for} \quad j = 2 \;\text{ to }\; m \quad , \tag{3.85}$$

and again, if $j = f$ then the partial reduces to

$$\frac{\partial \bar{V}_f}{\partial t_f} = \bar{a}_f \quad , \tag{3.86}$$

where $\bar{a}_f$ is the final acceleration at time t_f. Given these general expressions, any number of maneuvers can be implemented in the trajectory. An appropriate S matrix

can then be constructed relating changes in the velocities and times corresponding to all the maneuver points with changes in the final state.

This methodology is appropriate if the desired position and velocity states of the final point are known or specified. However, frequently, the final state is not prescribed directly, but instead, a set of constraints on this state is specified, for example, altitude, inclination, right ascension, etc. In order to accommodate constraints on the end state, relationships must be determined between the constraints (α_k) and the final state ($\bar{R}_f, \bar{V}_f, t_f$). These relationships will then be used in conjunction with Equation (3.77), for example, to determine the changes in velocities and times necessary to meet the constraints.

The same set of constraints, examined previously in Section 3.3.5, is derived for the new methodology, beginning with altitude. Recall that for altitude, the constraint function is written

$$\alpha_1 = |\bar{R}_f| - R_{des} \quad , \tag{3.87}$$

and the variation with respect to the final state can be written

$$\delta\alpha_1 = \frac{\bar{R}_f^T}{|\bar{R}_f|}\delta\bar{R}_f \quad . \tag{3.88}$$

Likewise, the apse constraint is defined to be

$$\alpha_2 = (\bar{R}_f \bullet \bar{V}_f) - (\bar{R} \bullet \bar{V})_{des} \quad , \tag{3.89}$$

so that the variation is

$$\delta\alpha_2 = \left[\bar{V}_F^T \delta\bar{R}_f + \bar{R}_F^T \delta\bar{V}_f\right] \quad . \tag{3.90}$$

Note that now both $\bar{R}_f$ and $\bar{V}_f$ are functions of the independent parameters in the problem, where in the original derivation $\bar{R}_f$ was one of the independent parameters. The different assumptions in this derivation lead to very different results from those obtained in Section 3.3.5 using the position and times as the independent variations in the original SRM. Next, the flight path angle constraint is defined to be

$$\alpha_3 = \sin\gamma - \sin\gamma_{des} \quad , \tag{3.91}$$

so that the variation can be written

$$\delta\alpha_3 = \left[\frac{\bar{V}_f^T}{|\bar{R}_f||\bar{V}_f|} - \sin\gamma\frac{\bar{R}_f^T}{|\bar{R}_f|^2}\right]\delta\bar{R}_f + \left[\frac{\bar{R}_f^T}{|\bar{R}_f||\bar{V}_f|} - \sin\gamma\frac{\bar{V}_f^T}{|\bar{V}_f|^2}\right]\delta\bar{V}_f \quad . \tag{3.92}$$

The inclination constraint function is

$$\alpha_4 = \cos i - \cos i_{des} \quad . \tag{3.93}$$

The variation of inclination with respect to the final state is expressed as

$$\begin{aligned}\delta\alpha_4 \quad = \quad & \left[\frac{(\bar{V}_f \times \hat{Z}_{eq})^T}{|\bar{R}_f \times \bar{V}_f|} - \cos i \cdot \frac{|\bar{V}_f|^2\bar{R}_f^T - (\bar{R}_f \bullet \bar{V}_f)\bar{V}_f^T}{|\bar{R}_f \times \bar{V}_f|^2}\right]\delta\bar{R}_f \\ & + \left[\frac{(\hat{Z}_{eq} \times \bar{R}_f)^T}{|\bar{R}_f \times \bar{V}_f|} - \cos i \cdot \frac{|\bar{R}_f|^2\bar{V}_f^T - (\bar{R}_f \bullet \bar{V}_f)\bar{R}_f^T}{|\bar{R}_f \times \bar{V}_f|^2}\right]\delta\bar{V}_f \quad .\end{aligned} \tag{3.94}$$

The declination constraint is defined as

$$\alpha_5 = \sin(dec) - \sin(dec)_{des} \quad , \tag{3.95}$$

and the resulting variational equation is

$$\delta\alpha_5 = \left[\frac{\hat{Z}_{eq}^T}{|\bar{R}|} - \sin(dec)\frac{\bar{R}_f^T}{|\bar{R}|^2}\right]\delta\bar{R}_f \quad . \tag{3.96}$$

Finally, the constraint function for right ascension is expressed as

$$\alpha_6 = rt.asc - rt.asc_{des} \quad , \tag{3.97}$$

so that the variation with respect to the final state is

$$\delta\alpha_6 = \frac{\left(\bar{R}_f \bullet \hat{x}_{bf}\right)\hat{y}_{bf}^T - \left(\bar{R}_f \bullet \hat{y}_{bf}\right)\hat{x}_{bf}^T}{\left[\left(\bar{R}_f \bullet \hat{x}_{bf}\right) + \left(\bar{R}_f \bullet \hat{y}_{bf}\right)\right]^2}\delta\bar{R}_f + \omega_e\frac{\left(\bar{R}_f \bullet \hat{x}_{bf}\right)^2 + \left(\bar{R}_f \bullet \hat{y}_{bf}\right)^2}{\left[\left(\bar{R}_f \bullet \hat{x}_{bf}\right) + \left(\bar{R}_f \bullet \hat{y}_{bf}\right)\right]^2}\delta t_f \quad . \tag{3.98}$$

Note that this is the only constraint partial that includes a variation in the independent parameter t_f. All other partials are functions solely of the dependent variables $\bar{R}_f$ and $\bar{V}_f$.

In general, the relationship between the constraints and the variations in the final state can be written

$$\{\delta\alpha_k\} = Q\left\{\begin{array}{c}\delta\bar{R}_f \\ \delta\bar{V}_f\end{array}\right\} + \bar{q}\;\delta t_f \quad , \tag{3.99}$$

where Q is a matrix whose elements are the coefficients of $\delta\bar{R}_f$ and $\delta\bar{V}_f$ from the constraint variational equations. The quantity $\bar{q}$ is a k dimensional vector whose only non-zero element is the coefficient for the right ascension partial with respect to δt_f. By substituting in the expressions for $\delta\bar{R}_f$ and $\delta\bar{V}_f$ from Equation (3.77), for example, the relationship between the constraints and the variations in the velocities and times can now be written

$$\{\delta\alpha_k\} = Q\ S \left\{ \begin{array}{c} \delta\bar{V}_i^+ \\ \delta t_j \end{array} \right\} + \bar{q}\ \delta t_f \quad , \tag{3.100}$$

or

$$\{\delta\alpha_k\} = P \left\{ \begin{array}{c} \delta\bar{V}_i^+ \\ \delta t_j \end{array} \right\} \quad , \tag{3.101}$$

where $P = QS$, with the lone partial from $\bar{q}$ incorporated into the matrix in the appropriate location. Now the standard procedure is applied, i.e., the smallest Euclidean norm,

$$\left\{ \begin{array}{c} \delta\bar{V}_i \\ \delta t_j \end{array} \right\} = P^T(PP^T)^{-1}\ \{\delta\alpha_k\} \quad , \tag{3.102}$$

is computed to determine the changes in the velocity states and times necessary to enforce the desired constraints at the final time. An example of the application of this targeting methodology will be presented in the discussion of the GENESIS trajectory design.

4. APPLICATION OF THE THREE STEP METHODOLOGY

The previous chapters have included a discussion of the basic three step methodology that is successfully used to determine particular solutions in the four body problem. This chapter presents a number of applications and extensions of this technique including: additional MLS solutions, escape trajectories, transfers to libration point orbits (LPO), and the GENESIS trajectory. All of these varied types of solutions attest to the versatility and robustness of the algorithm. In the process of developing these different applications, a number of extensions to the algorithm have been required, including: generalized launch segments, multiple phasing loops, and the inclusion of deterministic maneuvers into the three step methodology.

4.1 MLS Trajectories

The original impetus behind this work was the development of a methodology to determine trajectory solutions representing double lunar swingby trajectories, similar to the concept proposed by Farquhar and Dunham[8] in 1980. This led to the development of the Timing Condition by Marsh and Howell[7,13,38] to determine a conic approximation for these types of trajectories. Marsh[13] proposed using a semi-analytical corrections scheme to improve the conic solution sufficiently to allow successful numerical integration of the trajectory; this, however, proved to be a somewhat cumbersome process and required much user interaction. Building on the efforts of Marsh, Spencer[14] proposed using multi-conic approximations in the intermediate step to incorporate the lunar gravity that was neglected in the initial approximation. Although this approach is successful in improving the initial trajectory to allow numerical integration, large velocity discontinuities are introduced into the solution.

This difficulty is resolved by the introduction of the state relationship matrix to eliminate the velocity discontinuities.[15,39] The current work has expanded upon the previous contributions by incorporating trajectory constraints and improving the efficiency of the algorithm, as well as expanding the scope of the solution process to include many other types of solutions. The following multiple lunar swingby examples are presented as testimony to the previous contributors.

4.1.1 Anti-Solar Pointing Apogee Solutions

4.1.1.a Case MLS-A1

The goal for the first example is the construction of a multiple lunar swingby trajectory with anti-solar pointing apogees (towards L_2); it is based on a solution from Marsh,[13] Spencer,[14] and Wilson.[15] The inputs to the TC algorithm are listed in Table 4.1, as well as the resulting conic elements for each segment. The trajectory consists of four conic segments, beginning with a launch or insertion onto the trajectory on May 19, 1993. The initial conic arc includes one phasing loop followed by a one month outer loop with apogee in the anti-solar direction. The third segment is an inner loop that sets up a two month outer loop with apogee close to L_2 at roughly 1.4 million km from the Earth. The resulting conic solution appears in Figure 4.1, projected onto the $\hat{x}\hat{y}$ plane in the SR frame. The patch points selected as input to the intermediate step are marked by symbols at various locations along the trajectory. A circle is used to denote a patch point along the first segment, while a diamond is used for the second segment, squares denote points along the third segment, and triangles are for the final segment. In conjunction with perigee, apogee, and swingby states, additional patch points are determined at various times along the trajectory. The selection of these additional patch points is aided by visualization of the solution in the SR frame. The designer places extra points, as necessary, to preserve the general shape of the trajectory, and to aid in the convergence process.

After application of the intermediate step, a numerically integrated solution using JPL DE405 ephemerides is generated that closely matches this initial approximation.

Table 4.1 Input/Output Parameters for Case MLS-A1

Segment No.	1	2	3	4
		Inputs		
N_{mos}	1	1	1	2
N_{apo}	1	1	1	1
N_{peri}	2	0	2	0
R_p (km)	6578	–	50000	–
ψ (deg)	0.0	0.0	0.0	0.0
		Outputs		
a_c/L^*	0.57180	1.30301	0.71632	1.90736
e_c	0.97007	0.81255	0.81841	0.79861
Δt (days)	14.9937	34.3443	24.1227	65.0356

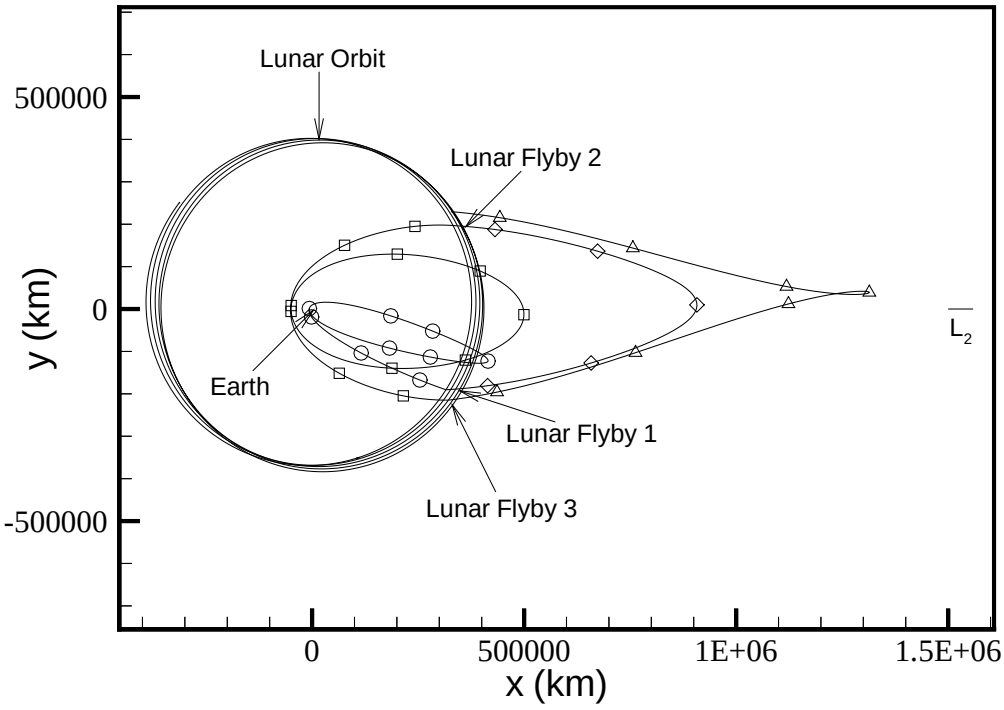

Figure 4.1. Conic Approximation for Case MLS-A1

Since the MCA/PSA solution has been shown to accurately reflect the final integrated solution, only the integrated trajectory is plotted in Figure 4.2. This trajectory meets the design criteria and satisfies the given injection constraints, namely: altitude = 200 km, inclination = 28.5 deg, and insertion at perigee. Additionally, an apse constraint is placed on all interior perigee and apogee locations. This constraint helps to maintain the overall shape of the trajectory closer to that designed in the initial approximation.

4.1.1.b Case MLS-A2

The second anti-solar solution is a variation on the first case, where the length of the final outer loop is increased by roughly one month. The launch/insertion date is now September 12, 1993 and the relevant input/output parameters for the conic arc selection algorithm are listed in Table 4.2. The integrated trajectory is plotted in Figure 4.3, with similar launch, perigee, and apogee constraints as in Case MLS-A1. Note that the first three conic arcs are similar to the previous solution. The final

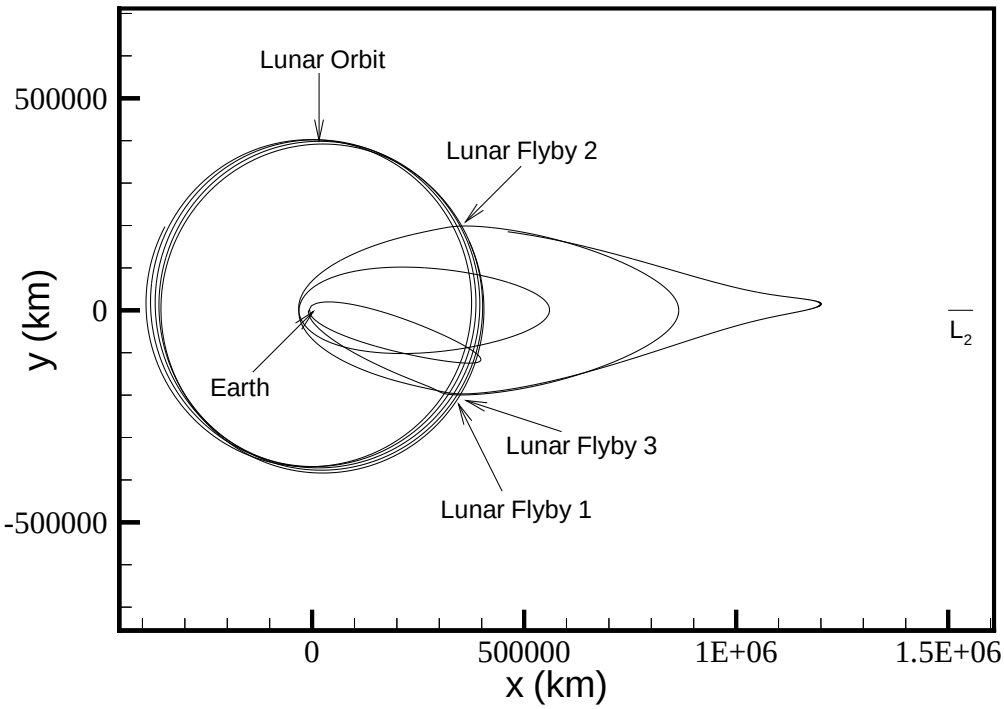

Figure 4.2. Integrated Solution for Case MLS-A1

Table 4.2 Input/Output Parameters for Case MLS-A2

Segment No.	1	2	3	4
		Inputs		
N_{mos}	1	1	1	3
N_{apo}	1	1	1	1
N_{peri}	2	0	2	0
R_p (km)	6578	–	50000	–
ψ (deg)	0.0	0.0	0.0	0.0
		Outputs		
a_c/L^*	0.55358	1.32395	0.70607	2.38273
e_c	0.96909	0.81273	0.81577	0.79009
Δt (days)	15.6255	34.8671	24.2269	94.3876

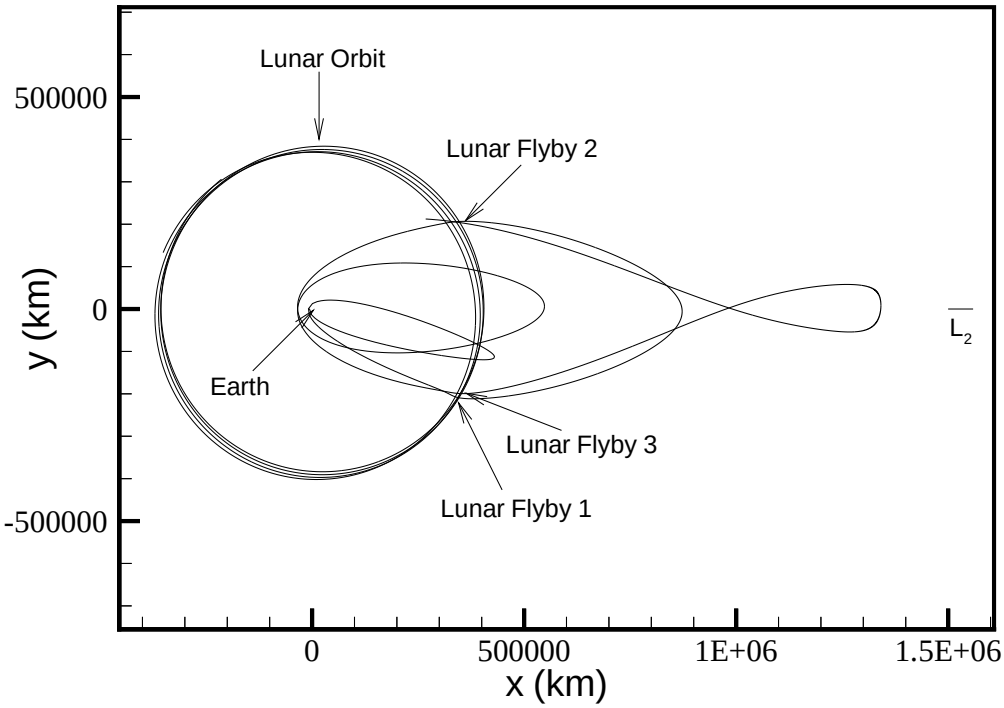

Figure 4.3. Integrated Solution for Case MLS-A2

segment is noticeably longer, and now appears to cross itself when viewed in the $\hat{x}\hat{y}$ plane. In reality, the solution is three dimensional, so the trajectory does not intersect when viewed in the $\hat{x}\hat{z}$ or $\hat{z}\hat{y}$ projections.

4.1.2 Solar Pointing Apogee Solutions

Trajectories with solar pointing apogees analogous to the anti-solar cases, are also presented. Each case is a close analog to the corresponding anti-solar case.

4.1.2.a Case MLS-S1

Table 4.3 and Figure 4.4 represent the solar pointing analog to Case MLS-A1, with trajectory insertion on June 1, 1993, and with injection and apse constraints similar to those for the previous example.

4.1.2.b Case MLS-S2

Finally, Table 4.4 and Figure 4.5 present the solar pointing analog to Case MLS-A2 with a insertion on June 2, 1993 and a three month final segment. With a few minor exceptions, the solar pointing cases mirror the anti-solar cases quite well. It is noted that the methodology is not restricted to solutions with apogees near the $\hat{x}$ axis, but is generalized to include other desired orientations.

4.2 General Launch Segments

The current formulation of the Timing Condition is well suited to the determination of conic arcs for the segments that comprise the initial approximation of a multiple lunar swingby trajectory. However, the TC is based on the primary assumption that a lunar encounter occurs at each end point of any given conic arc. This assumption is overly restrictive for more general types of solutions that have perhaps only one or even no lunar gravity assists. A more general methodology has been developed to allow a larger range of conic arcs to be available for the designer.

Consider then, a more general approach to the design and construction of conic segments between launch and the first lunar encounter. (Note that the term "launch"

Table 4.3 Input/Output Parameters for Case MLS-S1

Segment No.	1	2	3	4
		Inputs		
N_{mos}	1	1	1	2
N_{apo}	1	1	1	1
N_{peri}	2	0	2	0
R_p (km)	6578	–	50000	–
ψ (deg)	180.0	180.0	180.0	180.0
		Outputs		
a_c/L^*	0.56035	1.29670	0.74142	1.88813
e_c	0.96946	0.81432	0.82456	0.77822
Δt (days)	15.2660	34.1773	24.0729	64.7144

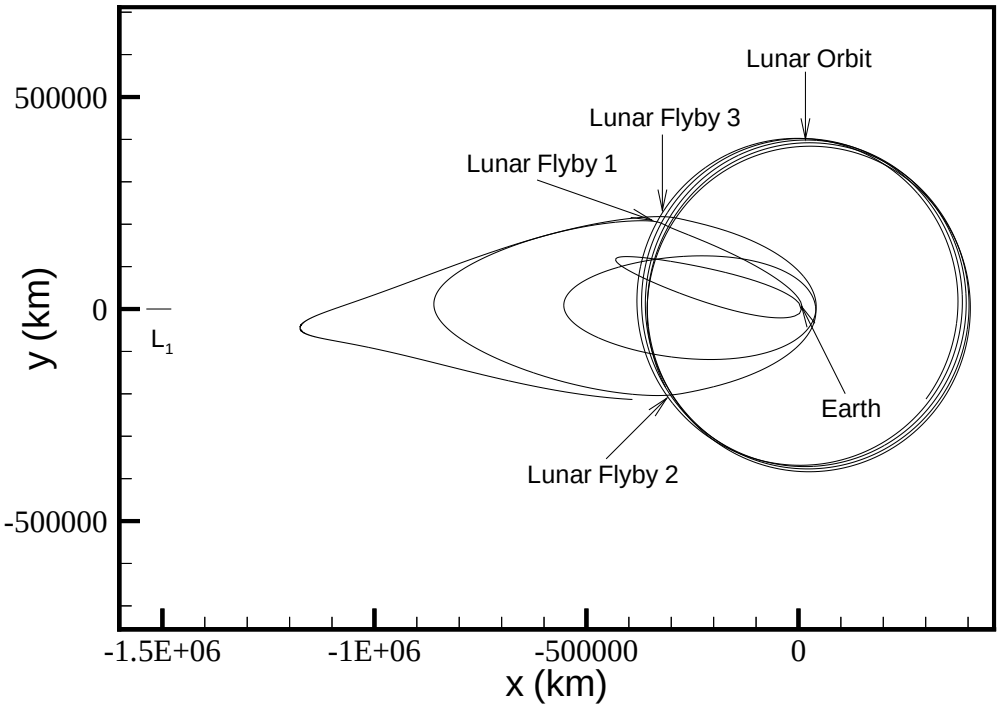

Figure 4.4. Integrated Solution for Case MLS-S1

Table 4.4 Input/Output Parameters for Case MLS-S2

Segment No.	1	2	3	4
		Inputs		
N_{mos}	1	1	1	3
N_{apo}	1	1	1	1
N_{peri}	2	0	2	0
R_p (km)	6578	–	50000	–
ψ (deg)	180.0	180.0	180.0	180.0
		Outputs		
a_c/L^*	0.56035	1.29670	0.74142	2.37395
e_c	0.96946	0.81432	0.82456	0.78475
Δt (days)	15.2660	34.1774	24.0729	93.9121

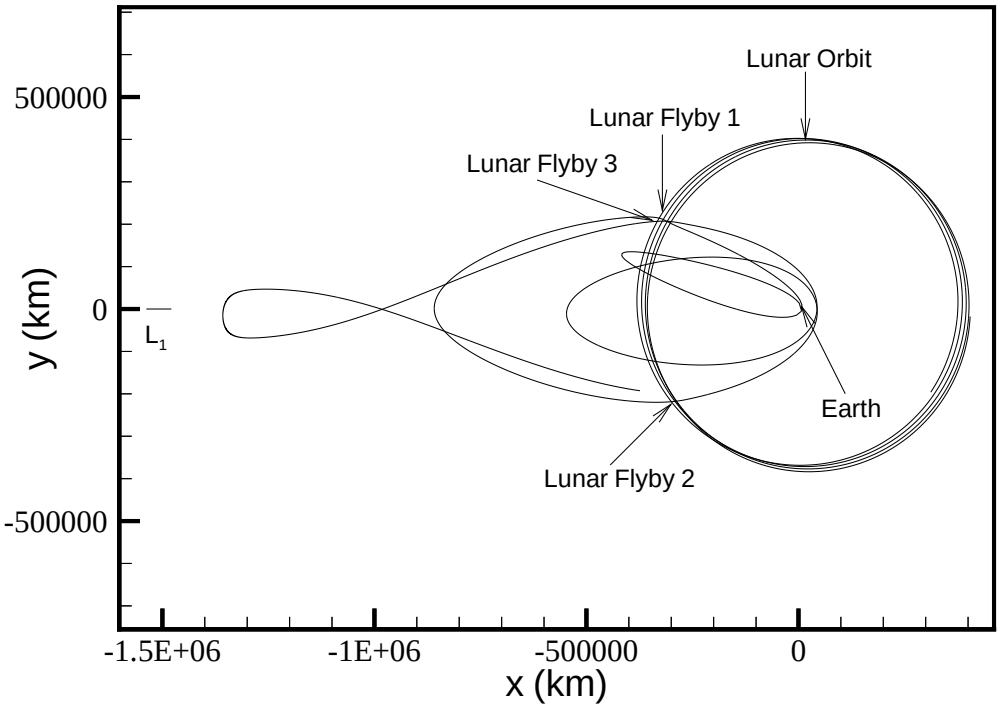

Figure 4.5. Integrated Solution for Case MLS-S2

actually refers to the injection onto the trajectory.) The launch segment from a solution to the Timing Condition of Marsh and Howell[7,13,38] is actually half of an "inner loop" segment. This implies that the "launch segment", in the form of a single phasing loop as employed in the MLS cases described in Section 4.1, is actually the second half of an inner loop solution consisting of two phasing loops that originates at some fictitious lunar encounter. Although there is no intention of actually using this lunar encounter (hence, the term *fictitious*), the algorithm times the loops assuming that the lunar passage is real. This assumption then tends to place undue restrictions on the available launch dates and configurations.

A more general method to determine launch segments has been developed that requires the following inputs: launch distance (R_p), approximate apogee distance (R_a), launch date (JD_p), number of phasing loops (N_p) and elongation angle of the Moon (ψ_m) at the first encounter, as well as the number of complete lunar months (N_m) during the launch segment. The launch is still assumed to occur at perigee, so that the launch/injection conditions specified are also the initial perigee conditions. Given the desired R_p, then, and the estimate of the apogee distance, R_a, initial estimates of the semi-major axis, a_c, and eccentricity, e_c of the conic that represents the launch segment can be determined as,

$$a_c = \frac{R_p + R_a}{2} \quad ; \quad e_c = 1 - \frac{R_p}{a_c} \quad , \tag{4.1}$$

from the definitions of perigee and apogee in terms of orbital elements.

An iterative search through the lunar ephemerides produces the time (JD_m) and state ($\bar{R}_m, \bar{V}_m$) of the Moon at the desired elongation angle (ψ_m), with the given number of complete lunar months (N_m) incorporated into the process. This lunar state is selected to be the final state along the launch segment; hence the actual time of flight from injection to lunar encounter is now computed as

$$TOF_{act} = \mathrm{JD}_m - \mathrm{JD}_p \quad , \tag{4.2}$$

based on the desired launch date JD_p.

The radial distance between the Moon and the Earth at the final time (R_m) is used to solve Kepler's equation for an estimated time of flight based on the estimated values of a_c and e_c. Since the lunar position is also the final position along the conic arc, the eccentric anomaly corresponding to the final spacecraft position (E_f) can be evaluated as

$$E_f = \arccos\left[\frac{1}{e_c}\left(1 - \frac{R_m}{a_c}\right)\right] \quad . \tag{4.3}$$

The initial state on the trajectory is assumed to be perigee, hence the initial eccentric anomaly is zero, and Kepler's equation yields an estimate of the time of flight as

$$TOF_{est} = \sqrt{\frac{a_c^3}{\mu_e}}\left(2\pi N_p + E_f - e_c \sin E_f\right) \quad , \tag{4.4}$$

where μ_e is the gravitational parameter of the Earth and N_p is the number of complete periods of the spacecraft motion. This estimated time of flight for the launch segment, with orbital elements a_c and e_c, is compared to the true time of flight to define the time error, that is,, that is,

$$\Delta t = TOF_{act} - TOF_{est} \quad . \tag{4.5}$$

Kepler's equation in Equation (4.4) is now differentiated with respect to a_c such that the following relationship is determined

$$\Delta a_c = \Delta t \left[\frac{1.5\ TOF_{est}}{a_c} - \sqrt{\frac{a_c}{\mu_e}} \sin E_f (1 - e_c) - \sqrt{\frac{a_c}{\mu_e}} R_m \frac{1 - \cos E_f}{a_c e_c \sin E_f}\right]^{-1} \quad . \tag{4.6}$$

This equation relates changes in semi-major axis to the error in the time of flight along the launch segment in terms of the estimates of the orbital elements. Evaluating this expression and adding this Δa_c to the original guess yields a better estimate of the values of a_c and $e_c = 1 - \frac{R_p}{a_c}$ that are necessary to reduce the error in the time of flight. A new estimate of the flight time is then computed and this process is repeated until the time error is within some prescribed tolerance.

After the desired time of flight is achieved, a_c and e_c that define the launch conic are known, as well as E_f (and therefore true anomaly θ_f^*) at the final time. If the conic orbit plane is assumed coincident with the lunar orbit plane (similar to the

assumptions made for the Timing Condition), the entire conic segment can be quantified by the orbital elements (a_c, e_c, i_{moon}, Ω_{moon}, ω_c, $E_i = 0$, and E_f). (Note that the argument of perigee ω_c is determined from the known position vector $\bar{R}_m$ at the final time, as well as the other orbital elements.) This methodology is not limited to elliptical orbits, but can be generalized to include hyperbolic conic segments, such that a continuous range of launch solutions is made available.

As an example of this new methodology, consider the design of a launch segment from injection to a lunar encounter on April 11, 2001, corresponding to a lunar elongation angle of -45 deg. A series of launch dates from March 15 to April 10, 2001 are examined. The results are presented graphically in Figure 4.6, projected into the $\hat{x}\hat{y}$ SR plane. The figures depict the spacecraft trajectory as a solid line, while the Moon's orbit during the given time of flight is plotted as a dotted line. In Case (a), corresponding to launch on April 10, the solution is hyperbolic. In general, if the time of flight from launch (injection) to lunar encounter is less that 2 days, the ensuing solution will be hyperbolic with respect to the Earth. The trajectory in Case (b), with launch on April 8, has a time of flight of 3 days. In this analysis, segments with flight times between 2 and 10 days utilize no phasing loops, since the minimum period for a phasing loop with apogee beyond the Moon is roughly 10 days. For flight times greater than 10 days, trajectories that utilize one or more phasing loops are selected. Cases (c), (d), and (e) then demonstrate solutions with a single phasing loop, and orbital periods of 11, 18, and 25 days, respectively. As the time of flight increases, the size of the phasing loop continues to increase until it actually appears to cross itself when viewed in the $\hat{x}\hat{y}$ plane. As the phasing loop becomes larger, the launch cost to inject onto such an orbit also increases, due to the increase in required orbital energy. For trajectories with times of flight of greater than roughly 20 days, a two phasing loop solution becomes feasible, and presents an alternative solution with a lower injection cost than the single loop solution. The solution in Case (f) represents such an example with the same launch date as Case (e) on March 15, but including

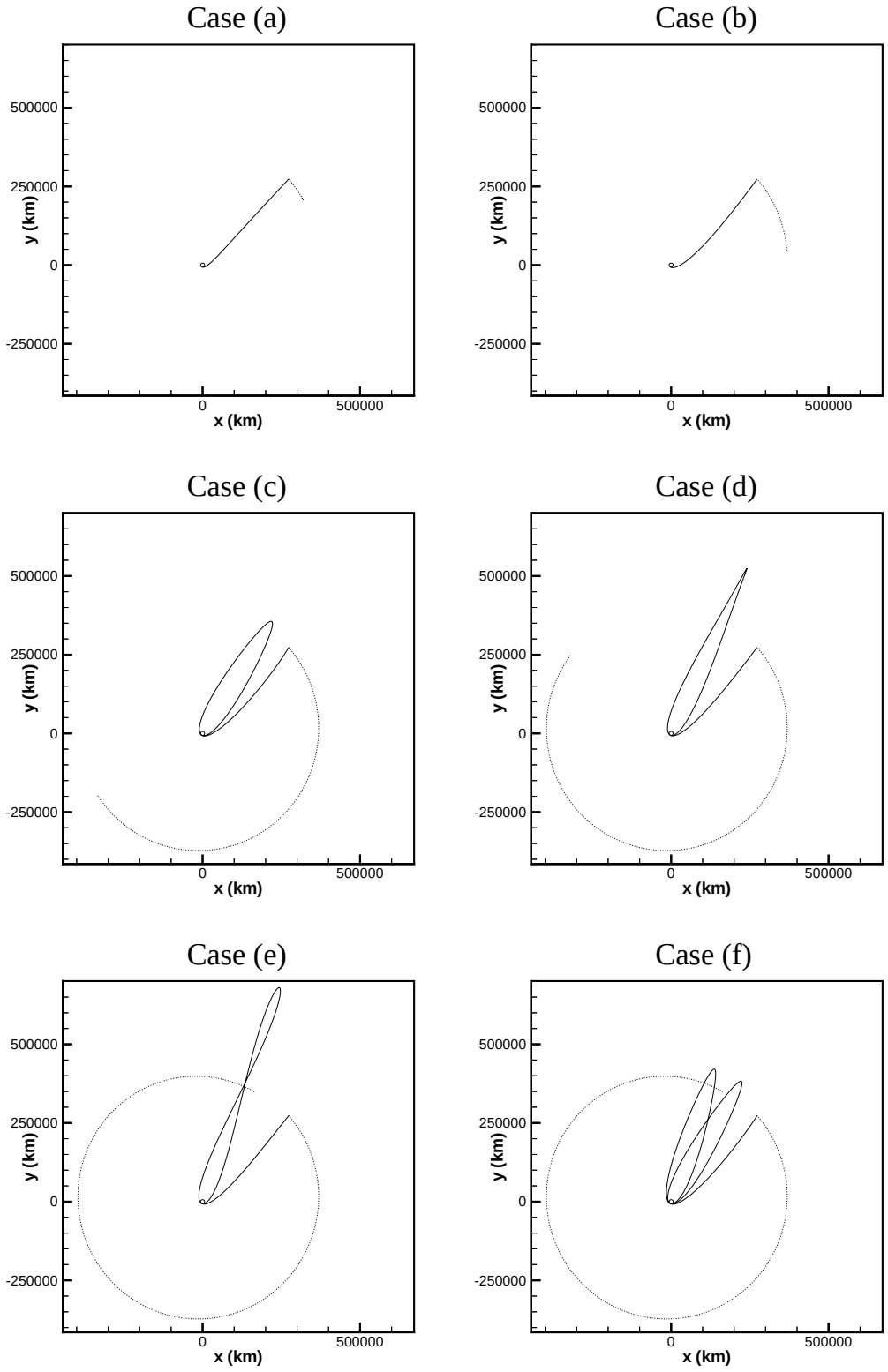

Figure 4.6. Conic Launch Segments for April 11, 2001 Lunar Encounter

an additional phasing loop. The methodology is not limited to those cases presented here, but encompasses a wide range of options.

All of the cases in Figure 4.6 exhibit what is termed an *ascending* lunar encounter. That is, the spacecraft encounters the Moon on the outbound leg along the conic arc. Sometimes in the design process, however, it is also desirable to utilize *descending* lunar encounters that pass the Moon on the inbound portion of the conic. By modifying the form of Kepler's equation in Equation (4.4) that is used in the iteration process, a conic that includes a descending lunar encounter can be specified. To do so, note that the conic orbit for the launch segment actually passes through the desired lunar radial distance (R_m) twice in a given conic loop, once on the ascending portion of the orbit and again on the descending half. Due to the near symmetry of the orbit with respect to the Moon, the eccentric anomaly E_f for the descending solution can be approximated as

$$E_f = 2\pi - \arccos\left[\frac{1}{e_c}\left(1 - \frac{R_m}{a_c}\right)\right] \quad . \tag{4.7}$$

This new expression is employed in the previously described iteration process to determine a_c and e_c for a launch segment that includes a descending lunar encounter.

As an example of a solution with a descending encounter, consider the design of a trajectory that incorporates a single lunar gravity assist to achieve escape velocity with respect to the Earth. For this case, a launch date of February 10, 2000 is selected to begin a one month launch segment that includes a descending lunar encounter. The lunar gravity assist is utilized to increase the energy of the orbit sufficiently to escape the Earth's gravity field. The conic computed for this segment is defined such that $a_c = 638386$ km and $e_c = 0.98970$. This yields a perigee altitude of 200 km with a descending lunar encounter on April 7, 2000 at an elongation angle of 150 deg. A hyperbolic conic arc is designed between the lunar encounter and some desired target point, selected for this example at $x = 1.0e6$ km, $y = 1.0e6$ km, $z = 50,000$ km on April 15, 2000. (The selection of this target point is somewhat arbitrary; however, the timing of the Moon must be considered when determining the final state. Due to timing constraints with the Moon, the selection of *any* target

point may not be possible.) The resulting conic solution appears as a dotted line in Figure 4.7, as plotted in the SR frame. The three step methodology is applied to this initial approximation to produce an integrated four body solution, plotted as the solid line in the figure. Although the elongation angle of the integrated solution is advanced by roughly 30 degrees from the conic solution, the trajectory still achieves escape with a final eccentricity of 1.3942 relative to the Earth.

In conclusion, the new generalized launch algorithm offers greater flexibility for the trajectory designer. Thus, the applicability of the three step process is further extended to include other types of solutions in the four body problem.

4.3 Design of Phasing Loops

A number of missions have been proposed in recent years that make use of lunar gravity assists, for example, to insert into a Lissajous orbit about one of the collinear libration points in the Sun-Earth system. An example of this type of trajectory is

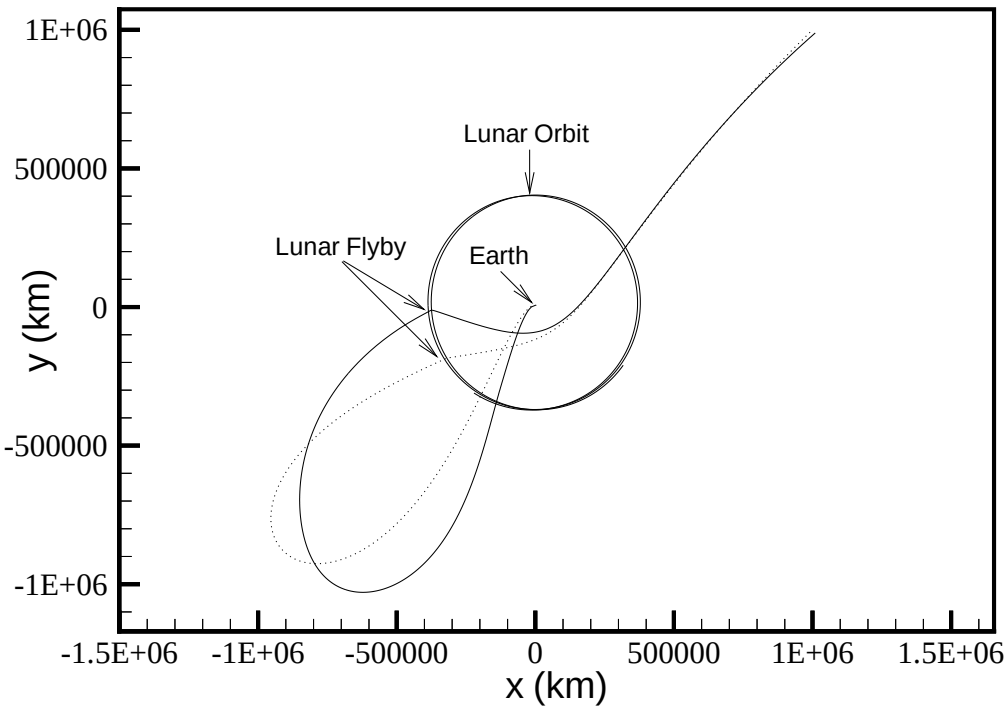

Figure 4.7. Escape Using a Single Lunar Gravity Assist

presented in the previous chapter to demonstrate the design of transfer trajectories to libration point orbits. This trajectory uses a state along a stable manifold associated with the desired Lissajous orbit as the target state for the transfer. In the development of the methodology thus far, the transfer itself, then, can be designed using two body conic segments that incorporate a lunar encounter, as described in detail in the previous chapter.

In the transfer example, a single phasing loop is arbitrarily selected to demonstrate the design process. One of the motivating factors for including phasing loops in the transfer between the insertion point from the parking orbit and the first lunar encounter is timing concerns for possible trajectory correction maneuvers. The incorporation of a lunar gravity assist into the mission design generally increases the complexity of the trajectory and requires highly accurate timing and targeting to ensure a successful encounter. Thus, any inaccuracies in the trajectory due to insertion errors or maneuver errors must be corrected prior to the lunar encounter to achieve the desired gravity assist. The use of phasing loops in the trajectory facilitates the implementation of these correction maneuvers.

For the types of solutions that are studied here (with $a_c \cong$ 200,000 km and $e_c \cong$ 0.95) the typical time from the final perigee on the launch segment to the lunar orbit is roughly 2.5 to 3 days. From a mission operations standpoint, this is insufficient time to correct any launch errors and accurately target the desired lunar flyby using only a direct launch to the Moon. By introducing phasing orbits with typical periods of 10 to 13 days, more time is allowed to generate and process orbit determination information, and to devise a method to compensate for the trajectory errors. Additionally, maneuvers can be pre-planned at specific locations during the phasing loops, for example, at such states as perigee, apogee, or ascending/descending nodes. These maneuvers may be exploited, for example, to more precisely target the lunar gravity assist, or to alter the trajectory, in some specified way, such as incorporating an orbital plane change into the trajectory design. To demonstrate the use of phasing loops, a series of variations on the previous transfer example are presented.

4.3.1 Case PhL-0

The first example is a trajectory with no phasing loops. In this solution, the vehicle is inserted onto the transfer path from the parking orbit on September 20, 2007. The trajectory is plotted in Figure 4.8 in the SR frame. All of the cases that will be presented have the typical injection constraints, defined as: 200 km altitude, 28.5 deg inclination relative to the equator, and insertion from perigee. The cost to inject onto the manifold, or Lissajous Orbit Insertion (LOI) cost, is 1.93 m/s for this case. This minimal insertion cost is due to the fact that the integrated solution is very similar to the actual manifold trajectory selected from the numerous manifolds associated with the specified Lissajous; this cost will increase when the phasing loops are introduced.

4.3.2 Case PhL-1

The second solution is actually the one loop case presented previously with transfer insertion on September 9, 2007, and a phasing loop period of 10.2 days. This trajectory is plotted in Figure 4.9, and has an LOI cost of 20.64 m/s. (Note that for comparison purposes, all of the cases that are presented target the same final state along the desired manifold. This is not necessary, but simply serves as a reasonable starting point.)

4.3.3 Case PhL-2

The third case extends the solution to include two phasing loops with injection onto the transfer on August 28, 2007, and has a phasing loop period of 11.75 days. The LOI cost has now increased to 30.35 m/s for this transfer. This solution appears in Figure 4.10.

4.3.4 Case PhL-3

One of the major concerns when utilizing multiple phasing loops is the effect of lunar perturbations on the trajectory. If the timing of the phasing loops is not

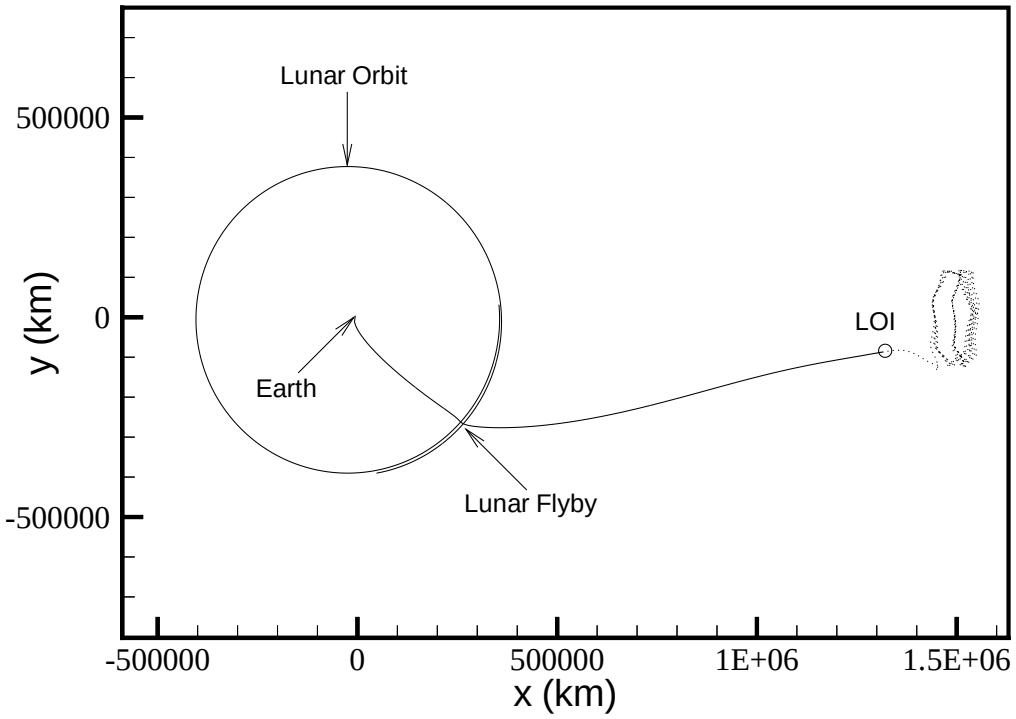

Figure 4.8. Earth-to-L_2 Transfer Using Zero Phasing Loops – Case PhL-0

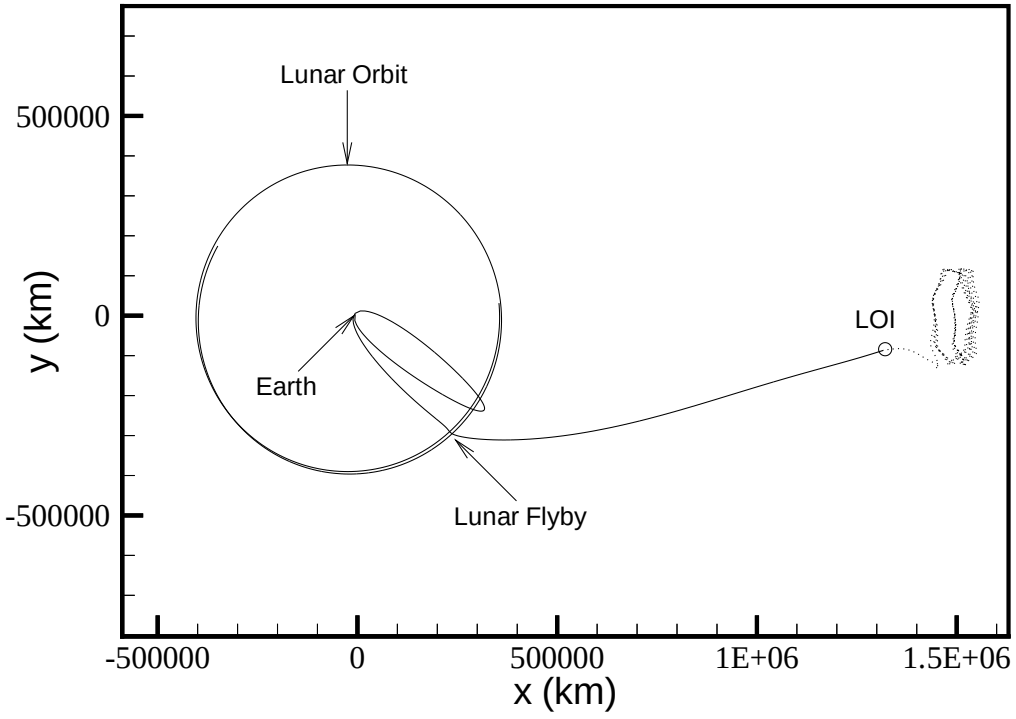

Figure 4.9. Earth-to-L_2 Transfer Using One Phasing Loop – Case PhL-1

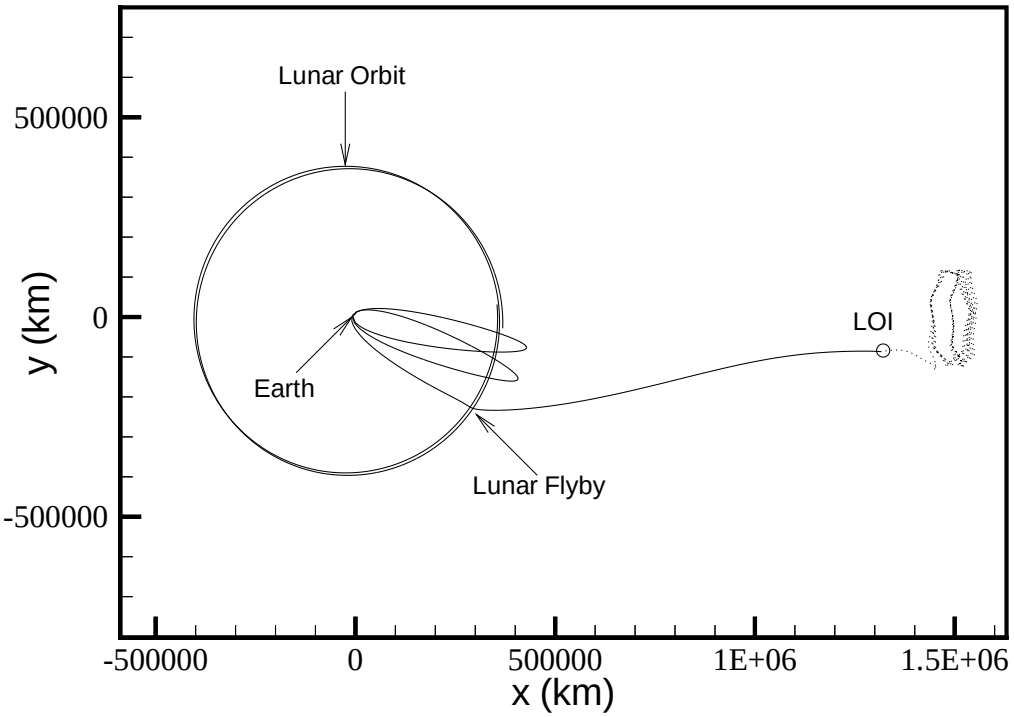

Figure 4.10. Earth-to-L_2 Transfer Using Two Phasing Loops – Case PhL-2

designed properly, an unintended lunar encounter may occur prior to the desired flyby, with possibly catastrophic effects. For the 0, 1, and 2 loop solutions, the period of the phasing loops is roughly 10–13 days. Since the lunar period is about 29 days, while the time of flight along the insertion-to-encounter segment is 13–27 days, these solutions will naturally avoid any major lunar perturbations. However, solutions that involve three or more phasing loops may have flight times longer than one month and can exhibit a strong tendency to suffer severe orbital changes due to undesired lunar perturbations. To demonstrate this, examine Figure 4.11. In Case (a), a conic representation of a two phasing loop solution is depicted, with the lunar orbit plotted as a dotted line that originates at the launch (transfer insertion) date of the spacecraft into its orbit; the initial (I) and final (E) lunar positions are marked with a circle and square respectively. The times corresponding to the spacecraft perigees (P_i) in the phasing loops are also marked on the lunar orbit with triangles, while the apogees (A_i) are denoted with diamonds. Clearly for the two loop nominal, the Moon will

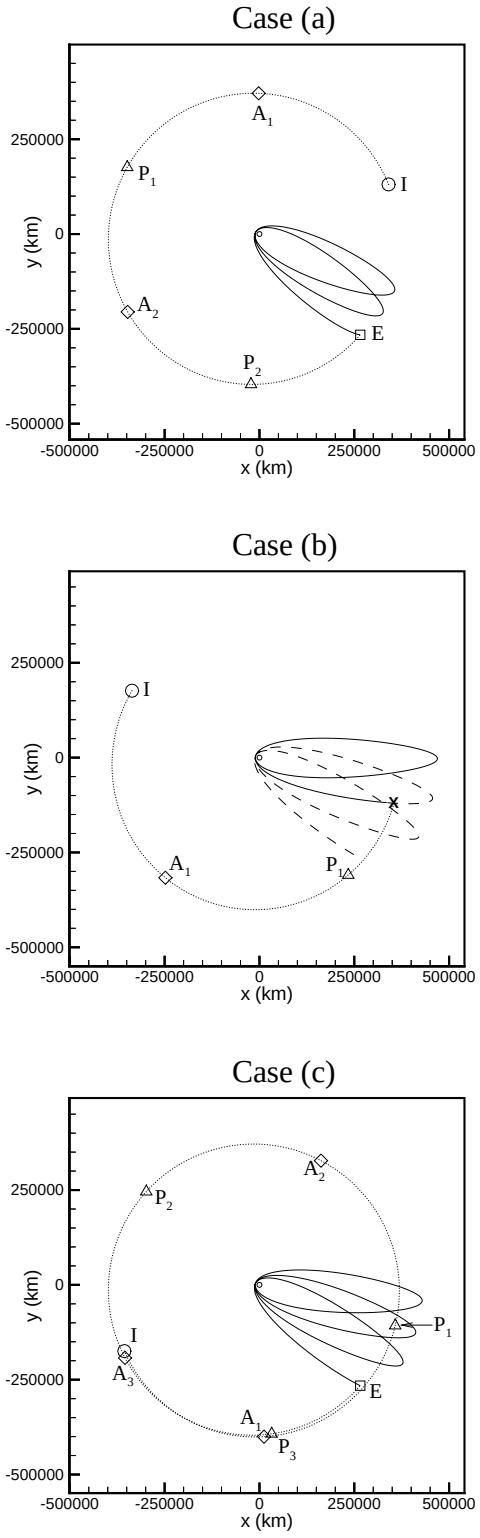

Figure 4.11. Comparison of 2 and 3 Phasing Loop Trajectories

not adversely affect the spacecraft trajectory during the given flight time and the spacecraft encounters the Moon only at the desired time. The solution in Case (b) of the figure shows a similar conic solution, but for three phasing loops. In this case, it is seen that as the spacecraft approaches the lunar orbit on the second phasing loop, the Moon is passing close by and in fact, the spacecraft experiences an unintended lunar flyby. This location is denoted by an 'X' on the figure. (Note that the spacecraft orbit from insertion up to the time of the undesired lunar pass is plotted with a solid line, while the rest of the conic solution appears as a dashed line.) Of course, in the conic approximation, the lunar gravity is ignored, however, this configuration can create large lunar perturbations when the lunar gravity is actually modeled in the trajectory. These perturbations may cause catastrophic errors, such as, impact with the Earth or the Moon, or possibly even escape from the system.

One possible solution to this dilemma is to utilize phasing loops that are skewed out of the lunar orbit plane, thereby reducing the possibility for lunar perturbations. However, this type of scenario may result in a larger maneuver at LOI depending upon the manifold trajectory selected in the initial approximation. This difficulty may actually be avoided without large orbital plane changes through judicious selection of the period for the phasing orbits. The design process involves adjusting the timing of the insertion from the parking orbit such that the spacecraft is located at perigee near the beginning of the second phasing loop when the Moon is opposite the spacecraft along the conic segment line of apsides (i.e., near apogee). This configuration is shown graphically in Case (c). Notice now that the location of the Moon at the time of the first perigee (P_1) after insertion is designed such that the spacecraft is approaching the second apogee (A_2) as the Moon is moving away from the spacecraft. This ensures that the trajectory will avoid any large lunar perturbations throughout the remaining phasing loops.

Using this timing constraint, a three loop solution to the transfer problem is designed, with the integrated trajectory appearing in Figure 4.12. In this case, the trajectory has a launch/insertion date of August 15, 2007 and phasing loop period of

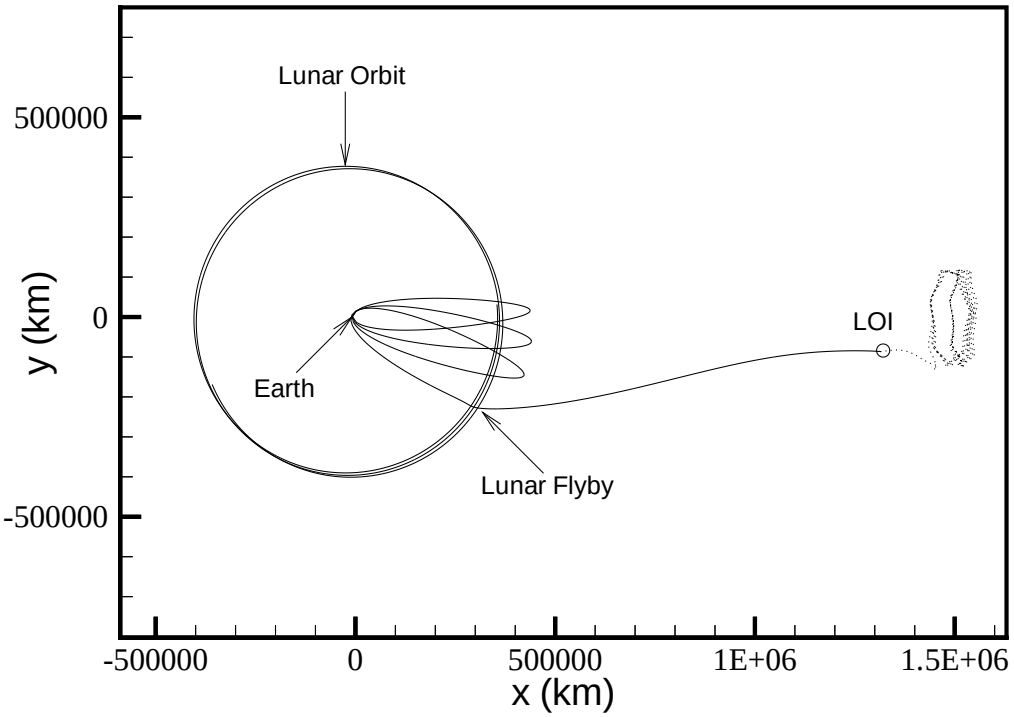

Figure 4.12. Earth-to-L_2 Transfer Using Three Phasing Loops – Case PhL-3

11.78 days to avoid any severe perturbations from the Moon. The LOI for this three loop solution is 32.75 m/s.

4.3.5 Case PhL-4

The design of the four loop solution is guided by the same timing constraints as the three loop case. Now, however, the difficulties arise near apogee of the third loop, in the same problem region defined in the case with three phasing loops. The orbital period of the phasing loops is thus adjusted to place the spacecraft at perigee of the third phasing loop when the Moon is along the spacecraft line of apsides near apogee of the conic segment. The final four loop integrated solution is plotted in Figure 4.13. This solution has an injection date of August 3, 2007 and phasing loop period of 12.1 days; the LOI for this solution is 32.19 m/s. Note that in the design of the four loop case, it is necessary to insert a maneuver of 23.00 m/s magnitude at the first apogee to ensure positive clearance of the Earth at the proceeding perigees.

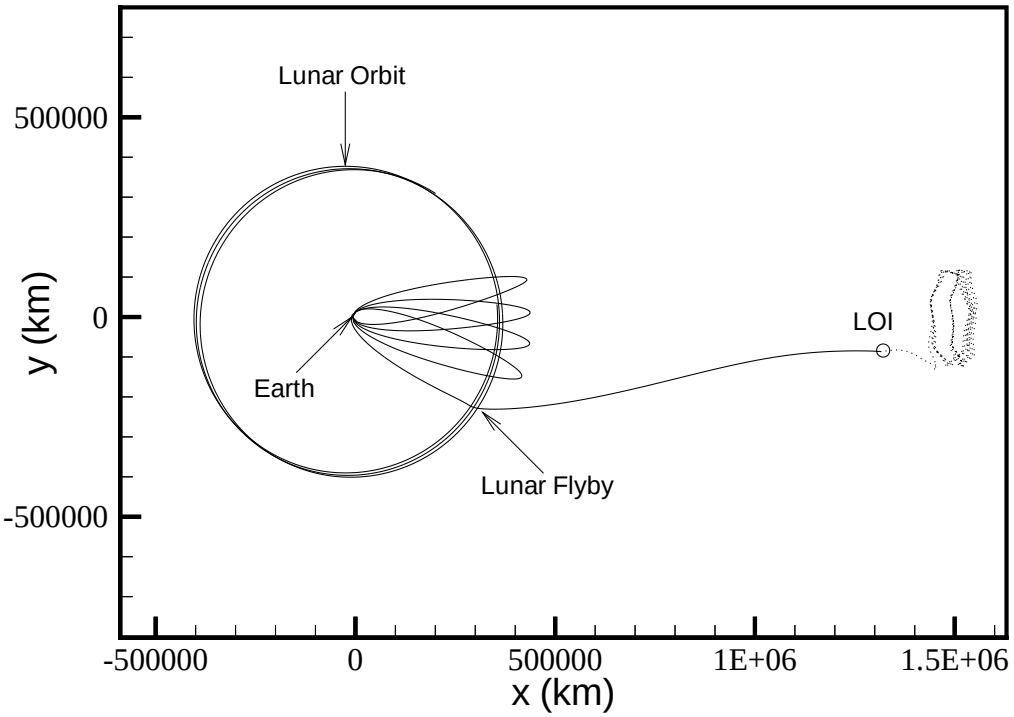

Figure 4.13. Earth-to-L_2 Transfer Using Four Phasing Loops – Case PhL-4

(The implementation of interior deterministic maneuvers using the three step process will be discussed in the next section.) Additional solutions with even more phasing loops are possible. However, these solutions become problematic to implement and frequently require deterministic maneuvers to achieve an acceptable solution, such as the first apogee burn in the four loop case. The use of these phasing loop solutions to aid in injection error correction will be discussed in the next chapter.

4.4 The GENESIS Trajectory

The GENESIS mission is a recent addition to NASA's Discovery program, selected to expand understanding of the composition of the solar system. The mission is a solar wind sample return slated for launch in January 2001. The primary scientific goal is the collection of solar wind particles during an interval of approximately two years. These particles should provide useful information regarding the chemical and isotopic composition of the Sun. This information can then be used to validate

theories concerning the composition of several objects in the solar system, including planetary atmospheres. To successfully collect these particles, the spacecraft must be beyond the magnetosphere of the Earth. On the other hand, since this is a Discovery class mission, the mission operation costs must be kept low; hence, it is desirable that the spacecraft remain as close to the Earth as possible. Therefore, an L_1 libration point trajectory is the ideal platform for this mission. In addition, to further reduce costs and to provide opportunities for future scientific research, the actual scientific analysis of the collected samples is to be performed on Earth. Thus, the trajectory must accommodate the added challenge of returning the spacecraft (with its samples) from the vicinity of L_1 to the Earth, and then reentering the atmosphere at some set of specified coordinates. As an added complication, a day side reentry is required to facilitate airborne capture of the spacecraft. Note that much of this discussion follows from Howell, Barden, Wilson, and Lo[1] and is based on Barden, Howell, and Lo.[34]

4.4.1 Initial Approximation

The first step in the trajectory design process for GENESIS is the selection of a suitable libration point orbit in the vicinity of the Sun-Earth L_1 point. The selected Lissajous orbit originates at Julian date 2452123.23 (August 1, 2001) with a period of 355.63 days, corresponding to two revolutions of the motion.[1] (Note that since Lissajous orbits are, by definition, quasi-periodic, the "period" associated with the orbit is only an approximation; however, it serves well in the application of dynamical systems theory to this problem.) Consistent with the procedures to compute manifolds, as previously discussed, the initial state vector $\bar{X}_o^{W^s}$ is computed to generate stable manifolds along the corresponding two revolutions of the Lissajous. Note that the original computations for the initial GENESIS trajectory were done by Barden.[43]

Within the time frame of interest for the mission, stable manifolds associated with various regions along the trajectory are then available. One particular region along the two revolution Lissajous can be identified as being associated with the stable manifolds that pass close to the Earth.[34] In this region, there exists at least one

stable manifold, associated with a point along the Lissajous trajectory, that represents a good starting point for the design of a transfer. The trajectory associated with this manifold passes the Earth at an altitude of 1112.1 km and an inclination of 15.3 degrees with respect to the equator. The date of the closest approach to the Earth is January 16, 2001 (within the desired time frame for the GENESIS launch). Thus, this serves as the initial guess for the transfer from Earth to the Lissajous trajectory.

The return portion of the trajectory, i.e., the transfer from the L_1 Lissajous trajectory back to Earth reentry, can be considered in much the same way. Since a day-side reentry is required, the final state must have an $\hat{x}$ position component that is negative with respect to the the SR frame, i.e., facing the Sun. Thus, experience with the three body problem dictates that a direct return from L_1 is not feasible under these conditions.[33] The spacecraft must approach reentry from the side of the Earth opposite the Sun. Therefore, an *unstable* manifold must be generated that leaves the Lissajous and approaches the L_2 region before returning to Earth. Additionally, departure from the vicinity of L_1 must occur only after sufficient time has elapsed to perform the science investigations. Thus, further downstream along the same quasi-periodic Lissajous orbit, two additional revolutions are defined to represent the "period" for computation of an appropriate unstable manifold. In this case, the period originates on Julian date 2452300.34 (January 25, 2002); the resulting two revolution interval is 356.03 days in duration. Investigation of the unstable manifolds along different regions of the appropriate revolutions reveals a region where the corresponding unstable manifolds have the characteristics necessary for the return. Specifically, an unstable manifold is required that reaches L_2 and then passes close to the Earth on the daylight side. One such path returns to the Earth at an altitude of 197.4 km with an inclination of 52.1 degrees and a declination of 35.8 degrees on August 21, 2003.[1]

Combining the stable manifold for the launch segment, the Lissajous trajectory, and the unstable manifold for the return segment provides the first guess for an end-to-end solution in the real system (using JPL DE202 ephemerides) for the GENESIS

mission. (Note that the full model may also include additional perturbations, such as solar radiation pressure.) The initial approximation is presented in Figure 4.14 as projections onto the $\hat{x}\hat{y}$ and $\hat{x}\hat{z}$ planes in the SR frame. Each of the three trajectory arcs that comprise the solution are plotted; an "o" marks the locations where the arcs are patched together. Note that, in these projections, the Earth is located at (0,0,0) and the arrows indicate the direction of motion of the spacecraft.

4.4.2 Enforcing Launch/Return Constraints

Unlike the previous solutions examined in this work, the entire initial GENESIS approximation is itself a numerically integrated solution in the four body problem. Therefore, a formal intermediate step using multi-conics is redundant and unnecessary. However, the SRM reduction procedure described in Section 3.3 can be utilized in a numerical integration process to enforce the desired constraints at launch and reentry. Ideally, a single end-to-end (launch/insertion to reentry) trajectory is sought that meets the constraints at each end point. However, the current formulation of the algorithm only allows launch type constraints (e.g. altitude, inclination, etc.) at one end point. The other end point may be free (as in the MLS cases) or fixed in position and time (as in the Earth-to-L_2 transfer cases), but no other constraints are currently possible. Therefore, the trajectory must be analyzed in segments with the knowledge that velocity discontinuities will be introduced at the locations where the segments are patched together; these velocity discontinuities translate into deterministic $\Delta\bar{V}$'s in the complete solution.

For this particular mission, there is a requirement for a minimum time interval of 23 months, mostly during the Lissajous orbit, without any significant deterministic maneuvers (due to potential contamination of the science experiments by the thrusters). Because of this constraint, it is desirable that the Lissajous orbit insertion (LOI) maneuver occur early in the trajectory. To accommodate this requirement, the location for LOI is selected, somewhat arbitrarily, to be near the first xz-plane crossing (below the ecliptic) on April 23, 2001. The LOI state serves as the first break point separating the launch segment from the Lissajous segment.

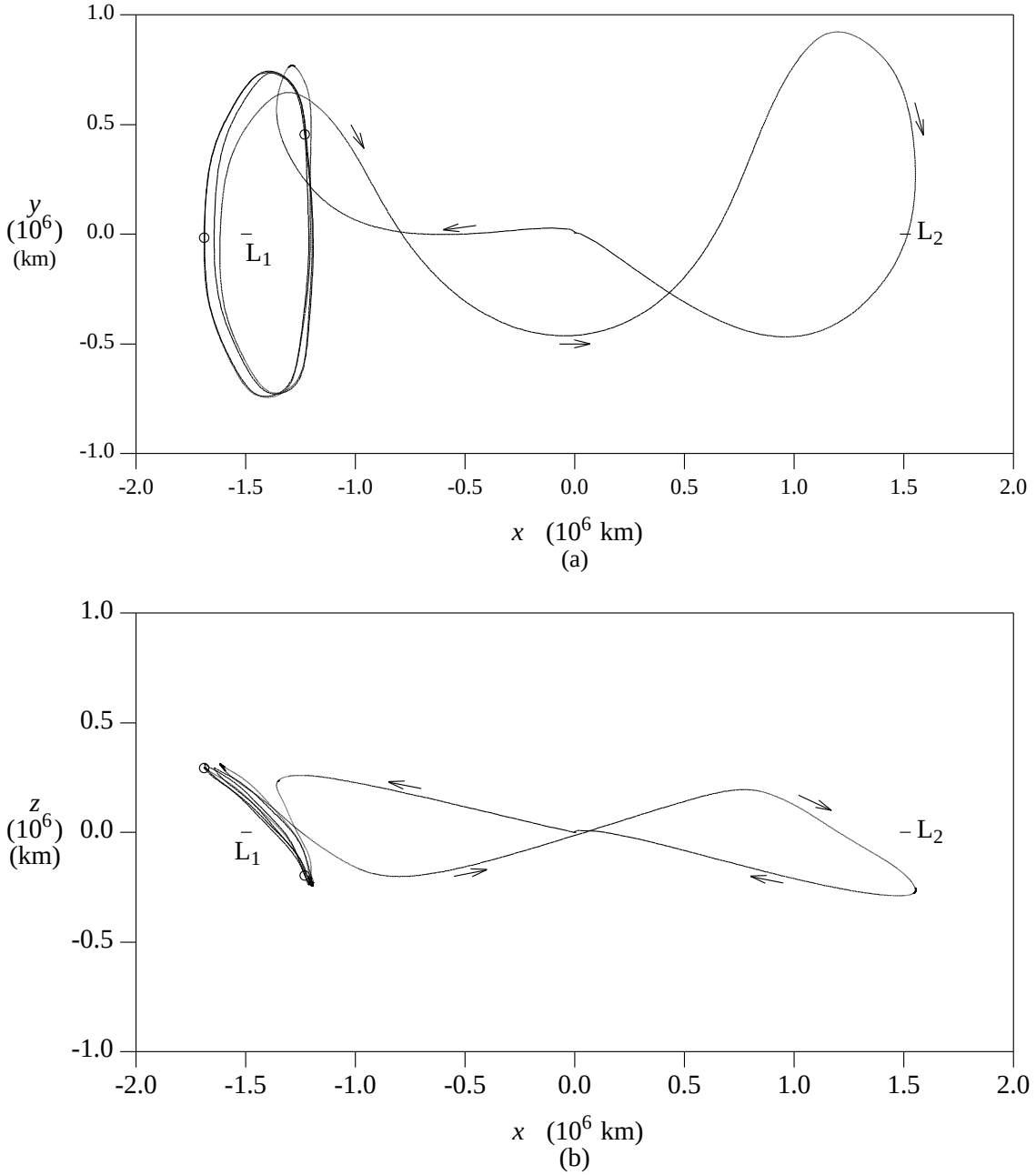

Figure 4.14. Original GENESIS Approximation[1]

The first guess for the launch segment (the segment from trajectory insertion near the Earth to LOI) is taken directly from the first part of the stable manifold that was previously generated. A total of 5 state vectors (position, velocity, and time) are used to describe the transfer, including the initial and final states. The three interior states are selected at approximately 30 day intervals along the transfer after the point where the vehicle crosses the lunar orbit on the outbound leg of the trajectory. Although there is no lunar encounter in this solution, placing a patch point near the lunar orbit aids in the convergence of solutions with initial or final states near the Earth. The differential corrections process then yields a solution that is continuous in position and velocity and departs an Earth parking orbit with characteristics of 200 km altitude, 28.5 deg inclination relative to the equator, and departure from perigee on January 15, 2001.

The next segment along the trajectory is the intermediate leg that includes the portion of the stable manifold beyond LOI, and the Lissajous trajectory. The LOI point is defined as the initial state for this intermediate leg; the position and time that correspond to this state are held fixed throughout the solution process. From experience, patch points are then selected every quarter revolution around the Lissajous, that is, approximately every 45 days. The final state along this segment is the end of the nominal Lissajous; the corresponding position and time of this state are again held fixed for the subsequent corrections process. The corrections algorithm quickly generates a smooth (in position and velocity) trajectory segment from the LOI point to the end of the Lissajous. This end state is purposefully selected as the initiation point for the unstable manifold that was previously generated. Note that velocity discontinuities now exist at both ends of this intermediate section due to the differential corrections process used to ensure position and time continuity along the trajectory.

The GENESIS project has selected the Utah Test and Targeting Range (UTTR) as the recovery site for the spacecraft. Thus, an appropriate set of conditions must be satisfied to achieve a successful reentry and recovery. At this time, the project has

specified conditions that define the end state along the trajectory and properly set up the reentry into the atmosphere. These conditions, then, become the constraints that must be met at the end of the trajectory. The reentry constraints are specified as a declination of +40.6 deg relative to the equator and a right ascension of –114 deg relative to the Greenwich meridian. Since the atmospheric reentry is not modeled in this analysis, a target altitude of 125 km is selected with a flight path angle of -7.9 deg to ensure proper entry into the atmosphere.

As the final leg of the trajectory, then, the unstable manifold is employed as the initial approximation of the return. Due to the extreme sensitivity of targeting final states close to the Earth, and to accommodate the current implementation of the algorithm, this segment utilizes numerical integration that proceeds backwards in time. The final leg then has an "initial" state at the reentry point and a "final" state at the end of the previous segment, i.e., the beginning state along the unstable manifold. Thus, the return actually appears similar (in negative time) to an insertion-to-LOI transfer that moves from the Earth towards an L_1 Lissajous. This technique has proven to be a highly effective way to handle convergence of the return and does not affect the complete solution from injection to reentry.

In order to provide some flexibility before the final approach toward Earth, and to gain additional control over the trajectory, two deterministic maneuvers are placed along the return trajectory. Recall that a minimum of 23 months is required after LOI before another maneuver can be implemented; thus, the first return $\Delta\bar{V}$ is placed along the unstable manifold near the xz-plane crossing immediately following the spacecraft departure from the vicinity of L_1 (nearly mid-way between the Earth and L_1). The option of a second maneuver then occurs near the L_2 point. To accommodate these maneuvers, deterministic $\Delta\bar{V}$'s must now be possible at *any* patch point.

Recall that the equation relating the velocity discontinuities and constraints to the patch point positions and times, from Equation (3.65), is written

$$\left\{ \begin{array}{c} \delta\bar{R}_j \\ \delta t_j \end{array} \right\} = M^T \left(M M^T \right)^{-1} \left\{ \begin{array}{c} \delta\Delta\bar{V}_i \\ \delta\alpha_k \end{array} \right\} \quad . \tag{4.8}$$

In the original formulation, the discontinuities ($\Delta\bar{V}_i$) are iteratively driven to zero, that is, the changes are selected such that $\delta\Delta\bar{V}_i = -\Delta\bar{V}_i$. One possible method of introducing deterministic maneuvers into the solution process is to force a particular $\Delta\bar{V}_n$ to some non-zero value. To accomplish this objective, the change in $\delta\Delta\bar{V}_n$ is selected such that

$$\delta\Delta\bar{V}_n = \frac{\Delta V_{des} - |\Delta\bar{V}_n|}{|\Delta\bar{V}_n|} \cdot \Delta\bar{V}_n \quad , \tag{4.9}$$

where ΔV_{des} is the desired magnitude of the deterministic maneuver. This technique is employed to allow deterministic $\Delta\bar{V}$'s equal to or less than the specified magnitude at selected points along the trajectory. Note that only the maneuver magnitude is specified; no attempt has been made to control the maneuver direction, although such a strategy could be implemented, if desired. There are other methods to introduce deterministic maneuvers into the trajectory, however the technique just described is selected for the GENESIS mission to allow limits to be placed on the magnitudes of each individual maneuver.

At this stage, an entire end-to-end solution exists that meets the constraints at both insertion and reentry; however, four deterministic $\Delta\bar{V}$'s have been introduced into the trajectory. The first two maneuvers, at LOI and the end of the Lissajous, are due to patching the three trajectory segments together. The last two $\Delta\bar{V}$'s are introduced in the return segment to facilitate convergence to the reentry constraint conditions.

The two segments after LOI (the Lissajous and the return) can be combined to produce a complete solution that consists of only two segments with a break point deterministic maneuver at LOI. Combining the Lissajous and return segments places the last three maneuvers into one trajectory segment that is now propagated backwards in time from reentry to LOI. A continuation process is then employed to reduce the magnitudes of these three deterministic maneuvers simultaneously to values of zero, if possible. In this formulation, with two trajectory segments (insertion to LOI and reentry back to LOI), the position and time of the LOI point are fixed. Thus, the selection of the LOI state is essentially an additional constraint on the trajectory,

introduced by the design process. The result is not truly optimal, however, the procedure has proven to be *very* successful for preliminary analysis.

From the intermediate solution with four $\Delta\bar{V}$'s, a complete trajectory has been determined, through continuation, that contains no deterministic $\Delta\bar{V}$'s except the LOI maneuver at the break point between the launch and Lissajous/return trajectories. This solution is summarized in Table 4.5. The table lists the times of key events along the trajectory, as well as the magnitudes of any maneuvers. Note that the only maneuver in the final solution, aside from the injection onto the trajectory, is the 8.47 m/s burn at LOI. The natural dynamics of the system are employed to facilitate the return and the ultimate reentry over Utah without any additional deterministic maneuvers. The trajectory is shown in Figures 4.15 and 4.16 as projections onto the $\hat{x}\hat{y}$ and $\hat{x}\hat{z}$ planes in the SR frame. Note that the LOI location is marked with an "o" in the $\hat{x}\hat{y}$ projection. The overall shape of the solution is consistent with the manifolds in this region of space, however, this solution meets all launch and return constraints.

4.4.3 Retargeting New Reentry Conditions

As is true in any mission design process, the trajectory constraints are updated as more detailed analysis becomes available. The return conditions specified for the reentry state are not truly representative of a recovery at the UTTR. This is primarily due to the selection of a 125 km altitude directly over the target site. The current

Table 4.5 Summary of GENESIS Trajectory

	Date	$\lvert\Delta\bar{V}\rvert$
Launch/Injection	January 15, 2001	3193.76 m/s
LOI	April 23, 2001	8.47 m/s
End of Science	March 23, 2003	—
Reentry	August 19, 2003	—

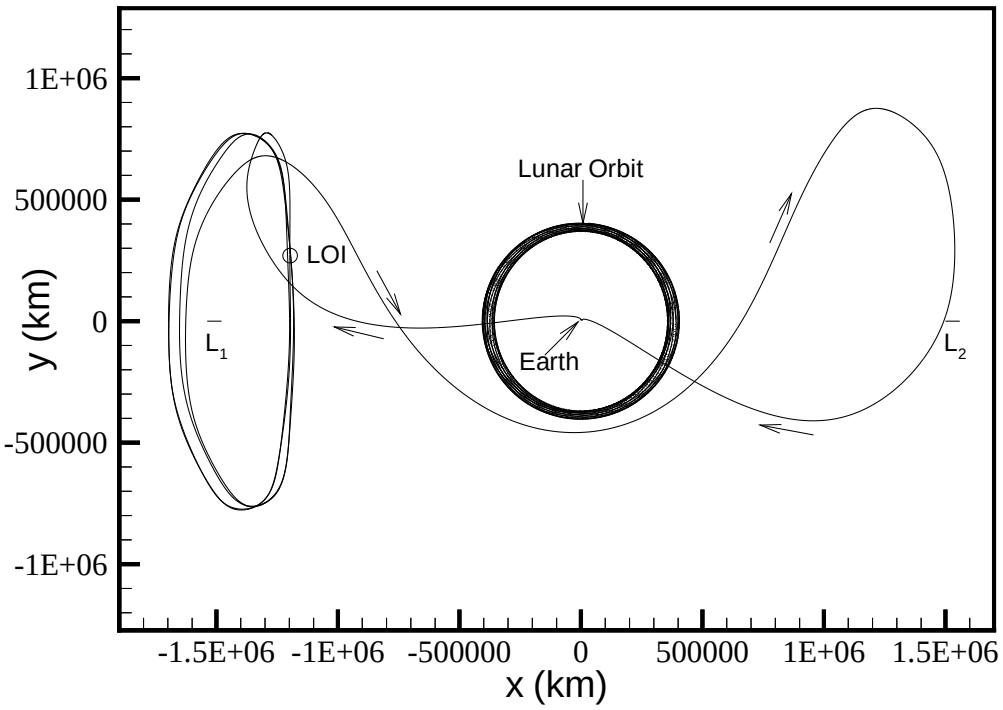

Figure 4.15. Original GENESIS Solution – $\hat{x}\hat{y}$ Projection

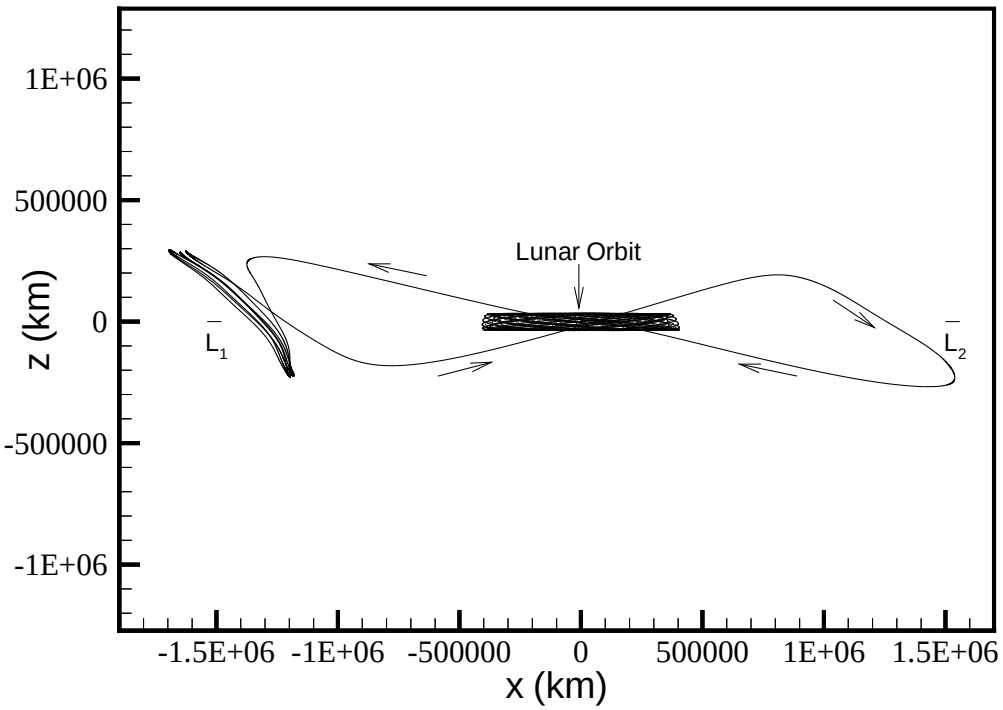

Figure 4.16. Original GENESIS Solution – $\hat{x}\hat{z}$ Projection

constraints would lead to a final landing at 0 km altitude further down range from the UTTR. To assess the range of trajectories in this region of space and the flexibility of the algorithm, a new set of return conditions are examined that move the final altitude from 125 km to 0 km and force the return state to perigee (flight path angle equal zero). (Actual reentry conditions will be determined once a complete reentry analysis that incorporates atmospheric models is completed.)

Modification of the current solution to accommodate slightly altered reentry constraints appears, at first glance, to be simple and straightforward. However, attempts to introduce maneuvers into the return trajectory to force the final state to a 0 km perigee proved to be extremely costly in terms of $\Delta\bar{V}$ magnitudes. The difficulties seem to arise as a result of the dynamical nature of the manifolds near the Earth. The desired final state may, in fact, lie on a different region of the manifold surface, or a different surface altogether. Since these surfaces are very complex near a gravitational body such as the Earth, this complicates the determination of a new solution from the previous one.

4.4.3.a Application of Supplemental Targeter

In the light of the difficulties to retarget a different reentry state for the GENESIS solution, the supplemental targeting methodology developed in Section 3.5 is applied here to study the use of other strategies to achieve new reentry conditions. In the original three step algorithm developed in Chapter 3, the patch point positions and times are selected as the independent parameters in the problem. A linear relationship is then developed between these positions and times and the velocity discontinuities and constraints in the problem. As an alternative, the velocities and times at certain points along the nominal trajectory can be selected as the independent quantities in the solution, resulting in a solution that utilizes deterministic $\Delta\bar{V}$'s along the trajectory to meet the specified end state criteria.

Recall that the original GENESIS solution has a final state with constraints of 125 km altitude, 40.6 deg declination, -114 deg right ascension, and a flight path

angle of -7.9 deg. The new target state selected for this analysis is 0 km altitude, 40.6 deg declination, -114 deg right ascension, with a flight path angle of 0 deg (at perigee). The supplemental targeting scheme is employed on the known nominal solution from Section 4.4.2 to investigate possible configurations and costs to converge to the new reentry state. A set of four states is selected from the nominal solution as potential maneuver locations. These states are located on the $+\hat{y}$ half of the L_2 loop, on the Julian dates 2452753.4, 2452771.0, 2452799.6, and 2452832.9. Various combinations of states from this set are selected to examine solutions with 2 and 3 maneuvers (including the initial state) that meet the required reentry conditions. The resulting segments of the trajectory from the initial state (of the first maneuver) to the final reentry state are shown in Figures 4.17, 4.18, and 4.19 for the 2 maneuver cases, and Figures 4.20 and 4.21 for the 3 maneuver cases. All of the cases examined met the desired end constraints, and the maneuver costs for each case are summarized in Table 4.6. As can be seen from the table, though, the total cost of such solutions ranges from 47.67 m/s to 67.89 m/s. These costs are unacceptable for this particular mission, but prove to be insightful for this and other types of mission scenarios. The methodology, however, works well to incorporate a series of maneuvers to retarget the end state of a known nominal, and expands the capabilities for future design options.

4.4.3.b Variation of LOI State

Another approach to overcome the difficulty that is dynamically inherent in altering the return state is to vary the fixed LOI state at the beginning of the Lissajous. (Recall that the LOI state is fixed in position and time from the initial analysis; however, this is not a mission constraint.) By allowing this state to vary, a slightly different Lissajous and associated unstable manifold are constructed that meet the final return constraints. Essentially, the method involves overlapping the insertion-to-LOI and Lissajous/return trajectories to allow some flexibility in the LOI state, that to this stage has remained fixed. As a first step, the last 3 states along the launch segment, including the original LOI point, are shifted to the Lissajous/return segment

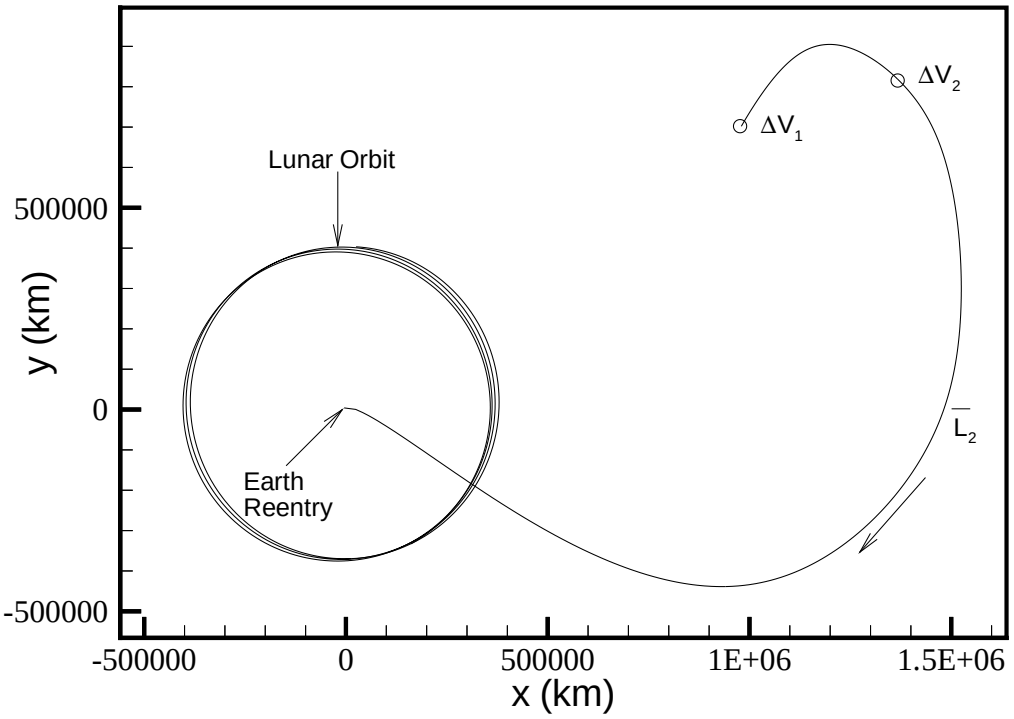

Figure 4.17. GENESIS Reentry Retargeting Case 1

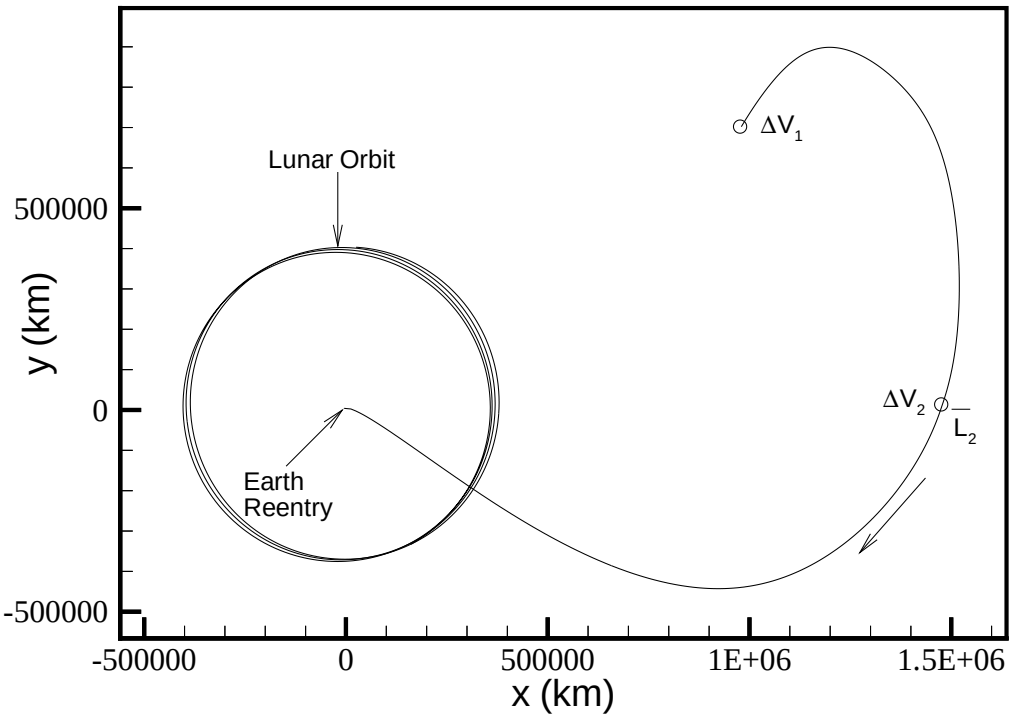

Figure 4.18. GENESIS Reentry Retargeting Case 2

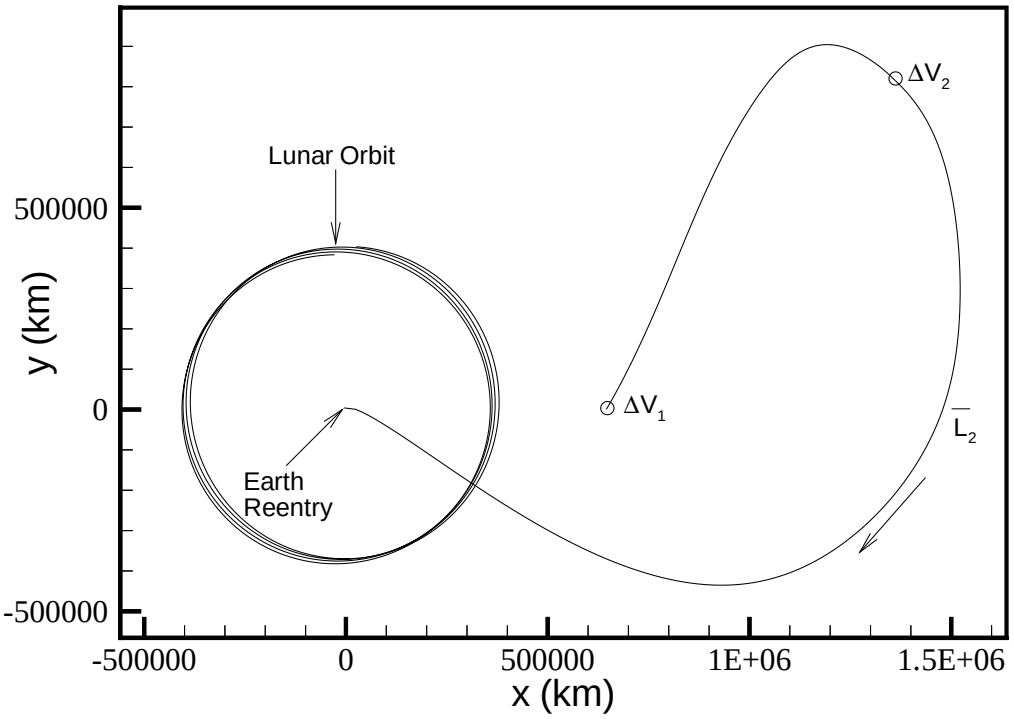

Figure 4.19. GENESIS Reentry Retargeting Case 3

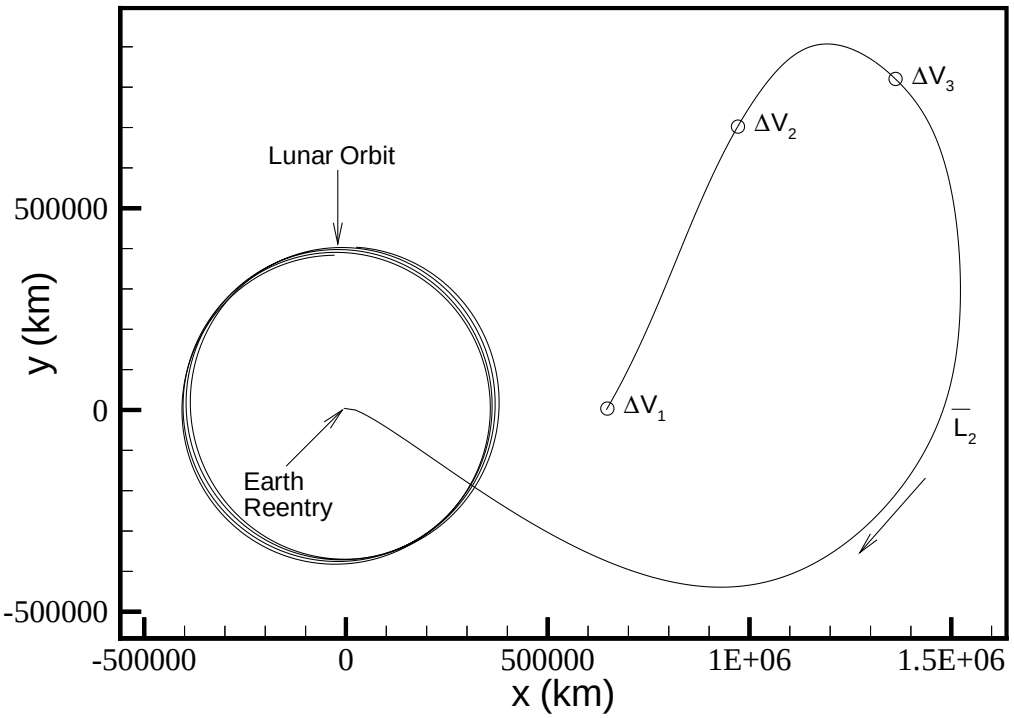

Figure 4.20. GENESIS Reentry Retargeting Case 4

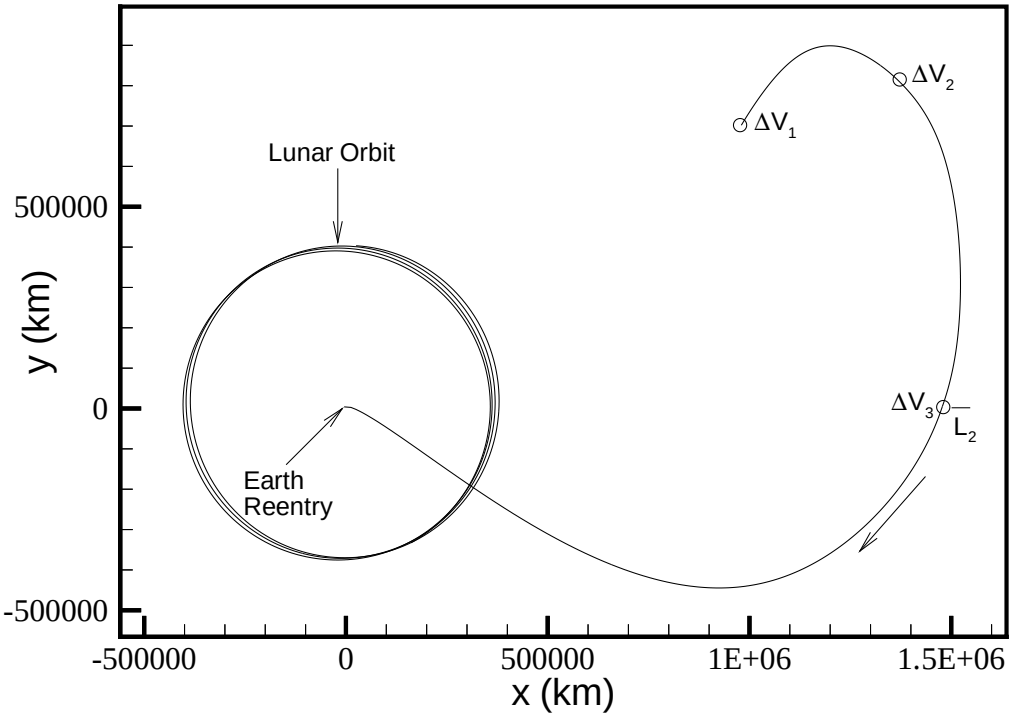

Figure 4.21. GENESIS Reentry Retargeting Case 5

Table 4.6 Summary of GENESIS Reentry Retargeting Cases

	ΔV_1 (m/s)	ΔV_2 (m/s)	ΔV_3 (m/s)	ΔV_{TOT} (m/s)
Case 1	19.94	27.73	—	47.67
Case 2	45.82	22.07	—	67.89
Case 3	20.07	41.42	—	61.49
Case 4	6.82	16.25	30.30	53.37
Case 5	17.07	29.09	13.49	59.65

and a new initial state is selected along the launch segment. This new "overlapped" trajectory is then converged to the desired return conditions, while constraining the new initial state (from the launch segment) to be fixed. Since the old LOI state is now an interior patch point, some variation in this state is introduced by the SRM reduction process. After a new Lissajous and return segment have been determined, the altered patch point corresponding to the old LOI point is again fixed in position and time. A new insertion-to-LOI segment is then constructed to transfer from Earth parking orbit to this new LOI state to complete the trajectory; the new end-to-end solution now satisfies the desired constraints on the reentry conditions.

This alternate trajectory is summarized in Table 4.7. Note that the solution is quite similar to the original trajectory, but differs enough to alter the final state along the return to meet the desired end constraints. As a side note, this solution is produced using DE405, JPL's current definitive ephemeris, however, the changes between DE405 and DE202 do not affect the overall nature of the trajectory. Again the solution is plotted in Figures 4.22 and 4.23 as projections in the SR frame. By comparing the $\hat{x}\hat{z}$ projection with the previous solution in Figure 4.16, it is evident that the Lissajous has been altered by the process to accommodate the new reentry constraints and the new LOI point. There is still much to investigate in this area of retargeting new return conditions, and work is continuing.

Table 4.7 Summary of Alternate GENESIS Trajectory

	Date	$\lvert\Delta\bar{V}\rvert$
Launch/Injection	January 9, 2001	3191.37 m/s
LOI	April 24, 2001	6.75 m/s
End of Science	March 24, 2003	—
Reentry	August 19, 2003	—

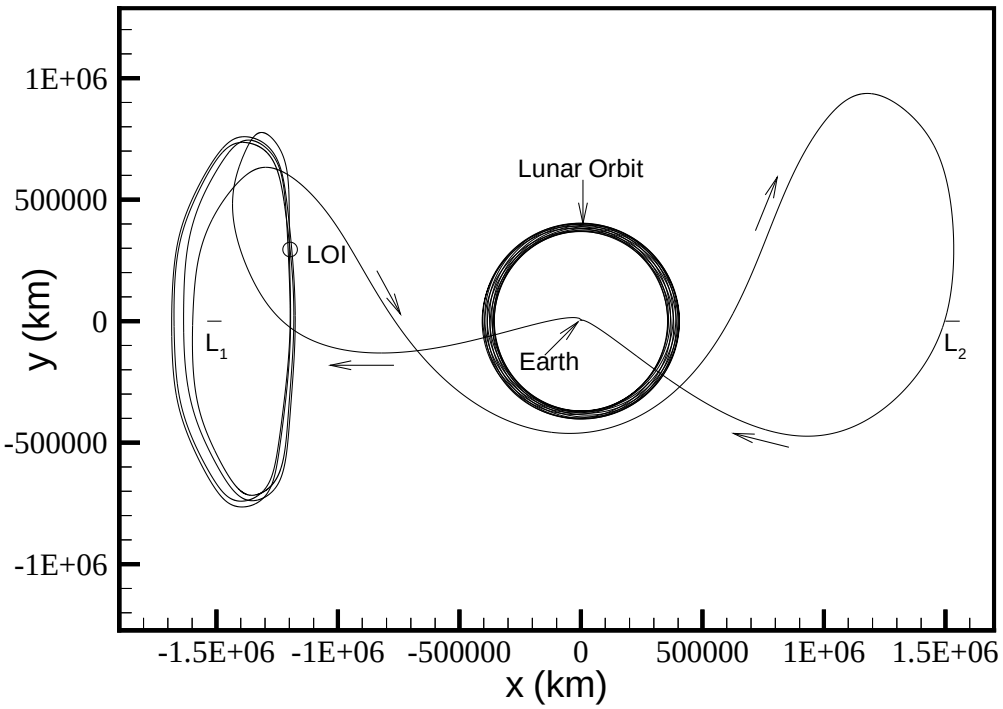

Figure 4.22. Alternate GENESIS Solution – $\hat{x}\hat{y}$ Projection

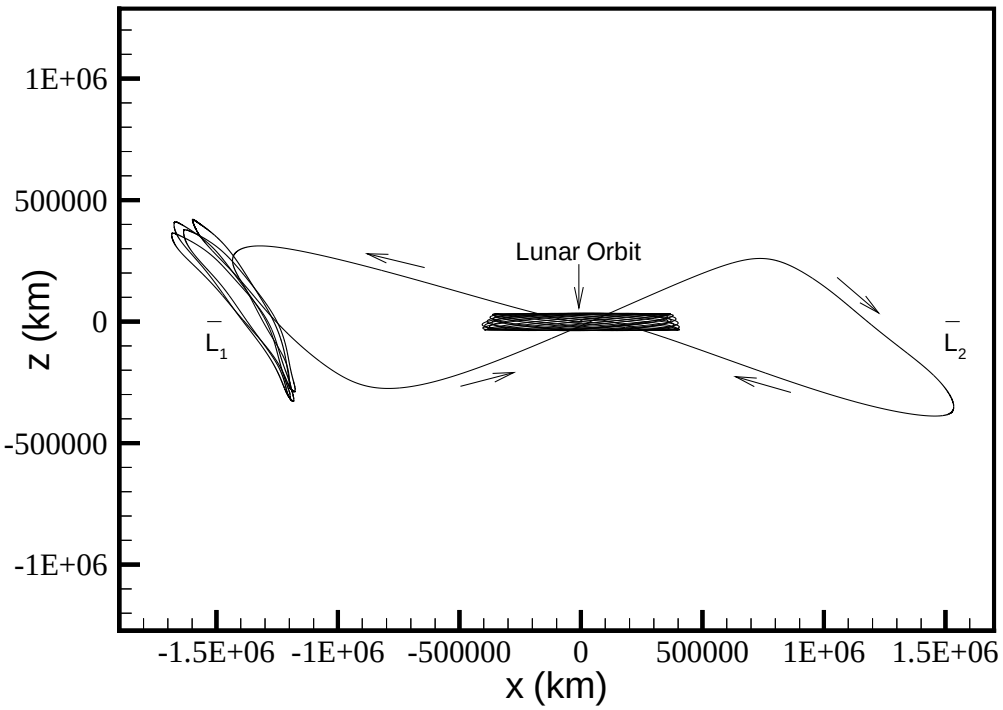

Figure 4.23. Alternate GENESIS Solution – $\hat{x}\hat{z}$ Projection

4.4.4 Launch Opportunities in Other Months

There are essentially two issues involved in exploring the possibility of multiple launch opportunities. First, launch opportunities should be available in other months surrounding the nominal solution. Specifically, additional solutions are sought with launch dates in the months of December 2000 and February 2001. The previous process could be repeated, of course, since it is straightforward and the individual steps are well understood. However, another simpler approach can be used for this part of the analysis, as discussed in Howell, Barden, Wilson and Lo.[1]

Often in the restricted three and four body problems, the key to successfully understanding a problem is to view the shape of the solution in rotating coordinates. The significance of halo orbits, for example, is apparent only in the rotating frame. In the case of the GENESIS trajectory, preserving the shape of the solution in the rotating frame is critical. To accomplish this objective, patch points along the nominal solution are first transformed from the inertial frame to an appropriate rotating frame.[1] The rotating frame of choice depends on the location of the patch point relative to certain critical locations. Specifically, patch points that are near L_1 are transformed to rotating coordinates with L_1 as the origin. Similarly, those states near L_2 are transformed to rotating coordinates relative to L_2, and those near the Earth are transformed into rotating coordinates relative to the Earth. Next, the date associated with the patch point state in the rotating frame is advanced 28 days for February or slipped 28 days for December (based on the approximate period of the Moon in the rotating frame). The states are then transformed back into inertial coordinates using the adjusted times. These transformed inertial states then serve as the initial estimate for the patch point states in the new months. This maintains the structure of the solution in the rotating frame and provides a sufficient first guess that quickly leads to solutions in both months. The results are summarized in Table 4.8. Note that the key dates are all shifted approximately ± 1 month accordingly. Also note that there is still only a single maneuver at LOI for all three cases, but the LOI cost

Table 4.8 Summary of Solutions for Launch in December and February

	December 2000		February 2001	
	Date	$\|\Delta\bar{V}\|$	Date	$\|\Delta\bar{V}\|$
Injection	December 10, 2000	3191.02 m/s	February 12, 2001	3193.14 m/s
LOI	March 26, 2001	26.70 m/s	May 21, 2001	18.50 m/s
Reentry	July 22, 2003	—	September 16, 2003	—

for these solutions has increased significantly; no attempt has been made to optimize these costs. Note that the same procedure could be applied to determine solutions in December and February for the alternate solution from Section 4.4.3.b, if desired.

4.4.5 Launch Period Analysis

The second part of the launch study is the standard analysis where solutions are sought over a number of days surrounding the nominal launch date. The strategy for the launch period analysis for a given nominal comes in part from the intuition gained in investigating the unstable manifolds,[1,33] and also from experience. The primary issue that drives the methodology is the sensitivity of the return portion of the trajectory. A very slight change in the state near L_1 can result in escape from the vicinity of the Earth, or perhaps a return to Earth thousands of kilometers off target, as is evidenced by the retargeting difficulties. In addition, the position of the Moon as the spacecraft passes from L_1 toward L_2 can have a significant impact on the trajectory. Therefore, the strategy for the launch period analysis within a single month begins by freezing the return segment, i.e., the portion of the trajectory from LOI to reentry. Thus, only the initial launch segment is analyzed. To generate a series of launch segments (insertion to LOI) on the days surrounding the nominal, an additional time constraint in the form of a specified Julian date is placed on the launch/insertion state. This constraint allows the insertion state to be shifted to each day in the launch period. The results of this analysis are presented in Figure 4.24 for

the three months surrounding the nominal January launch. The nominal solutions with launches on December 10, 2000, January 15, 2001 and February 12, 2001 are marked with solid symbols for each of the months. The data for the curves in this figure are computed by adjusting the launch dates at one day increments and then recomputing the transfer. The figure demonstrates how the LOI cost varies over a given range of dates throughout the three month interval that is examined. The launch period for the alternate solution (discussed in Section 4.4.3.b) is presented in Figure 4.25 for the dates surrounding the nominal on January 9, 2001. (Note that the same procedures could be applied to analyze the launch period for December and February, if desired.)

Of additional interest here is the observation that two local minimums appear during each month. In each case, the minimum with the larger magnitude corresponds to the dynamical situation where the spacecraft passes closer to the Moon than any other solution during that same month. For most of the transfers corresponding to the original trajectory in Figure 4.24, the closest approach to the Moon during the launch segment ranges from 300,000 to 400,000 km. In the region of the higher local minimum, the spacecraft passes much closer to the Moon; within 83,000 km for launch on December 23rd, 106,000 km for a January 21st launch, and 124,000 km for launch on February 20th. (The same trends are evident in the alternative solution in Figure 4.25.) For various reasons, it is specified that a lunar encounter is to be avoided for GENESIS. Nonetheless, the Moon's impact is clear, and could be useful if a lunar encounter were incorporated into the launch strategy.

In conclusion, the GENESIS trajectory demonstrates how the current methodology can be utilized to aid in the development of solutions that are based entirely on dynamical systems theory for an initial approximation to the trajectory. In addition, much insight can be gained that is valuable in the design of other types of trajectories.

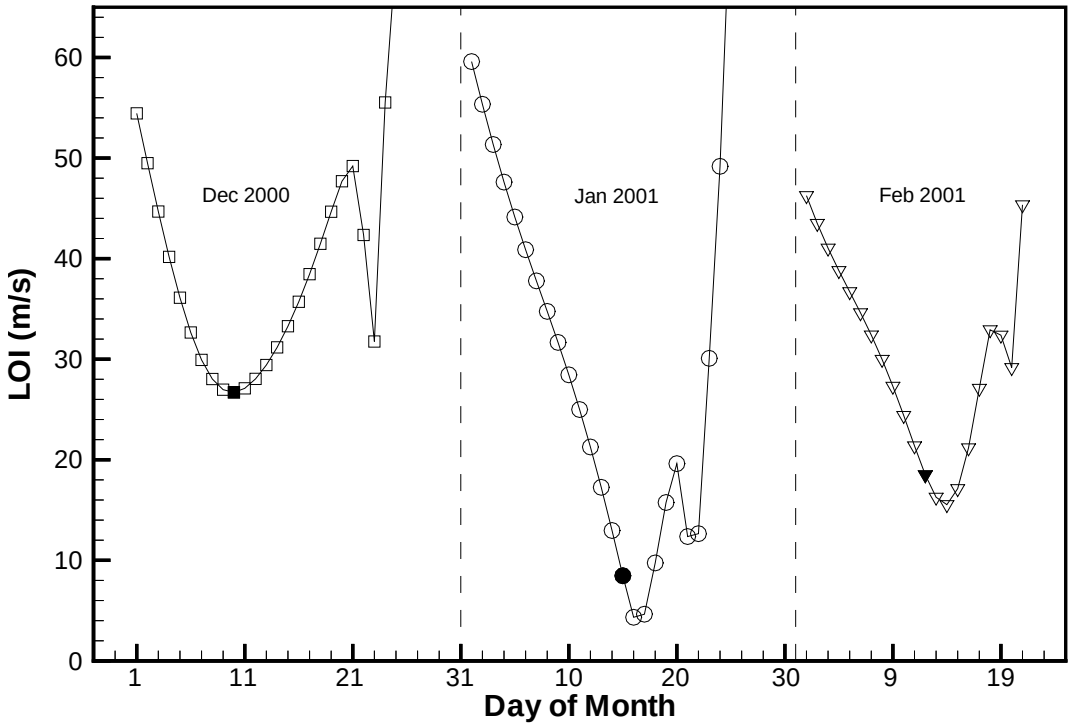

Figure 4.24. Launch Period Analysis for Original GENESIS Solution

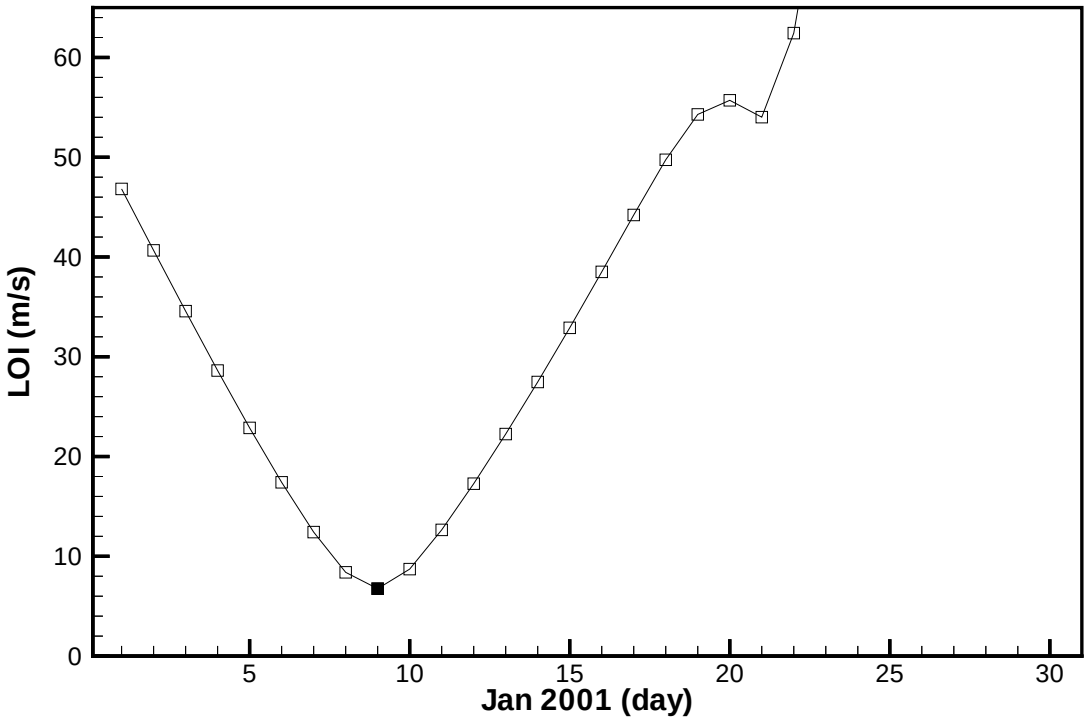

Figure 4.25. Launch Period Analysis for Alternate GENESIS Solution

5. ERROR ANALYSIS AND RECOVERY STRATEGIES

A number of trajectories designed for current or planned missions in the four body regime involve one or more deterministic maneuvers during the course of the mission, and all involve some launch or injection maneuver to initiate the trajectory. Limitations and uncertainties in the propulsion components used to implement these maneuvers demand contingency planning for a response to potential errors in position and/or velocity along the path. This chapter offers a preliminary investigation of the application of the current three step methodology to correct a wide range of errors. The recoveries designed using this process are accomplished for a very reasonable cost. The source of the errors in the solution dictate to a large degree the steps required to correct the trajectory or design a recovery solution. Initially, correction back to the nominal will be examined for the GENESIS mission and for transfer trajectories to libration point orbits, in general. Next, a technique is presented to determine lower cost alternative recovery strategies for trajectories that include phasing loops during the launch/insertion segment. Finally, the use of lunar gravity assists is examined as a potential source for mission recovery.

5.1 Error Analysis Algorithm

In designing a trajectory to meet certain specifications, the initial state is generally considered to be variable, although possibly subject to constraints, such as altitude, inclination, etc. However, for error analysis, the initial state is fixed in position, velocity, and time at some value determined by the error. It is reasonable to assume that, in most instances, no variation is allowed in the error state; that is, no correction maneuver is permitted at the initial time. All necessary corrective maneuvers are

assumed to occur at some point beyond the initial state. The current methodology does allow for a fixed initial position and time, but can place no direct restrictions on the initial velocity. The algorithm must therefore be modified to restrict all position, velocity, and time variations in the initial state. This is accomplished by propagating the initial state, including errors, to the time of the first trajectory correction maneuver (TCM). Thus, the first TCM is redefined to be the beginning of the trajectory; this first TCM state is fixed in position and time, but does allow for a deterministic maneuver. The methodology developed in the last few chapters can now be applied to determine solutions based on this new initial state.

5.1.1 GENESIS Launch Error Analysis

As an example of this technique, consider the launch segment for the GENESIS trajectory with injection date of January 15, 2001, as described in Table 4.5. The nominal transfer trajectory insertion is assumed to occur at perigee, such that a tangential maneuver of 3194 m/s is required to inject onto the transfer path from a circular parking orbit of 200 km altitude. The cost (ΔV_{COR}) to correct a given injection error is the sum of the magnitudes of required maneuvers at the TCM location (ΔV_{TCM}) plus the new LOI cost (ΔV_{LOI}) minus the nominal LOI cost (ΔV_{NOM}), i.e.,

$$\Delta V_{COR} = (\Delta V_{TCM} + \Delta V_{LOI}) - \Delta V_{NOM} \quad . \tag{5.1}$$

Note that the nominal LOI cost for this case is 8.47 m/s.

For the insertion from the parking orbit, a number of different errors in the initial state are examined, beginning with errors in position. These position deviations are represented here in two forms: as a magnitude error along the position vector ($\Delta|\bar{R}|$), or as Cartesian components of position. The Cartesian components can be expressed in terms of either SR ($\Delta x, \Delta y, \Delta z$) or EI ($\Delta X, \Delta Y, \Delta Z$) coordinates. Table 5.1 presents results for the cost to correct the trajectory for a range of position errors. Included in the table are the maneuver magnitude at TCM and the resulting LOI cost. The expression in Equation 5.1 is then used to compute the overall cost

to correct a particular error. The costs are computed for two different TCM times: launch/insertion plus 4 hours, and launch/insertion plus 18 hours. These cases are denoted TTI + 4 hr and TTI + 18 hr, where TTI represents Transfer Trajectory Insertion. Not surprisingly, the ΔV_{COR} increases significantly in most cases as the time to TCM increases. Currently, the GENESIS project has specified that the first TCM occur no sooner than insertion plus 18 hours. However, this requirement may eventually be relaxed to decrease correction costs and thus, reduce the amount of

Table 5.1 ΔV Costs to Correct Position Errors in GENESIS Injection Maneuver

		TTI + 4 hr			TTI + 18 hr		
Type	Error (km)	ΔV_{TCM} (m/s)	ΔV_{LOI} (m/s)	ΔV_{COR} (m/s)	ΔV_{TCM} (m/s)	ΔV_{LOI} (m/s)	ΔV_{COR} (m/s)
$\Delta\lvert\bar{R}\rvert$	–5	16.76	8.23	16.52	27.66	7.45	26.64
	+5	16.69	8.72	16.94	27.42	9.73	28.68
	–20	67.48	7.61	66.62	112.21	7.05	110.79
	+20	66.35	9.55	67.43	108.25	14.23	114.01
SR Δx	–20	61.65	7.79	60.97	103.67	6.91	102.11
	+20	60.70	9.31	61.54	100.29	13.36	105.18
SR Δy	–20	22.44	8.08	22.05	32.66	7.22	31.41
	+20	22.52	8.93	22.98	32.65	10.50	34.68
SR Δz	–20	18.07	9.10	18.70	27.28	10.64	29.45
	+20	17.95	7.85	17.33	27.20	6.53	25.26
EI ΔX	–20	45.60	9.26	46.39	71.69	12.48	75.70
	+20	45.97	7.85	45.35	73.15	6.93	71.61
EI ΔY	–20	49.48	7.79	48.80	84.02	6.33	81.88
	+20	48.92	9.22	49.67	81.88	12.47	85.88
EI ΔZ	–20	7.25	8.84	7.62	8.51	9.25	9.29
	+20	7.33	8.10	6.96	8.76	7.71	8.00

propellant required for the mission. From the results, it is evident that radial errors along the nominal position vector are the most costly to correct, even for shorter TCM times. The costs associated with errors in x component of position in the SR frame are similarly expensive, since the radial direction is nearly aligned with the x axis at insertion onto the transfer; however, in general, this is not necessarily the case. Note also that in each case, the impact of the error is evaluated independently of any other variations; combinations of different error components can, of course, be evaluated, if desired.

Similar to position, errors in velocity during injection onto the transfer path can be modeled. As done previously, one way to describe velocity errors is in terms of Cartesian components, expressed in either SR $(\Delta v_x, \Delta v_y, \Delta v_z)$ or EI $(\Delta V_X, \Delta V_Y, \Delta V_Z)$ coordinates. A second possibility is to utilize a set of non-inertial coordinates that move with the spacecraft along the trajectory. Define then, a unit vector $\hat{r}$ parallel to the position vector of the spacecraft with respect to the Earth. A second unit vector $\hat{n}$ is defined coincident with the instantaneous orbital angular momentum vector, i.e., $\bar{R} \times \bar{V}$. The third unit vector $\hat{t}$ completes the orthonormal triad, such that $\hat{t} = \hat{n} \times \hat{r}$. This coordinate system is called the radial–tangential–normal system, or RTN, for short. A third possible coordinate system is related to the RTN system, where $\hat{r}$ is replaced by a unit vector $\hat{v}$ defined along the velocity vector. The second unit vector is again $\hat{n}$ as defined previously, and the third unit vector $\hat{b}$ completes the triad such that $\hat{b} = \hat{n} \times \hat{v}$. This coordinate system is denoted VBN, or magnitude–binormal–normal. As with the other velocity components, the RTN and VBN systems can be specified relative to either the EI or SR frames.

Results are presented in Table 5.2, where the costs to correct the trajectory are listed for a range of velocity errors. As with the position errors, each case is evaluated independently of any other variations. The error range of ± 20 m/s is determined from the expected 3σ error variation for the GENESIS launch vehicle, a Delta 7326 with a Star 37 upper stage. For the GENESIS launch, errors in the velocity magnitude (V_{mag}) produce the largest correction costs. This is expected, since the injection onto

Table 5.2 $|\Delta\bar{V}|$ Costs to Correct Velocity Errors in GENESIS Injection Maneuver

		TTI + 4 hr			TTI + 18 hr		
Type	Error (m/s)	ΔV_{TCM} (m/s)	ΔV_{LOI} (m/s)	ΔV_{COR} (m/s)	ΔV_{TCM} (m/s)	ΔV_{LOI} (m/s)	ΔV_{COR} (m/s)
EI ΔV_{mag}	–20	79.83	7.56	78.92	133.33	7.54	132.40
	+20	78.88	9.64	80.05	128.84	15.25	135.62
EI ΔV_{rad}	–20	8.46	8.14	8.13	7.21	7.64	6.38
	+20	8.53	8.82	8.88	7.28	9.47	8.28
EI ΔV_{tang}	–20	79.83	7.56	78.92	133.33	7.54	132.40
	+20	78.88	9.64	80.05	128.84	15.25	135.62
EI ΔV_{norm}	–20	0.42	8.32	0.27	0.33	8.28	0.14
	+20	0.45	8.62	0.60	0.38	8.67	0.58
EI ΔV_X	–20	58.73	9.57	59.83	93.10	13.91	98.54
	+20	59.15	7.58	58.26	95.24	6.86	93.63
EI ΔV_Y	–20	39.10	8.84	39.47	67.24	11.03	69.80
	+20	39.25	8.12	38.90	68.33	6.77	66.63
EI ΔV_Z	–20	36.85	8.83	37.21	60.93	11.18	63.64
	+20	36.94	8.16	36.63	61.73	6.92	60.18
SR Δv_x	–20	21.77	8.47	21.77	38.94	9.35	39.82
	+20	21.72	8.47	21.72	39.17	7.71	38.41
SR Δv_y	–20	74.94	7.51	73.98	123.73	7.38	122.64
	+20	74.14	9.69	75.36	119.92	15.06	126.51
SR Δv_z	–20	18.51	8.65	18.69	29.40	9.84	30.77
	+20	18.42	8.32	18.27	29.40	7.48	28.41

the transfer path is a tangential maneuver performed at perigee; hence the largest velocity component, as well as the change in velocity, occurs in the $\hat{v}$ direction. This is also evidenced by the small correction costs associated with errors in the radial (V_{rad}) and normal (V_{norm}) directions. (Note that for injection at perigee, velocity magnitude and tangential velocity, V_{tang}, are equivalent.) For velocity errors, as with position errors, the cost to correct most errors increases as the time to TCM increases.

For completeness, Table 5.3 contains representative costs to correct various errors in the time of injection onto the transfer trajectory. There are two ways to view errors in the "initial" time. The first possibility, denoted EI Δt, is simply an absolute time error for the given injection state. The second type, termed SR Δt, is a time differential, but is related to the inertial changes through a coordinate transformation. Even if there are no errors in position or velocity relative to the SR frame, this transformation will induce errors in EI position and velocity for a given SR time error. For example, suppose that the nominal position and velocity are precisely satisfied relative to the SR frame, but an error in SR time occurs. When the initial state

Table 5.3 $|\Delta\bar{V}|$ Costs to Correct Time Errors in GENESIS Injection Maneuver

		TTI + 4 hr			TTI + 18 hr		
Type	Error (hrs)	ΔV_{TCM} (m/s)	ΔV_{LOI} (m/s)	ΔV_{COR} (m/s)	ΔV_{TCM} (m/s)	ΔV_{LOI} (m/s)	ΔV_{COR} (m/s)
SR Δt	–1	2.06	8.78	2.37	1.81	8.98	2.32
	+1	12.25	10.35	14.13	10.63	11.52	13.68
	–6	2.07	8.15	1.75	1.82	7.96	1.31
	+6	12.56	6.60	10.69	11.18	5.55	8.26
EI Δt	–1	0.53	8.68	0.74	0.44	8.73	0.70
	+1	3.13	9.76	4.42	2.56	10.01	4.10
	–6	0.53	8.68	0.74	0.44	8.20	0.17
	+6	3.30	7.17	2.00	2.72	6.87	1.12

is transformed from SR to EI coordinates, the change in time results in a different inertial state than that corresponding to the nominal, due to the rotation of the Earth about the Sun during the time interval Δt. It should be noted that actual injection errors will be a combination of position, velocity, and time in various formats. All of these errors can be handled by the algorithm simultaneously to determine the necessary corrective maneuver, based on the time to TCM.

5.1.2 Error Analysis Along the GENESIS Return Trajectory

Since the GENESIS mission includes a sample return, the transfer from the L_1 Lissajous back to the Earth for reentry and recovery in Utah is a critical component of the solution. However, errors are expected to occur during each phase of the mission that may affect the viability of the return and recovery. These errors could come from a variety of sources. One source is the daily precession maneuvers that are required to maintain the particle collection instruments oriented toward the Sun during the science collection portion of the mission. Although these maneuvers are small ($\sim$ 5 mm/s per day) and can be modeled in the nominal trajectory, errors may build up due to the large number of maneuvers ($\sim$ 700) to be performed during the 23 month science phase; implementation errors on 700+ maneuvers may also be non-trivial. A second source of errors is simply inaccuracies in the models used to simulate the motion. These errors include everything from spacecraft physical properties, to thruster model uncertainties, to incomplete modeling of all the forces that drive the dynamics of the trajectory. Although very detailed models do exist to simulate the motion, errors are inevitable. A third possibility for errors is in the tracking and orbit determination of the spacecraft trajectory during the mission. The information determined about the actual trajectory path is utilized in station-keeping algorithms to maintain the trajectory close to some defined nominal solution. Station-keeping maneuvers are performed, when required, to correct any errors that may develop during the mission. However, errors in the orbit determination procedures, as well as in the corrective maneuvers themselves, introduce additional uncertainties into the solution.

Regardless of the source of the errors, the impact and subsequent corrective maneuvers can be analyzed using the current methodology. The effect of any errors in the Lissajous orbit can be quantified as a change in the state at some point along the nominal return. Three such states have been selected (not entirely arbitrarily) to analyze possible recovery costs for various types of errors; these states are denoted TCM-A, TCM-B, and TCM-C. The locations of these states are shown in Figure 5.1 along the nominal GENESIS trajectory. The location of TCM-A (with a corresponding date of March 31, 2003) is near the first $\hat{x}\hat{z}$ plane crossing after the spacecraft has departed the Lissajous (where the trajectory appears to cross the $\hat{x}$ axis as viewed in the $\hat{x}\hat{y}$ plane). This location is very useful in the trajectory design phase. In an operational sense, it is also an important state that serves as a guide for control of the vehicle during the Lissajous part of the mission. The second point, TCM-B on April 5, 2003, occurs along the L_2 portion of the trajectory at a location that preliminary station-keeping analysis suggests may be a good place to insert a correction

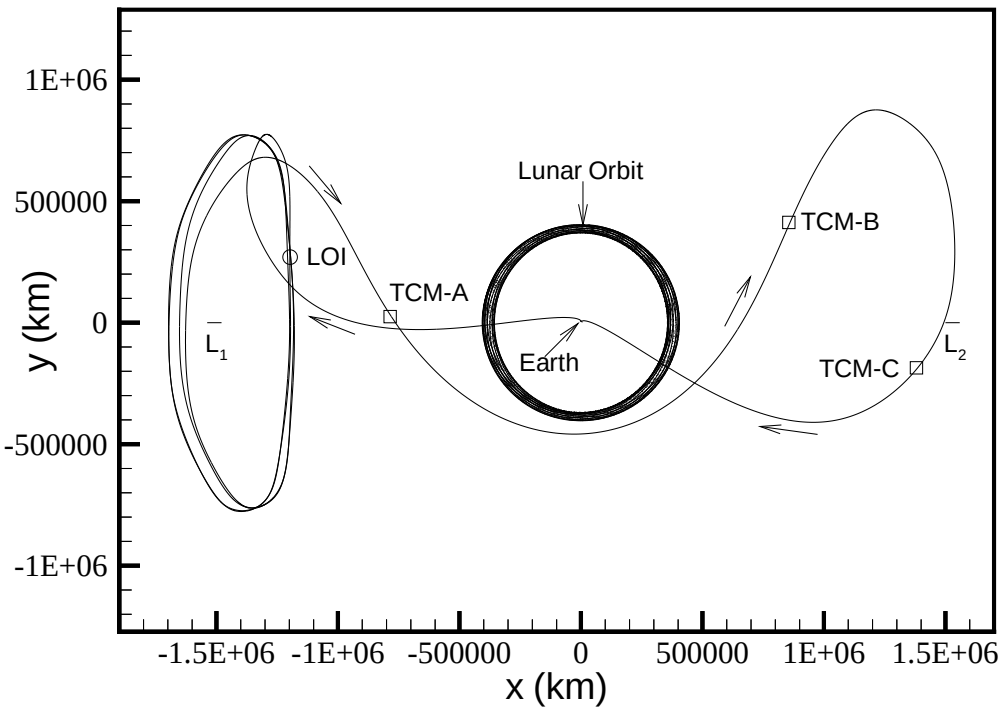

Figure 5.1. TCM Locations for GENESIS Return Error Analysis

maneuver. The last point, TCM-C, corresponds to the state on July, 20, 2003, thirty days prior to nominal reentry. This state provides support analysis of the sensitivity of the reentry state to errors in this portion of the return. The nominal selected for this analysis has reentry conditions of 125 km altitude, 40.6 deg declination, −114 deg right ascension, and −7.9 deg flight path angle. (Note that this is the return portion of the original nominal trajectory that is analyzed in Section 5.1.1.)

Recall that the return from the Lissajous is designed using numerical integration backwards in time from the reentry state to a fixed state along the Lissajous. Originally, the LOI state is selected as the fixed target state for the nominal solution. If instead, a state along the return after the end of the Lissajous is selected as the fixed point, then the effect of various errors on the solution can be studied. By perturbing this new target state with some set of errors, and then reconverging the trajectory from the desired reentry conditions to this point, an excellent preliminary estimate of the maneuver costs to correct and recover the solution can be obtained. Note that in this process, the TCM is performed at the same location where the error is introduced. The methodology is not restricted to implementing the TCM at the location of the error, but can be generalized to include maneuvers at other times. However, for preliminary analysis, the current choice is sufficient, and provides a tool to examine the sensitivity of state variations at various points along the return.

First, the effects of position and time errors on the return are examined. Preliminary station-keeping analysis has suggested that errors on the order of ±5000 km are possible at TCM-A. For comparison purposes, this position error is applied at each TCM state independently to determine the recovery costs associated with errors at each TCM point. The cost (ΔV_{TCM}) to correct various types of position errors is presented in Table 5.4 for each of the TCM's examined. Note that each case is treated independently; that is, the only errors introduced into the solution are at the specified point, and the correction maneuver is also performed at this time. The analysis shows that the cost to recover the solution at a given TCM location is very reasonable, ranging from 0.79–3.90 m/s over all cases examined. (However, it

is noted that the TCM's are not directly comparable, since the errors are applied at different locations along the trajectory.) By employing a design based on the natural dynamics of the system, the trajectory is relatively insensitive to errors in the solution. However, investigation is still required to determine how precisely the nominal solution must be maintained to ensure a viable reentry at Earth return.

Table 5.4 TCM Costs for Position Errors in GENESIS Return

		TCM-A	TCM-B	TCM-C
Type	Error	ΔV_{TCM} (m/s)	ΔV_{TCM} (m/s)	ΔV_{TCM} (m/s)
$\Delta\lvert\bar{R}\rvert$	–5000 (km)	1.02	3.82	3.61
	+5000 (km)	0.79	3.80	3.60
SR Δx	–5000 (km)	1.79	3.84	3.61
	+5000 (km)	2.33	3.83	3.60
SR Δy	–5000 (km)	1.26	1.39	1.30
	+5000 (km)	0.99	1.40	1.29
SR Δz	–5000 (km)	3.90	1.05	1.17
	+5000 (km)	3.55	1.04	1.17
EI ΔX	–5000 (km)	1.50	1.14	1.34
	+5000 (km)	1.08	1.14	1.35
EI ΔY	–5000 (km)	2.05	3.51	2.85
	+5000 (km)	2.48	3.53	2.85
EI ΔZ	–5000 (km)	3.26	1.48	2.04
	+5000 (km)	3.20	1.47	2.04
SR Δt	–6 (hr)	10.22	2.17	5.20
	+6 (hr)	9.94	2.15	5.25
EI Δt	–6 (hr)	12.97	0.81	4.96
	+6 (hr)	12.46	0.81	5.01

The costs to correct time errors of ± 6 hours are also presented in Table 5.4 relative to both SR and EI time differentials. Notice that errors in the time at TCM-A are the most expensive to correct of all the cases examined. This increase in cost is likely due to the location of the Moon as the spacecraft passes by the lunar orbit immediately following the $\hat{x}\hat{z}$ plane crossing. Although no formal lunar encounter occurs, in contrast to the MLS examples, the Moon is in the vicinity when the spacecraft passes through this point along the return path. The Moon contributes a perturbing effect on the solution that helps to initiate the L_2 loop and ultimately facilitates the proper reentry. Relatively small changes in timing at TCM-A can drastically change the nature of the rest of the solution. The timing at this point is thus crucial to a viable return; this is reflected in the increase in cost to correct a given timing offset. The cost to correct time errors at TCM-B are smaller compared to those at TCM-A, since timing is less of a factor at this location. However, as might be expected, as the spacecraft nears reentry, the time again becomes an issue, as is evidenced by the increase in cost at TCM-C. Table 5.5 presents results for different combinations of timing and position errors at the various target states. The results are *not* linear combinations of the individual errors from Table 5.4, but are clearly dominated by the timing issues just mentioned.

In addition to position and timing errors, variations in velocity may also be present at any given TCM location. Clearly, for this analysis, these velocity errors in isolation can simply be corrected with a maneuver of equal magnitude and opposite direction. It is more insightful to examine these velocity errors in conjunction with other errors, for instance, position deviations. Again, from the preliminary station-keeping analysis, velocity errors in the range ± 2.5 m/s are selected for this analysis. The results for position errors of ± 5000 km combined with errors only in the magnitude of the velocity state are presented in Table 5.6. The correction maneuvers required for these cases range from 1.32 to 6.41 m/s, well within reasonable limits for the mission. Notice that some of the more costly corrections occur at TCM-B, perhaps suggesting that this location is more sensitive to velocity variations. Similar results

Table 5.5 TCM Costs for Position+Time Errors in GENESIS Return

		TCM-A	TCM-B	TCM-C
Type	Error (km – hr)	ΔV_{TCM} (m/s)	ΔV_{TCM} (m/s)	ΔV_{TCM} (m/s)
SR $\Delta\|\bar{R}\|$, Δt	–5000 / –6	13.34	4.12	8.77
	+5000 / –6	14.08	4.98	2.32
	–5000 / +6	11.83	5.01	2.33
	+5000 / +6	12.22	4.07	8.84
SR $\Delta x, \Delta t$	–5000 / –6	11.09	3.82	8.60
	+5000 / –6	9.83	4.93	2.44
	–5000 / +6	9.26	4.95	2.45
	+5000 / +6	10.38	4.95	8.67
SR $\Delta y, \Delta t$	–5000 / –6	9.90	2.75	3.99
	+5000 / –6	11.68	2.38	6.43
	–5000 / +6	10.15	2.37	6.50
	+5000 / +6	9.31	2.76	4.04
SR $\Delta z, \Delta t$	–5000 / –6	13.30	2.34	4.80
	+5000 / –6	8.47	2.50	5.80
	–5000 / +6	7.66	2.46	5.87
	+5000 / +6	12.52	2.30	4.85

are presented in Table 5.7 for variations in position and the component of velocity that is normal to the plane of motion at the given instant (termed "normal" velocity). The correction maneuvers range from 1.63 to 6.03 m/s. All of the results presented attest to the robustness of both the GENESIS trajectory and the methodology used to generate the solution.

Table 5.6 TCM Costs for Position+Velocity Magnitude Errors in GENESIS Return

		TCM-A	TCM-B	TCM-C
Type	Error (km – m/s)	ΔV_{TCM} (m/s)	ΔV_{TCM} (m/s)	ΔV_{TCM} (m/s)
SR $\Delta\lvert\bar{R}\rvert$, ΔV_{mag}	–5000 / –2.5	4.09	6.41	2.53
	+5000 / –2.5	1.33	1.95	5.87
	–5000 / +2.5	1.84	1.96	5.87
	+5000 / +2.5	3.91	6.39	2.52
SR $\Delta x, \Delta V_{mag}$	–5000 / –2.5	1.30	6.18	2.35
	+5000 / –2.5	4.41	1.95	5.74
	–5000 / +2.5	4.15	1.96	5.74
	+5000 / +2.5	1.98	6.17	2.34
SR $\Delta y, \Delta V_{mag}$	–5000 / –2.5	3.39	3.82	3.51
	+5000 / –2.5	1.90	1.32	1.88
	–5000 / +2.5	2.04	1.33	1.89
	+5000 / +2.5	3.29	3.83	3.51
SR $\Delta z, \Delta V_{mag}$	–5000 / –2.5	5.06	3.28	2.87
	+5000 / –2.5	3.81	1.97	2.66
	–5000 / +2.5	4.16	1.98	2.64
	+5000 / +2.5	4.82	3.29	2.86

5.1.3 Phasing Loop Error Analysis

One of the principal reasons for incorporating phasing loops into a trajectory that includes lunar gravity assists is to provide additional opportunities to perform trajectory correction maneuvers prior to the first lunar encounter. Ideally, the first TCM should be implemented as soon as possible after injection onto the transfer path. However, a *single* correction maneuver shortly after launch may not be possible, since

Table 5.7 TCM Costs for Position+Normal Velocity Errors in GENESIS Return

		TCM-A	TCM-B	TCM-C
Type	Error (km – m/s)	ΔV_{TCM} (m/s)	ΔV_{TCM} (m/s)	ΔV_{TCM} (m/s)
SR $\Delta\lvert\bar{R}\rvert$, ΔV_{norm}	–5000 / –2.5	3.52	4.76	4.51
	+5000 / –2.5	2.31	4.71	4.53
	–5000 / +2.5	2.78	4.73	4.54
	+5000 / +2.5	3.42	4.74	4.50
SR $\Delta x, \Delta V_{norm}$	–5000 / –2.5	3.11	4.56	4.48
	+5000 / –2.5	3.29	4.60	4.29
	–5000 / +2.5	3.04	4.61	4.29
	+5000 / +2.5	3.54	4.55	4.47
SR $\Delta y, \Delta V_{norm}$	–5000 / –2.5	2.55	3.26	2.86
	+5000 / –2.5	2.90	2.39	2.78
	–5000 / +2.5	3.03	2.39	2.78
	+5000 / +2.5	2.46	3.27	2.85
SR $\Delta z, \Delta V_{norm}$	–5000 / –2.5	2.57	1.97	3.53
	+5000 / –2.5	5.76	3.29	1.63
	–5000 / +2.5	6.03	3.29	1.65
	+5000 / +2.5	2.14	1.97	3.54

accurate tracking information may not be available for some time. On the other hand, even a short delay in the execution of the maneuver may cause the correction cost to be prohibitively expensive. Thus, more sophisticated recovery strategies may be necessary to reduce this cost.

As an example of a trajectory with phasing loops, consider the transfer to an L_2 libration point orbit that is developed in Sections 4.3.1 to 4.3.5. Recall that solutions are available that include 0, 1, 2, 3, and 4 phasing loops. Each of these five

solutions are examined for various position and velocity errors in the initial (or insertion/injection) state on the transfer trajectory. A single TCM is then implemented at injection plus 18 hours to determine baseline costs to correct the given errors. For this example, position errors of ± 20 km in the radial direction are examined, since this direction proves to be the most costly to correct. Isolated velocity errors are also examined, that is, errors in velocity magnitude, and then radial and normal components are each evaluated separately, independent of any position errors; variations of ± 5, ± 10, and ± 20 m/s are selected for each velocity component. Not surprisingly, the resulting solutions are visually indistinguishable from the corresponding nominal. This is demonstrated by comparing the nominal two loop solution in Figure 4.10 with the corrected solution for a +20 m/s error in the V_{mag} direction, that appears in Figure 5.2. (Note that the segment from injection to the 18 hour TCM is plotted as a dotted line, the rest of the corrected trajectory from TCM to LOI is plotted with a solid line.) All such solutions demonstrate this same similarity to their respective nominals.

The correction costs using a single maneuver at 18 hours after injection are presented in Table 5.8. The most costly errors again occur in the radial position and tangential velocity directions. An asterix indicates cases in which the resulting corrected solution now contains a perigee (the perigee following injection and the TCM) with an unacceptable clearance of the atmosphere, defined as having an altitude less than 200 km. This situation occurs for errors that decrease the orbital energy of the trajectory, i.e., those that leave the initial state at a slower speed and closer to the Earth. No attempt is made to rectify this situation at this time, although an additional maneuver could be inserted at the first apogee to raise the perigees to acceptable levels. It is also of note that the nominal solution in the four loop case already contains an apogee burn of 23 m/s to raise the following perigee. For comparison purposes, this maneuver is treated as fixed in all of these cases, and is not included in ΔV_{TCM}. This may explain the larger corrections that are required for the radial and normal velocity errors in the four loop case. However, for all the other

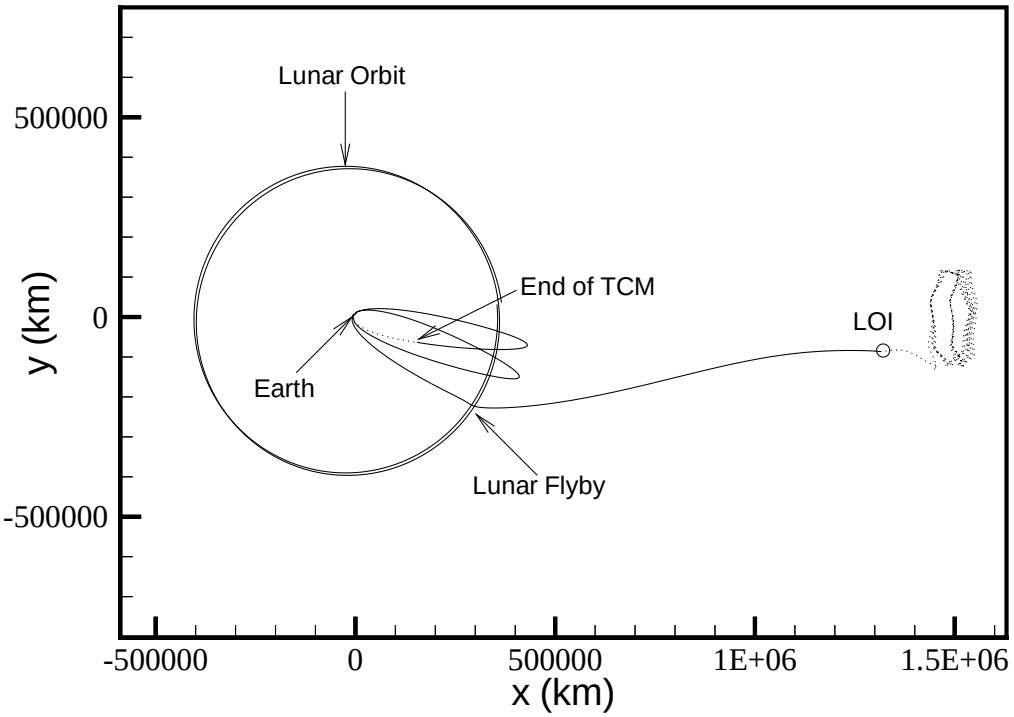

Figure 5.2. Two Loop Error Correction for +20 m/s V_{mag} Error

solutions, large velocity errors in the radial and normal velocity directions require very little cost to correct, typically less than the magnitude of the actual error! The development of alternative recovery strategies will therefore focus on the much more costly radial position and tangential velocity errors only.

The results in Table 5.8 reveal only part of the story. To correct the given errors, a new transfer to the specified Lissajous trajectory is required; thus the corresponding LOI maneuvers for each case change, depending upon the error. Table 5.9 presents the resulting LOI maneuvers for the cases examined in Table 5.8. The nominal LOI costs are listed in the first row of the table. The results from Tables 5.8 and 5.9 are used with Equation 5.1 to compute the total corrective cost (ΔV_{COR}) attributed to the error in any particular case. These total costs are tabulated in Table 5.10. When viewing Tables 5.8, 5.9, and 5.10, recall that the corrective action is implemented in terms of a single maneuver. For some errors, the cost savings inherent in using a lunar gravity assist has nearly been offset by the increase in cost to correct injection

Table 5.8 TCM Costs for LPO Transfer Example: Correction at Injection + 18 hr

		0-Loop	1-Loop	2-Loop	3-Loop	4-Loop
Type	Error	ΔV_{TCM} (m/s)	ΔV_{TCM} (m/s)	ΔV_{TCM} (m/s)	ΔV_{TCM} (m/s)	ΔV_{TCM} (m/s)
EI $\Delta\lvert\bar{R}\rvert$	–20 (km)	120.95	121.31	118.37(∗)	118.15	120.48(∗)
	+20 (km)	116.16	116.83	113.81	113.59	111.23
EI ΔV_{mag}	–5 (m/s)	35.33	35.44	34.60	34.54	38.26
	+5 (m/s)	34.99	35.12	34.28	34.22	33.33
	–10 (m/s)	71.01	71.21	69.54(∗)	69.42	72.31(∗)
	+10 (m/s)	69.63	69.94	68.24	68.12	66.26
	–20 (m/s)	143.45	143.75	140.44(∗)	140.21	142.44(∗)
	+20 (m/s)	137.95	138.69	135.25	135.00	132.48
EI ΔV_{rad}	–5 (m/s)	1.26	0.35	0.44	0.48	11.04
	+5 (m/s)	1.26	0.37	0.45	0.48	10.26
	–10 (m/s)	2.51	0.70	0.88	0.95	11.43
	+10 (m/s)	2.53	0.75	0.90	0.97	9.87
	–20 (m/s)	5.01	1.34	1.73	1.89	12.21
	+20 (m/s)	5.09	1.55	1.82	1.97	9.08
EI ΔV_{norm}	–5 (m/s)	0.08	0.07	0.09	0.08	10.66
	+5 (m/s)	0.08	0.06	0.09	0.08	10.64
	–10 (m/s)	0.17	0.13	0.19	0.17	10.68
	+10 (m/s)	0.16	0.13	0.19	0.17	10.62
	–20 (m/s)	0.35	0.29	0.40	0.36	10.69
	+20 (m/s)	0.35	0.29	0.39	0.35	10.57

Table 5.9 LOI Costs for LPO Transfer Example: Correction at Injection + 18 hr

		0-Loop	1-Loop	2-Loop	3-Loop	4-Loop
Nominal LOI Cost (m/s)		1.93	20.64	30.35	32.75	32.19
Type	Error	ΔV_{LOI} (m/s)	ΔV_{LOI} (m/s)	ΔV_{LOI} (m/s)	ΔV_{LOI} (m/s)	ΔV_{LOI} (m/s)
EI $\Delta\lvert\bar{R}\rvert$	–20 (km)	3.92	16.69	33.65(∗)	36.07	33.82(∗)
	+20 (km)	0.33	24.51	27.14	29.53	27.03
EI ΔV_{mag}	–5 (m/s)	2.50	19.51	31.29	33.70	31.36
	+5 (m/s)	1.36	21.77	29.41	31.81	29.39
	–10 (m/s)	3.08	18.37	32.24(∗)	34.66	32.36(∗)
	+10 (m/s)	0.81	22.89	28.48	30.87	28.42
	–20 (m/s)	4.25	16.07	34.17(∗)	36.60	34.37(∗)
	+20 (m/s)	0.51	25.12	26.64	29.01	26.50
EI ΔV_{rad}	–5 (m/s)	1.98	20.45	30.49	32.89	30.53
	+5 (m/s)	1.87	20.84	30.20	32.61	30.22
	–10 (m/s)	2.04	20.26	30.64	33.04	30.68
	+10 (m/s)	1.81	21.03	30.05	32.46	30.07
	–20 (m/s)	2.16	19.89	30.93	33.32	30.98
	+20 (m/s)	1.69	21.42	29.75	32.17	29.76
EI ΔV_{norm}	–5 (m/s)	1.93	20.64	30.35	32.75	30.37
	+5 (m/s)	1.92	20.64	30.34	32.75	30.37
	–10 (m/s)	1.93	20.64	30.35	32.75	30.37
	+10 (m/s)	1.92	20.65	30.34	32.75	30.37
	–20 (m/s)	1.93	20.65	30.34	32.75	30.37
	+20 (m/s)	1.92	20.65	30.34	32.75	30.37

Table 5.10 Total Corrective Costs for LPO Transfer Example

		0-Loop	1-Loop	2-Loop	3-Loop	4-Loop
Type	Error	ΔV_{COR} (m/s)	ΔV_{COR} (m/s)	ΔV_{COR} (m/s)	ΔV_{COR} (m/s)	ΔV_{COR} (m/s)
EI $\Delta\lvert\bar{R}\rvert$	–20 (km)	122.94	117.36	121.67(∗)	121.47	122.11(∗)
	+20 (km)	114.56	120.70	110.60	110.37	106.07
EI ΔV_{mag}	–5 (m/s)	35.90	34.31	35.54	35.49	37.43
	+5 (m/s)	34.42	36.25	33.34	33.28	30.53
	–10 (m/s)	72.16	68.94	71.43(∗)	71.33	72.48(∗)
	+10 (m/s)	68.51	72.19	66.37	66.24	62.49
	–20 (m/s)	145.77	139.18	144.26(∗)	144.06	144.62(∗)
	+20 (m/s)	136.53	143.17	131.54	131.26	126.79
EI ΔV_{rad}	–5 (m/s)	1.31	0.16	0.58	0.62	9.38
	+5 (m/s)	1.20	0.57	0.30	0.34	8.29
	–10 (m/s)	2.62	0.32	1.17	1.24	9.92
	+10 (m/s)	2.41	1.14	0.60	0.68	7.75
	–20 (m/s)	5.24	0.59	2.31	2.46	11.00
	+20 (m/s)	4.85	2.33	1.22	1.39	6.65
EI ΔV_{norm}	–5 (m/s)	0.08	0.07	0.09	0.08	8.84
	+5 (m/s)	0.07	0.06	0.08	0.08	8.82
	–10 (m/s)	0.17	0.13	0.19	0.17	8.86
	+10 (m/s)	0.15	0.14	0.18	0.17	8.80
	–20 (m/s)	0.35	0.30	0.39	0.36	8.87
	+20 (m/s)	0.34	0.30	0.38	0.35	8.75

errors. The value of including phasing loops into the design, however, provides the opportunity to spread the necessary corrections over more maneuvers and to consider more creative approaches. This issue will be explored further in the next sections.

5.2 Recovery Strategies for Trajectories with Phasing Loops

As demonstrated in the previous sections, it is generally possible to utilize a trajectory correction maneuver sometime shortly after launch to recover from possible injection errors. The cost of the maneuver is a function of the type and magnitude of the error, as well as the timing. For certain errors, however, the cost to recover the nominal solution, even a short time after launch, can be prohibitively expensive for present mission design. It is therefore desired to utilize the current methodology to examine alternative recovery strategies with costs that are potentially lower than straight correction back to the nominal. The transfer to an L_2 Lissajous orbit is again selected to demonstrate the design of various recovery strategies, although the techniques are applicable to any trajectory with phasing loops. The cost of any potential recovery is compared to the straight correction costs at injection plus 18 hours, presented in Section 5.1.3. A feasible recovery is then defined as a new trajectory solution with a lower cost than the corresponding straight error correction solution.

5.2.1 Recoveries for One Phasing Loop

The use of phasing loops in a trajectory that includes a lunar encounter allows a number of alternatives to recover an acceptable solution in the event of errors in the injection maneuver. However, not all trajectories with phasing loops permit the same kind of recovery. For solutions that include a single phasing loop, the most costly injection errors (tangential velocity and radial distance) essentially alter the orbital energy, and thus the orbital period of the phasing loop. However, altering the period of the loop changes the timing of the perigee directly prior to the lunar encounter (at the end of the phasing loop). The effects of various errors on the

conic periods and perigee times (JD_{peri}) in terms of Julian dates are presented in Table 5.11 for uncorrected errors in the one loop transfer example. Even a modest error of +5 m/s, if left uncorrected, results in a change in perigee time of 22.5 hours. However, the timing of this perigee is critical to reaching the proper lunar encounter that achieves the desired trajectory. Even errors of ±6 hours can drastically alter the ensuing lunar flyby, and result in a failure to meet the design criteria. Hence, any effective recovery strategy will need to compensate for this period difference at some point along the phasing loop. However, since only a single phasing loop is available, the only way to adjust the timing of the perigee is through a maneuver placed between injection and the next perigee. Given a +5 m/s injection overburn, Figure 5.3 presents the maneuver cost to correct the timing at perigee for various maneuver times relative to the transfer insertion point. Clearly, the sooner the TCM is performed, the lower the overall cost. Similar results are seen for a -5 m/s injection underburn. It is therefore concluded that there are no feasible recovery strategies, at this time, for the single phasing loop trajectory with a cost that is less than the straight correction back to the nominal. Similar reasoning excludes feasible recovery strategies for trajectories involving no phasing loops, such as the zero loop L_2 transfer, or the GENESIS trajectory.

5.2.2 Recoveries for Two Phasing Loops

The one loop solution does not provide any feasible recovery strategies; however, the addition of a second phasing loop improves the possibility of a viable recovery with a lower cost than the straight correction. Errors in tangential velocity and radial position still produce significant shifts in the time of the next perigee (as in Table 5.11); now however, an additional phasing loop is available between this next perigee state and the target perigee prior to the lunar encounter. With this additional loop, the timing error at the first perigee, caused by any injection errors, can be offset by altering the period of the second loop. One of the most effective methods to alter the period of a trajectory is through a tangential maneuver at perigee; thus,

Table 5.11 One Phasing Loop: Perigee Timing Changes for Various Errors

	Conic Period (day)	JD_{peri}	ΔJD_{peri} (hrs)
Nominal	10.3999	2454363.1694	—
–5 m/s V_{mag}	9.6122	2454362.3529	–19.5960
+5 m/s V_{mag}	11.3511	2454364.1085	22.5384
–20 m/s V_{mag}	7.6592	2454360.4496	–65.2752
+20 m/s V_{mag}	14.7547	2454367.9634	115.0560
–20 km $\Delta\|\bar{R}\|$	7.9937	2454360.7838	–57.2544
+20 km $\Delta\|\bar{R}\|$	14.0936	2454366.9813	91.4856

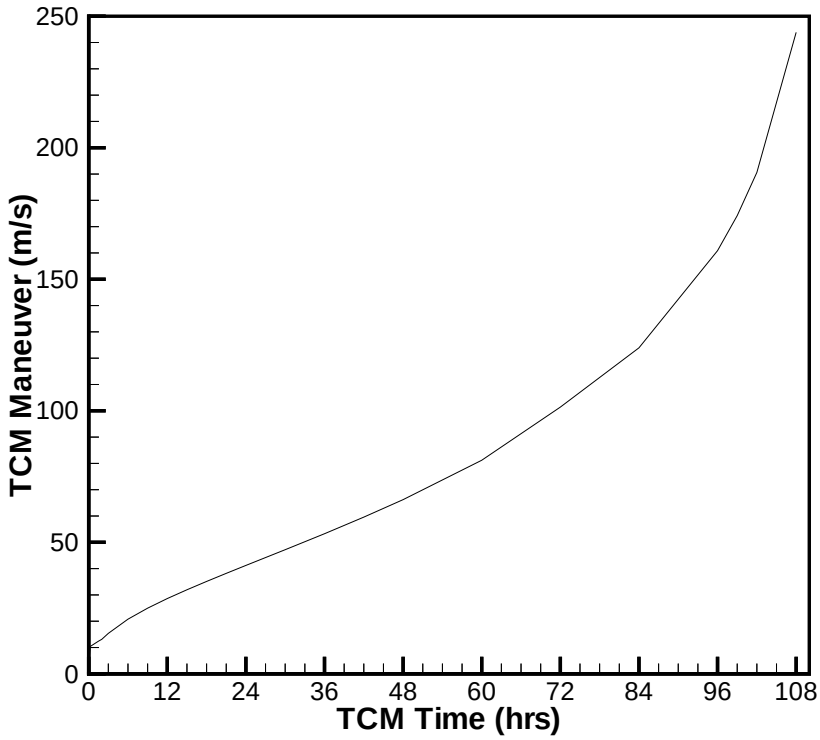

Figure 5.3. One Phasing Loop: TCM Maneuver Cost vs. Time from Injection

a deterministic $\Delta\bar{V}$ is inserted at the first perigee (at the end of the first phasing loop). This maneuver is utilized to adjust the period of the second phasing loop such that the target date for the last perigee prior to the lunar encounter is the same as that in the nominal solution. This ensures a proper lunar encounter that meets the trajectory design requirements.

5.2.2.a Introduction of Multiple Correction Maneuvers

To aid in the development of a feasible recovery, the algorithm to implement this strategy decomposes the trajectory into three parts: transfer trajectory insertion (TTI) to first perigee following insertion (P_1), first perigee to the next perigee (P_2) directly prior to the lunar encounter, and P_2 to LOI (or the end of the transfer). For the first segment, the injection state, including any errors, is numerically propagated to P_1 using the full force model. Thus, P_1 becomes the first TCM location, and the new initial state for the three step methodology, similar to the discussion in Section 5.1. Note that certain error types decrease orbital energy and also tend to lower the perigee altitude. If the altitude is unacceptable, a maneuver is inserted at the first apogee to raise the altitude of this perigee; this apogee then becomes the location of the first TCM maneuver and the "beginning" of the recovery trajectory.

The next part of the recovery is accomplished in the second phasing loop. Modification of this loop is used to compensate for timing changes at P_1 caused by the errors at insertion. In order to ensure a recovery consistent with the nominal, a "solution" for the second loop is sought between the actual P_1 state at the end of the error propagation and the nominal P_2 state prior to the lunar flyby. This segment is essentially a Lambert solution between two positions ($\bar{R}_{P1}$ and $\bar{R}_{P2}$) with a given time of flight ($\mathrm{JD}_{P2} - \mathrm{JD}_{P1}$). In practice, this is extremely difficult to implement, since a trajectory between two consecutive perigees requires the transfer angle (the angle between the two position vectors) to be close to 2π. Lambert solutions with transfer angles close to 2π are notoriously difficult to determine. However, as discussed earlier, to achieve a successful lunar encounter, the most critical target at P_2 is the time of perigee. A

procedure has been developed that approximates the desired second loop using a two body conic solution. For this conic (called here the singular Lambert solution), it is assumed that the same inertial position vector ($\bar{R}_{P1}$) is desired at each end point with the times JD_{P1} and JD_{P2}. The second phasing loop then connects the perigees P_1 and P_2 with a transfer angle of exactly 2π. Under this assumption, the given time of flight $\mathrm{JD}_{P2} - \mathrm{JD}_{P1}$ is exactly one period of the conic orbit. The semi-major axis a_c of the conic approximation can then be obtained from the relationship between a_c and the orbital period $\mathbb{P}_c$, that is,

$$a_c = \sqrt[3]{\mu_e \left(\frac{\mathbb{P}_c}{2\pi}\right)^2} \quad , \tag{5.2}$$

where $\mathbb{P}_c = \mathrm{JD}_{P2} - \mathrm{JD}_{P1}$ and μ_e is the gravitational parameter defined for the Earth. The perigee radius $|\bar{R}_{P1}|$ is available from the first phasing loop, so that the eccentricity of the conic is

$$e_c = 1 - \frac{|\bar{R}_{P1}|}{a_c} \quad . \tag{5.3}$$

It is assumed in this procedure that the orientation of the conic orbital plane can be determined from the known six dimensional state at P_1 (prior to any maneuver), such that the inclination and ascending node corresponding to the singular Lambert conic are also known. Since the true anomaly (and eccentric anomaly) at P_1 and P_2 are both zero, the argument of perigee ω_c can also be determined from the position vector $\bar{R}_{P1}$, and the other orbital elements. Using this approximation, the two body conic from P_1 to P_2 that matches the nominal date at P_2 can be completely specified.

The intermediate multi-conic improvement step is now applied to this conic solution (between the first perigee state and the new state at P_2) to obtain an approximation to the four body solution. After convergence is achieved, this in turn leads to an integrated four body solution for the second segment in the recovery. Since the position and time of P_1 is fixed by the propagation of the injection error, a deterministic maneuver $\Delta\bar{V}_{P1}$ is introduced at this first perigee. This maneuver effectively alters the period of the second phasing loop to force the date of the second perigee to the same date obtained for the nominal solution. Note that, in practice, the time of flight

along the trajectory arc from insertion to P_1 is adjusted to minimize the magnitude of $\Delta\bar{V}_{P1}$. This is an iterative process that results in an actual P_1 state that is displaced slightly from the true perigee location by 0 to 2 degrees in true anomaly.

For the final trajectory arc along the recovery path from P_2 to LOI, the initial position and time (at P_2) of the segment are fixed from the converged solution of the second segment. A numerically integrated solution is then determined from P_2 to LOI using the nominal trajectory as an initial guess. Since P_2 is fixed, a second deterministic maneuver $\Delta\bar{V}_{P2}$ is thus introduced at the second perigee. This maneuver effectively sets up the proper lunar encounter to achieve the desired transfer trajectory.

From experience with this procedure, it is apparent that certain adjustments can help reduce the magnitude of the maneuver at P_2. First, the normal component of velocity at the second apogee, A_2, can be altered to reduce the normal component of the maneuver at P_2; this maneuver is usually on the order of 1–3 m/s. This has proven to be a highly cost effective technique to minimize the inclination changes required at P_2. Next, similar to the motivation for the introduction of the maneuver at the first perigee ($\Delta\bar{V}_{P1}$), the time of flight of the second phasing loop can be adjusted slightly to help reduce the magnitude of $\Delta\bar{V}_{P2}$, at the expense of some drift away from perigee. Additionally, the tangential component of the maneuver at P_1 can be adjusted to further reduce the magnitude of the second perigee maneuver. Ideally, both maneuvers should occur at perigee, but in practice this is rarely the case; they are, however, still within a few degrees of zero true anomaly, i.e., perigee.

After suitable solutions are determined for all three segments of the recovery path and estimates of any deterministic maneuvers are obtained, the entire trajectory from transfer injection to LOI is incorporated into a single end-to-end solution. For this solution, the injection errors are generally only propagated to the first apogee to allow a perigee raise maneuver to be added, if necessary. The rest of the solution, including all deterministic maneuvers, is then constructed, and the algorithm converges quickly onto the desired recovery trajectory. It should be noted that the recovery determined

with this procedure inserts onto the *same* Lissajous as the nominal solution; this is a key factor in the design of these types of recovery strategies.

5.2.2.b Recoveries from Two Loop Overburn Errors

A number of different errors in the tangential injection velocity component have been examined. First, consider a +5 m/s overburn error in tangential velocity. The algorithm is applied to determine a recovery solution that is summarized in Table 5.12. The table lists the magnitudes of the maneuvers that correspond to the nominal solution (Nominal), the straight correction at TTI plus 18 hours (Straight), and the recovery scenario (Recovery). The total cost then is simply the sum of all the magnitudes of the individual maneuvers. Notice that the the straight error correction at injection plus 18 hours produces a total cost of 63.69 m/s, while the recovery solution has resulted in a total cost of 48.36 m/s; this is a savings of 15.33 m/s, and only 18.01 m/s above the nominal cost. (It is noted that the recovery solution does include four maneuvers rather than just one, thus increasing the opportunity for additional execution errors. However, opportunities for additional adjustments such as station-keeping are also available.) Also notice that the maximum maneuver magnitude (aside from LOI) has been reduced from 34.28 m/s at TTI+18 to 10.44 m/s at P_1 utilizing this recovery strategy. For completeness, the perigee altitudes are also listed for all three solutions. It is of note that the last perigee altitude has a direct impact on the LOI cost; the cost increases slightly as the perigee altitude decreases, and vice versa. This can be factored into the recovery design, but the timing of P_2 is always the dominating factor. The resulting recovery trajectory appears in Figure 5.4 as projected onto the $\hat{x}\hat{y}$ plane. It is clear from the figure that the injection error increases the period of the first phasing loop. This increase is then offset by a smaller second loop to achieve the desired P_2 timing. Note that the propagation of the injection error is again represented as a dotted line that terminates at the first apogee A_1.

Table 5.12 Two Phasing Loops: Recovery from +5 m/s V_{mag} Error

	Nominal	Straight	Recovery
TTI+18 ΔV (m/s)	—	34.28	—
A_1 ΔV (m/s)	—	—	0.56
P_1 ΔV (m/s)	—	—	10.44
A_2 ΔV (m/s)	—	—	—
P_2 ΔV (m/s)	—	—	6.01
LOI ΔV (m/s)	30.35	29.41	31.35
Total ΔV (m/s)	30.35	63.69	48.36
P_1 Altitude (km)	331.6	428.6	216.2
P_2 Altitude (km)	2356.2	2473.3	1876.0

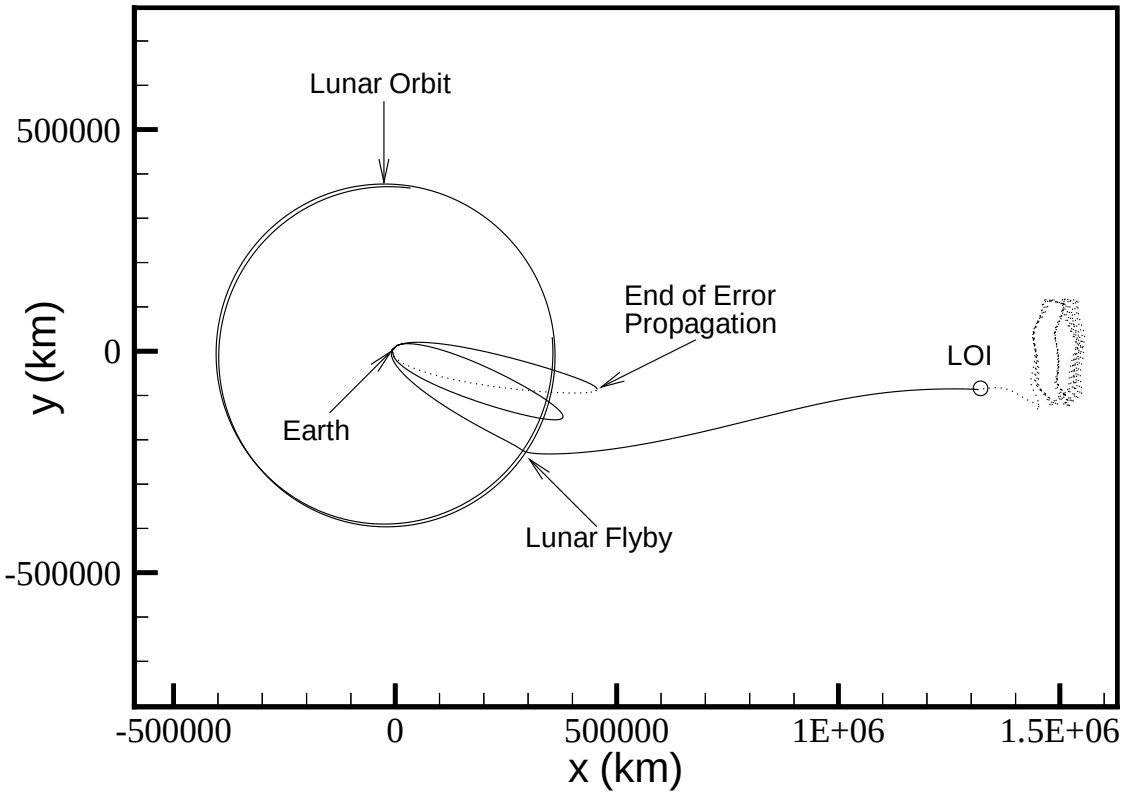

Figure 5.4. Two Loop Recovery for +5 m/s V_{mag} Error

Similar results for a +10 m/s velocity magnitude error appear in Table 5.13 and Figure 5.5. Note the distinct difference between the periods of the two loops designed through the recovery algorithm. This solution achieves a savings of 25.91 m/s, while reducing the maximum non-LOI maneuver to 23.21 m/s from the single 68.24 m/s maneuver required for the straight correction option. The results for a +20 m/s velocity magnitude error are presented in Table 5.14 and Figure 5.6. In this case, the recovery solution actually has a increase of 6.29 m/s over the straight correction cost, but reduces the maximum maneuver from 135.25 m/s to 77.11 m/s. Since the cost for the recovery has exceeded the straight correction, this is the largest velocity overburn that is examined with this particular recovery. Later, a modified recovery strategy is presented for overburns greater than 20 m/s.

5.2.2.c Recoveries from Two Loop Underburn Errors

The current strategy works equally well, if not better, for velocity underburns at injection. The recovery solution for a −5 m/s underburn in velocity magnitude is summarized in Table 5.15. For this case, the solution produces a savings of 22.97 m/s over straight correction and reduces the maximum maneuver in the phasing loops to 8.88 m/s. The resulting trajectory is plotted in Figure 5.7. Notice that for underburns, the first phasing loop is shorter in period than the nominal solution; hence the second loop becomes larger to compensate for the time difference. The recovery for a −10 m/s velocity magnitude error is presented in Table 5.16 and plotted in Figure 5.8. This recovery solution results in a savings of 48.02 m/s and a reduction of the maximum non-LOI maneuver from 69.54 m/s in the straight correction to only 16.99 m/s. Also note that the straight correction solution may have an unacceptable perigee altitude at P_1, while, the recovery solution has ample clearance of 636.6 km altitude without additional adjustment of the A_1 maneuver. Similarly, the results for a −20 m/s underburn are presented in Table 5.17 and Figure 5.9. In this case, a savings of 106.07 m/s is achieved through the recovery solution, with a maximum phasing loop maneuver of only 32.00 m/s, in comparison to 140.44 m/s for straight

Table 5.13 Two Phasing Loops: Recovery from +10 m/s V_{mag} Error

	Nominal	Straight	Recovery
TTI+18 ΔV (m/s)	—	68.24	—
A_1 ΔV (m/s)	—	—	1.05
P_1 ΔV (m/s)	—	—	23.21
A_2 ΔV (m/s)	—	—	—
P_2 ΔV (m/s)	—	—	14.63
LOI ΔV (m/s)	30.35	28.48	31.92
Total ΔV (m/s)	30.35	96.72	70.81
P_1 Altitude (km)	331.6	525.5	229.8
P_2 Altitude (km)	2356.2	2590.1	1458.9

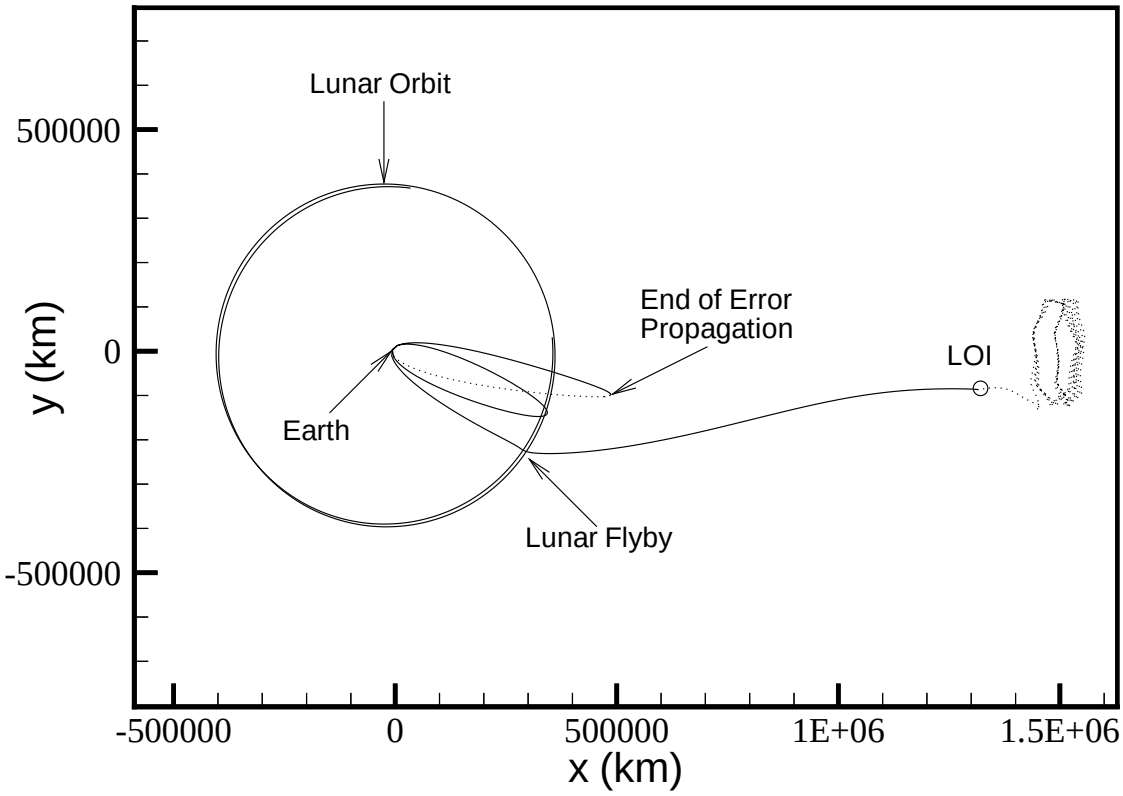

Figure 5.5. Two Loop Recovery for +10 m/s V_{mag} Error

Table 5.14 Two Phasing Loops: Recovery from +20 m/s V_{mag} Error

	Nominal	Straight	Recovery
TTI+18 ΔV (m/s)	—	135.25	—
A_1 ΔV (m/s)	—	—	2.34
P_1 ΔV (m/s)	—	—	77.11
A_2 ΔV (m/s)	—	—	—
P_2 ΔV (m/s)	—	—	57.54
LOI ΔV (m/s)	30.35	26.64	31.19
Total ΔV (m/s)	30.35	161.89	168.18
P_1 Altitude (km)	331.6	718.4	867.5
P_2 Altitude (km)	2356.2	2822.4	1105.2

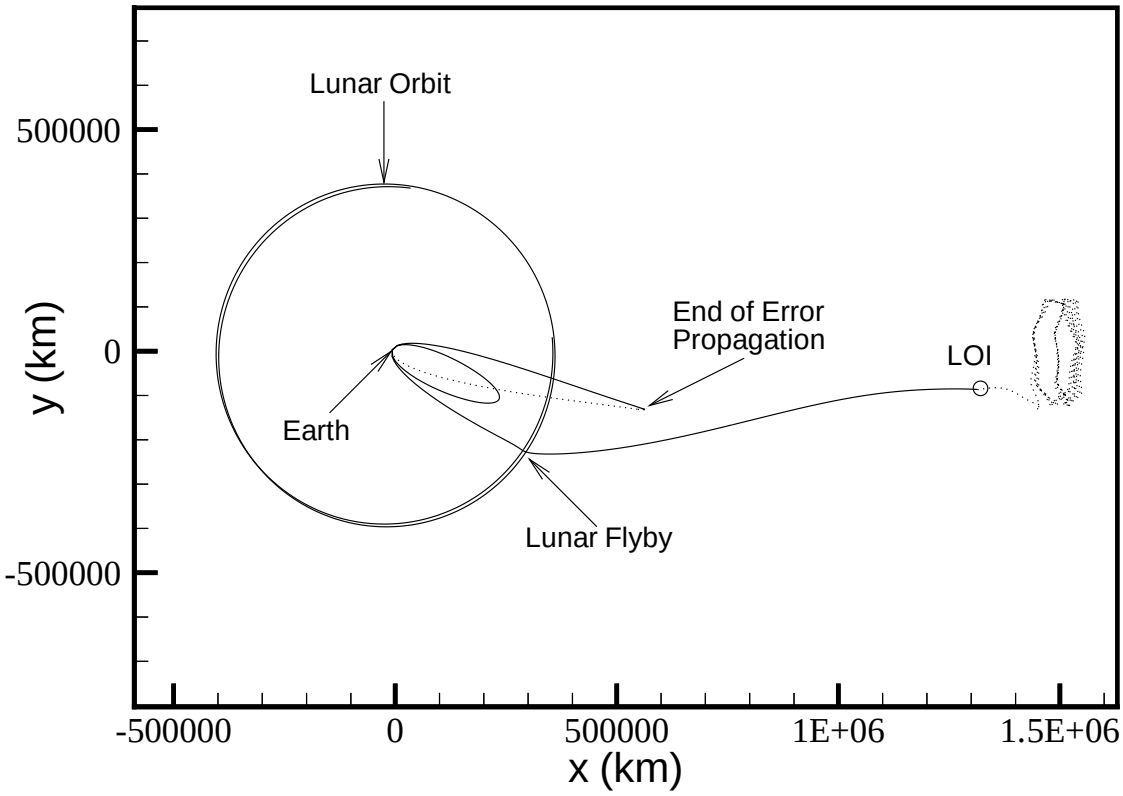

Figure 5.6. Two Loop Recovery for +20 m/s V_{mag} Error

Table 5.15 Two Phasing Loops: Recovery from –5 m/s V_{mag} Error

	Nominal	Straight	Recovery
TTI+18 ΔV (m/s)	—	34.60	—
A_1 ΔV (m/s)	—	—	0.23
P_1 ΔV (m/s)	—	—	8.88
A_2 ΔV (m/s)	—	—	—
P_2 ΔV (m/s)	—	—	4.53
LOI ΔV (m/s)	30.35	31.29	29.28
Total ΔV (m/s)	30.35	65.89	42.92
P_1 Altitude (km)	331.6	234.3	478.8
P_2 Altitude (km)	2356.2	2238.7	2796.2

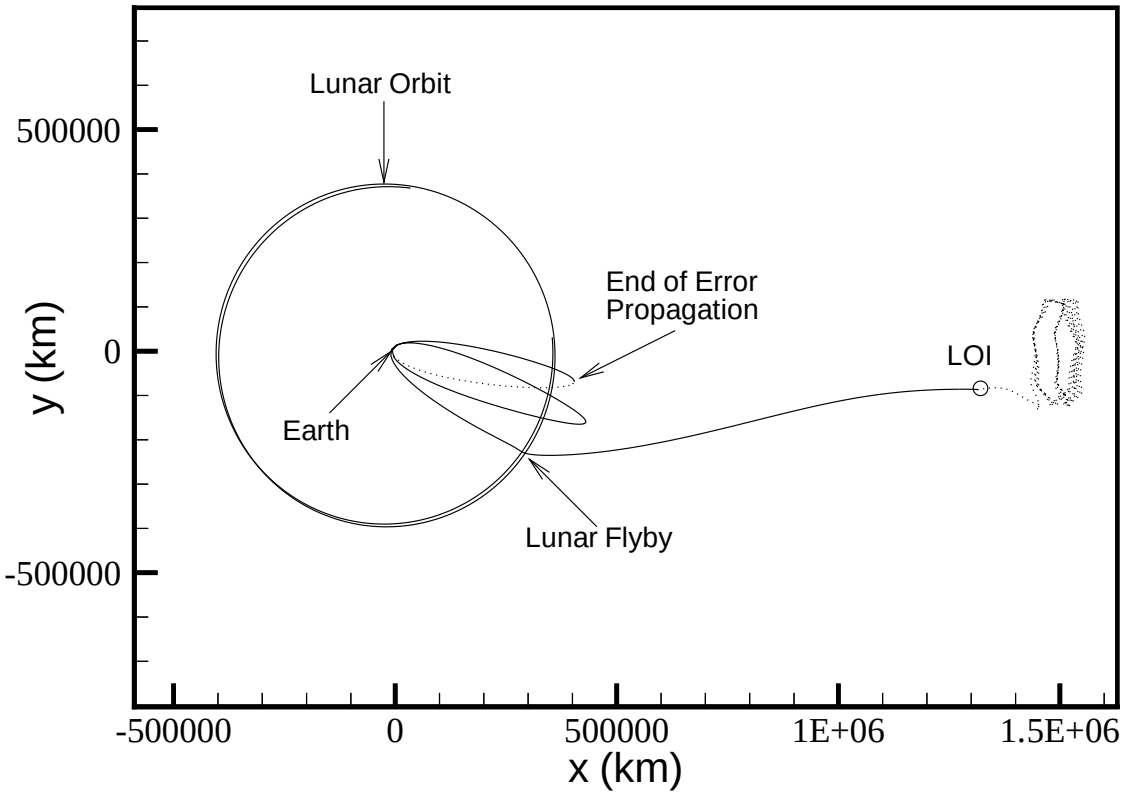

Figure 5.7. Two Loop Recovery for –5 m/s V_{mag} Error

Table 5.16 Two Phasing Loops: Recovery from –10 m/s V_{mag} Error

	Nominal	Straight	Recovery
TTI+18 ΔV (m/s)	—	69.54	—
A_1 ΔV (m/s)	—	—	0.43
P_1 ΔV (m/s)	—	—	16.99
A_2 ΔV (m/s)	—	—	—
P_2 ΔV (m/s)	—	—	8.12
LOI ΔV (m/s)	30.35	32.24	28.22
Total ΔV (m/s)	30.35	101.78	53.76
P_1 Altitude (km)	331.6	136.8	636.6
P_2 Altitude (km)	2356.2	2120.8	3185.3

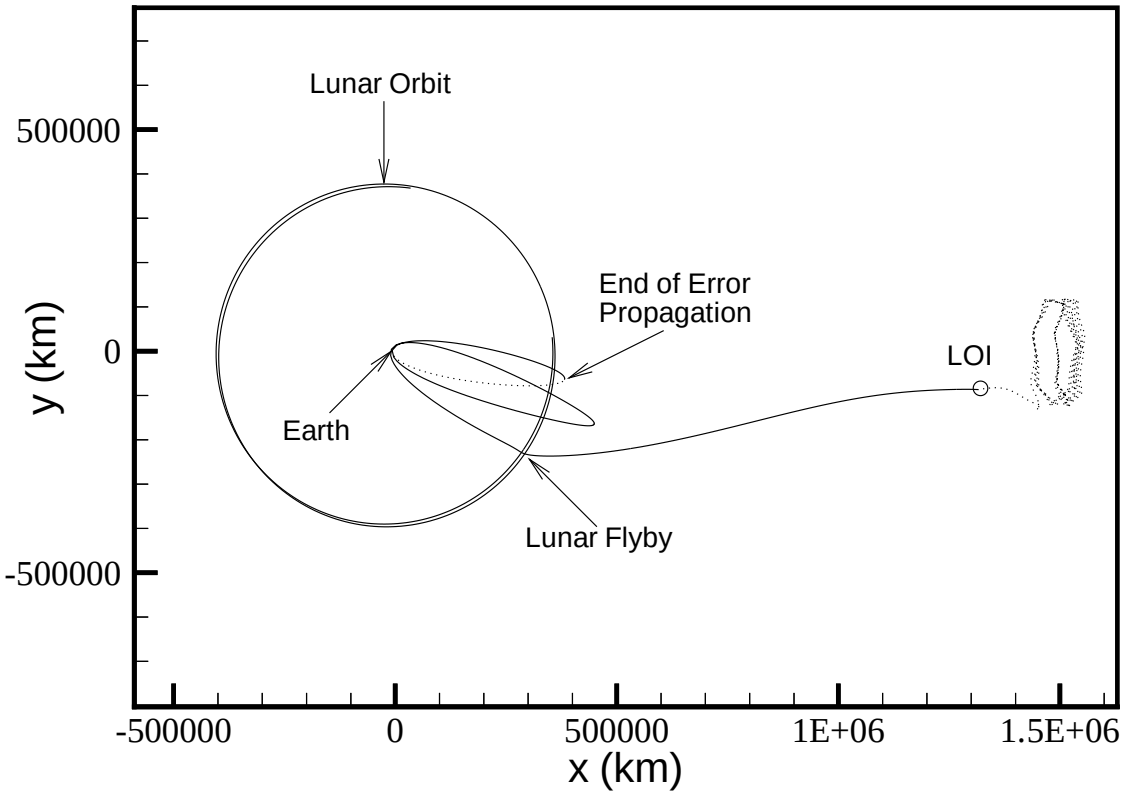

Figure 5.8. Two Loop Recovery for –10 m/s V_{mag} Error

Table 5.17 Two Phasing Loops: Recovery from –20 m/s V_{mag} Error

	Nominal	Straight	Recovery
TTI+18 ΔV (m/s)	—	140.44	—
A_1 ΔV (m/s)	—	—	0.74
P_1 ΔV (m/s)	—	—	32.00
A_2 ΔV (m/s)	—	—	—
P_2 ΔV (m/s)	—	—	13.55
LOI ΔV (m/s)	30.35	34.17	26.25
Total ΔV (m/s)	30.35	178.61	72.54
P_1 Altitude (km)	331.6	-58.8	925.7
P_2 Altitude (km)	2356.2	1883.8	3790.6

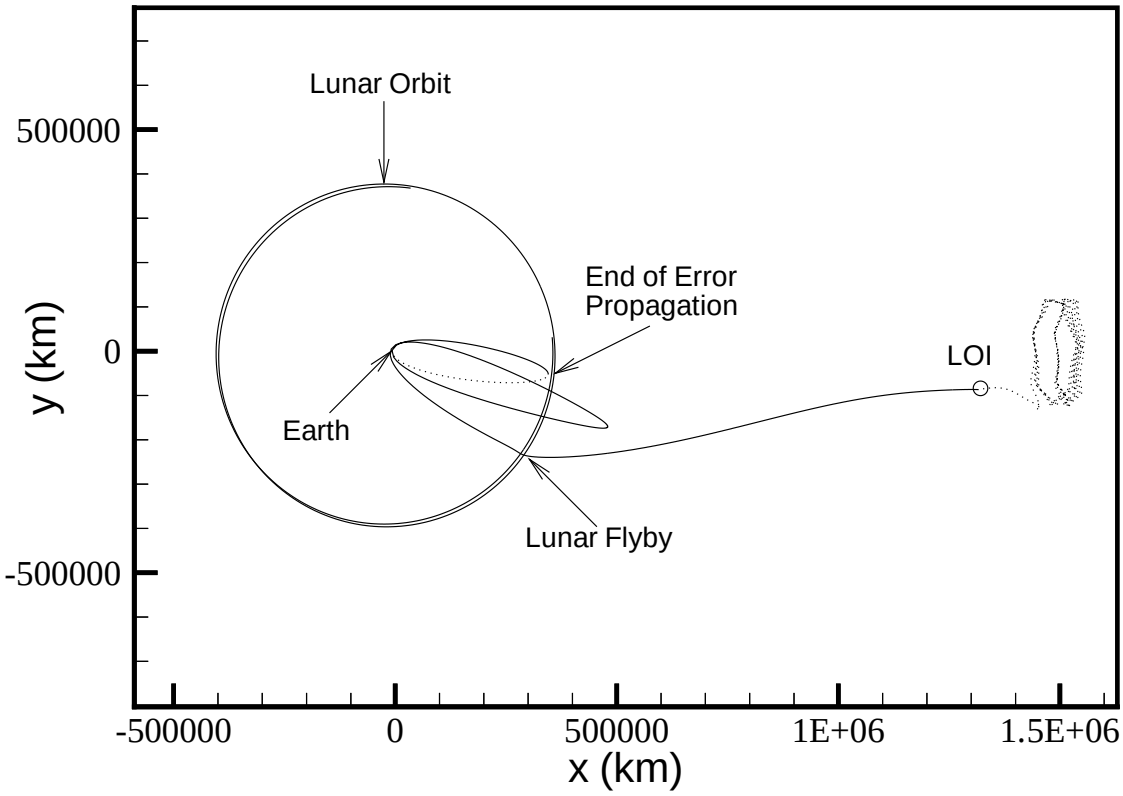

Figure 5.9. Two Loop Recovery for –20 m/s V_{mag} Error

correction. As an added benefit, the P_1 altitude in the recovery solution is also acceptable, in contrast to the straight correction solution that impacts the Earth. Recall that for +20 m/s velocity magnitude error the recovery solution failed to match the straight correction cost, while the corresponding recovery solution in the underburn case is over 100 m/s more cost effective! Thus, two additional examples with errors of −30 and −40 m/s are investigated to explore the range of velocity errors that can be reasonably recovered utilizing this strategy. The −30 m/s underburn is summarized in Table 5.18 and plotted in Figure 5.10. For this case, the straight correction produces a total cost of 248.90 m/s, while recovery can actually be achieved for only 88.81 m/s; this alternate approach also raises the first perigee to an acceptable level. Finally, the recovery for −40 m/s is presented in Table 5.19 and in Figure 5.11. For this case, a savings of 220.88 m/s is achieved over the straight correction at injection plus 18 hours. These cases demonstrate that this particular recovery strategy works very well for the two loop phasing solution, especially for large underburns.

5.2.2.d Recoveries from Two Loop Radial Position Errors

This strategy is not restricted only to errors in velocity magnitude, but can also be employed to determine recoveries for errors in radial position. As an example, consider an error of +20 km in the radial direction. The results from the application of the current recovery strategy to this error are presented in Table 5.20. The cost to execute the recovery is 18.33 m/s less than the corresponding straight correction solution, and the maximum non-LOI maneuver is decreased from 113.81 m/s for straight recovery to 51.92 m/s. The resulting trajectory appears in Figure 5.12. Notice that the solution appears similar to the +20 m/s velocity magnitude case in Figure 5.6, since both errors increase the period of the initial phasing loop. The solution for −20 km radial position error is presented in Table 5.21 and Figure 5.13. A savings of 84.90 m/s is achieved for this recovery solution, and the maximum maneuver is reduced from 118.37 m/s to 27.69 m/s. In addition, the altitude of the first perigee is raised to an acceptable level by the solution process.

Table 5.18 Two Phasing Loops: Recovery from –30 m/s V_{mag} Error

	Nominal	Straight	Recovery
TTI+18 ΔV (m/s)	—	212.78	—
A_1 ΔV (m/s)	—	—	0.62
P_1 ΔV (m/s)	—	—	46.06
A_2 ΔV (m/s)	—	—	—
P_2 ΔV (m/s)	—	—	17.33
LOI ΔV (m/s)	30.35	36.12	24.80
Total ΔV (m/s)	30.35	248.90	88.81
P_1 Altitude (km)	331.6	-255.3	1128.1
P_2 Altitude (km)	2356.2	1645.4	4174.5

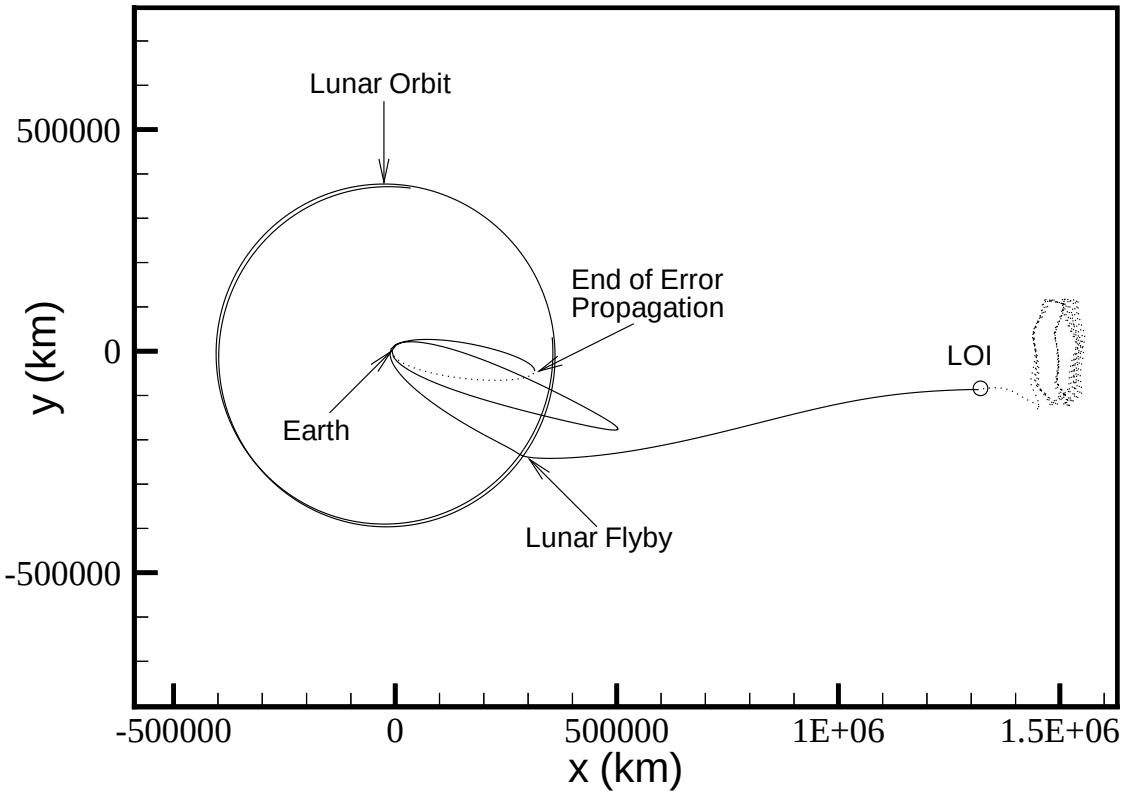

Figure 5.10. Two Loop Recovery for –30 m/s V_{mag} Error

Table 5.19 Two Phasing Loops: Recovery from –40 m/s V_{mag} Error

	Nominal	Straight	Recovery
TTI+18 ΔV (m/s)	—	286.61	—
A_1 ΔV (m/s)	—	—	0.46
P_1 ΔV (m/s)	—	—	59.42
A_2 ΔV (m/s)	—	—	—
P_2 ΔV (m/s)	—	—	20.22
LOI ΔV (m/s)	30.35	38.11	23.74
Total ΔV (m/s)	30.35	324.72	103.84
P_1 Altitude (km)	331.6	-452.5	1231.9
P_2 Altitude (km)	2356.2	1405.5	4372.0

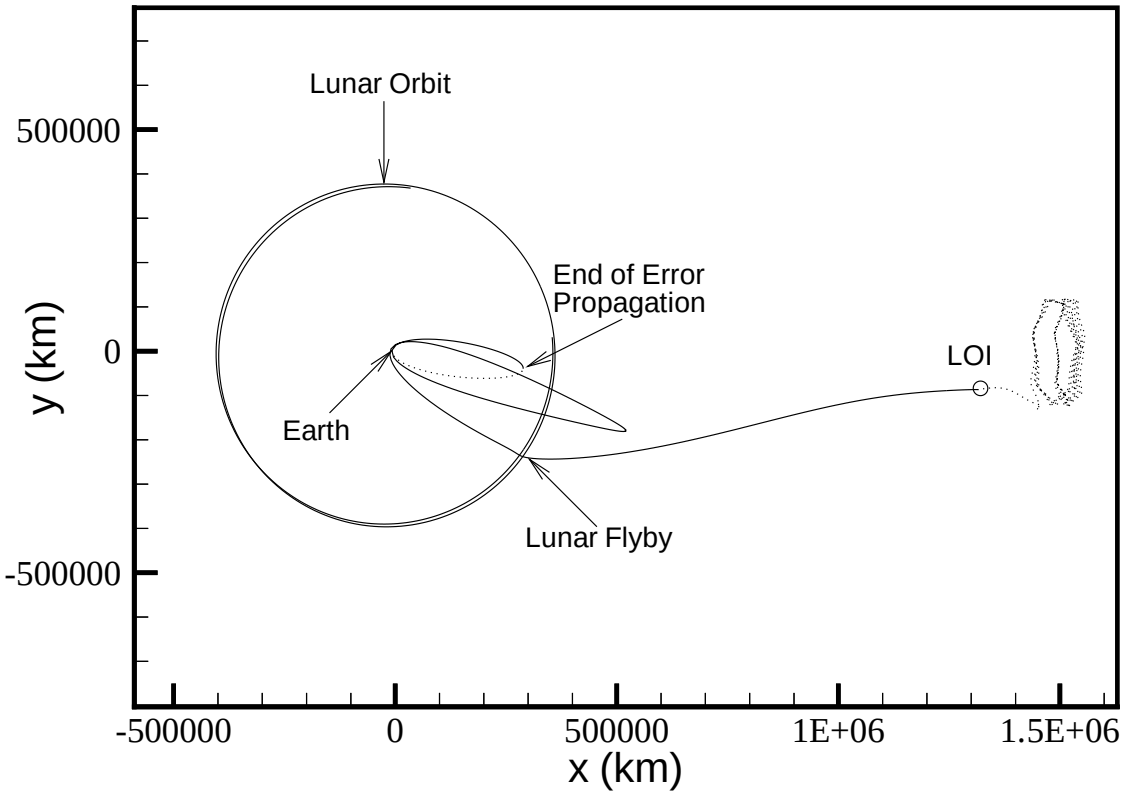

Figure 5.11. Two Loop Recovery for –40 m/s V_{mag} Error

Table 5.20 Two Phasing Loops: Recovery from +20 km $\Delta|\bar{R}|$ Error

	Nominal	Straight	Recovery
TTI+18 ΔV (m/s)	—	113.81	—
A_1 ΔV (m/s)	—	—	2.23
P_1 ΔV (m/s)	—	—	51.92
A_2 ΔV (m/s)	—	—	—
P_2 ΔV (m/s)	—	—	36.50
LOI ΔV (m/s)	30.35	27.14	31.97
Total ΔV (m/s)	30.35	140.95	122.62
P_1 Altitude (km)	331.6	663.5	501.1
P_2 Altitude (km)	2356.2	2756.3	1044.7

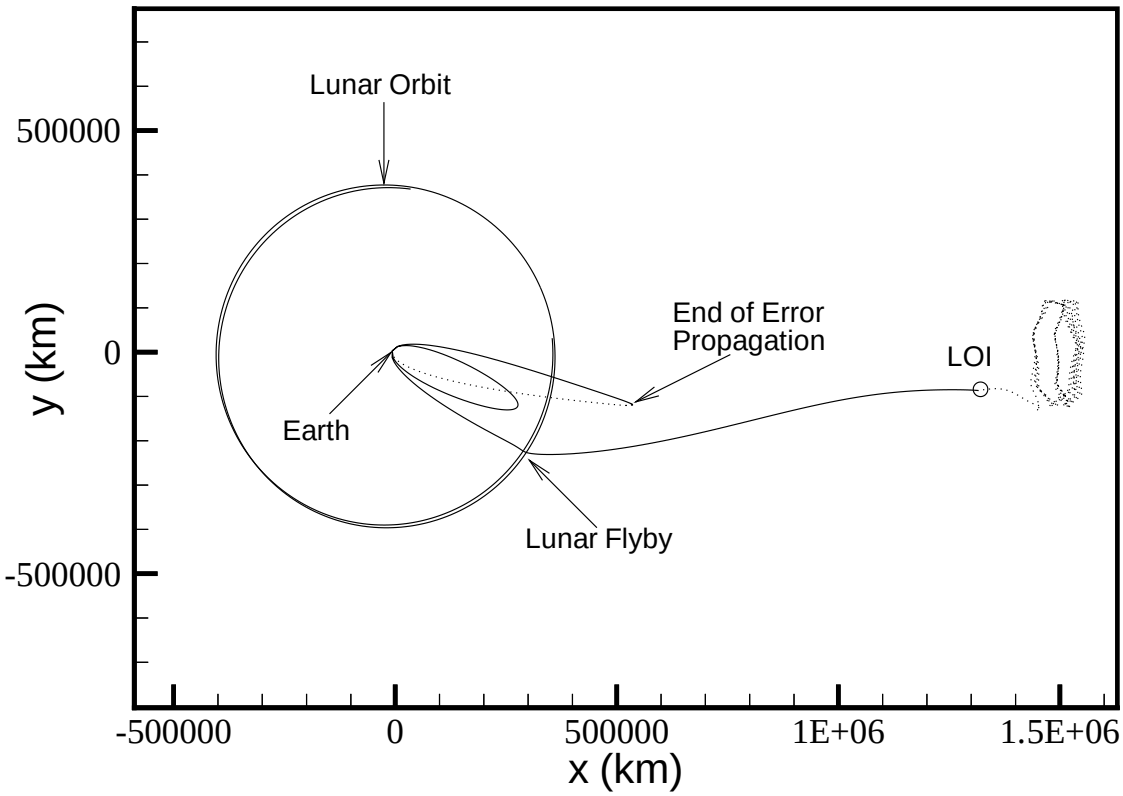

Figure 5.12. Two Loop Recovery for +20 km $\Delta|\bar{R}|$ Error

Table 5.21 Two Phasing Loops: Recovery from –20 km $\Delta|\bar{R}|$ Error

	Nominal	Straight	Recovery
TTI+18 ΔV (m/s)	—	118.37	—
A_1 ΔV (m/s)	—	—	0.49
P_1 ΔV (m/s)	—	—	27.69
A_2 ΔV (m/s)	—	—	—
P_2 ΔV (m/s)	—	—	12.04
LOI ΔV (m/s)	30.35	33.64	26.89
Total ΔV (m/s)	30.35	152.01	67.11
P_1 Altitude (km)	331.6	-4.6	823.6
P_2 Altitude (km)	2356.2	1949.6	3606.0

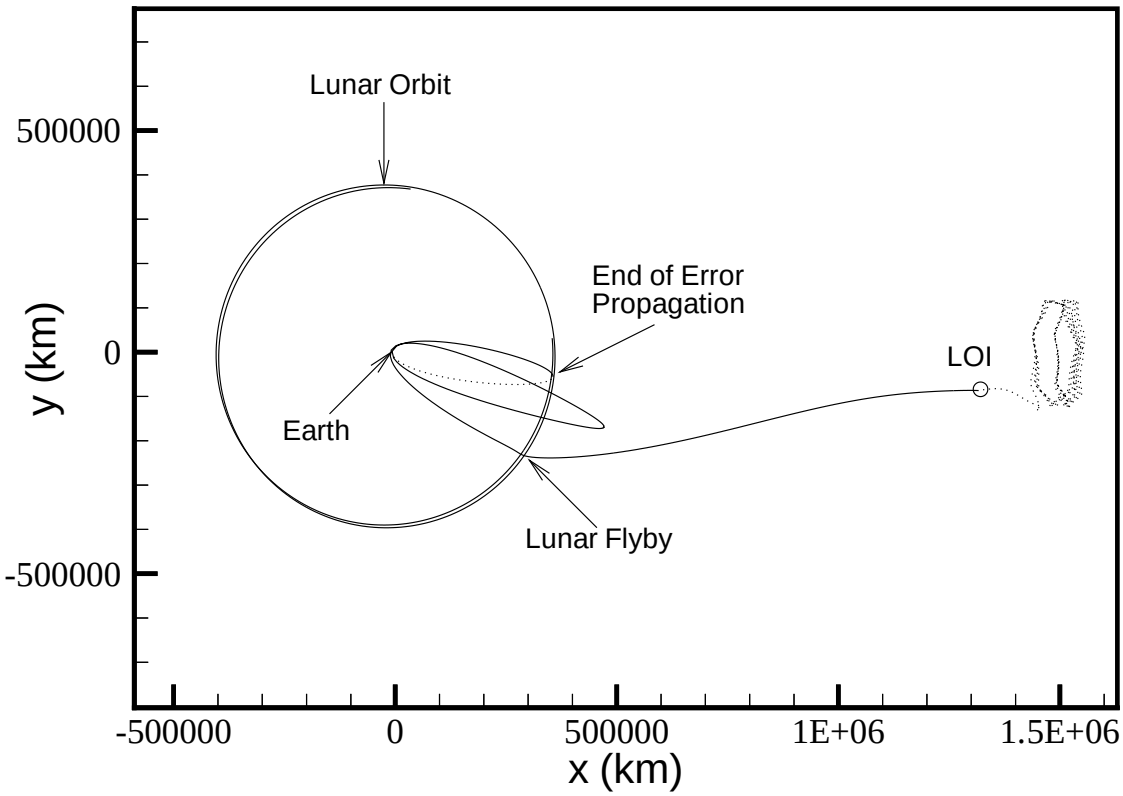

Figure 5.13. Two Loop Recovery for –20 km $\Delta|\bar{R}|$ Error

5.2.2.e Recoveries with a Constraint on Maneuver Magnitude

A slightly modified recovery strategy based on the previous algorithm may also be useful for missions with an upper limit on the size of any one particular maneuver. In this approach, the maximum allowable maneuver is performed at some time shortly after launch in the same direction as that specified by the straight error correction solution at this point. The goal behind this strategy is to correct as much of the trajectory as soon as possible, and then design a recovery to account for the remaining error. As an example, an upper limit of 30 m/s is arbitrarily selected as the maximum allowable maneuver. Three of the example cases (+20, −30, and −40 m/s) from the previous section, with maneuvers that exceed this limit, are selected to test this technique. A maneuver of 30 m/s magnitude is implemented at injection plus 18 hours in the same direction that is computed for the straight correction associated with the given error. The results for the +20 m/s overburn are presented in Table 5.22. This recovery actually presents a lower cost than the straight correction by 22.69 m/s, and thus is considered a feasible recovery. Notice, however, that although the recovery lowers the magnitudes of the two perigee maneuvers, $|\Delta\bar{V}_{P1}|$ is still beyond the maximum limit. This might be rectified by performing the first correction maneuver earlier after injection. The resulting trajectory appears in Figure 5.14. Notice that the period of the first phasing loop is shorter than the previous +20 m/s recovery in Figure 5.6. This is also evidenced by the fact that the second loop has increased in size from the previous solution, indicating that the perigee timing error is not as large for this type of recovery. The results for the −30 m/s underburn using this modified strategy are summarized in Table 5.23 and plotted in Figure 5.15. In this case, the cost of this modified recovery actually increases by 24.04 m/s over the previous recovery solution, while only trimming 5.74 m/s off the maximum maneuver. Similar results are apparent for the −40 m/s case, presented in Table 5.24 and Figure 5.16. For this case, the cost increases by a mere 0.05 m/s over the previous recovery and the maximum maneuver is reduced by only 5.36 m/s. It is concluded, at least for

Table 5.22 Two Phasing Loop Recovery: +20 m/s V_{mag} Error with TTI+18 hr TCM

	Nominal	Straight	Recovery
TTI+18 ΔV (m/s)	—	135.25	30.00
A_1 ΔV (m/s)	—	—	1.43
P_1 ΔV (m/s)	—	—	44.46
A_2 ΔV (m/s)	—	—	1.45
P_2 ΔV (m/s)	—	—	30.55
LOI ΔV (m/s)	30.35	26.64	31.31
Total ΔV (m/s)	30.35	161.89	139.20
P_1 Altitude (km)	331.6	718.4	476.3
P_2 Altitude (km)	2356.2	2822.4	1167.1

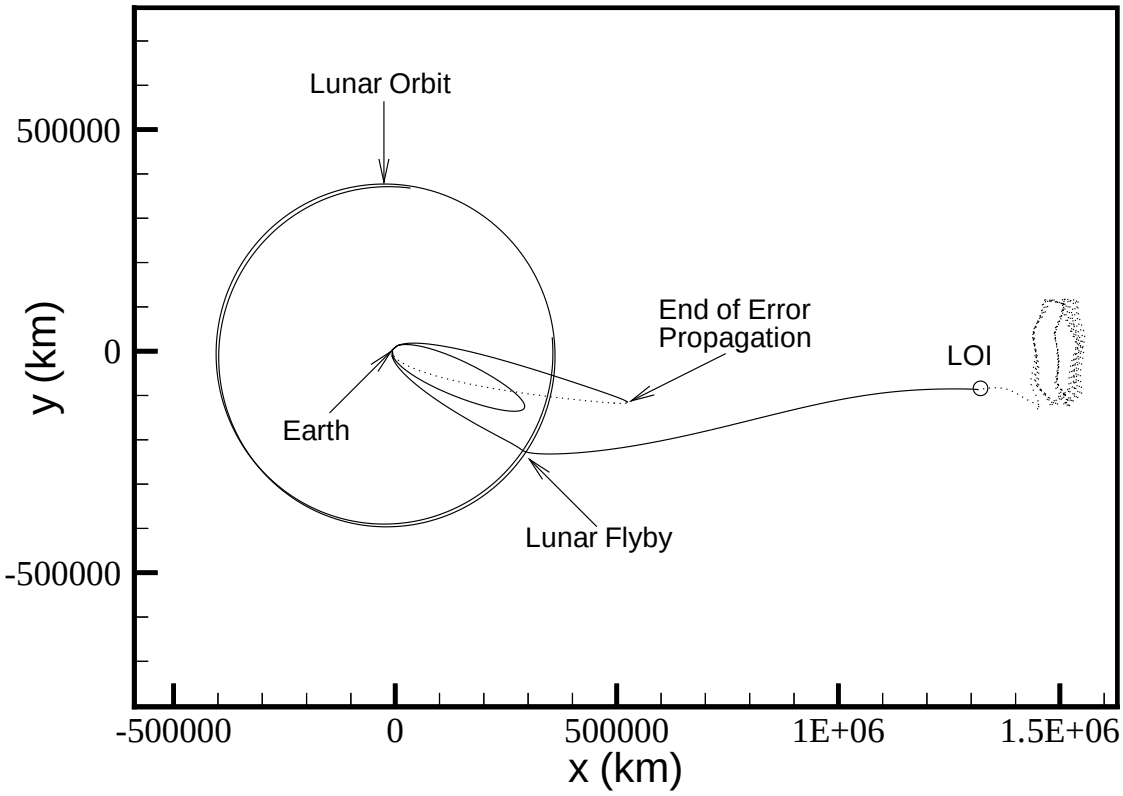

Figure 5.14. Two Loop Recovery for +20 m/s V_{mag} Error with TTI+18 hr TCM

Table 5.23 Two Phasing Loop Recovery: –30 m/s V_{mag} Error with TTI+18 hr TCM

	Nominal	Straight	Recovery
TTI+18 ΔV (m/s)	—	212.78	30.00
A_1 ΔV (m/s)	—	—	0.51
P_1 ΔV (m/s)	—	—	40.32
A_2 ΔV (m/s)	—	—	—
P_2 ΔV (m/s)	—	—	15.84
LOI ΔV (m/s)	30.35	36.12	26.18
Total ΔV (m/s)	30.35	248.90	112.85
P_1 Altitude (km)	331.6	-255.3	973.6
P_2 Altitude (km)	2356.2	1645.4	3931.3

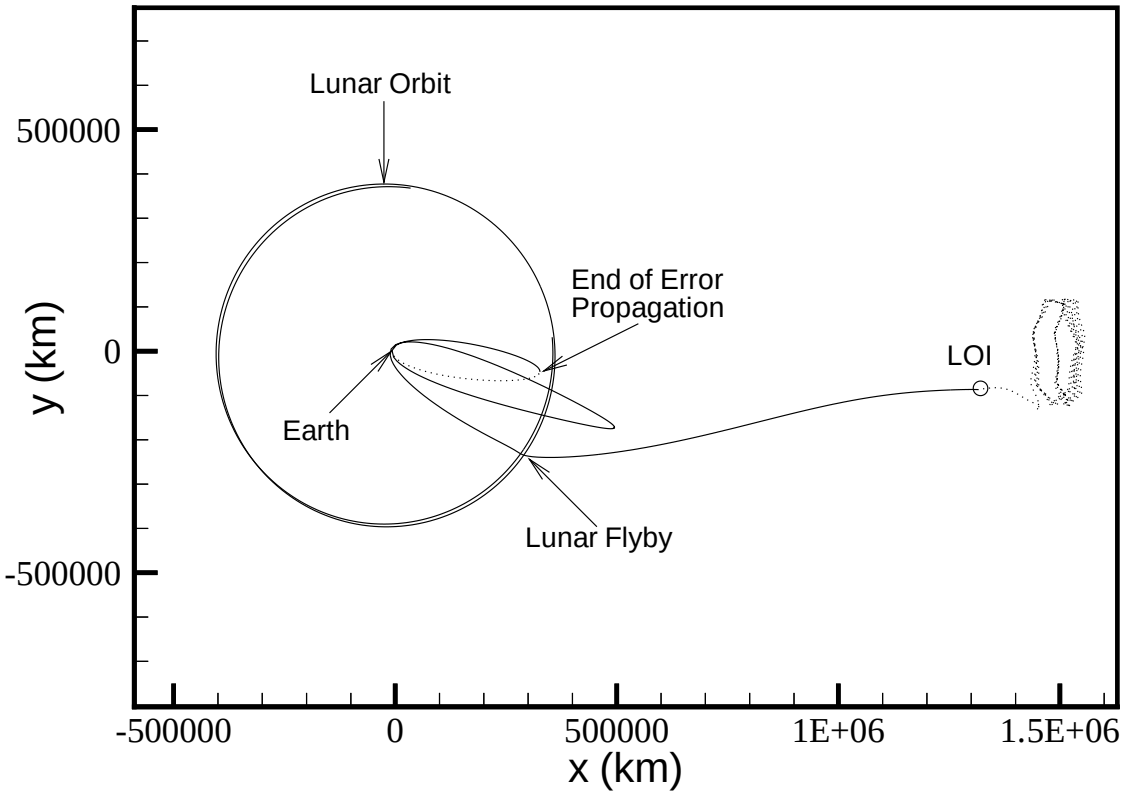

Figure 5.15. Two Loop Recovery for –30 m/s V_{mag} Error with TTI+18 hr TCM

Table 5.24 Two Phasing Loop Recovery: –40 m/s V_{mag} Error with TTI+18 hr TCM

	Nominal	Straight	Recovery
TTI+18 ΔV (m/s)	—	286.61	30.00
A_1 ΔV (m/s)	—	—	0.74
P_1 ΔV (m/s)	—	—	54.06
A_2 ΔV (m/s)	—	—	—
P_2 ΔV (m/s)	—	—	19.09
LOI ΔV (m/s)	30.35	38.11	24.95
Total ΔV (m/s)	30.35	324.72	103.89
P_1 Altitude (km)	331.6	-452.5	1119.5
P_2 Altitude (km)	2356.2	1405.5	4199.5

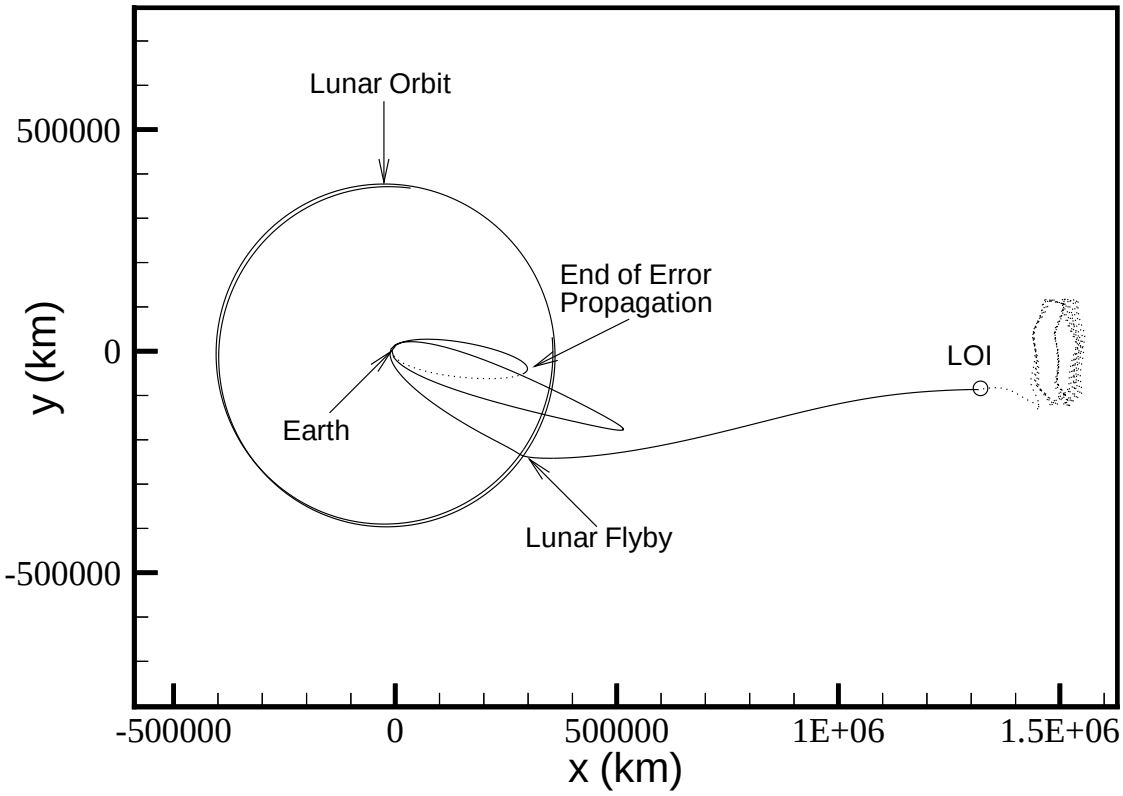

Figure 5.16. Two Loop Recovery for –40 m/s V_{mag} Error with TTI+18 hr TCM

this particular strategy, that the inclusion of a TCM maneuver shortly after launch to reduce some of the error is very beneficial for overburns such as the +20 m/s case, but provides very little improvement for the cases involving large underburns.

5.2.2.f Recovery by Adjusting the Number of Phasing Loops

The final recovery strategy that is investigated for the two loop solution involves very large velocity overburns at injection. In this alternate approach, the two loop solution is reduced to a single, very large phasing loop that passes through perigee at the nominal date/time that corresponds to the final perigee before the lunar encounter. To accomplish this reduction from two loops to one loop, a maneuver at injection plus 18 hours is implemented to modify the period of the phasing loop to about 23.6 days. This is the period of the single phasing loop that will reach the proper perigee timing, regardless of the magnitude of the error at launch. The difference between solutions then lies primarily in the magnitude of the maneuver that is required to change the period of the phasing loop; although small differences do occur in the other maneuvers throughout the solution.

The results for recovery solutions with injection velocity magnitude errors of +20, +30, and +40 m/s are presented in Table 5.25. Note first that the magnitude of the TCM at TTI+18 hours reaches a minimum around the +30 m/s error. This is true because the period of the orbit immediately after the 30 m/s error at injection, but before any maneuver is performed, is 23.0 days; this is already very close to the desired period. Thus, the TCM actually increases the period of the orbit by only about 0.6 days, hence the small magnitude of the maneuver. In contrast, the period of the +20 m/s error solution before any maneuver is 17.8 days, and requires a large TCM maneuver to increase the period. Likewise, the +40 m/s error solution has a period of 31.5 days, and requires a large maneuver to decrease the period to the necessary 23.6 days. Also note that the maneuver implemented at perigee just prior to the lunar encounter (denoted P_2 in the table for consistency with the nominal) is fairly constant across all three solutions. This underscores the fact that the actual

trajectories are very similar. The recovery trajectory for the example with a +20 m/s error appears in Figure 5.17. This plot clearly demonstrates the single large phasing loop used to recover the solution. The other two cases are very similar in appearance.

In summary, three strategies are presented to determine alternative recovery trajectories for a range of errors that are costly to correct using straight error correction. For velocity magnitude errors between −40 and +20 m/s, or for radial position errors in the range between ±20 km, the first approach yields solutions with costs less than the straight correction. For velocity errors greater than +20 m/s, either the modified strategy that includes a TCM shortly after launch, or the two-to-one loop reduction strategy provides feasible recoveries with reasonable costs. These modified strategies can also be applied to larger errors in radial position.

5.2.3 Recoveries for Three Phasing Loops

For two phasing loop solutions, a variety of recovery strategies are available to correct a wide range of errors. However, the addition of a third phasing loop complicates the determination of feasible recovery trajectories. Recall from Section 4.3.4 that the proper phasing of the Moon is crucial in the determination of a nominal three loop solution that does not encounter the Moon prematurely. The baseline three loop solution is designed such that the spacecraft must be located at perigee at the end of the first loop, when the Moon is positioned along the spacecraft line of apsides, near apogee. This phasing must be maintained, within some specified bounds, in any recovery strategy to ensure a solution that is consistent with the nominal, and avoids any large lunar perturbations. Thus, the timing of the first perigee after injection must be preserved, in the same manner as the timing of the first perigee in the single phasing loop discussion, although somewhat less strictly. However, with just one loop between the insertion maneuver and this first perigee, a situation arises similar to that encountered for the single phasing loop. To ensure that the timing requirement for the first perigee is satisfied, a maneuver is required sometime between insertion onto the transfer and the first perigee. Not surprisingly, the cost of this maneuver reflects

Table 5.25 Two Phasing Loop Recovery: 2-to-1 Loop Reduction

	Nominal	+20 m/s	+30 m/s	+40 m/s
TTI+18 ΔV (m/s)	—	55.44	7.42	66.21
A_2 ΔV (m/s)	—	—	—	—
P_2 ΔV (m/s)	—	34.38	34.79	35.35
LOI ΔV (m/s)	30.35	28.14	24.52	20.04
Total ΔV (m/s)	30.35	117.96	66.73	121.60
P_2 Altitude (km)	2356.2	4231.7	4003.2	3494.8

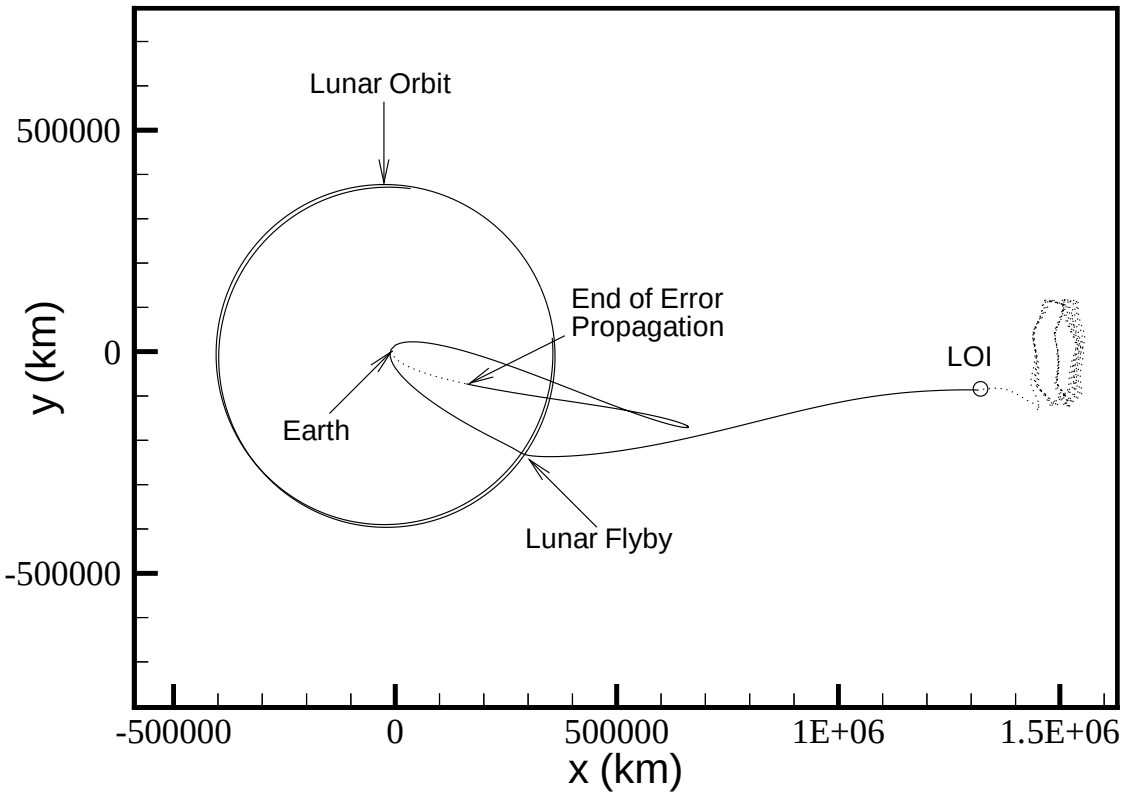

Figure 5.17. Two Loop Recovery of +20 m/s V_{mag} Error: Reduction to One Loop

the same trend as that in Figure 5.3 for the single loop case, where the maneuver cost increases as the time past launch increases. Again, it is concluded that, over the range of errors examined here, types of recoveries similar to those exploited in the two loop case are unlikely to produce feasible recoveries with costs lower than the straight error correction; this conclusion is due to these timing constraints.

Unlike the one phasing loop case, though, there are exceptions. Small errors in the transfer insertion maneuver do alter the timing of the first perigee in a manner similar to the single loop results in Table 5.11. However, due to the precise design of the nominal solution, and the availability of two additional phasing loops, it is possible to determine recoveries in the three loop case for velocity magnitude errors of less than 5 m/s. The recovery solution for a +5 m/s velocity magnitude error is summarized in Table 5.26. This solution uses relatively small maneuvers at the first apogee and the first perigee that permit the spacecraft to pass through the difficult A_2 apogee region without large changes in the trajectory. A two loop singular Lambert conic is then patched between the actual P_1 state (at the end of the propagation of the injection error) and the nominal P_3 state just prior to the lunar encounter. This results in maneuvers at the third apogee (A_3) and the last perigee (P_3) to set up the desired lunar encounter. Notice that this recovery does result in a cost that is 18.27 m/s lower than the corresponding straight correction, and now contains four maneuvers rather than the two or three maneuvers necessary in the two phasing loop case. Also notice that the second perigee pass (P_2) is very close to the Earth and lower than the previous perigee. This indicates that although a viable solution has been determined, the Moon is still contributing a significant perturbation. The resulting trajectory is plotted in Figure 5.18. Note that the second and third loops are slightly smaller than the first loop, indicating the compensation required for the timing error after the first perigee.

With the same strategy, a similar recovery is determined for a -5 m/s velocity magnitude error. The results from this case are summarized in Table 5.27 and the trajectory is plotted in Figure 5.19. The recovery solution has a cost just 6.70 m/s

Table 5.26 Three Phasing Loops: Recovery from +5 m/s V_{mag} Error

	Nominal	Straight	Recovery
TTI+18 ΔV (m/s)	—	34.22	—
A_1 ΔV (m/s)	—	—	1.98
P_1 ΔV (m/s)	—	—	5.54
A_3 ΔV (m/s)	—	—	1.69
P_3 ΔV (m/s)	—	—	3.12
LOI ΔV (m/s)	32.75	31.81	35.44
Total ΔV (m/s)	32.75	66.03	47.76
P_1 Altitude (km)	696.1	806.5	334.9
P_2 Altitude (km)	1740.8	1856.0	258.8
P_3 Altitude (km)	4039.7	4178.6	2189.0

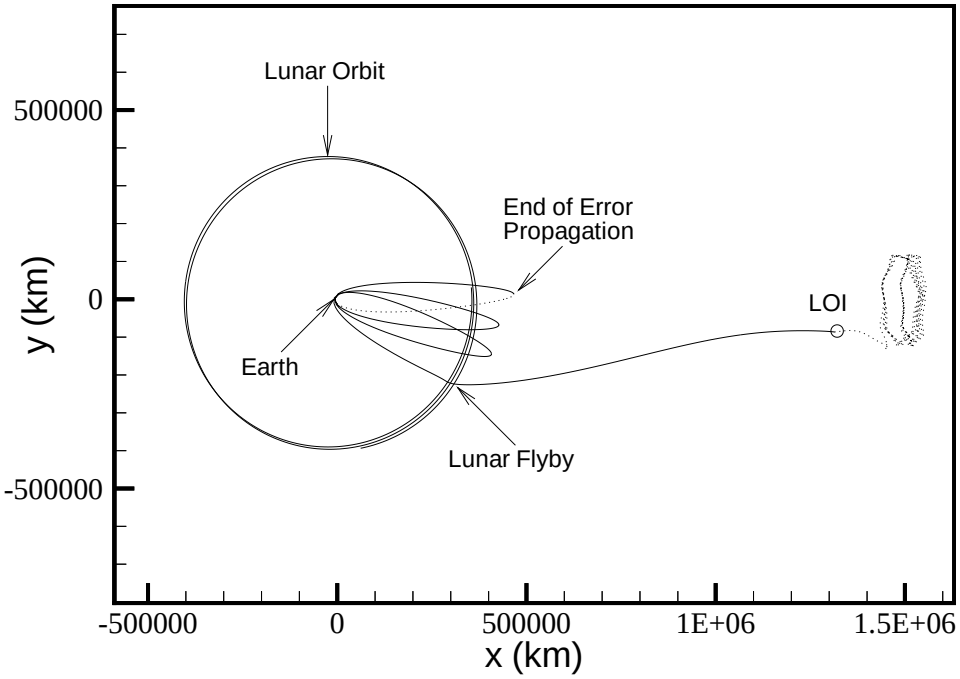

Figure 5.18. Three Loop Recovery for +5 m/s V_{mag} Error

Table 5.27 Three Phasing Loops: Recovery from –5 m/s V_{mag} Error

	Nominal	Straight	Recovery
TTI+18 ΔV (m/s)	—	34.54	—
A_1 ΔV (m/s)	—	—	0.23
P_1 ΔV (m/s)	—	—	3.88
A_3 ΔV (m/s)	—	—	2.42
P_3 ΔV (m/s)	—	—	1.71
LOI ΔV (m/s)	32.75	33.70	31.22
Total ΔV (m/s)	32.75	68.25	39.45
P_1 Altitude (km)	696.1	585.5	826.6
P_2 Altitude (km)	1740.8	1625.4	4862.3
P_3 Altitude (km)	4039.7	3900.5	7631.1

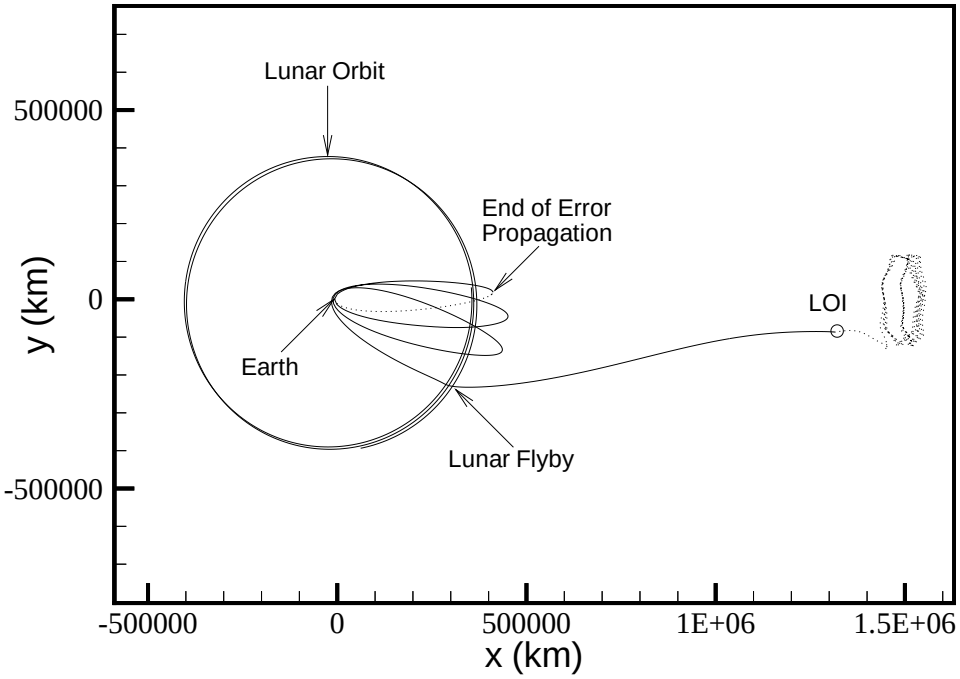

Figure 5.19. Three Loop Recovery for –5 m/s V_{mag} Error

above the nominal and 28.80 m/s less than the straight correction. Upon examination of the solution, this low cost is attributed again to lunar perturbations, although this time to the benefit of the solution. No other recoveries are achieved for errors greater than ± 5 m/s, due to lunar perturbations caused by the timing issues.

The possibility does exist to utilize this "unwanted" lunar encounter near apogee on the second loop to determine a possible recovery strategy. The use of the Moon in the design of recovery solutions will be explored later in relation to all of the phasing loop solutions under consideration.

5.2.4 Recoveries for Four Phasing Loops

As might be expected from the relationship between the one and two loop solutions, the addition of another phasing loop to the three loop case again opens up the possibilities for feasible recoveries over a broad range of errors. The lunar phasing issues described in the three loop case are still relevant for the four loop solution. Now, however, there are two phasing loops between transfer insertion and the crucial perigee (now designated perigee P_2 at the end of the second loop). This allows the period of the second loop to be altered to compensate for timing errors at the first perigee, and thus target a specific date for the second perigee. By constraining the P_2 date to be the same as that along nominal solution, the Moon and spacecraft are again properly phased to avoid any undesired encounters.

5.2.4.a Adding Multiple Correction Maneuvers

A recovery strategy similar to the original two loop procedure has been determined that is based on preserving the date of the second perigee. First, the insertion state with errors is propagated to the first apogee state A_1, since the nominal four loop solution contains a deterministic maneuver at this point. For consistency, the nominal apogee maneuver is applied, and the trajectory is then propagated to the first perigee P_1. Next, a singular Lambert conic is determined between the current state at P_1 and the desired nominal date corresponding to perigee P_2. This conic arc approximation

alters the period of the second loop to compensate for the timing errors at P_1, while maintaining the date at P_2. The intermediate multi-conic step is applied to this conic segment to allow a numerically integrated solution to be determined for the second phasing loop. In the process of developing this piece of the recovery, a maneuver is allowed at the second apogee (A_2) to aid in convergence of the solution, and to minimize the cost of any plane changes determined by the algorithm. As in the two loop case, the time of flight from transfer insertion to first perigee is adjusted to minimize the maneuver magnitude at P_1 (at the expense of some drift away from perigee). At this point, there are now deterministic maneuvers present at A_1, P_1, and A_2 to achieve the desired timing for the second perigee. Finally then, a solution from P_2 to LOI (or the end of the trajectory) is determined based on the nominal solution, including the last two phasing loops and the transfer out to the manifold state. This last portion of the recovery introduces a final phasing loop maneuver into the solution at perigee P_2. Note that by ensuring the proper timing for P_2, and by using the nominal solution for the last two phasing loops as an initial guess, the critical timing of the final perigee before the lunar encounter is also preserved. The entire trajectory from transfer insertion to LOI is then collected into a single end-to-end solution, with the end of the error propagation at the first apogee; this solution includes all deterministic maneuvers designed from the recovery algorithm.

5.2.4.b Recoveries from Four Loop Overburn Errors

Since the recoveries for radial position errors have been shown to be extremely similar in nature to those for errors in velocity magnitude, only deviations in velocity magnitude are examined for the four loop case. The solution for a velocity magnitude error of +5 m/s is summarized in Table 5.28. The recovery solution yields a savings of 20.53 m/s over the straight error correction. (Note that the apogee A_1 maneuver in the straight correction is increased by 3 m/s over the nominal to compensate for an unacceptable P_1 perigee altitude.) The resulting trajectory is shown in Figure 5.20. Since the period of the first loop is increased by the error, the second loop is shorter

Table 5.28 Four Phasing Loops: Recovery from +5 m/s V_{mag} Error

	Nominal	Straight	Recovery
TTI+18 ΔV (m/s)	—	35.72	—
A_1 ΔV (m/s)	23.00	26.00	22.75
P_1 ΔV (m/s)	—	—	9.97
A_2 ΔV (m/s)	—	—	3.82
P_2 ΔV (m/s)	—	—	5.00
LOI ΔV (m/s)	32.19	32.41	32.06
Total ΔV (m/s)	55.19	94.13	73.60
P_1 Altitude (km)	226.9	217.4	217.8
P_2 Altitude (km)	444.3	427.8	269.7
P_3 Altitude (km)	838.4	813.9	507.0
P_4 Altitude (km)	2948.4	2914.9	2549.3

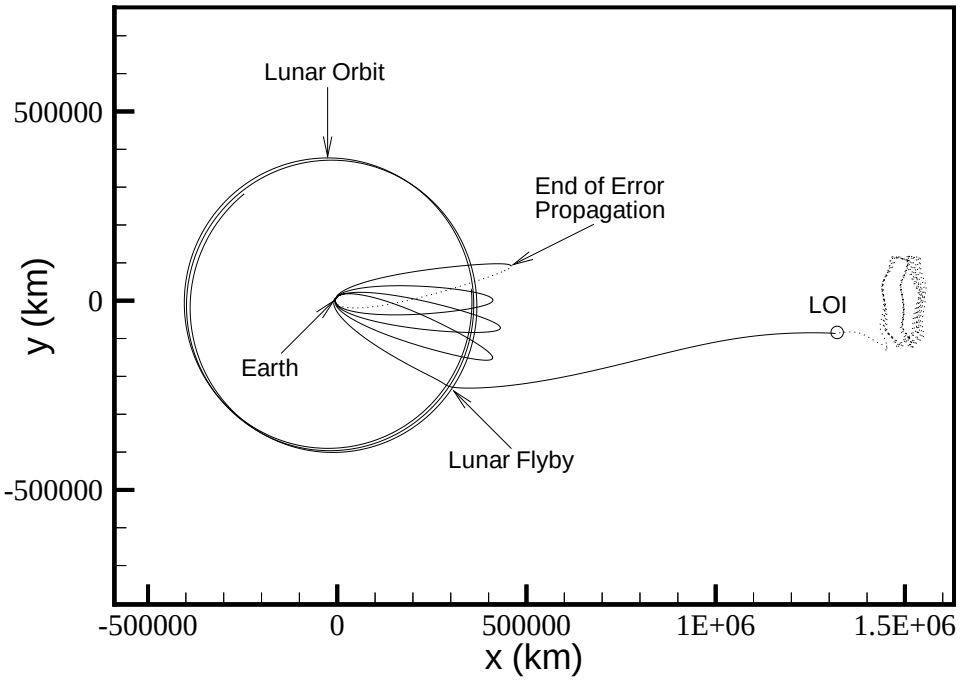

Figure 5.20. Four Loop Recovery for +5 m/s V_{mag} Error

to maintain the desired P_2 date. The final two loops are similar to the nominal solution in order to preserve the date of the final perigee before the lunar encounter. The solution for a +10 m/s error is detailed in Table 5.29 and shown in Figure 5.21. For this case, the recovery produces a savings of 21.84 m/s over straight correction. Note that this recovery strategy tends to lower the altitude of the second perigee. This is primarily due to some minor lunar perturbations and must be monitored to ensure acceptable clearance at Earth close approach. Results for a +20 m/s overburn are presented in Table 5.30 and Figure 5.22. For this case, the recovery solution is 10.14 m/s more expensive than the straight correction, similar to the result seen for the +20 m/s two loop recovery; the maximum maneuver is also decreased by 55.77 m/s using this recovery strategy.

5.2.4.c Recoveries from Four Loop Underburn Errors

From the discussion of the two loop recoveries, it is no surprise that this strategy produces greater savings for velocity magnitude underburns at transfer trajectory insertion. The solution for a −5 m/s underburn is summarized in Table 5.31 and the trajectory appears in Figure 5.23. This recovery produces a reduction in cost of 14.15 m/s from the straight correction at TTI plus 18 hours. The first loop is now shorter in duration than the nominal, necessitating a larger second loop. The results for a −10 m/s underburn are presented in Table 5.32 and Figure 5.24. This case yields a savings of 46.26 m/s and reduces the maximum non-LOI maneuver to 22.91 m/s at the A_1 apogee location. Note that, as the size of the underburn increases, this A_1 maneuver is also increasing for the straight correction solution. This increase in cost is necessary to keep the P_1 altitude acceptable. The recovery solution, however, maintains roughly the same A_1 maneuver as designed in the nominal solution; this is an added benefit of utilizing this type of recovery strategy. The same trend continues for a −20 m/s underburn, presented in Table 5.33 and Figure 5.25. This recovery has a savings of 103.12 m/s over the straight correction solution. Furthermore, the maximum maneuver is reduced by 113.35 m/s using this strategy. The solution for

Table 5.29 Four Phasing Loops: Recovery from +10 m/s V_{mag} Error

	Nominal	Straight	Recovery
TTI+18 ΔV (m/s)	—	67.84	—
A_1 ΔV (m/s)	23.00	22.99	23.05
P_1 ΔV (m/s)	—	—	23.29
A_2 ΔV (m/s)	—	—	8.00
P_2 ΔV (m/s)	—	—	13.38
LOI ΔV (m/s)	32.19	30.23	31.50
Total ΔV (m/s)	55.19	121.06	99.22
P_1 Altitude (km)	226.9	424.1	270.5
P_2 Altitude (km)	444.3	666.4	209.8
P_3 Altitude (km)	838.4	1075.6	372.6
P_4 Altitude (km)	2948.4	3234.3	2386.8

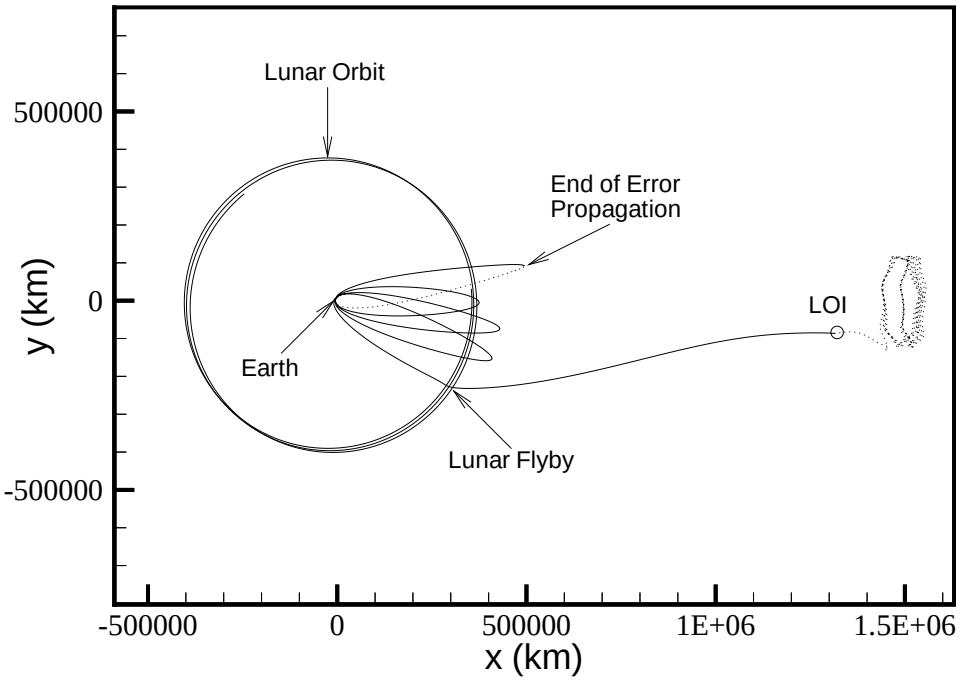

Figure 5.21. Four Loop Recovery for +10 m/s V_{mag} Error

Table 5.30 Four Phasing Loops: Recovery from +20 m/s V_{mag} Error

	Nominal	Straight	Recovery
TTI+18 ΔV (m/s)	—	134.46	—
A_1 ΔV (m/s)	23.00	22.98	23.05
P_1 ΔV (m/s)	—	—	78.69
A_2 ΔV (m/s)	—	—	10.49
P_2 ΔV (m/s)	—	—	55.30
LOI ΔV (m/s)	32.19	28.30	28.35
Total ΔV (m/s)	55.19	185.74	195.88
P_1 Altitude (km)	226.9	620.5	902.4
P_2 Altitude (km)	444.3	887.9	336.8
P_3 Altitude (km)	838.4	1312.5	410.1
P_4 Altitude (km)	2948.4	3519.3	2431.1

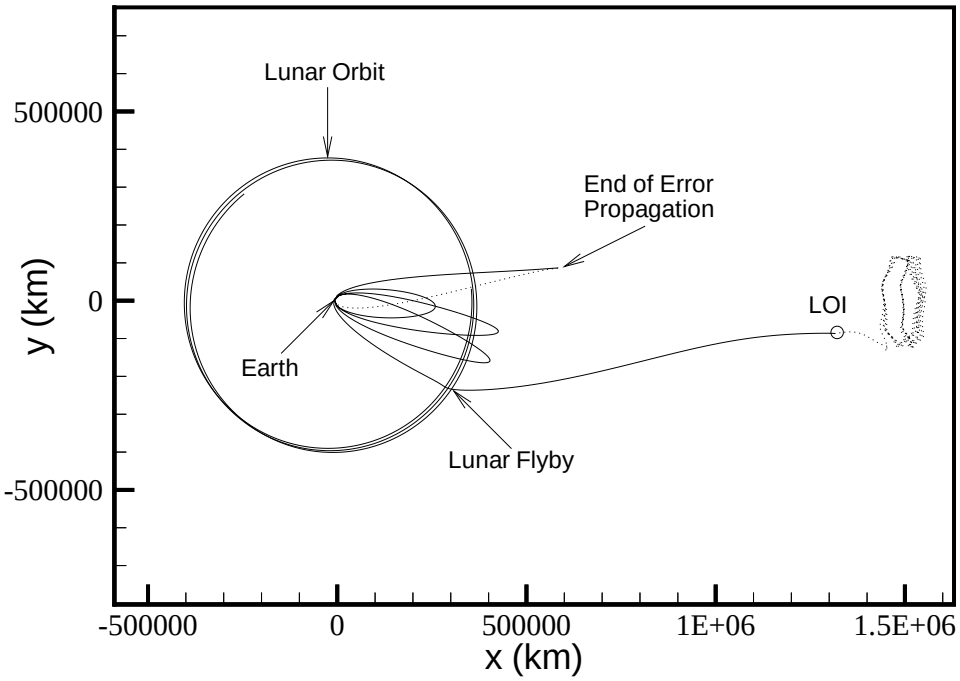

Figure 5.22. Four Loop Recovery for +20 m/s V_{mag} Error

Table 5.31 Four Phasing Loops: Recovery from –5 m/s V_{mag} Error

	Nominal	Straight	Recovery
TTI+18 ΔV (m/s)	—	35.72	—
A_1 ΔV (m/s)	23.00	26.00	22.84
P_1 ΔV (m/s)	—	—	9.49
A_2 ΔV (m/s)	—	—	4.54
P_2 ΔV (m/s)	—	—	9.56
LOI ΔV (m/s)	32.19	32.41	32.75
Total ΔV (m/s)	55.19	94.13	79.18
P_1 Altitude (km)	226.9	217.4	311.9
P_2 Altitude (km)	444.3	427.8	332.0
P_3 Altitude (km)	838.4	813.9	676.2
P_4 Altitude (km)	2948.4	2914.9	2753.3

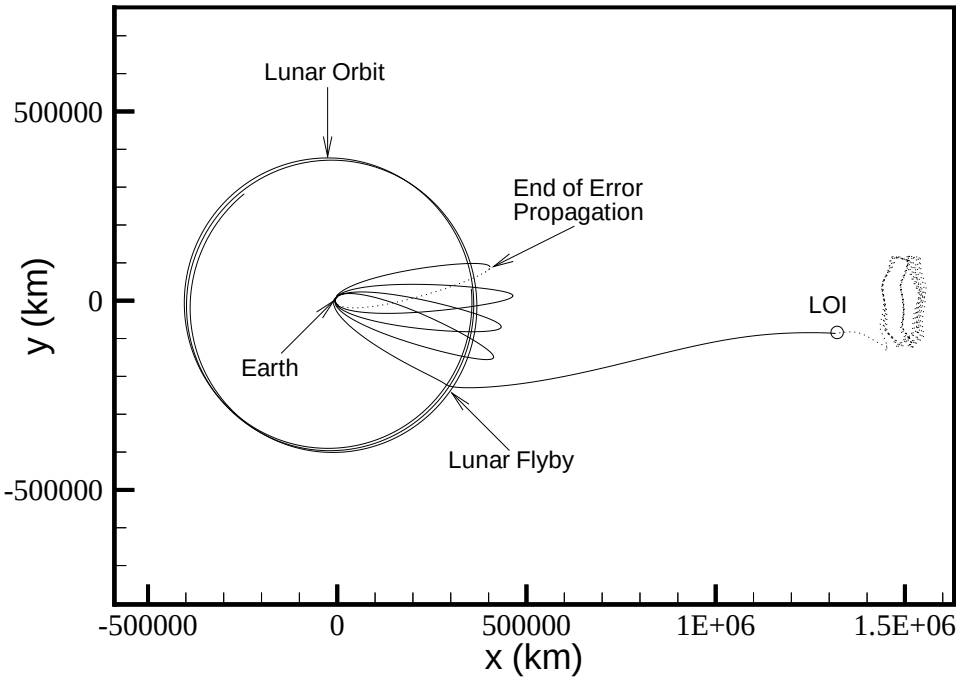

Figure 5.23. Four Loop Recovery for –5 m/s V_{mag} Error

Table 5.32 Four Phasing Loops: Recovery from –10 m/s V_{mag} Error

	Nominal	Straight	Recovery
TTI+18 ΔV (m/s)	—	72.31	—
A_1 ΔV (m/s)	23.00	30.00	22.91
P_1 ΔV (m/s)	—	—	17.50
A_2 ΔV (m/s)	—	—	6.95
P_2 ΔV (m/s)	—	—	8.03
LOI ΔV (m/s)	32.19	32.36	33.02
Total ΔV (m/s)	55.19	134.67	88.41
P_1 Altitude (km)	226.9	240.2	392.8
P_2 Altitude (km)	444.3	445.3	329.0
P_3 Altitude (km)	838.4	823.3	694.4
P_4 Altitude (km)	2948.4	2920.3	2774.5

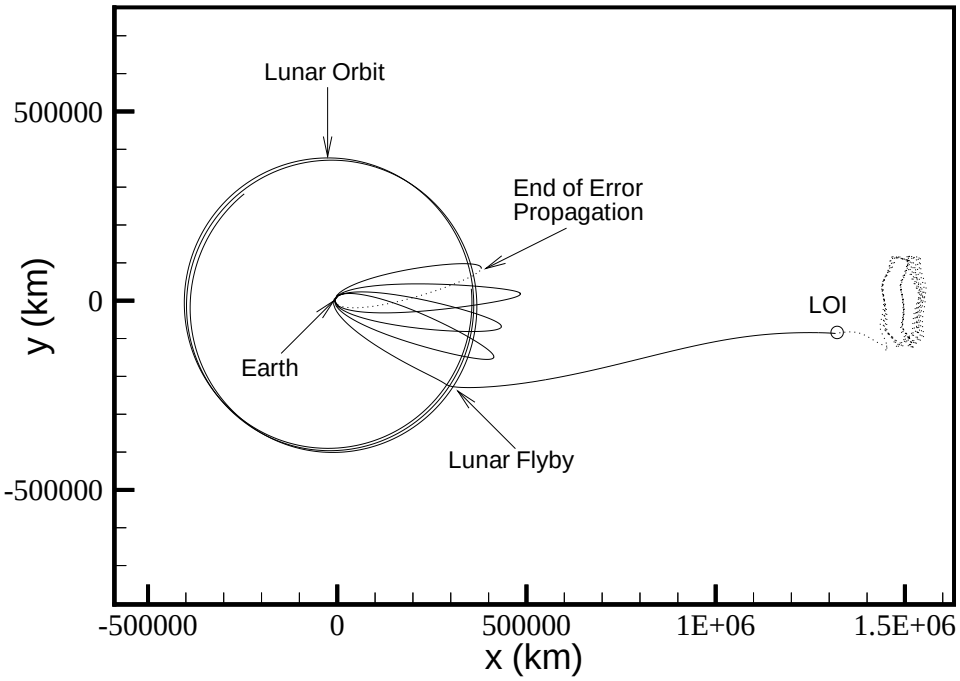

Figure 5.24. Four Loop Recovery for –10 m/s V_{mag} Error

Table 5.33 Four Phasing Loops: Recovery from –20 m/s V_{mag} Error

	Nominal	Straight	Recovery
TTI+18 ΔV (m/s)	—	145.42	—
A_1 ΔV (m/s)	23.00	36.00	22.85
P_1 ΔV (m/s)	—	—	32.07
A_2 ΔV (m/s)	—	—	10.21
P_2 ΔV (m/s)	—	—	12.96
LOI ΔV (m/s)	32.19	32.80	33.01
Total ΔV (m/s)	55.19	214.22	111.10
P_1 Altitude (km)	226.9	229.3	588.4
P_2 Altitude (km)	444.3	419.8	330.1
P_3 Altitude (km)	838.4	782.0	696.5
P_4 Altitude (km)	2948.4	2860.5	2777.4

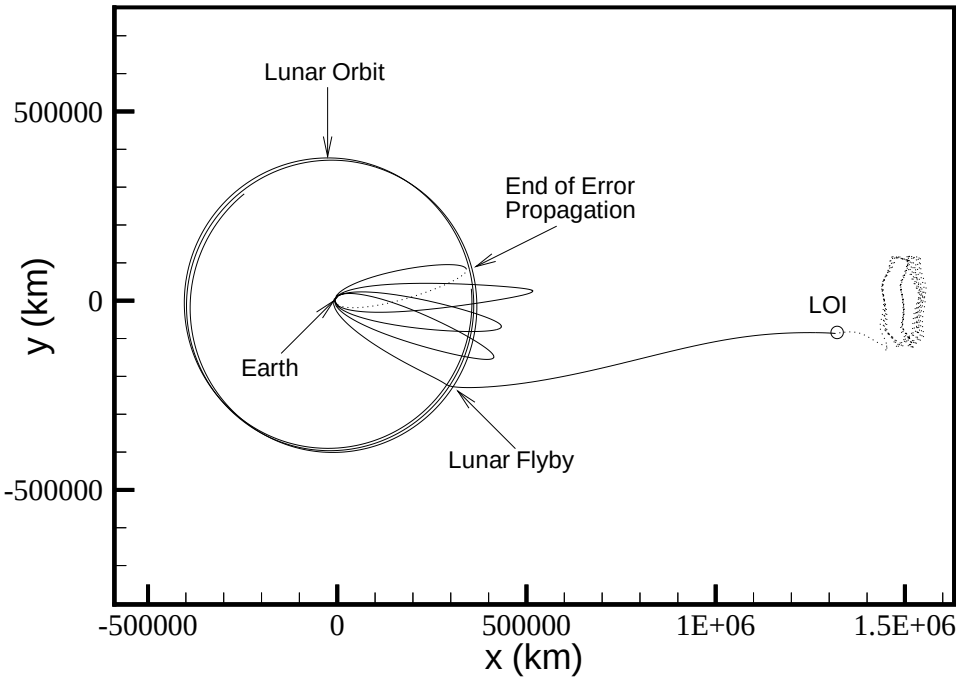

Figure 5.25. Four Loop Recovery for –20 m/s V_{mag} Error

a -30 m/s velocity magnitude error is tabulated in Table 5.34 and the resulting trajectory is plotted in Figure 5.26. The straight correction is clearly unreasonable, while this new solution has a savings in cost of 190.55 m/s, as well as reducing the maximum maneuver to only 45.68 m/s. Finally, for completeness, the -40 m/s underburn is presented in Table 5.35 and Figure 5.27. This recovery has a savings of 234.80 m/s over the impractical straight correction, and the maximum maneuver is still only 58.68 m/s. Clearly, this particular strategy for recovery produces very reasonable solutions over a range of errors and is consistent with the two loop recovery solutions.

5.2.4.d Recovery by Reducing the Number of Phasing Loops

The similarities between this recovery strategy and the corresponding two loop cases also apply to the two modified strategies presented in Sections 5.2.2.e and 5.2.2.f, with similar results. As an example, consider the approach that eliminates one of the phasing loops in the recovery. As before, a maneuver is implemented at insertion plus 18 hours to increase the period of the first loop, such that the second phasing loop is eliminated. Now, the first perigee after insertion is targeted as the critical P_2 date, obtained from the nominal trajectory. The remainder of the nominal path beyond P_2 is then employed to construct the portion of the recovery from P_2 to LOI. The results from application of this method are presented in Table 5.36 for a $+20$ m/s overburn. This reduction to three loops produces a solution with a savings of 60.59 m/s over straight correction, and more importantly presents a feasible recovery, where the first strategy did not. (Note that the first perigee is still denoted P_2 for consistency with the other solutions.) The resulting three loop solution appears in Figure 5.28. The injection error is propagated to apogee A_1 (including the maneuver at TTI+18 hours) in order to aid in the convergence, and to help maintain an acceptable P_2 altitude. Similar results are available for overburns greater than $+20$ m/s as well.

In conclusion, the four phasing loop trajectory presents the same variety of recovery strategies as those determined for the two loop solutions, depending upon the

Table 5.34 Four Phasing Loops: Recovery from –30 m/s V_{mag} Error

	Nominal	Straight	Recovery
TTI+18 ΔV (m/s)	—	220.48	—
A_1 ΔV (m/s)	23.00	43.00	22.79
P_1 ΔV (m/s)	—	—	45.68
A_2 ΔV (m/s)	—	—	11.85
P_2 ΔV (m/s)	—	—	15.54
LOI ΔV (m/s)	32.19	32.98	32.84
Total ΔV (m/s)	55.19	296.46	105.91
P_1 Altitude (km)	226.9	256.7	758.0
P_2 Altitude (km)	444.3	434.0	319.1
P_3 Altitude (km)	838.4	780.3	659.7
P_4 Altitude (km)	2948.4	2844.9	2733.3

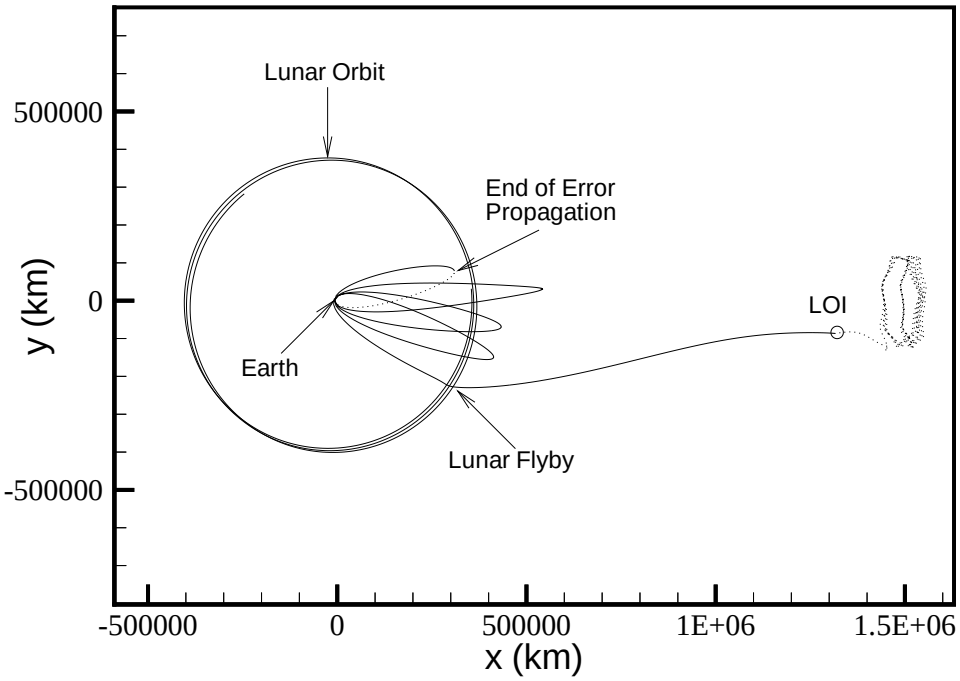

Figure 5.26. Four Loop Recovery for –30 m/s V_{mag} Error

Table 5.35 Four Phasing Loops: Recovery from –40 m/s V_{mag} Error

	Nominal	Straight	Recovery
TTI+18 ΔV (m/s)	—	295.98	—
A_1 ΔV (m/s)	23.00	48.00	22.63
P_1 ΔV (m/s)	—	—	58.68
A_2 ΔV (m/s)	—	—	12.00
P_2 ΔV (m/s)	—	—	18.11
LOI ΔV (m/s)	32.19	33.71	32.47
Total ΔV (m/s)	55.19	378.69	143.89
P_1 Altitude (km)	226.9	221.9	856.2
P_2 Altitude (km)	444.3	382.3	326.3
P_3 Altitude (km)	838.4	712.9	638.9
P_4 Altitude (km)	2948.4	2752.9	2708.1

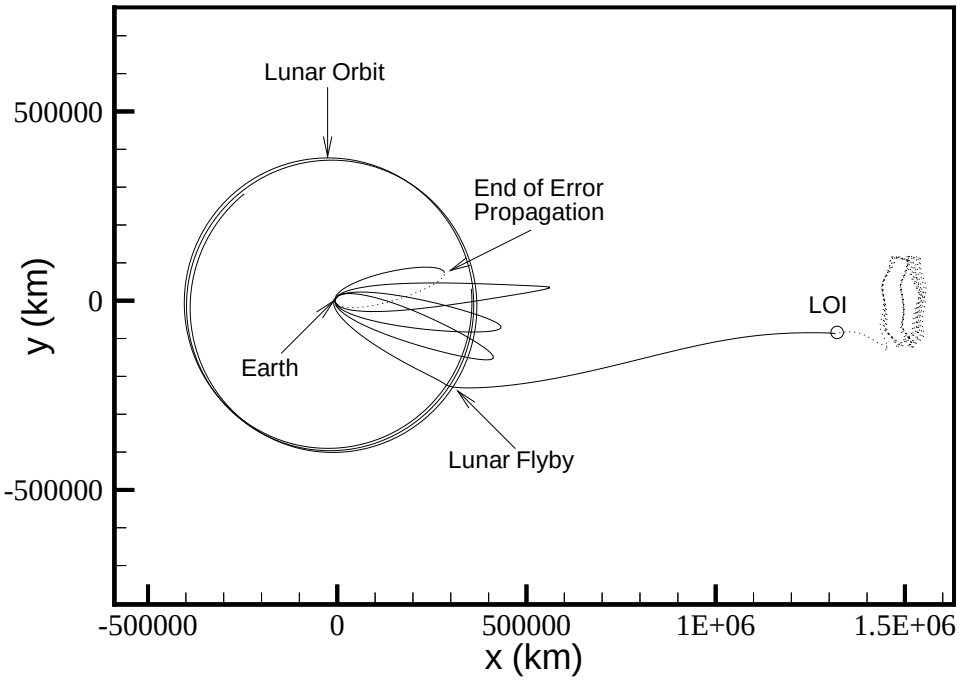

Figure 5.27. Four Loop Recovery for –40 m/s V_{mag} Error

Table 5.36 Four Phasing Loops: 4-to-3 Loop Recovery for +20 m/s V_{mag} Error

	Nominal	Straight	Recovery 1	4 to 3 Loops
TTI+18 ΔV (m/s)	—	134.46	—	50.15
A_1 ΔV (m/s)	23.00	22.98	23.05	12.87
P_1 ΔV (m/s)	—	—	78.69	—
A_2 ΔV (m/s)	—	—	10.49	—
P_2 ΔV (m/s)	—	—	55.30	29.68
LOI ΔV (m/s)	32.19	28.30	28.35	32.45
Total ΔV (m/s)	55.19	185.74	195.88	125.15
P_1 Altitude (km)	226.9	620.5	902.4	—
P_2 Altitude (km)	444.3	887.9	336.8	395.6
P_3 Altitude (km)	838.4	1312.5	410.1	762.3
P_4 Altitude (km)	2948.4	3519.3	2431.1	2854.7

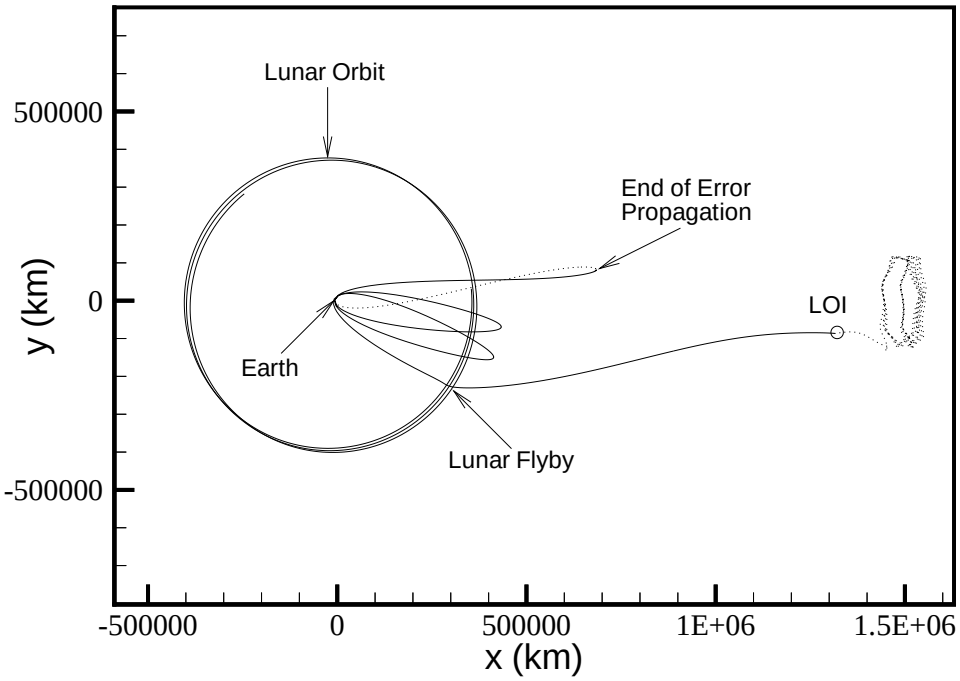

Figure 5.28. Four Loop Recovery of +20 m/s V_{mag} Error: Reduction to Three Loops

type and magnitude of the injection error. A number of feasible recoveries have been designed by targeting the nominal time of the second perigee during the solution process. This process again takes advantage of the automated nature of the procedure, once an initial approximation to the recovery is determined. It is also noted that, similar to the three loop case, the possibility exists to develop a recovery strategy that includes additional lunar encounters to achieve the desired design goals for the transfer. The development of these types of strategies is presented next.

5.3 Recoveries Using Additional Lunar Gravity Assists

The previous sections detail strategies that can be employed to recover from various types of launch or injection errors. All of these recoveries assume a solution that is consistent with the nominal; that is, one that maintains the same lunar encounter and inserts onto the same Lissajous orbit. This is not necessarily a poor assumption, since many feasible recoveries are available for solutions with two, four, and sometimes even three phasing loops. However, this assumption excludes recoveries for most errors in the case with three phasing loops, and all one loop solutions, since these trajectories do not generally provide a viable means to recover from the timing errors at critical points along the nominal path. If, however, a different lunar encounter and a new Lissajous orbit are permitted, then a limited number of additional feasible recoveries may become available. Specifically, strategies are sought that utilize a series of lunar encounters to insert onto a new Lissajous orbit. Note that this necessitates the design of a different Lissajous orbit, a step that is not required by the previous strategies.

The basis for this series of lunar gravity assists lies in the phasing of the Moon and spacecraft, similar to the timing issues discussed for the three loop case. Previously, solutions that avoid any encounters with the Moon prior to the desired lunar gravity assist were sought. Now, however, it is desired to utilize a lunar encounter during the phasing loop portion of the trajectory to initiate the recovery strategy. There are only a limited number of cases, though, that permit this type of recovery. For each type of phasing loop trajectory that is considered (with 1, 2, 3, and 4 loops),

two additional lunar encounters are possible other than the nominal lunar flyby. One encounter occurs over a small range of overburn errors, while the other can occur for some set of underburns.

The eight possibilities for additional lunar encounters are presented in Figure 5.29. For each of the cases, the nominal injection state, including errors, is numerically propagated using a four body model up to the lunar encounter. The trajectory in Case (A) represents a one loop arc for a +27.0 m/s overburn in velocity magnitude. The path includes a descending encounter with the Moon after passing through apogee, but before returning to the first perigee. The solution in Case (B) is also for the one loop trajectory, but with a small −5.0 m/s underburn. Note that this trajectory has an ascending encounter that is very close to the desired lunar flyby, varying by about 3 hours. For a two loop overburn of +13.0 m/s, an arc with a descending encounter appears in Case (C). The spacecraft now moves through one phasing loop and then encounters the Moon after the second apogee. The solution in Case (D) then presents the results for a −8.6 m/s underburn in the two loop case, also with a descending encounter after the third apogee. It is of note that all four of the these cases (A–D) encounter the Moon shortly before or shortly after the date of the nominal lunar encounter.

Beginning with the three loop solution, however, an additional lunar opportunity is available closer to the launch/injection date. Case (E) then presents a trajectory arc for a three loop overburn of +14.4 m/s. Here, the spacecraft passes through a descending encounter with the Moon after the first apogee, similar to Case (A). Now, however, the encounter takes place nearly one month before the nominal lunar flyby. The trajectory corresponding to a −13.0 m/s underburn appears in Case (F). This arc includes an ascending encounter on the second loop, again about one month prior to the nominal encounter. Since the four loop solution is based on the three loop case, the same opportunities are present with the addition of another phasing loop. A +7.7 m/s overburn produces the trajectory plotted in Case (G), with a descending encounter after the second apogee. Finally, a −7.7 m/s underburn results

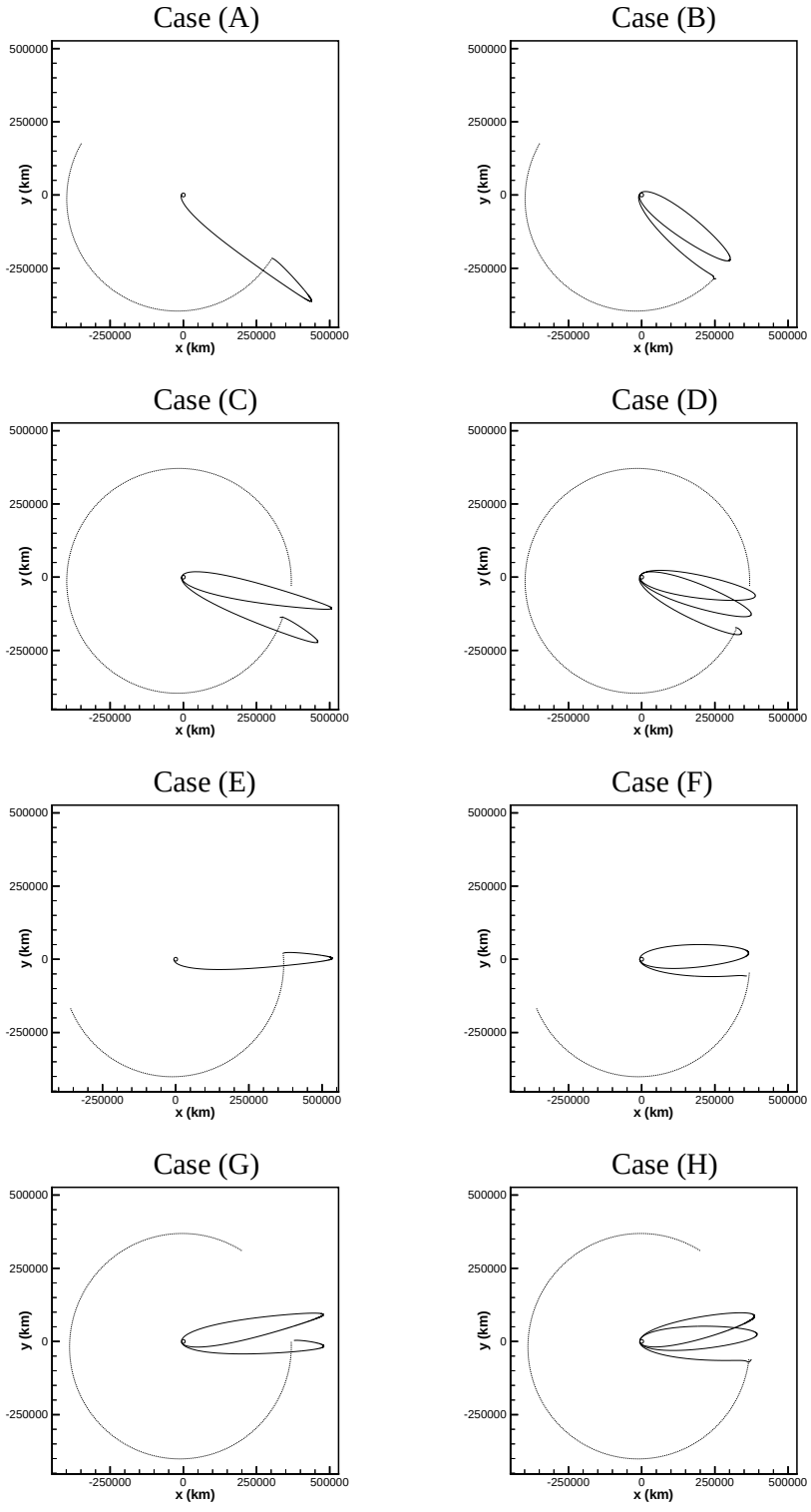

Figure 5.29. Potential Additional Lunar Encounters for Phasing Loop Solutions

in an ascending lunar encounter on the third phasing loop of the four loop solution, represented in Case (H).

These, then, are eight possible opportunities in which a velocity magnitude error may result in a lunar encounter other than the one designed in the nominal trajectory. Five of the cases are descending encounters, while the other three exhibit ascending lunar flybys. Unfortunately, the descending encounters are unsuitable choices to initiate this type of recovery strategy using lunar gravity assists. A descending encounter during phasing loops of this type almost always decreases the orbital energy and results in an impact with the Earth at the next perigee passage. (This is not true of all descending encounters, since it is shown in Chapter 4 that a descending encounter can be employed to achieve escape velocity relative to the Earth.) Attempts to determine a viable recovery using descending encounters all resulted in impact with the Earth. Recall, however, that the MLS trajectories presented in Section 4.1 utilize ascending encounters for the initial lunar flyby. This results in acceptable clearance of the Earth during all subsequent perigees; hence, the ascending cases should provide a suitable initial lunar encounter to initiate a recovery strategy. It is noted that the one loop ascending encounter is very close to the nominal for a small underburn; therefore, this case then is best handled using standard error correction. Instead, the three and four loop underburns represented in Cases (F) and (H), with an ascending encounter approximately one month prior to the nominal lunar flyby, offer more likely options for feasible recoveries.

5.3.1 Lunar Swingby Recoveries for Three Phasing Loop Solutions

The range of injection underburns that produce the ascending encounter represented in Case (F) for the three loop solution is very limited. Hence, it is reasonable to search for a specific error most suitable to initiate the desired lunar swingby recovery, and then base solutions for all other errors on this trajectory. For this approach, a baseline solution is sought that includes a total of three lunar encounters, with the final flyby designed to initiate the transfer out to the Lissajous orbit. Initially, an

error level is selected that achieves an ascending encounter, as seen in Case (F); this error essentially dictates the baseline elongation angle of the first lunar encounter. However, to determine the recovery solution, the injection error is actually only propagated to the first perigee P_1. (Note that a maneuver at apogee A_1 may be used to raise the altitude of P_1, if required.) The position and time at P_1 from the propagation of the injection state, including errors, then becomes the initial state for the multiple lunar swingby recovery. A conic arc is then determined between this initial state and the first lunar encounter, with the constraint that the lunar flyby must occur at the reference elongation angle. However, as the trajectory is developed further, the methodology does allow some flexibility in determining the precise lunar encounter that best fits the desired recovery.

The first lunar gravity assist shifts the trajectory onto an outer loop with a flight time greater than one month. Using the Timing Condition and the Conic Arc Selection algorithm detailed in Sections 3.1.1 and 3.1.2, this outer loop produces a second lunar flyby at the end of the outer conic arc to initiate the next segment. This next segment is an inner arc with a flight time of less than one month, and is also designed using the Conic Arc Selection algorithm to set up the third and final lunar encounter. This last lunar flyby actually initiates the transfer to the new Lissajous orbit, similar to the original single flyby solution.

The new Lissajous orbit is designed with characteristics similar to the original solution, but is advanced forward a specified amount of time based on the increase in flight time from injection to the new final lunar encounter. A stable manifold associated with this new Lissajous orbit is then computed. This new manifold trajectory includes a close passage by the Earth and encounters the Moon at an elongation angle similar to the final lunar encounter at the end of the third conic arc. A new target state is now selected along this one dimensional manifold to represent the new LOI target state (position and time) for the trajectory segment from the final lunar encounter to the Lissajous orbit insertion point. Note that, as before, the fourth and

final segment along the trajectory is approximated as a conic Lambert arc between the final lunar encounter state and the new LOI point.

After a conic approximation for the desired recovery trajectory is determined, the MCA/PSA intermediate step is applied to incorporate the lunar and solar gravitational effects into the solution. This multi-conic solution allows a numerically integrated trajectory to be determined in the final step to represent the recovery from the given injection error. Since the initial state at P_1 is fixed at some position and time based on the error and any maneuvers during the first loop, a deterministic maneuver is introduced by the procedure at this point. Several options exist to reduce the magnitude of this maneuver. First, the normal component of velocity at the first apogee A_1 can be adjusted with a maneuver to minimize the normal component of $|\Delta\bar{V}_{P1}|$ at P_1. This is a very effective means to reduce the required plane changes at P_1. The in-plane components of the maneuver at P_1 may also be adjusted by iterating on the value of the error at launch. (Recall that a specific error is sought to achieve the best possible lunar swingby trajectory.) Once an acceptable maneuver at P_1 is determined for a specified injection error, the entire trajectory from A_1 to LOI is patched together, and the converged three lunar swingby recovery is obtained.

This technique is applied to the three loop arc in Case (F) that has an insertion underburn of -13.0 m/s. The design of the three lunar swingbys is such that the final encounter occurs about 30 days after the nominal single flyby solution. This timing requires that the desired Lissajous orbit, as well as its associated manifolds, be advanced by about one month. For this example, a new Lissajous orbit is selected with approximately the same A_y and A_z amplitudes as the original nominal solution and a new LOI point is determined along one of the manifold trajectories associated with this new Lissajous. The resulting conic arcs that serve as the approximation to the recovery are summarized in Table 5.37. The elongation angles (elong) corresponding to the three lunar encounters are listed in the Outputs section of the table, along with the nondimensional semi-major axis (a_c/L^*), eccentricity (e_c), and time of flight (Δt) along the arc. The input parameters R_p and ψ for the conic arcs are selected

Table 5.37 Input/Output Parameters for Three Loop / Three Swingby Recovery

Segment No.	1	2	3	4
		Inputs		
N_{mos}	0	1	1	1
N_{apo}	0	1	1	0
N_{peri}	0	0	2	0
R_p (km)	7191	–	25000	–
ψ (deg)	0	–10	0	–
		Outputs		
elong (deg)	20.0	–40.3	22.8	–
a_c/L^*	4.80007	1.28161	0.79678	1.83420
e_c	0.99610	0.82069	0.91837	0.87755
Δt (days)	2.1084	33.7754	24.9024	31.9060

to produce a final lunar elongation angle at the end of the third conic arc that is as similar as possible to the original nominal value. Such a result tends to minimize the magnitude of the final LOI maneuver, since experience suggests that lunar encounters closer to the Sun-Earth line exhibit larger LOI maneuver costs for insertion onto a Lissajous orbit of this size. For this particular example, the final elongation angle for the swingby recovery is roughly 23 deg. The nominal elongation angle is about 36 deg, so an increase in the LOI cost is expected for this recovery.

Once the conic approximation has been determined, the intermediate step is applied to allow a numerically integrated solution to be obtained. The maneuver history and perigee altitudes corresponding to this four body solution are presented in Table 5.38. Note that the three swingby recovery solution yields a total cost that is 5.36 m/s higher than the straight correction back to the original nominal. As expected, the LOI cost has increased by 66.52 m/s over the original solution. This increase in cost certainly is related to a final lunar elongation angle that is closer to

the Sun-Earth line, but may also be a function of the final perigee altitude. In order to achieve a reasonable elongation angle for the final lunar encounter, the perigee distance on the third segment is raised by over 10,000 km. This increase in radial distance from the nominal perigee altitude may also contribute to the difference in LOI costs. The resulting trajectory appears in Figure 5.30. Again, the propagation of the injection error to the first apogee is plotted as a dotted line, while the three swingby recovery trajectory is represented as a solid line. Comparison of this trajectory with the nominal solution, in Figure 4.12, demonstrates the shift of the final lunar elongation angle closer to the Sun-Earth line. However, the use of three lunar gravity assists does shift the elongation angle forward by about 10 deg from the original value in Case (F), thereby providing a solution more consistent with the original lunar flyby. It is also observed that the selection of a particular stable manifold to move into the libration point orbit is somewhat arbitrary. More flexibility exists for this selection and, given this proof of concept, should be more fully explored.

This trajectory now serves as the baseline multiple lunar swingby recovery trajectory corresponding to an underburn error of -13 m/s in the three loop case. By introducing a TCM sometime shortly after launch, solutions over a range of errors surrounding this baseline value can be determined. This is accomplished through the same process that is utilized to determine the straight error correction at the beginning of this chapter. In this case however, the "nominal" solution is now the baseline lunar swingby recovery just presented. The TCM directly after launch is employed to correct back to this baseline solution. The results for a range of errors surrounding -13 m/s are presented in Table 5.39 for a TCM at trajectory transfer insertion plus 18 hours. The resulting TCM maneuvers increase as the underburn error level deviates from the baseline value. Notice, however, that the other maneuvers in the recovery remain fairly constant. This is consistent with the trends observed from straight error correction. From these results, the range for possible lunar swingby recoveries is expanded to include underburn errors from -5 to -20 m/s; although these lunar swingby recoveries are more costly than straight correction and therefore,

Table 5.38 Three Loop / Three Lunar Swingby Recovery from –13 m/s Underburn

	Nominal	Straight	Recovery
TTI+18 ΔV (m/s)	—	90.51	—
A_1 ΔV (m/s)	—	—	16.06
P_1 ΔV (m/s)	—	—	15.78
LOI ΔV (m/s)	32.75	35.24	99.27
Total ΔV (m/s)	32.75	125.75	131.11
P_1 Altitude (km)	696.1	408.0	1133.0
P_2 Altitude (km)	1740.8	1440.6	17227.1
P_3 Altitude (km)	4039.7	3677.3	14820.0

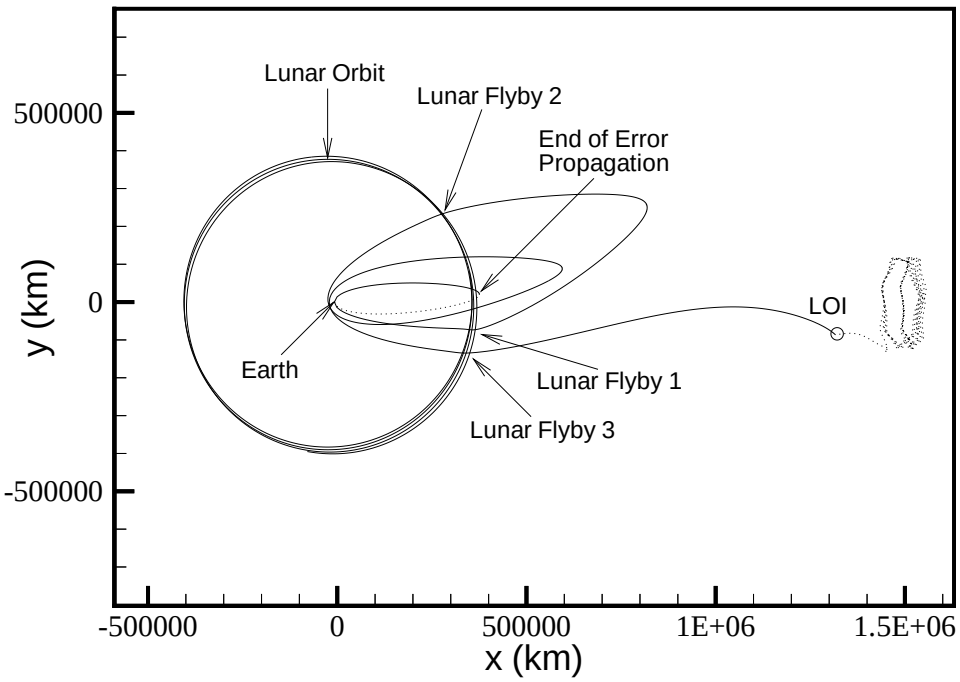

Figure 5.30. Three Lunar Swingby Recovery for Three Phasing Loop Solution

Table 5.39 Comparative Results for Three Loop / Three Swingby Recoveries

	Nominal	Baseline	V_{mag} Error			
			-5 m/s	-10 m/s	-15 m/s	-20 m/s
TTI+18 ΔV (m/s)	—	—	56.05	21.11	14.17	49.76
A_1 ΔV (m/s)	—	16.06	15.95	16.01	16.02	15.96
P_1 ΔV (m/s)	—	15.78	15.69	15.73	15.74	15.69
LOI ΔV (m/s)	32.75	99.27	97.00	98.42	99.77	101.11
Total ΔV (m/s)	32.75	131.11	184.69	151.27	145.70	182.52
P_1 Altitude (km)	696.1	1133.0	857.0	1022.4	1159.7	1260.5
P_2 Altitude (km)	1740.8	17227.1	17740.3	17422.8	17115.8	16822.3
P_3 Altitude (km)	4039.7	14820.0	15421.9	15049.7	14690.6	14348.2

are not *feasible* in the strict sense of the definition. If these results are combined with the recoveries determined previously in Section 5.2.3, then recovery strategies do exist in the three loop case for injection velocity errors less than +5 m/s. Note that a similar lunar swingby recovery strategy is also available for radial position errors. Although not optimal at this time, these multiple lunar swingby trajectories demonstrate a wide range of options for recovery from launch/injection errors.

5.3.2 Lunar Swingby Recoveries for Four Phasing Loop Solutions

The methodology to determine lunar swingby recoveries for nominal solutions involving four phasing loops is identical to the techniques presented for the three phasing loop swingby recoveries. The one difference is that the injection state, including errors, is now propagated to the *second* perigee state (P_2) to determine the "initial" state for the multiple lunar swingby portion of the recovery. This results in a trajectory that resembles Case (H) in Figure 5.29 with an underburn of -7.7 m/s. As before, a three swingby recovery is sought to transfer to the same Lissajous orbit and

LOI state that is utilized for the previous example. The resulting conic approximation is summarized in Table 5.40. Notice that, except for the first conic arc from P_2 to the first lunar encounter, the conic approximation is identical to the previous conic solution presented in Table 5.37. The first loop is of course altered, since the nominal path and the given underburn error are different. However, the same first lunar encounter is targeted in both the three and four loop recoveries, thus the remainder of the conic approximation should be very similar.

The resulting numerically integrated trajectory is summarized in Table 5.41. The lunar swingby recovery strategy produces a solution with a cost that is 19.94 m/s higher than the corresponding straight error correction. Even so, this type of recovery could be useful under certain circumstances. Further study of the selection process for the Lissajous orbit and the associated stable manifold will undoubtedly yield solutions with lower LOI costs. The resulting trajectory appears in Figure 5.31. The only significant difference between this trajectory and the one in Figure 5.30 is the

Table 5.40 Input/Output Parameters for Four Loop / Three Swingby Recovery

Segment No.	1	2	3	4
		Inputs		
N_{mos}	0	1	1	1
N_{apo}	0	1	1	0
N_{peri}	0	0	2	0
R_p (km)	7496	–	25000	–
ψ (deg)	0	–10	0	–
		Outputs		
elong (deg)	20.0	–40.3	22.8	–
a_c/L^*	3.04438	1.28161	0.79678	1.83420
e_c	0.99360	0.82069	0.91837	0.87755
Δt (days)	2.1537	33.7754	24.9024	31.9060

Table 5.41 Four Loop / Three Lunar Swingby Recovery from –7.7 m/s Underburn

	Nominal	Straight	Recovery
TTI+18 ΔV (m/s)	—	56.16	—
A_1 ΔV (m/s)	23.00	30.00	22.91
P_1 ΔV (m/s)	—	—	—
A_2 ΔV (m/s)	—	—	11.11
P_2 ΔV (m/s)	—	—	6.03
LOI ΔV (m/s)	32.19	31.89	97.94
Total ΔV (m/s)	55.19	118.05	137.99
P_1 Altitude (km)	226.9	287.3	346.2
P_2 Altitude (km)	444.3	498.2	1116.3
P_3 Altitude (km)	838.4	879.8	17529.5
P_4 Altitude (km)	2948.4	2988.4	15175.0

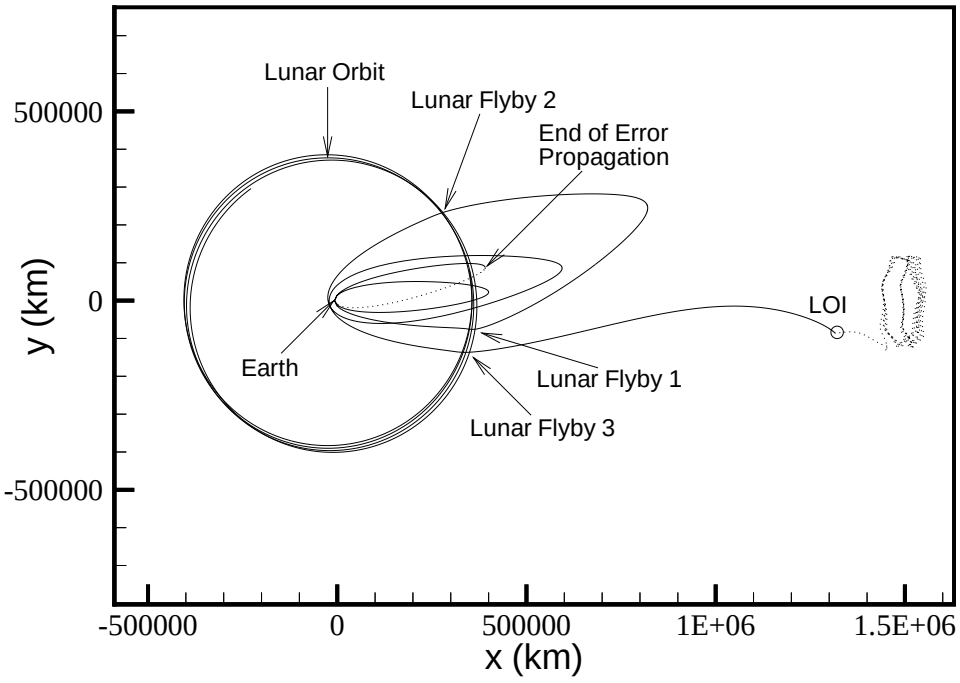

Figure 5.31. Three Lunar Swingby Recovery for Four Phasing Loop Solution

inclusion of an additional phasing loop between the injection state and the initial state along the swingby portion of the recovery (i.e., P_2 in this case). This is the baseline solution for the four loop case with an underburn error level of -7.7 m/s.

Again utilizing a TCM maneuver at TTI+18 hours, a range of errors surrounding this baseline trajectory can be computed. The results for a -10 m/s underburn are presented in Table 5.42. The table includes the nominal solution, the straight error correction, the original recovery strategy from Section 5.2.4, and this new lunar swingby recovery strategy. Notice that this recovery strategy utilizing additional lunar encounters is 66.26 m/s more expensive than the original recovery strategy designed previously and 20.00 m/s costlier than straight recovery, and therefore would not be considered the primary recovery strategy.

For both the three and four phasing loop solutions, the cost of the recoveries including additional lunar gravity assists is larger than the straight correction back to

Table 5.42 Four Loop Lunar Swingby Recovery Comparison for -10 m/s Underburn

	Nominal	Straight Correction	Original Recovery	Swingby Recovery
TTI+18 ΔV (m/s)	—	72.31	—	16.09
A_1 ΔV (m/s)	23.00	30.00	22.91	22.91
P_1 ΔV (m/s)	—	—	17.50	—
A_2 ΔV (m/s)	—	—	6.95	11.11
P_2 ΔV (m/s)	—	—	8.03	6.03
LOI ΔV (m/s)	32.19	32.36	33.02	98.53
Total ΔV (m/s)	55.19	134.67	88.41	154.67
P_1 Altitude (km)	226.9	240.2	392.8	365.5
P_2 Altitude (km)	444.3	445.3	329.0	1130.6
P_3 Altitude (km)	838.4	823.3	694.4	17398.4
P_4 Altitude (km)	2948.4	2920.3	2774.5	15021.4

the nominal, and the other types of recovery strategies presented in Sections 5.2.3 and 5.2.4. This is due primarily to the significant increase in the LOI cost to insert onto the manifold trajectory. This cost might be reduced by examining different nominal Lissajous trajectories in the same time frame that meet the mission requirements. Specifically, for lunar passages at the elongation angles determined in the example recoveries, utilizing Lissajous trajectories with larger amplitudes in the $\hat{y}$ direction of the rotating frame may decrease the required insertion costs.[43] This then may yield truly feasible recoveries, especially for the three phasing loop solution.

In summary, it is concluded that the use of lunar gravity assists is an option to create recovery strategies for a range of errors. The use of lunar swingby recoveries is especially appropriate for the three loop nominal and expands the range of underburn errors for which recoveries are possible. Similar solutions are also available for the four loop nominal, however, the costs are currently more expensive than the recovery strategies presented in Section 5.2.4. Further investigation of the multiple lunar swingby recovery option is warranted.

6. OPTIMIZATION OF THE LPO TRANSFER COST

Throughout the design and subsequent analysis of the example trajectory representing a transfer from the Earth to a libration point orbit (Sections 4.3, 5.1.3, and 5.2), the final state along the transfer has been fixed in position and time . Recall that this fixed state is selected somewhat arbitrarily approximately 30 days beyond the lunar orbit along a stable manifold associated with the desired Lissajous trajectory. Due to the inclusion of launch constraints and additional phasing loops in the transfer portion of the trajectory, a Lissajous Orbit Insertion (LOI) maneuver is introduced at this fixed state during the solution process. This maneuver, then, completes the transfer to the desired manifold state and hence, eventually, to the Lissajous orbit itself. A systematic approach is sought to gain a better understanding of the fundamental factors that impact the size of the LOI maneuver in an attempt to substantially reduce the cost of the transfer. First, a parametric study of various inputs to the solution process is presented to determine possible effects on the LOI maneuver. Then a procedure is developed to alter the fixed state along the manifold in order to determine a more optimal location to implement the insertion maneuver.

6.1 Parametric Study on LOI Cost

For the parametric analysis of the transfer problem, the effects on the LOI cost due to various input parameters in the solution process are examined. For this focused investigation, the fixed (in position and time) final state on the manifold is selected to be the same as the target state for the nominal transfer solutions in Chapters 4 and 5. Recall that the numerical representation of this point is:

$$\begin{aligned} \text{Julian date} &: 2454400.0582 \\ x, y, z \text{ position (km)} &: 1316756.51 \ , \ -86705.16 \ , \ -101952.81 \\ \dot{x}, \dot{y}, \dot{z} \text{ velocity (m/s)} &: 112.176 \ , \ 19.254 \ , \ 17.565 \end{aligned}$$

where the position and velocity are given in terms of SR coordinates.

Since this analysis involves numerous transfer solutions, it should be noted that there are multiple approaches to determine the necessary trajectories. In one approach, the nominal four body transfer trajectory is employed as the initial approximation to determine perturbed solutions in the vicinity of this nominal. This approach, however, may bias the results toward a nominal that may or may not be ideal. Instead, for this parametric study, each individual numerically integrated transfer is determined from a conic approximation using the three step procedure described in Chapter 3. Since each solution is thus developed separately, any biases introduced are systematic to the three step methodology and should not significantly affect the overall trends.

Since the segment from the lunar encounter to the target state is simply a two body Lambert solution, this segment is computed using endpoints defined at the lunar encounter and the desired fixed endstate. The lunar encounter, in turn, is specified by the initial conic, hence, all the input parameters identified for this study, then, are related to the conic arc from launch/injection to the Moon. The key parameters for this segment are launch date, phasing loop perigee altitude, and elongation angle of the lunar encounter for the conic solution. Each input is examined for all five nominals including 0, 1, 2, 3, and 4 phasing loops. As each input parameter is examined, the other two inputs are held fixed at the value used to design the respective nominal in Section 4.3.

6.1.1 Variations in Launch Date – Zero Loop Case

The variations in LOI cost for changes in launch date are examined first, beginning with the direct transfer to the Moon, that is, the zero phasing loop solution. For the 0-loop nominal in Section 4.3, the trajectory is actually designed utilizing the entire

manifold, from Earth close approach to the selected manifold target state (denoted as the LOI point), as the initial approximation. This nominal solution has a launch date on JD 2454363.816 and an LOI cost of 1.93 m/s. For this study, however, a conic approximation is employed as the first guess to minimize biasing of the results. Hence, based on the lunar encounter corresponding to the selected manifold trajectory, an initial lunar elongation angle of 45.0 deg is selected. A conic perigee altitude of 200 km then reflects the launch constraint on altitude. The launch date under consideration is selected, and the conic approximation is determined using the methodology that is described in Section 4.3. From this initial guess, the MCA/PSA intermediate step is applied to allow a numerically integrated solution to be obtained.

The results of varying the launch date in the vicinity of the nominal solution are presented in Figure 6.1. The minimum LOI cost across all of the cases is 0.38 m/s on JD 2454363.764 and is marked with a diamond on the figure. (For clarity, the abscissa is expressed as the Julian date minus 2454300.) Note that the nominal solution from Section 4.3 is denoted with a circle and is actually quite close to the minimum value. Clearly, there is a linear relationship between the launch date and the LOI cost for the 0-loop case when all other parameters are held fixed, and the launch date is within the relatively small range indicated. This cost increases rapidly as the launch date shifts away from the minimum.

6.1.2 Variations in Launch Date – One Loop Case

The same approach is utilized to study variations in launch date for the transfer with a single phasing loop. For the one loop case, the nominal LOI cost is 20.64 m/s corresponding to a launch on JD 2454352.731. Similar to the 0-loop case, the initial elongation angle is 45.0 deg and the conic perigee altitude is 200 km. The LOI costs over various launch dates appear in Figure 6.2. Again the minimum LOI cost is denoted by a diamond, while the nominal is marked with a circle. Obviously, the relationship between LOI cost and launch date for this case is very different from the 0-loop solutions. Here the minimum LOI cost of 1.26 m/s occurs near the latest

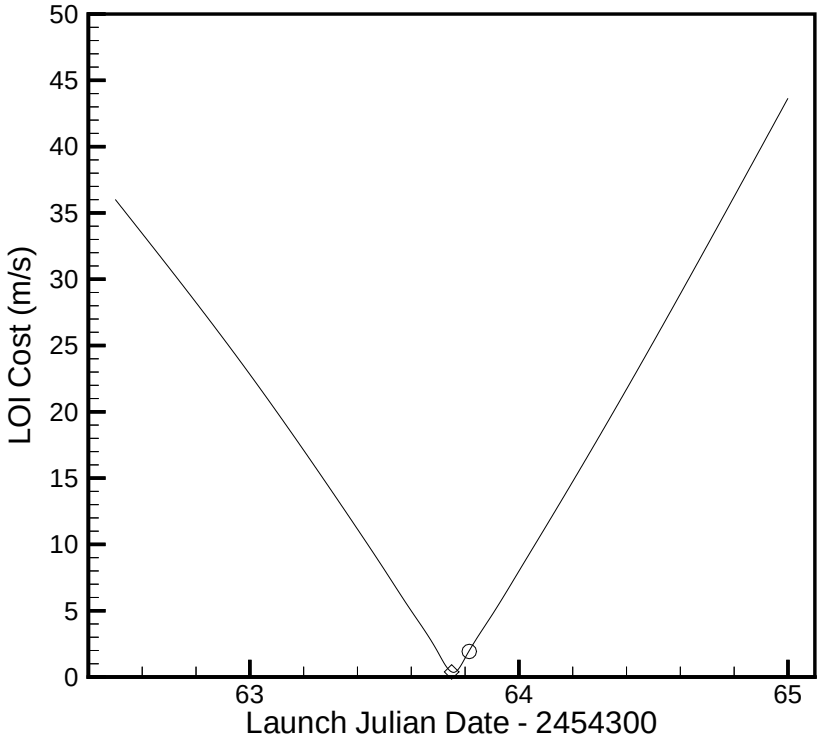

Figure 6.1. Launch Date Variation for Zero Loop Case

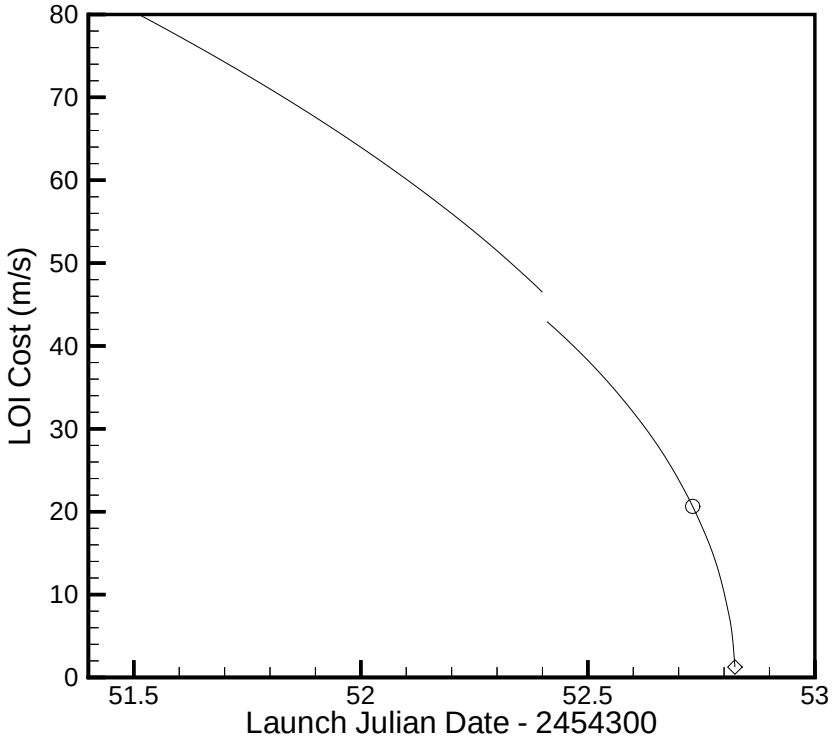

Figure 6.2. Launch Date Variation for One Loop Case

possible launch date on JD 2454352.824. Dates later than this require a phasing loop with an apogee distance smaller than the lunar orbit. Such a situation does not allow a lunar encounter to occur without a deterministic maneuver sometime during the phasing loop to increase the orbital energy (likely at the final perigee before the lunar encounter). This investigation does not include these types of solutions, so no trajectories are computed beyond this date.

Notice in the figure that, as the launch date is moved forward, the cost increases until an apparent discontinuity occurs around JD 2454352.4. The jump in cost at this point is actually due to a dramatic change in the final elongation angle of the lunar encounter. To demonstrate this change, the trajectory with a launch date on JD 2454352.410 (at the top of the lower curve) is plotted in Figure 6.3. The elongation angle corresponding to this solution is 57.6 deg at the lunar encounter and the associated LOI cost is 42.94 m/s. A plot of the trajectory with a launch date 15 minutes earlier on JD 2454352.400 (at the minimum point of the upper curve in Figure 6.2) appears in Figure 6.4. This solution has a lunar elongation angle of 34.0 deg and an LOI cost of 46.49 m/s. Thus, the earlier launch increases the LOI maneuver by 3.55 m/s and changes the elongation angle by 23.6 deg. This inconsistency arises because there are, in fact, two solutions possible over the range of launch dates from JD 2454352.410 to 2454352.824. The solutions are very close in cost and, in fact, coincide near the minimum cost on JD 2454352.824. Due to the sensitivities in the problem and in the solution process, it is difficult to determine the higher cost solution in this region. However, the higher cost solution should mimic the lower cost solution in the figure, but it will be displaced slightly above the lower cost curve. Launch dates earlier than JD 2454352.410 lead to only the higher cost solution. Trajectories with initial dates sooner than this time again reduce the apogee of the lower cost solution below the lunar orbit; this eliminates the lower solution possibility and produces the discontinuity, as seen in Figure 6.2.

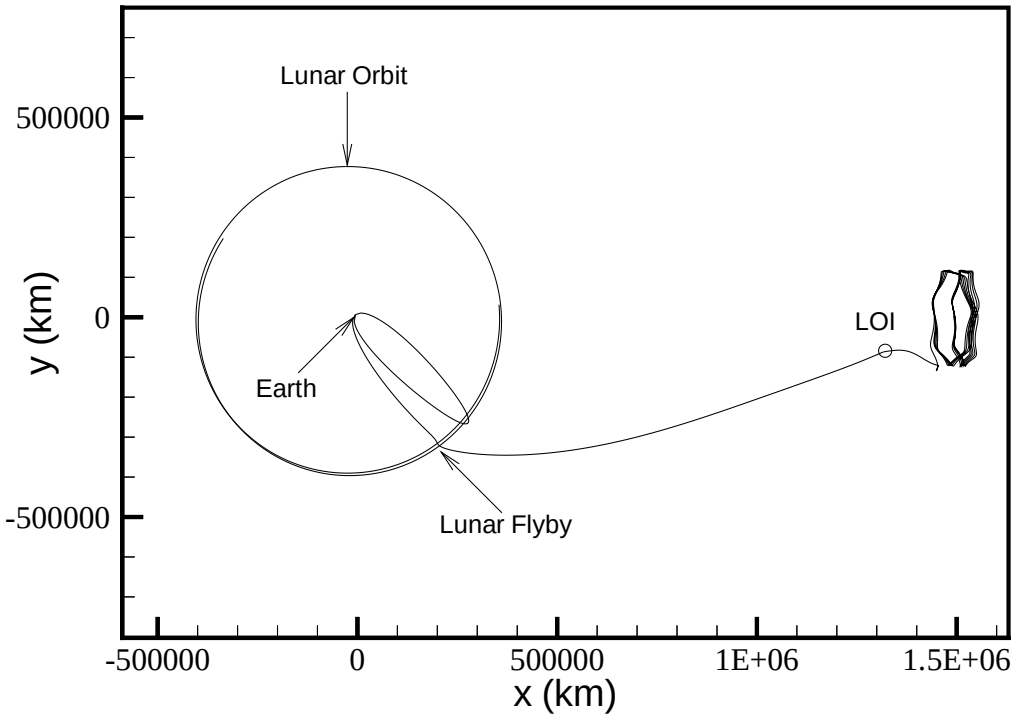

Figure 6.3. One Loop Solution with Launch Date on 2454352.41

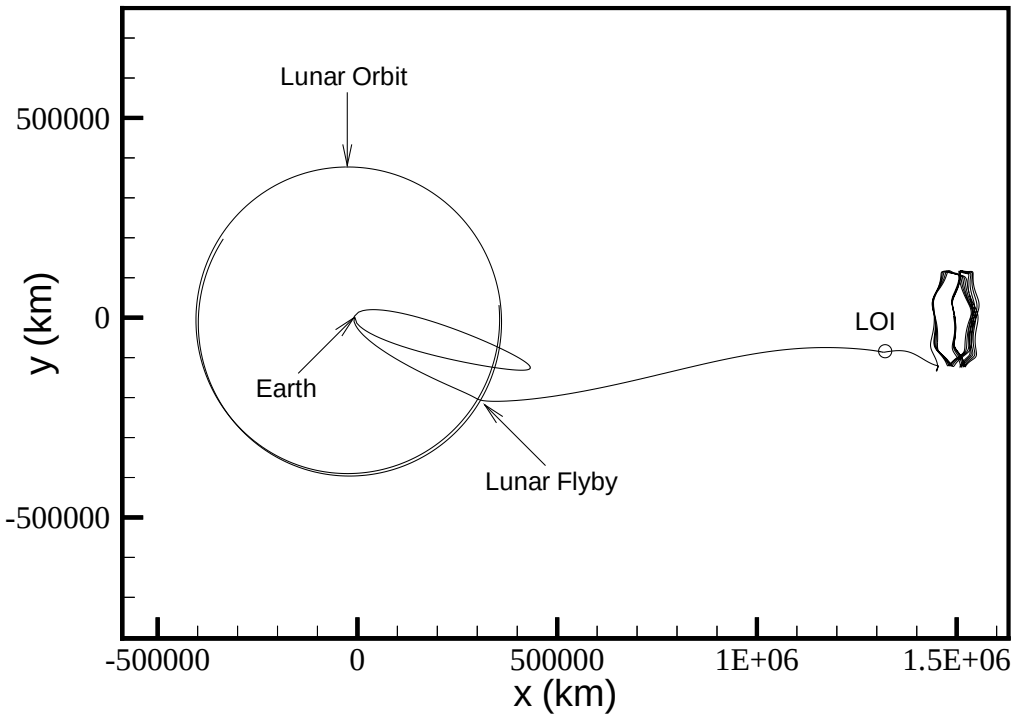

Figure 6.4. One Loop Solution with Launch Date on 2454352.40

6.1.3 Variations in Launch Date – Two Loop Case

Transfers with two phasing loops have also been computed for various launch dates. The initial elongation angle is again selected to be 45.0 deg. However, now the initial conic perigee altitude is 4622 km, to facilitate solutions with acceptable perigee altitudes on the subsequent Earth periapse passages. Note that the launch/injection state is still constrained to a 200 km altitude in the final solution; only the conic approximation varies from this constraint. The nominal two loop solution corresponds to a launch on JD 2454340.612 with an LOI cost of 30.35 m/s. Launch dates in the vicinity of this nominal are examined, and the resulting LOI costs are presented graphically in Figure 6.5. The relationship between LOI cost and launch date is different yet again from the previous two solutions. For the two loop case, the cost reaches a local maximum of 37.28 m/s on JD 2454339.600 and a minimum of 2.14 m/s on JD 2454337.310 (denoted by the diamond). The nominal cost (circle) is actually closer to the upper bound on possible launch times. This upper limit is again due to

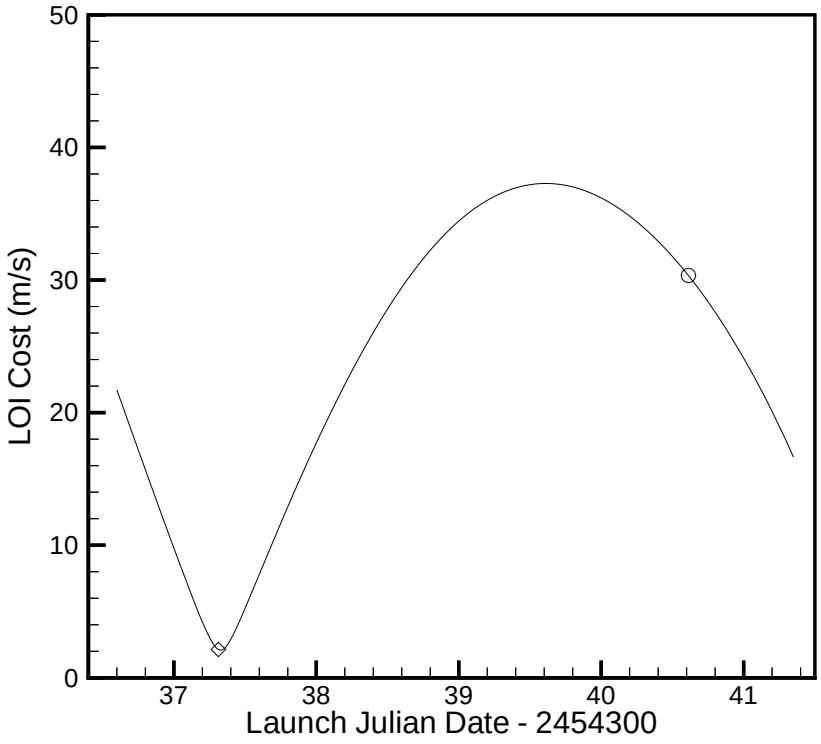

Figure 6.5. Launch Date Variation for Two Loop Case

a restriction that the apogee remain higher than the lunar orbit, and is violated for launches later than JD 2454341.350. For dates before the launch that corresponds to the minimum cost, the required LOI maneuver magnitude again increases. This is the result of larger orbital periods for the loops as the time of flight along the phasing loop portion of the trajectory increases. For dates earlier than JD 2454336.500, the period is large enough ($\sim$ 13.5 days) to cause an unwanted lunar encounter shortly after launch, similar to the difficulties seen in developing the three loop nominal in Section 4.3.4. This limits the launch opportunities for the two loop case to roughly 5 days; however, of the five types of solutions examined, this is the largest continuous launch window that maintains a reasonable LOI maneuver cost. It should also be noted that near the limits of this range, the perigee altitudes drop drastically. This analysis does not compensate for such problems, but the perigee altitude should be considered before evaluating the practicality of any particular solution.

6.1.4 Variations in Launch Date – Three Loop Case

Despite the problematic nature of the solutions with three phasing loops, a range of launch dates, albeit small, around the nominal solution is possible. As with the two loop case, the initial elongation angle is 45.0 deg and the initial conic perigee altitude is 4622 km. The nominal solution in this case includes an LOI cost of 32.75 m/s corresponding to a launch on JD 2454327.624. The results for variations in the timing of the launch are presented in Figure 6.6. The LOI cost variation for the three loop case is similar in nature to the two loop solutions with a local maximum and a minimum cost near the beginning of the launch window. The minimum cost here (denoted by a diamond) is 2.31 m/s for launch on JD 2454326.350. Note however, that the actual range of launch opportunities is now only about 2 days. At the limits of this range, the Moon interferes with the trajectory, eliminating realistic solutions beyond JD 2454328.000, or sooner than JD 2454326.150.

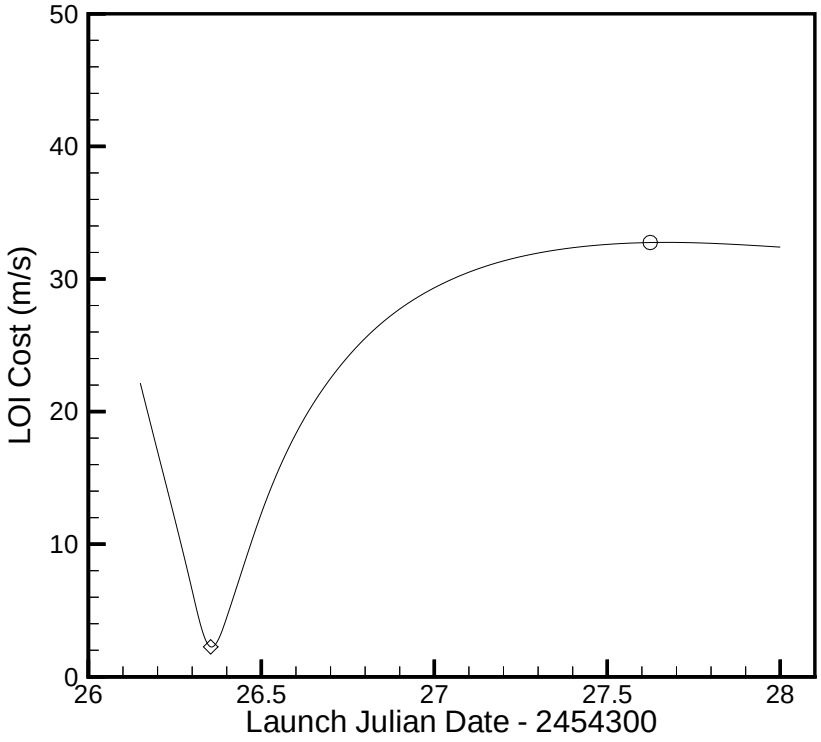

Figure 6.6. Launch Date Variation for Three Loop Case

6.1.5 Variations in Launch Date – Four Loop Case

The same analysis technique to examine various launch dates is also applied to the four loop nominal solution. Recall that this nominal trajectory has an LOI cost of 32.19 m/s with launch on JD 2454315.944, and a deterministic maneuver of 23.00 m/s magnitude at the first apogee. For this part of the analysis, the nominal four body solution is utilized as the initial approximation to determine the surrounding solutions. The primary reason for this is to expedite the lengthy process required to determine a single four phasing loop solution, and also because the results from the other phasing loop analyses for a fixed launch date do not suggest as much biasing of the trajectory as originally suspected. The results of varying the timing of the launch are presented in Figure 6.7. The general pattern is similar to the results in the two and three loop cases, however, the local minimum at the beginning of the launch window no longer exists. As in the previous cases, the Moon perturbs the trajectory such that no solutions are possible earlier than JD 2454314.878. This also

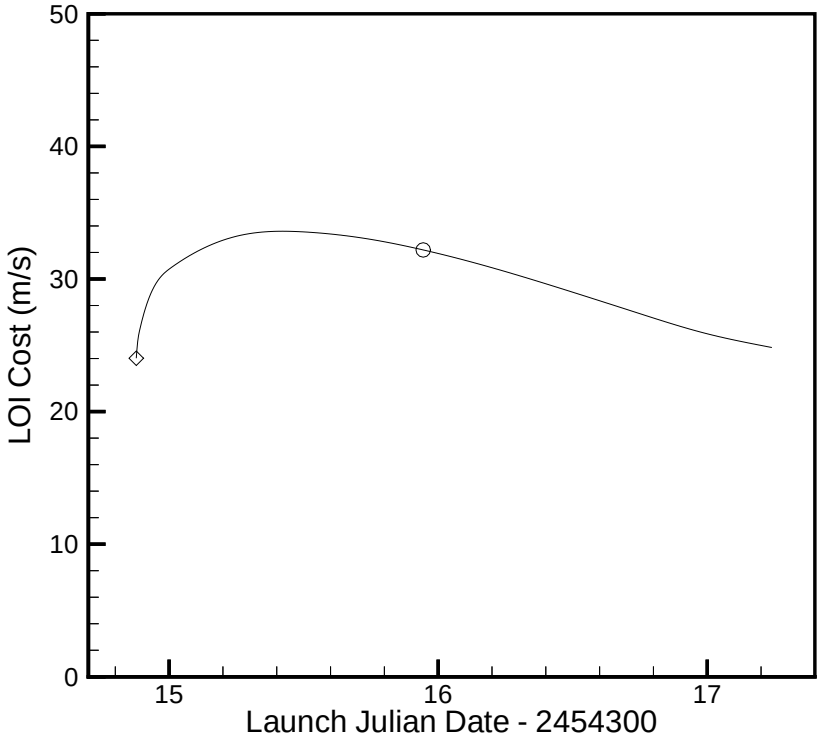

Figure 6.7. Launch Date Variation for Four Loop Case

corresponds to the solution with the minimum LOI cost of 24.02 m/s. It is noted that a solution with a similar cost of 24.83 m/s occurs at the upper bound of the launch window on JD 2454317.240. As with the lower limit, this upper bound is due to the unwanted interaction with the Moon prior to the desired lunar encounter.

In summary, it is evident from this part of the parametric study that launch (or injection) date is a major factor in the magnitude of the LOI maneuver cost. By varying the time of launch about the nominal, it is possible to significantly reduce the insertion cost at the target state on the selected manifold associated with the desired Lissajous orbit.

6.1.6 Variations in Elongation Angle

As one of the inputs to the solution process, the initial estimate of the elongation angle that defines the lunar encounter determines the final state along the segment from the injection point to the Moon. This conic approximation includes the desired

number of phasing loops and terminates at the lunar encounter (or collision in the two body problem) that is specified by the initial elongation angle. It is desired to investigate how variations in the estimate of this angle affect the LOI cost, while the launch date and conic perigee altitude are held fixed at the nominal values. The results of varying the initial elongation angle estimate for the 0, 1, and 2 phasing loop solutions are presented in Figure 6.8. Over a wide range of values around the nominal value of 45.0 deg (denoted with circles) the LOI costs are essentially constant. Notice in the one loop case that the selection of the initial angle does dictate which solution type is obtained. Not surprisingly, the lower elongation angles lead to the higher cost solution, as seen in Figure 6.4, while the larger elongation angles produce the lower cost solution, as observed in Figure 6.3. The solutions corresponding to the three and four loop trajectories are also constant and, thus, are not shown here. It is therefore concluded that the selection of the initial elongation angle does not affect the LOI cost, in general, although reasonable values do to aid in the convergence of the solution process.

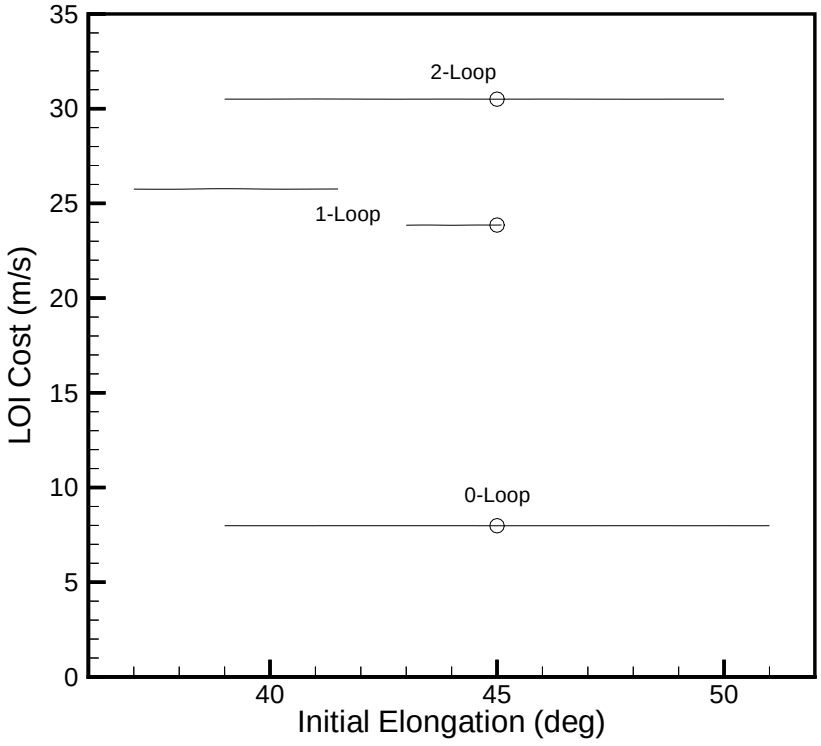

Figure 6.8. Initial Elongation Angle Variation

As an input, the initial estimate of the elongation angle has little impact on the total LOI cost. Unlike the launch date, however, that is fixed throughout the solution process, the actual elongation angle of the lunar encounter varies from the initial estimate in the conic solution to the final value that is obtained as part of the integrated solution. To demonstrate this change, consider the results from the launch date variation analysis presented in Sections 6.1.2 – 6.1.5. The LOI cost across all five types of phasing loop solutions is a function of the final elongation angle of the lunar encounter; this is presented graphically in Figure 6.9. It is evident that there is a nearly linear relationship between the final elongation angle for a given launch date and the LOI cost. Furthermore, the minimum cost in all five cases occurs around 46 deg elongation. This is directly correlated with the elongation angle of the manifold path computed for the given Lissajous trajectory; this manifold has an elongation angle of 45.8 deg as it passes the Moon. The locations of the nominal solutions (numbered 0 to 4) demonstrate that the increase in LOI cost as launch date

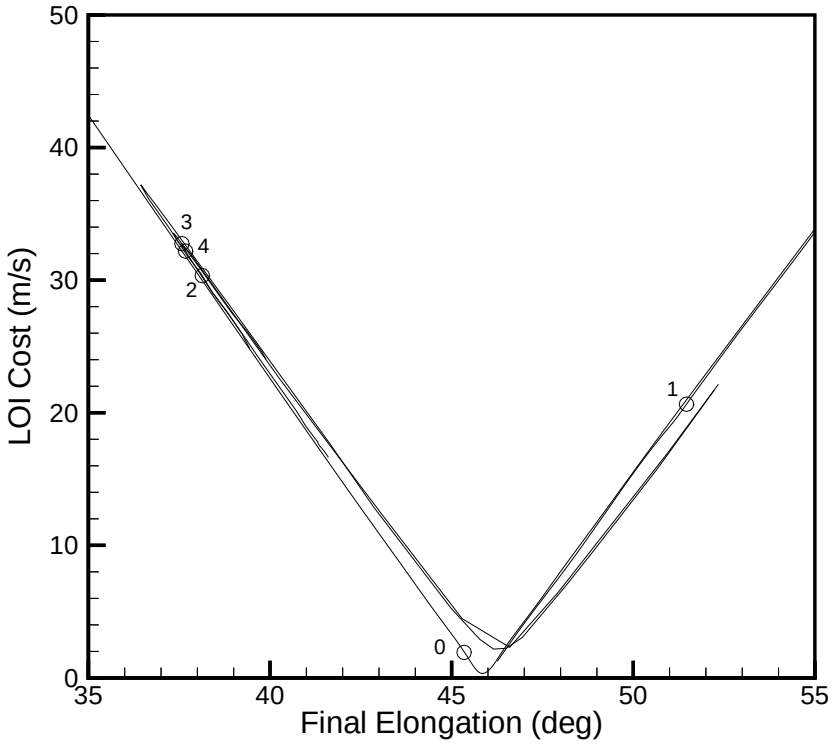

Figure 6.9. Final Elongation Angle Variation

varies is attributable to the deviation of the elongation angle away from the minimum (or manifold) value.

6.1.7 Variations in Perigee Altitude

The final input to be studied is the conic perigee altitude. This input determines the radial distance from the Earth for each perigee state in the conic solution; although, like elongation angle, these values are not fixed throughout the process to achieve the final solution. Since the launch date and estimate of the elongation angle are selected as the nominal values, the time of flight from launch/injection to the lunar encounter is known. Hence, the semi-major axis a_c corresponding to the conic from injection to the Moon can be determined through the iterative process described in Section 4.2 for general launch segments. Specifying the conic perigee altitude, then, essentially determines the initial eccentricity of the conic orbit. Higher altitudes produce lower eccentricities and vice versa. The impact of the conic perigee altitude on the LOI cost is presented in Figure 6.10 for the 0, 1, and 2 loop solutions. Similar to the results observed for the elongation angle, the LOI cost is essentially constant over a wide range of perigee altitudes. There is some variation, but the magnitude of the differences is on the order of 0.01 m/s, and is therefore inconsequential to the overall cost.

In summary, it is concluded from this parametric study that the launch/injection date is the most important factor, of the three inputs examined, affecting the LOI cost. Although elongation angle and perigee altitude provide insight into the relationships between the LOI cost and the characteristics of the trajectory, their effects as inputs to the solution process are negligible. The other possible factor affecting the LOI cost is the selection of the target state along the manifold. This issue is examined next.

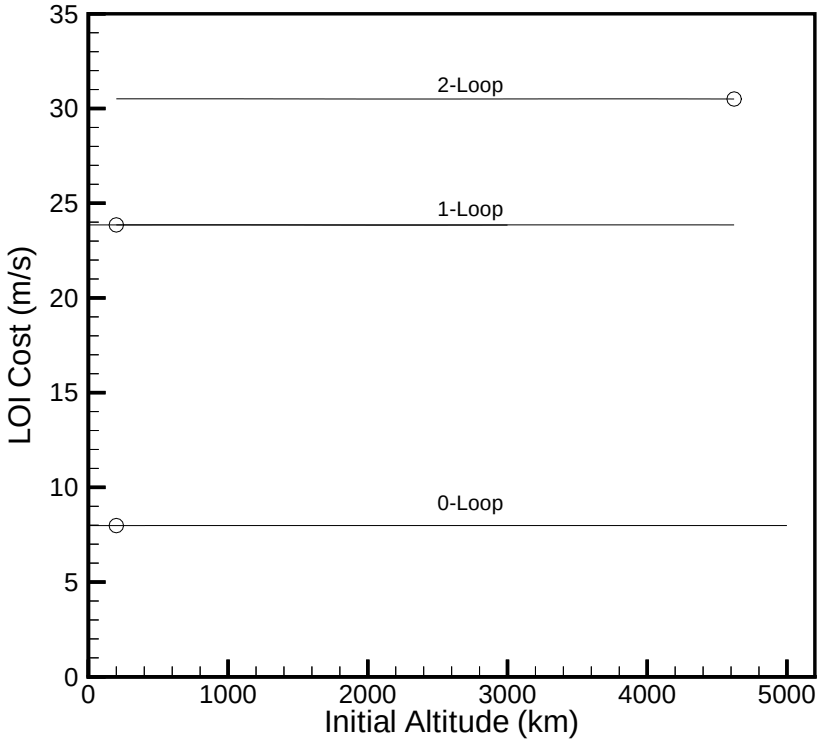

Figure 6.10. Conic Perigee Altitude Variation

6.2 Selection of an Optimal LOI Location

The general focus in this chapter is the Earth-to-LPO transfer trajectories; specifically, the goal is the identification of the inputs that have the most significant impact on the transfer cost. To complete this preliminary analysis, consider an investigation of the variation in the final target state along the manifold and its effects on the LOI cost. This state is selected along the desired manifold trajectory at a location approximately 30 days past the lunar orbit; once specified in a particular case, it is fixed for all subsequent analysis. The selection process is somewhat arbitrary, but the LOI target state is chosen to produce a reasonable insertion cost onto the desired manifold. It is now desired to allow this fixed state to vary in order to determine a more optimal location for the LOI maneuver. An automated procedure is developed to vary the position and time of this final manifold state, while preserving the solution obtained from dynamical systems theory. Thus, the resulting transfer trajectory will still insert onto the desired manifold and approach the Lissajous orbit asymptotically.

6.2.1 Manifold Surfaces

From dynamical systems theory[1,33,34] it is known that the stable and unstable manifolds associated with periodic (and quasi-periodic) solutions form surfaces in the six dimensional phase space (position plus velocity). Moreover, these manifolds appear as two dimensional surfaces when projected onto three dimensional configuration space (position only). An example of one of these surfaces in an L_1 centered rotating frame appears in Figure 6.11 for stable manifolds associated with an L_1 Lissajous trajectory.[43] Notice first that, as time tends to infinity, the manifold surface approaches the libration point orbit and, in fact, is virtually indistinguishable from the Lissajous trajectory; this is consistent with the asymptotic nature of the manifold structures, as discussed in Section 2.5. Then, as the manifold surface extends away backwards in time from the Lissajous orbit, it broadens and then contracts again as the manifolds approach the Earth (located in the "twisted" portion of the manifold on the right of the figure). States that lie on this surface will asymptotically approach the Lissajous orbit, provided that the state matches the 7 dimensional state (position, velocity, and time) on the manifold at the specified point.

To initiate the transfer to a libration point orbit, a single trajectory on the manifold surface is selected that includes a close passage by the Earth. Additionally, for the L_2 transfer under consideration, the selected manifold includes a lunar encounter with a specified elongation angle (46 deg in this case). From this solution then, a single point is selected to serve as the fixed LOI target point. The position and time corresponding to this state on the manifold surface are targeted by the three step methodology to produce the transfer trajectory. In order to precisely approach the desired Lissajous orbit, the state must in fact lie on the surface defined by the stable manifold. The position and time requirements can be met by the current methodology, however, the velocity at the final state is not constrained in the three step process. Therefore, a maneuver is required to correct any velocity discontinuity between the end of the transfer and the velocity state on the manifold; this maneuver, then, becomes the LOI cost. Once the state of the vehicle is actually on the manifold

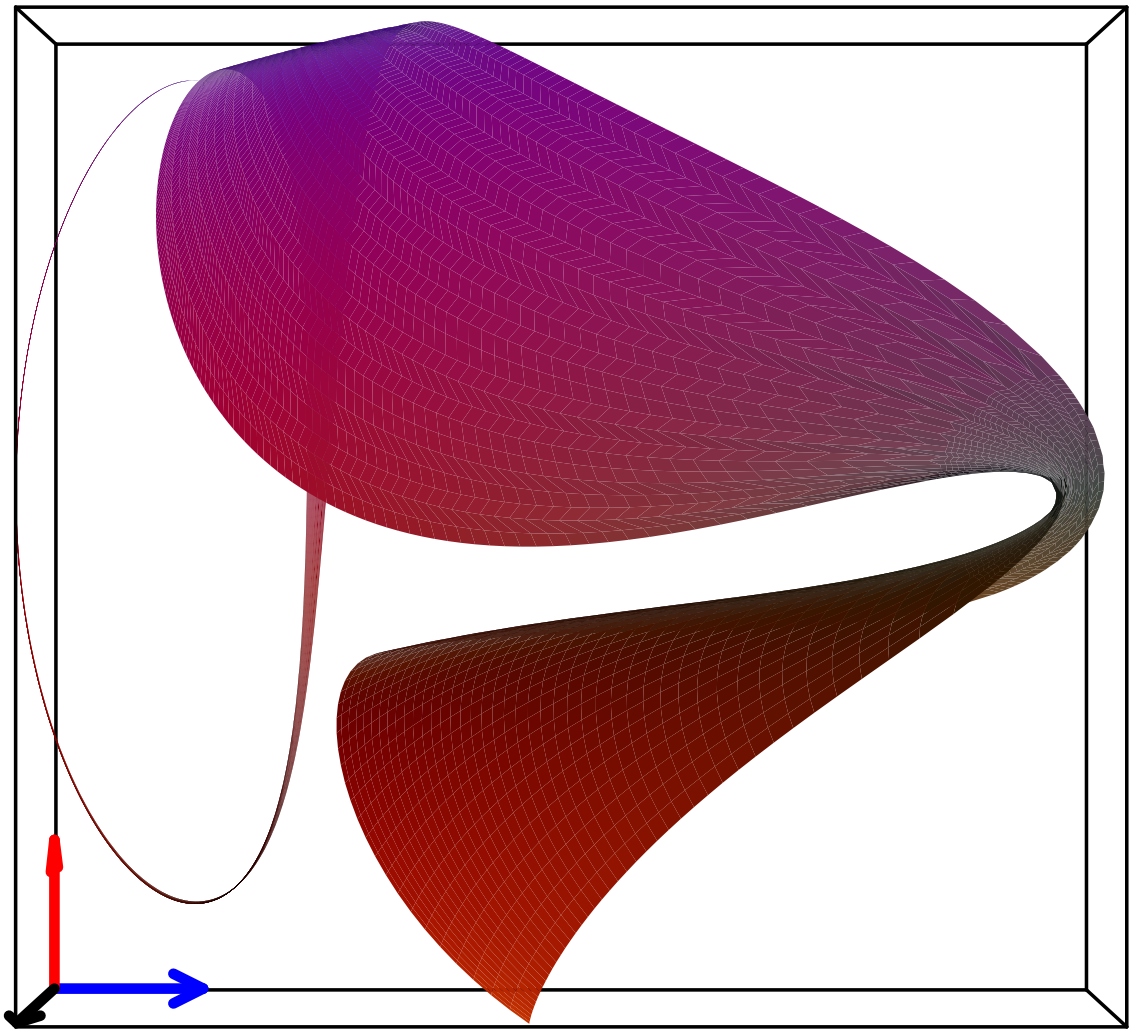

Figure 6.11. Portion of the Stable Manifold Projected onto Configuration Space (Courtesy: Brian Barden)[43]

surface, it will approach the Lissajous orbit, similar to the transfer in Figure 6.11. This completes the transfer from Earth to the Lissajous with, theoretically, no additional maneuvers.

The selected final target state on the manifold surface generates a solution that may or may not correspond to a transfer with an acceptable LOI cost. A methodology is sought to allow the "fixed" LOI target state to vary along the manifold surface to minimize the required insertion maneuver. Schematically, this is depicted in Figure 6.12. Initially, the target state $\bar{X}_{act}$ for the transfer lies on the desired manifold surface in position and time, but requires some associated LOI cost to achieve the 7 dimensional manifold state that will approach the Lissajous. Based on this cost, a change in state $\Delta\bar{X}$ is calculated in an attempt to reduce the magnitude of the required maneuver. This results in a new final state $\bar{X}_{des}$ that, in all likelihood, does not lie on the required manifold surface. However, if this new final state is projected back onto the manifold surface, another state $\bar{X}_{proj}$ is obtained that does lie on the desired surface, and therefore, is an acceptable final target state. A new transfer is determined to this new LOI point that requires a smaller maneuver to insert onto the manifold. This iteration process is repeated until some minimum cost is achieved.

6.2.2 One Dimensional Variations Along the Manifold

As an example of the application of this methodology, consider the variation of the LOI target state along a single manifold trajectory. In this case, the "surface" is, in fact, one dimensional, corresponding to the selected manifold solution. Some LOI target state $\bar{X}_{act}$ along the manifold is selected and the transfer is computed to meet the desired position and time. From this known solution, the velocity partials in Equations (3.61)–(3.64) of Section 3.3.5 are utilized to determine changes in the position and time ($\Delta\bar{X}$) of the final state that will reduce the velocity error. This change in state is added to the previous target position and time to produce a new final target state $\bar{X}_{des}$; however, this point no longer lies on the desired manifold trajectory.

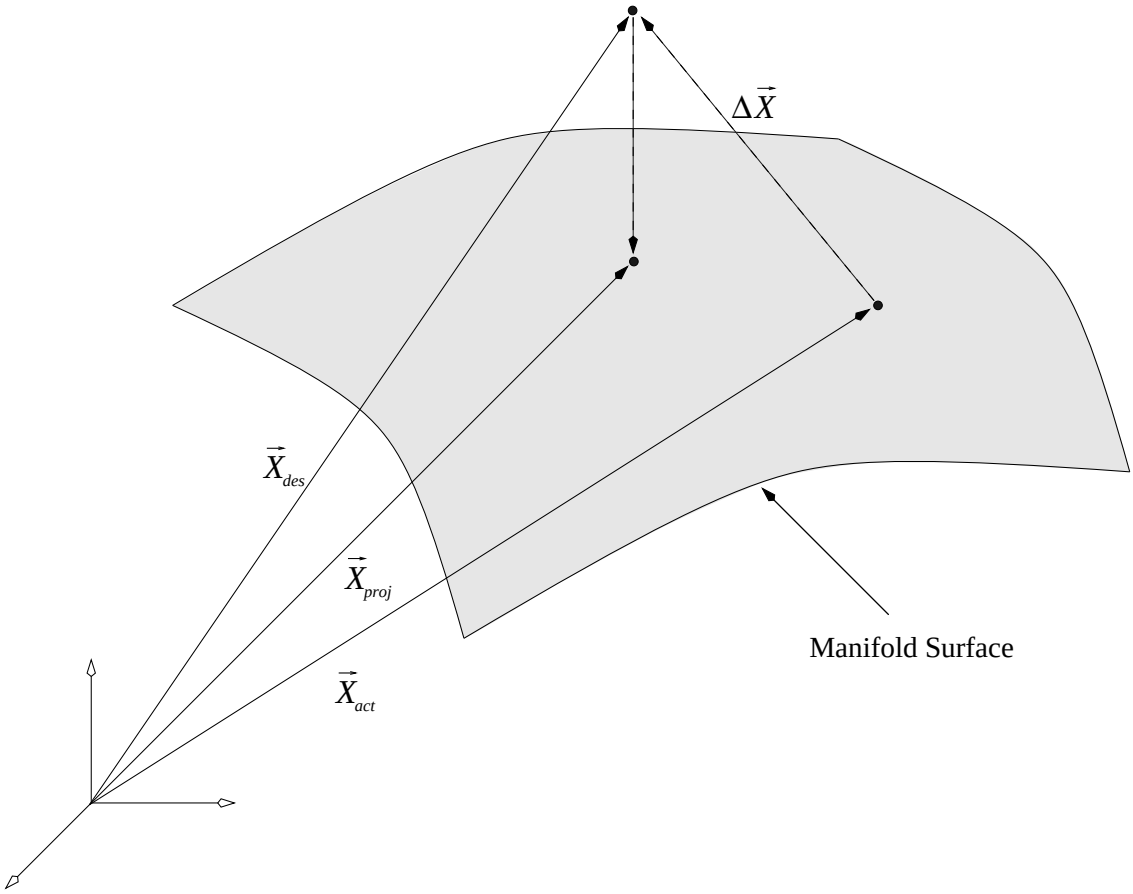

Figure 6.12. Stylized Representation of Manifold Targeting Procedure

By projecting $\bar{X}_{des}$ onto the manifold trajectory, a new final target state $\bar{X}_{proj}$ is determined. To project this state onto the manifold, the distance from the desired target, $\bar{X}_{des}$, to some point on the actual manifold trajectory is computed. The distance to a second point on the manifold is also determined, and a Newton-Raphson iteration process (in time) is utilized to minimize the position error between the desired end state $\bar{X}_{des}$ and the manifold solution. Once the new LOI target state is determined, a new transfer is computed using the previous solution as an initial guess. A new LOI cost is computed and the iteration process is repeated until some minimum insertion cost is achieved. Note that time is selected as the independent variable along the manifold when projecting the desired end state onto the manifold surface. The time along the manifold is monotonic and provides a one-to-one mapping

along the trajectory, i.e., there is only one state associated with each time along the one dimensional manifold. To ensure an adequate resolution for the time variable along the manifold, a 10^{th} order interpolation scheme is used with nodes selected every one day along the numerically integrated path. This proves to be an efficient method to both store and evaluate the manifold states over a given time interval.

6.2.3 Results for 1-D Variations Along a Selected Manifold

The one dimensional manifold trajectory selected for this analysis is plotted in Figure 6.13, and is the same manifold employed previously in the analysis of the Earth-to-L_2 transfer. In the figure, the manifold path extends from the lunar orbit to the state at JD 2454560.0, approximately half way through the first revolution along the Lissajous orbit. The square symbols on the plot denote 10 day intervals beginning at JD 2454370.0, just after the lunar encounter. The nominal LOI point

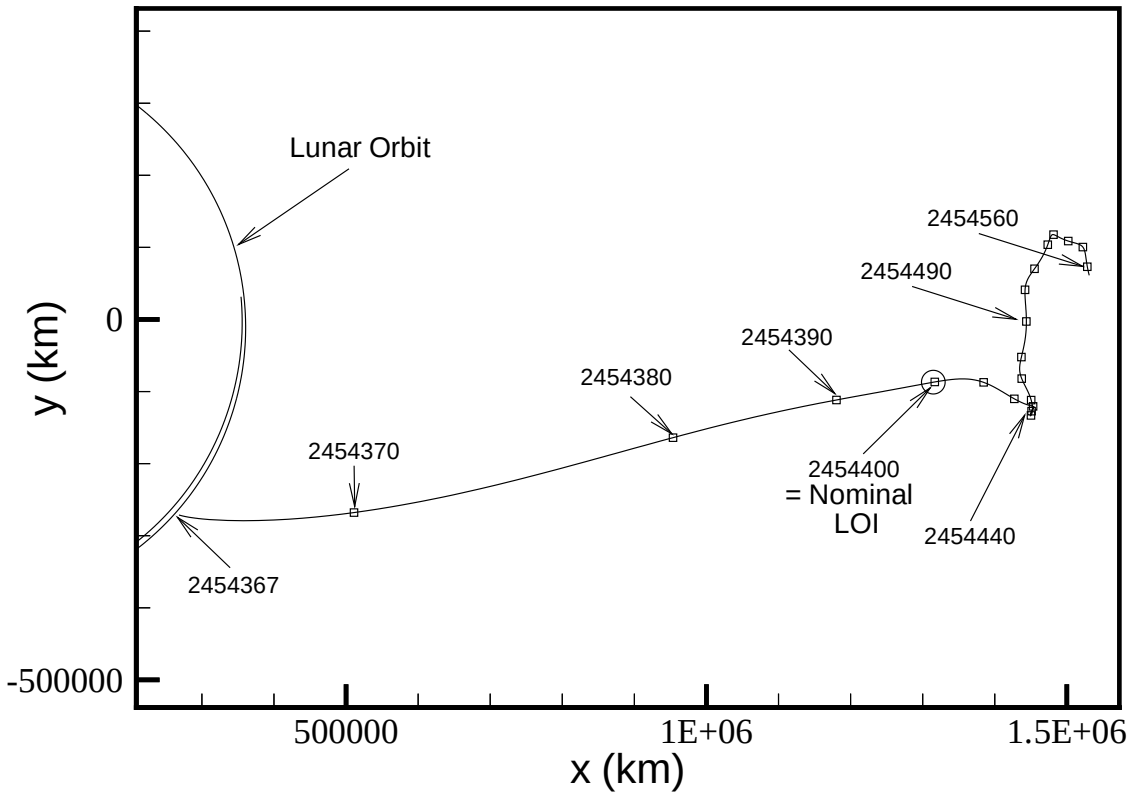

Figure 6.13. Selected Manifold Trajectory for Earth-to-L_2 Transfer Example

at JD 2454400.0, from the previous analyses, is also marked. Note from the figure that the velocity decreases significantly after the nominal LOI point. This causes the vehicle to spend 30–40 days in the "small loop" region around JD 2454440. The significance of this region will be explained in the discussion of the results.

To isolate the effects of the variations in the LOI target state location on the LOI cost, the launch date is fixed at some value that is within the range identified for the given nominal, as determined in Section 6.1. The transfer to the nominal LOI state is computed as before, and then the LOI target state variation scheme from Section 6.2.1 is applied to this solution.

6.2.3.a LOI Target State Variations in the Zero Loop Case

The results of this procedure are presented in Figure 6.14 for the zero phasing loop case. In the figure, the LOI maneuver cost is plotted as a function of the date corresponding to the LOI target state for a series of launch dates. (Again to clarify the figure, the abscissa corresponds to LOI target date minus 2454000.) Each curve in the figure represents the variation in cost for a specified fixed launch date and is denoted using the same notation as seen in Figure 6.1; for example, the label 62.5 corresponds to solutions with launch on JD (24543)62.5. The minimum LOI cost determined by the LOI target state variation procedure for each given launch date curve is marked with a diamond. These minimums are connected by a dotted line to signify that a continuum of solutions are possible over the range of launch dates examined. Note that the minimum LOI cost determined by this procedure is 0.31 m/s on JD 2454412.058, corresponding to a launch date of JD 2454363.764. This is the same minimum launch date observed in the parametric study in Section 6.1.1.

Notice that the curves in Figure 6.14 reflect the same general trend that was previously described in Figure 6.1. As the launch date varies, the LOI cost for a given LOI target state along the manifold decreases to a minimum and then increases again. Note also that for launch dates near JD 2454363.764, that corresponds to the solution with the minimum cost, the LOI costs are fairly constant over a 30 to 40

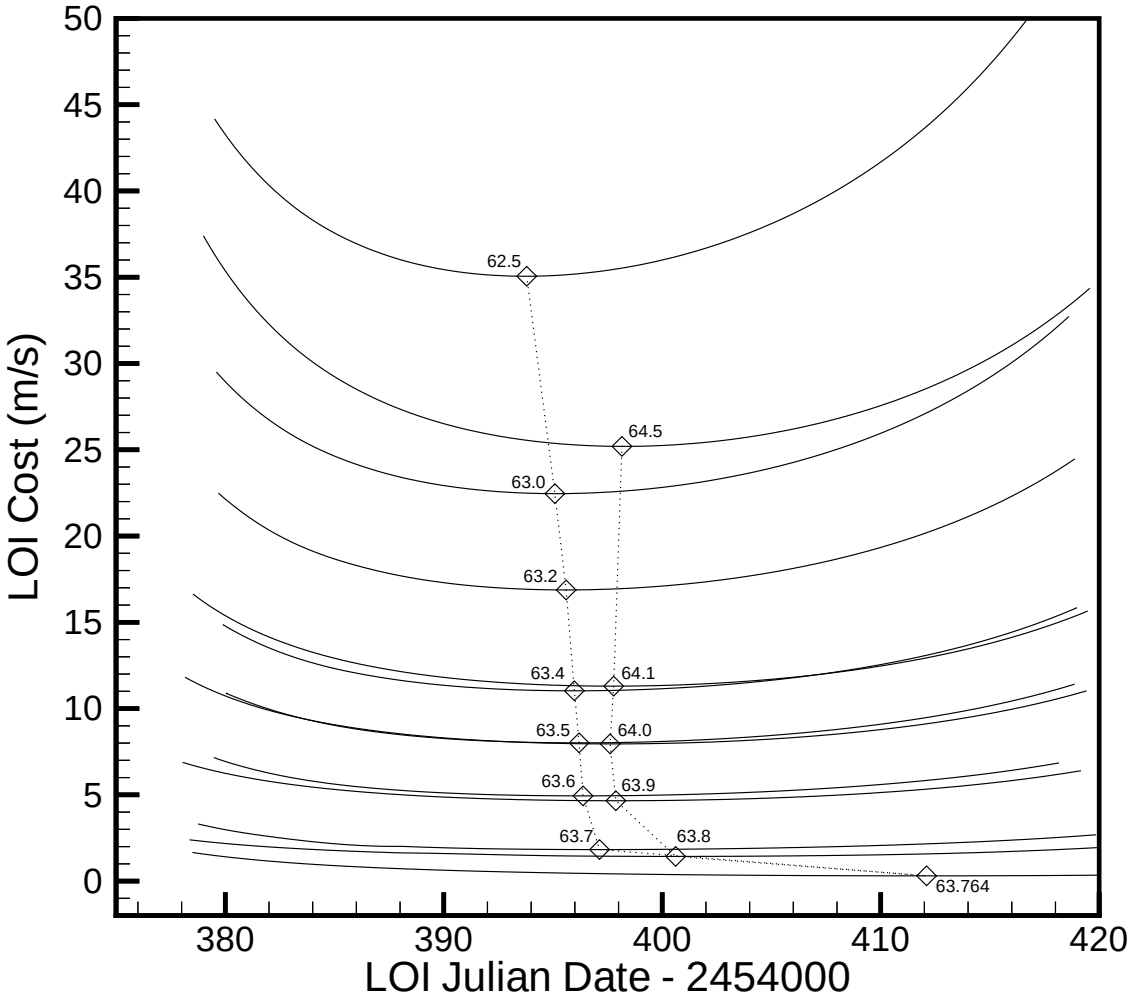

Figure 6.14. LOI Target Date Variation for Zero Loop Case

day range from JD 2454380.0 to JD 2454420.0. As the launch date varies from this minimum value, the LOI cost rises rapidly and the variations in LOI cost along a given curve slowly lose their linear nature. These results emphasize and reconfirm the assertion that the launch date is the largest contributing factor to the LOI cost.

For launch dates later than JD 2454420.0, the LOI cost rises dramatically. To demonstrate this, the lowest curve corresponding to the minimum LOI cost, and associated with launches on JD 2454363.764, appears in Figure 6.15 for a range of LOI target dates from JD 2454370.0 to 2454560.0. (Refer to Figure 6.13 for the correlation between the LOI target dates and positions along the manifold.) Notice

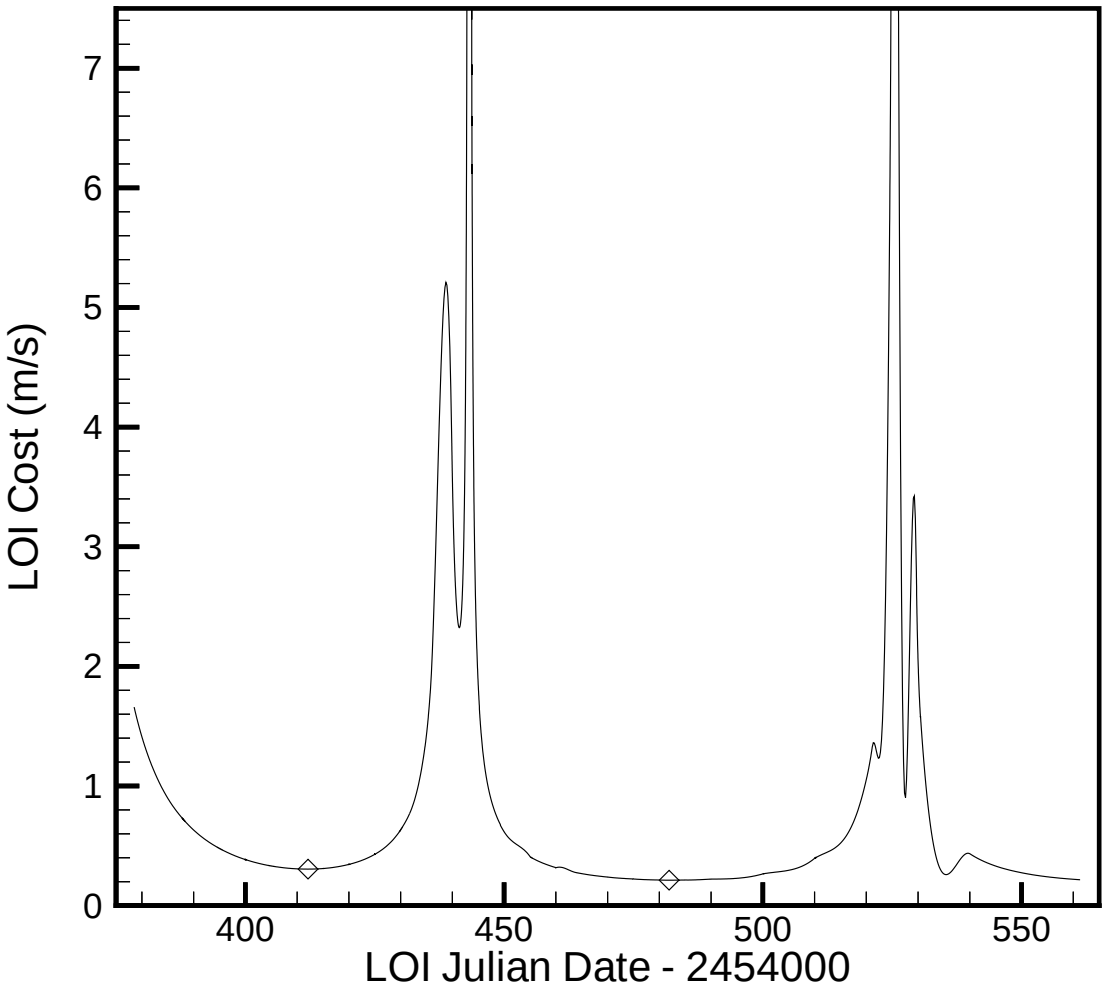

Figure 6.15. Minimum LOI Target Date Variation for Zero Loop Case

first that, aside from the two "spikes", the LOI cost is fairly constant over the entire range along the one dimensional manifold. This indicates that the precise location of the LOI maneuver is not critical to achieve a desirable insertion cost. The increase in LOI cost around JD 2454440.0 corresponds to the "small loop" portion of the manifold near this point (see Figure 6.13); a similar increase also occurs in the relatively smooth region along the manifold near JD 2454525.0. It has been determined that these increases occur near the locations where the trajectory passes through the ecliptic plane. More specifically, large increases in cost are apparently caused by a shift in the geometry of the lunar encounter and the Lissajous orbit insertion location. Since

the lunar orbit lies very close to the plane of the ecliptic, as the trajectory passes through the ecliptic, it also passes through the lunar orbit plane. For LOI locations above the lunar orbit plane, the required lunar encounter must pass below the Moon's orbit, and vice versa, due to the three dimensional nature of the Lissajous orbits. An increase in LOI cost occurs near the transition between solutions with lunar periapse passages above and below the lunar orbit; that is, the cost increases for solutions that lie very close to the lunar orbit plane. This explains the two large increases in LOI cost that are seen in the figure.

Between the spikes, a second local minimum exists near JD 2454480.0. This LOI cost is actually 0.09 m/s lower than the previous minimum. It is likely that any science activities for the mission would be underway at this point; thus, for this investigation the local minimum prior to JD 2454440.0 is selected for analysis. It is also noted that certain limitations exist in the current implementation of the multi-conic algorithm. Currently, the multi-conic procedures are formulated for the Earth-Moon system, including solar gravity as a perturbation. However, as the trajectory approaches a Sun-Earth libration point orbit, the primary gravitational forces become the Earth and the Sun, with minor perturbations from the Moon. This difference in modeling limits the usefulness of the Earth-Moon multi-conic formulation to dynamical regions where the solar gravity can be best modeled as a perturbing force. In particular for this trajectory, the multi-conic algorithms work best for dates earlier than JD 2454440.0. It should be noted that the data in Figure 6.15 is generated through a continuation procedure utilizing numerically integrated solutions. This is, of course, an option to determine the transfers. However, one of the primary goals of this investigation is the determination of transfers utilizing the full three step procedure. With this goal in mind, the region in the vicinity of the first local minimum is selected for possible LOI locations.

6.2.3.b LOI Target State Variations in the One Loop Case

The variation scheme for the LOI target state has also been applied to transfer solutions with one phasing loop. The results are presented graphically in Figure 6.16. The trajectories display many of the same trends that are observed in the 0-loop cases. As launch date changes, the curves shift in the same fashion as seen in Figure 6.2 from Section 6.1.2. (The curves are denoted by launch date minus 2454300 so that, for instance, 51.5 corresponds to transfers with launch date on JD 2454351.5.) The two transfer types described earlier for the 1-loop case are clearly evidenced again in this figure. The higher cost solution (with lower elongation angle) is represented

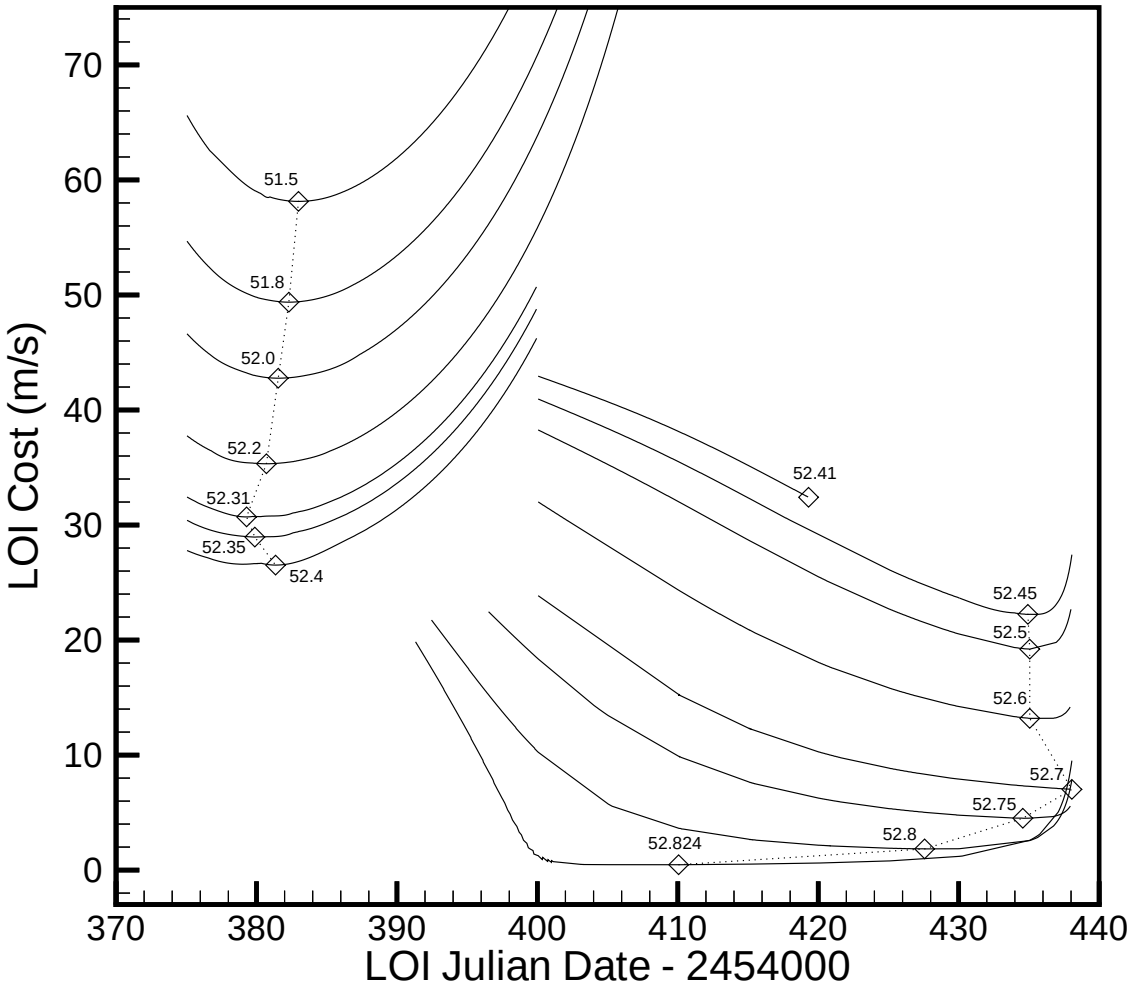

Figure 6.16. LOI Target Date Variation for One Loop Case

by the parabolic curves on the left of the figure. It is interesting to note that the minimum LOI costs for this type occur around JD 2454380, only 12-14 days beyond the lunar encounter. However, the other type of solution (with higher elongation angle) presents a much lower cost, with LOI target dates consistent with those in the 0-loop case. As in the direct case, the LOI costs increase rapidly as the LOI target state approaches the ecliptic plane around JD 2454440.0. For reference, the minimum LOI cost for the 1-loop case is 0.47 m/s on JD 2454410.058, that corresponds to a launch date on JD 2454352.824. Note that in this case, the best LOI target state is 10 days past the nominal target state. The variation curve in Figure 6.16 associated with this minimum cost, though, is very flat in this region, so neighboring solutions also present excellent choices for the LOI location.

6.2.3.c LOI Target State Variations in the Two Loop Case

Similar to the first two cases, the LOI target state variation procedure is also applied to the transfer that includes two phasing loops. The results are presented in Figure 6.17. Again, each curve corresponds to a specific launch date that is referenced to JD 2454300. Solutions along a single curve, then, represent the relationship between LOI cost and the position of the LOI target state (identified by the associated date). For two phasing loops, note that the curves are similar to the results seen in Figure 6.5 from Section 6.1.3. As launch date increases, each curve reaches a minimum, followed by a local maximum. Although it appears that there may be two separate types of solutions (similar to the one loop case), there is, in fact, only one transfer type represented here, with continuous solutions throughout the valid launch period. The minimum cost of 2.23 m/s corresponds to a solution with an LOI that occurs on JD 2454401.308, and has a launch on JD 2454337.300. As seen previously, the lowest curve, that includes the solution with the minimum cost, is very flat in this region. However, the cost begins to increase as the LOI dates approach JD 2454440; this is the region where the LOI target state lies close to the ecliptic and, thus, the lunar orbit plane, as described in Section 6.2.3.a.

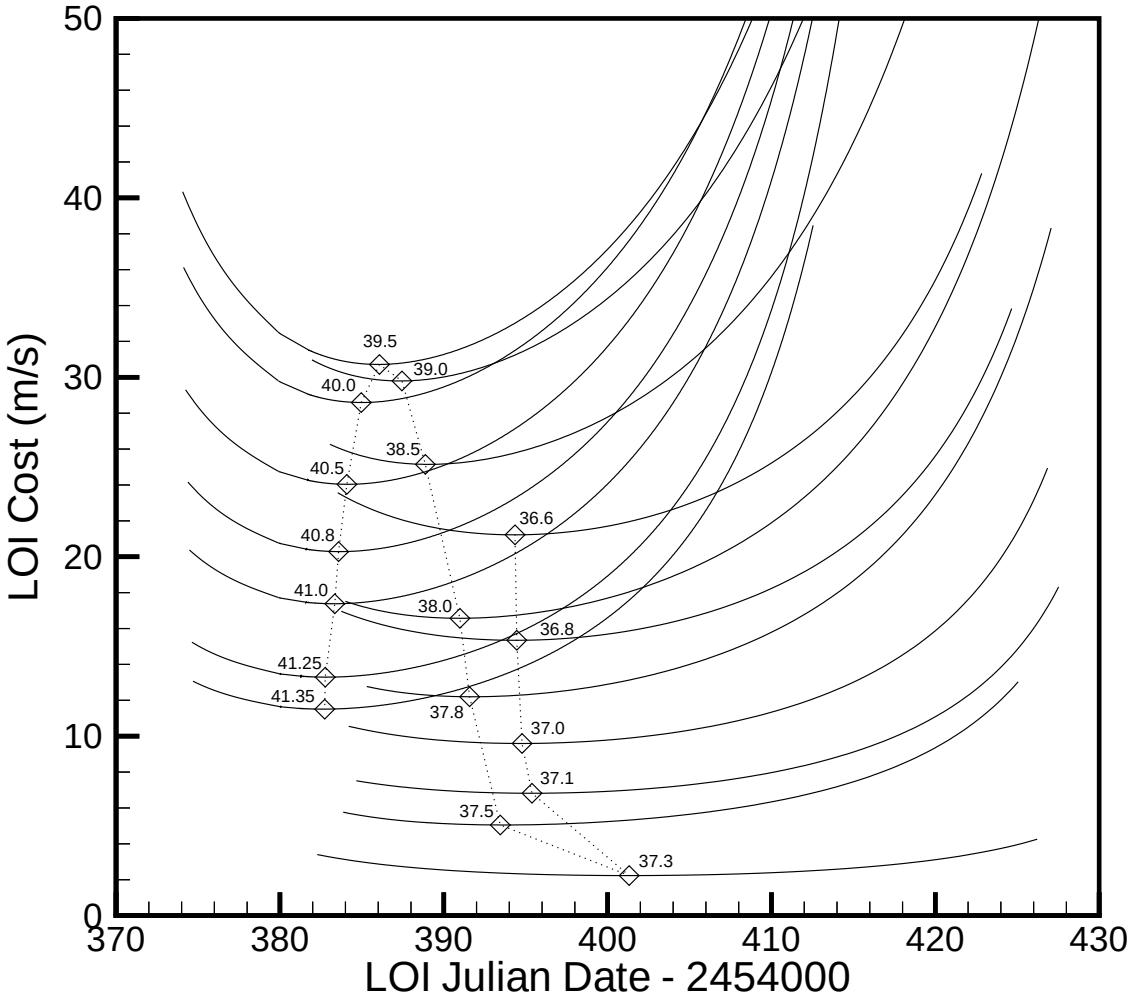

Figure 6.17. LOI Target Date Variation for Two Loop Case

6.2.3.d LOI Target State Variations in the Three Loop Case

Curves that represent the relationship between LOI cost and LOI location for the three phasing loop case are presented in Figure 6.18. Multiple curves again appear; each curve is again associated with a specific launch date. The curves appear similar in nature to those from Figure 6.6 in Section 6.1.4. Notice that, in this case, the curves with later launch dates have higher costs, in general, and are clustered together near the minimum LOI target dates for each curve. This is attributable to the interaction of the Moon on the transfers near the end of the acceptable range of launch dates, as discussed previously. The minimum LOI cost for this case is 2.28 m/s and is associated with a solution that arrives at the LOI target state on JD 2454402.058,

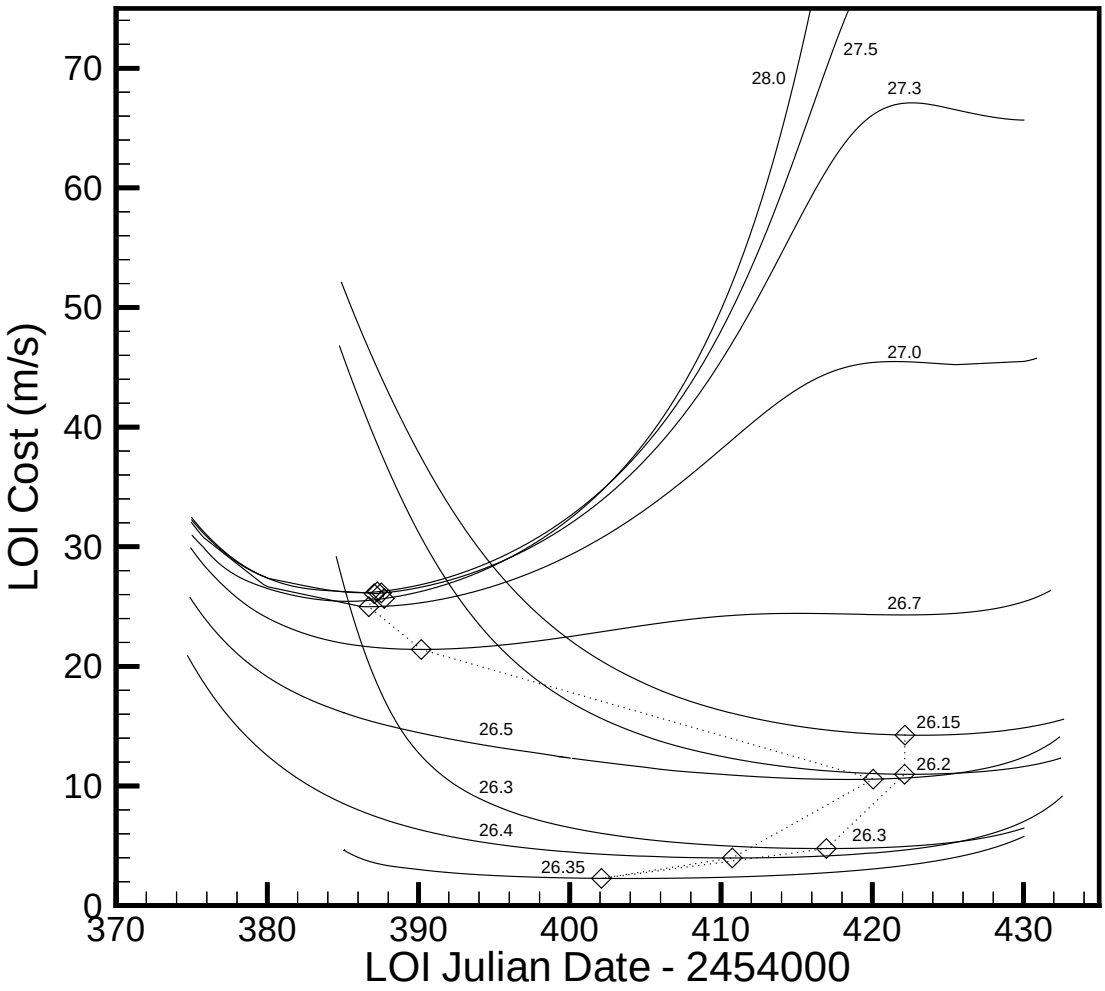

Figure 6.18. LOI Target Date Variation for Three Loop Case

following a launch on JD 2454326.350. As seen in the previous cases, this LOI cost curve is flat near the minimum cost solution, resulting in an LOI cost that is relatively insensitive to the precise location of the insertion point along the manifold.

6.3 Comparisons and Conclusions

It is, perhaps, insightful to compare the nominal solutions corresponding to each case with the best transfer obtained through the the search across various launch dates and LOI target states. Comparative data is presented in Table 6.1, detailing the differences between the nominal and "best" case trajectories, including such quantities

as: LOI cost, launch/injection date, LOI target date, final elongation angle, altitude at the lunar periapsis, and the altitude of the final perigee before the lunar encounter. The "best" solutions are those determined by the LOI target variation procedure for the 0, 1, 2, and 3 loop cases in Sections 6.2.3.a – 6.2.3.d. The case labeled "improved" for the four loop transfer results from the parametric study in Section 6.1.5. Some of the significance of the results in the table can be discussed by graphically comparing the resulting nominal and best case trajectories.

The graphical comparison for the 0-loop case is presented in Figure 6.19. In the figure, the nominal trajectory is shown with a dashed line, while the "best" solution is plotted with a solid line. Clearly, the two solutions are nearly identical, although the new LOI target state is about 12 days beyond the old LOI location. These results

Table 6.1 Comparison of Nominal and Best Case Solutions

Case	LOI Cost (m/s)	Launch Julian Date	LOI Julian Date	Elong. Angle (deg)	Lunar Periapse Alt. (km)	Final Perigee Alt. (km)
0–nominal	1.93	2454363.816	2454400.058	45.4	6757.8	200.0
0–best	0.31	2454363.764	2454412.058	45.8	6677.1	200.6
1–nominal	20.64	2454352.731	2454400.058	51.4	6698.6	2018.0
1–best	0.47	2454352.824	2454410.058	45.9	7508.6	2122.6
2–nominal	30.35	2454340.612	2454400.058	38.1	8732.5	2356.2
2–best	2.23	2454337.300	2454401.308	46.5	11887.6	15440.9
3–nominal	32.75	2454327.624	2454400.058	37.6	9473.7	4039.7
3–best	2.28	2454326.350	2454402.058	46.6	11743.2	15053.3
4–nominal	32.19	2454315.944	2454400.058	37.7	8921.2	2948.4
4–improved	24.02	2454314.878	2454400.058	39.9	10428.8	7989.3

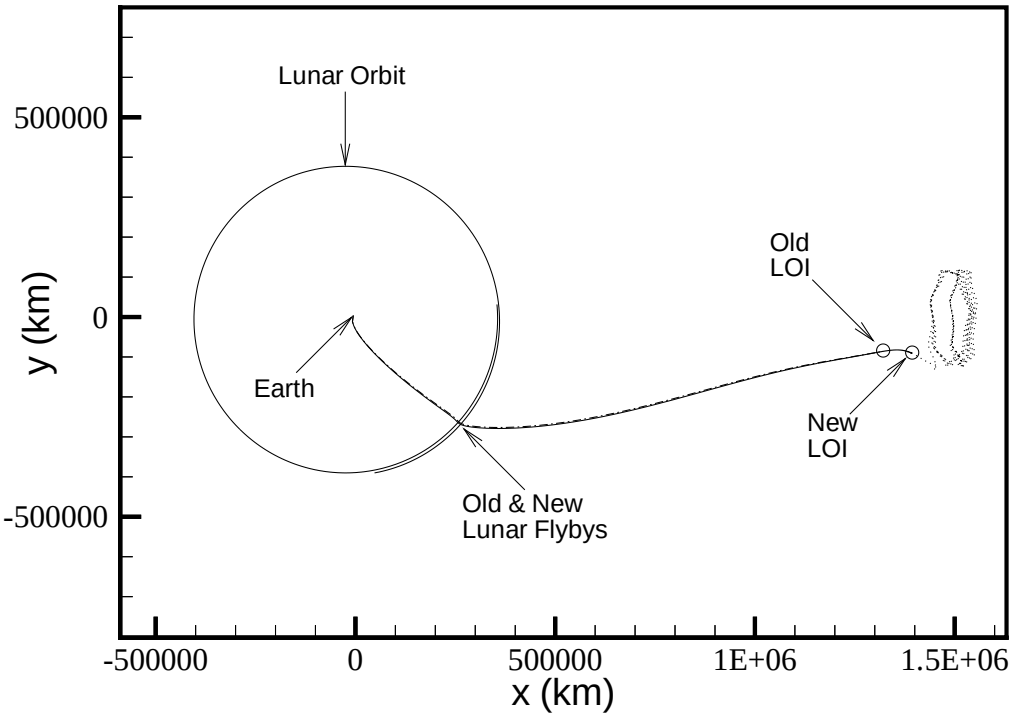

Figure 6.19. Nominal and Best Solutions for Zero Loop Case

are consistent with the fact that the nominal solution for the 0-loop case has been shown to be close to the optimal solution; the LOI costs differ by only 1.62 m/s

The comparison of the trajectories for the one loop case appears in Figure 6.20. Recall that, in this case, the nominal and "best" solutions are further apart than the 0-loop case, both physically and in terms of LOI cost. This is evidenced by the distinct change in the solution from the old transfer to the new one. In the figure, the shift in final elongation angle is quite apparent. From Table 6.1, the nominal solution corresponds to a final elongation angle of 51.4 deg, while the best case transfer passes the Moon at 45.9 deg; this is very close to the manifold passage at 45.8 deg. The nominal LOI cost for this case is 20.64 m/s. Through the parametric results and a more careful examination of the LOI location utilizing the LOI target state variation procedure, this cost is reduced to 0.47 m/s. This is a savings of 20.17 m/s and lowers the total deterministic cost of the mission to under 1 m/s! Also note that, in the process of determining the best case transfer, the location of the LOI point is shifted forward by about 10 days from the nominal.

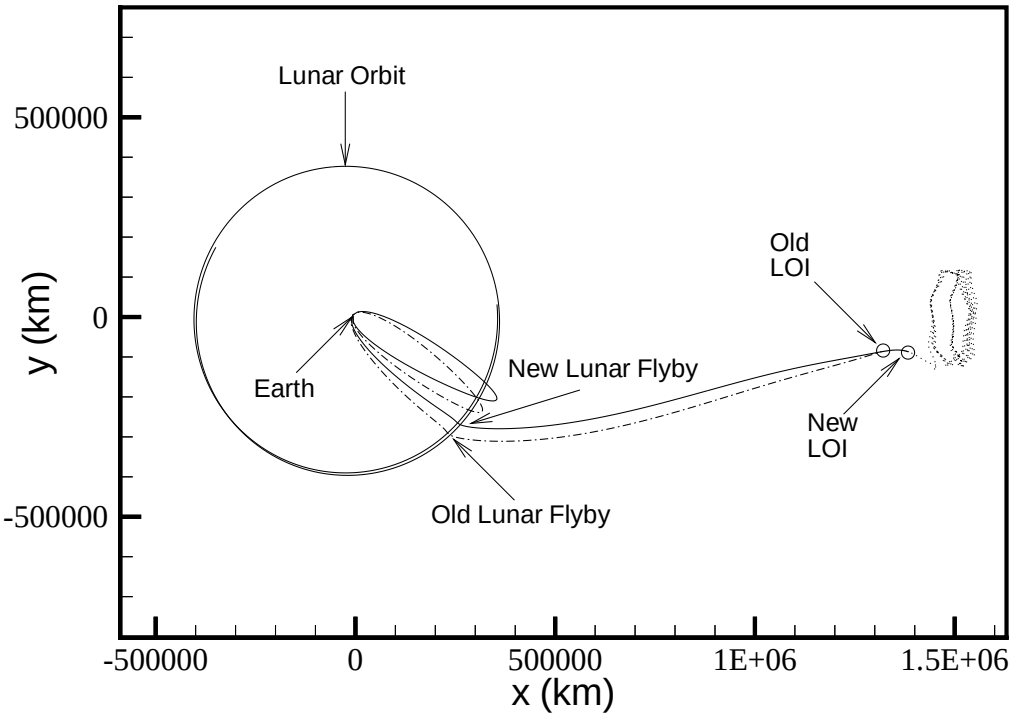

Figure 6.20. Nominal and Best Solutions for One Loop Case

For the solution that includes two phasing loops, the comparison of the nominal and "best" cases is presented in Figure 6.21. Here again, the shift in the final elongation angle is apparent from the nominal (dashed line) to the best case (solid line). Also notice that the eccentricity of the phasing loops for the best case solution has decreased. This is evidenced by a large increase in the altitude of the final perigee prior to the lunar encounter. From Table 6.1, the nominal solution has a final perigee altitude of 2256.2 km, while the perigee altitude associated with the "best" transfer is 15440.9 km; this is an increase of over 13000 km. This change in due almost entirely to the shift in launch date of 3.3 days, since the LOI target state for the best case solution is only one day later than that on the nominal trajectory.

Lastly, the three phasing loop comparison is plotted in Figure 6.22. For this case, the nominal LOI cost is 32.75 m/s, while the "best" LOI cost is only 2.28 m/s, for a savings of 30.47 m/s. It is very interesting to notice the differences in the trajectory between the nominal and the best case. The nominal solution contains three phasing

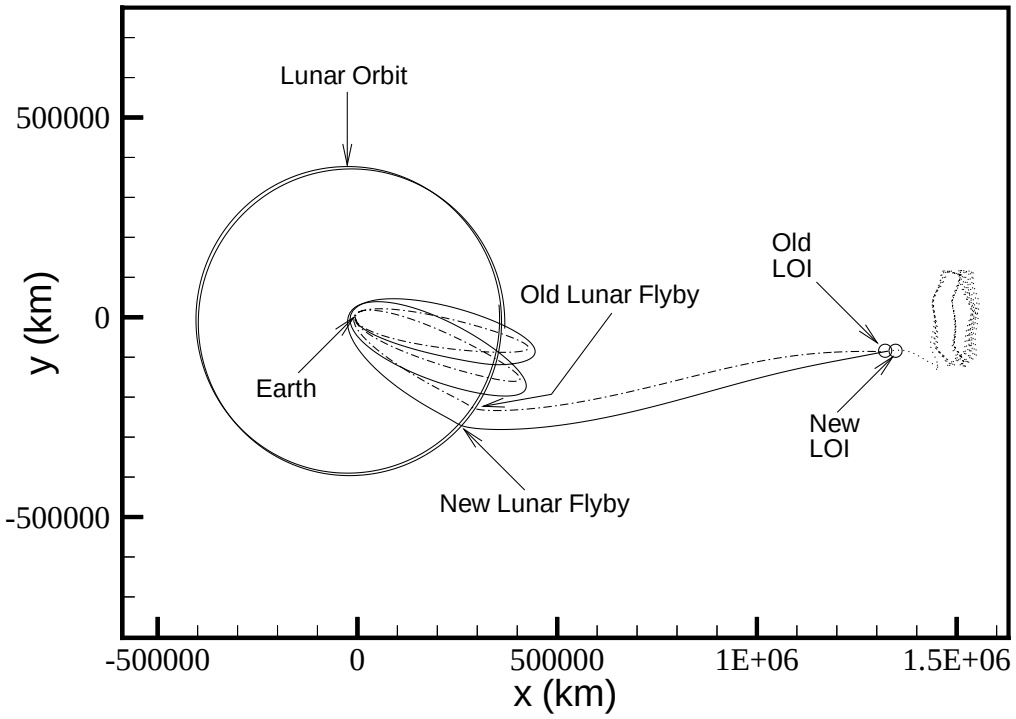

Figure 6.21. Nominal and Best Solutions for Two Loop Case

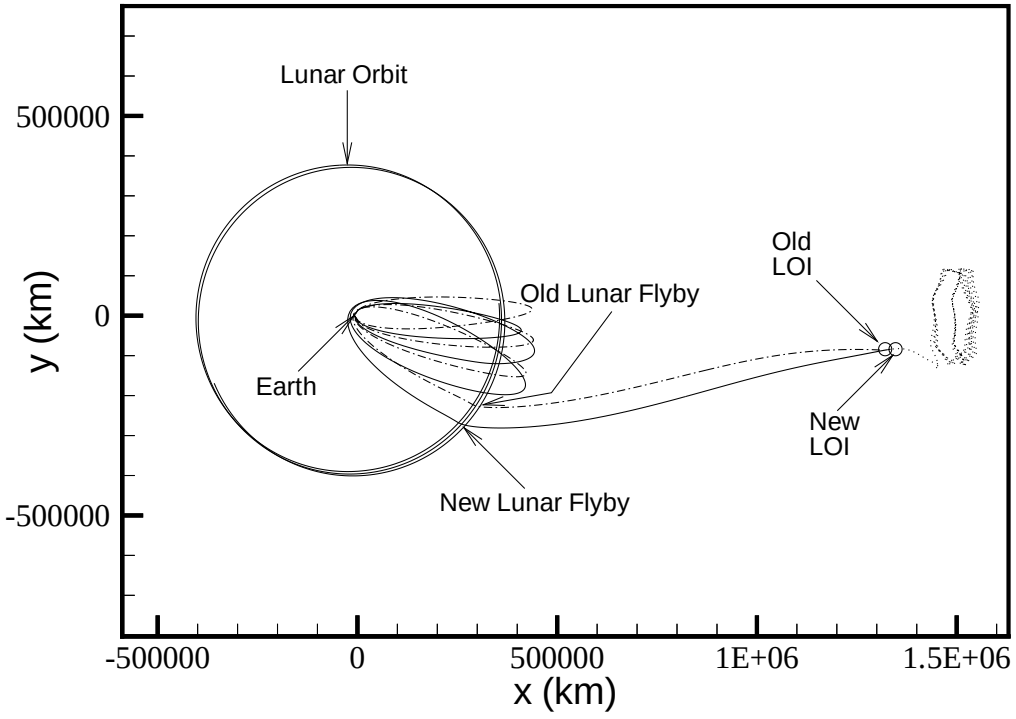

Figure 6.22. Nominal and Best Solutions for Three Loop Case

loops with roughly equal periods. However, the best case solution actually includes a smaller first loop than that in the nominal, followed by larger second and third loops. This allows the final perigee altitude to be raised, thereby decreasing the eccentricity of the last two phasing loops (similar to the 2-loop case). Most interestingly, though, is the fact that there are no deterministic maneuvers present in the final trajectory. The changes in the phasing loops are initiated by beneficial lunar perturbations near the second apogee. These perturbation effects are incorporated automatically by the procedures developed throughout this work to determine a solution with a very acceptable LOI cost.

In summary, it is concluded from this study that the single most important factor affecting the LOI cost is the selection of the launch/injection date. The location of the LOI target state along the manifold also affects the LOI maneuver cost, but to a seemingly lesser degree. A procedure to vary the LOI point along a single manifold trajectory is developed, based on the understanding of the manifold surfaces from dynamical systems theory. This procedure is then employed successfully to significantly reduce the LOI costs required for solutions containing 0, 1, 2, and 3 phasing loops.

7. CONCLUSIONS

The primary focus of this research has been the development of a methodology to design trajectories in the Sun-Earth-Moon restricted four body problem. This design process is presented as a three step procedure consistent with previous contributors.[13–15] The current work improves upon these contributions by incorporating trajectory constraints into the design process. This is accomplished by deriving variational equations relating any particular constraint to the independent variables selected for the procedure. Once this relationship is determined, the constraints are incorporated into the state relationship matrix, along with variations in any velocity discontinuities associated with the solution. The SRM is then utilized in an iterative process to reduce the velocity discontinuities and enforce the necessary constraints. This procedure is sufficiently general to allow inclusion of other constraints, provided that the constraint is expressible in terms of variations in the independent parameters. Furthermore, the inclusion of deterministic maneuvers throughout the trajectory is also introduced into the solution process. This expands the available solution space by allowing the designer freedom to place maneuvers anywhere in the solution to meet the specified mission constraints. At the same time, the overall design philosophy represented by the three step methodology is maintained.

The development of this design philosophy and the three step process has led to a variety of applications for different trajectory design problems. First, the design of multiple lunar swingby trajectories is presented. These solutions include one or more lunar encounters and have been utilized in the past for primary mission trajectories, such as WIND and GEOTAIL, and for extended missions, such as the ISEE-3/ICE cometary encounter. The methodology and application of the three step procedure to this problem has been improved through this work to allow more design options

for launch dates and also to better maintain the initial trajectory characteristics in the final integrated solution. The experience gained through the design of these types of solutions is used to develop the three swingby recovery strategy for the transfer example to an L_2 Lissajous orbit.

These transfers to libration point orbits are a second class of trajectories that can be investigated through this procedure, in conjunction with dynamical systems theory. By targeting a specified state on a stable manifold surface associated with some libration point orbit, transfers can be designed that meet all mission constraints for very reasonable costs; furthermore, much of the transfer trajectory design process can be automated. These trajectories may include lunar gravity assists, such as the L_2 transfer example, or no lunar flybys. The GENESIS trajectory is an example with no gravity assists, that is designed using a combination of dynamical systems theory and the current work. By utilizing the dynamics of the four body problem in the design process, a trajectory for the GENESIS mission is determined that meets all the mission constraints with only a single, relatively small, deterministic maneuver near the beginning of the Lissajous orbit.

A third type of application for this methodology is the analysis of errors that are likely to exist in a given nominal trajectory. This error analysis can be utilized to study the sensitivities of various portions of a nominal solution, such as the return sensitivity analysis for the GENESIS mission. It is also applicable to examine the effects of injection errors on the trajectory, and to design corrective maneuver(s) to recover the mission. From the trajectory injection error analysis, it is determined that tangential velocity (velocity magnitude) and radial position errors are by far the costliest to correct. At times, the required single correction maneuver is beyond the limits of the mission constraints. To rectify this problem, a series of recovery strategies are presented for cases involving various numbers of phasing loops in the Earth-to-L_2 transfer example. The results of these various strategies indicate that, for trajectories involving one or more lunar gravity assists, the use of two phasing loops is preferred. Utilizing two loops provides the possibility to recover from the

more costly tangential velocity and radial position errors with very reasonable costs. Additionally, the two loop case generally avoids any unwanted lunar encounters that are present in the three and four loop solutions.

Lastly, returning again to dynamical systems theory, a procedure is developed to reduce the required cost to insert onto the manifold associated with the desired Lissajous trajectory. By allowing the LOI target state to vary along the manifold surface (or single trajectory for the 1-D case), a more optimal location for the LOI maneuver can be determined for all of the cases studied. Through this investigation into the optimization of the LOI cost, it is determined that the launch date is actually the largest contributing factor to the LOI cost. The cost is minimized by selecting a launch date such that the final elongation angle of the spacecraft, as it passes the Moon, is as close as possible to the original elongation angle of the manifold solution from dynamical systems theory.

Recommendations for Future Study

Although the development of the three step procedure is quite mature, this research is by no means exhausted. The current formulation is restricted to the Sun-Earth-Moon four body problem. In particular, the multi-conic algorithms are implemented assuming that the Earth and Moon are the principal gravitational sources, with perturbations from the Sun. A more general approach is necessary to allow multi-conic schemes involving the Sun and Earth as the primary bodies, as well as other planetary systems. Employing multi-conics in the regions near the libration points may provide an alternative analysis tool to better understand the rich dynamics in these regions. Furthermore, a procedure is required to transition between different types of multi-conic formulations. This might facilitate, for example, better modeling of the region just prior to the libration point in the LPO transfer trajectories. This might also provide a means to model the transition between a launch sequence and an interplanetary trajectory, such as the example utilizing lunar gravity assists to achieve escape velocity.

For further generalizing the solution procedure, the conic timing condition that is employed to generate the initial approximation for a multiple lunar swingby trajectory should be extended. Currently, the timing condition is developed for the three body problem (Earth, Moon, and spacecraft, for example). In other planetary systems, like the Jovian system, a timing condition for multiple encounter bodies may be useful. This could be used to determine initial approximations for satellite tour trajectories, such as the Galileo mission to Jupiter.

The second major area for continued study is the design of transfers to libration point orbits. This is a broad area of research that has only begun to be fully investigated. Perhaps the most intriguing future research involves expanding the procedure to shift the LOI target state to include LOI states that lie on the entire two dimensional manifold surface. Conceptually, this is the same as the one dimensional variation along a single manifold trajectory, but would require a method to store and evaluate states on an some 2-D surface. This could also be extended to a three dimensional manifold "volume" by including other manifold surfaces from neighboring Lissajous trajectories. These developments may lead to a fully automated procedure to determine transfers to LPO's with an optimal cost, that meet the given mission constraints.

This automation might also extend to the recovery design aspect of the transfer problem. By introducing variations in the LOI target state into the recovery design strategies, the insertion cost onto the manifold may be significantly reduced. Furthermore, if the LOI state is truly allowed to vary on the 2-D manifold surface, a recovery that has a much lower total cost may, in fact, be possible. This, in turn, may lead to a more automated procedure to design recoveries for any given launch errors.

In conclusion, the methodology presented in this work has proven to be a highly versatile and robust design tool for generating trajectories in the restricted four body problem. It is hoped that this research will prove beneficial to others interested in this problem, as well as all of those who may benefit from its application.

BIBLIOGRAPHY

BIBLIOGRAPHY

[1] K. C. Howell, B. T. Barden, R. S. Wilson, and M. W. Lo, "Trajectory Design Using a Dynamical Systems Approach with Application to GENESIS," AIAA Paper 97-709, *AAS/AIAA Astrodynamics Conference*, Sun Valley, Idaho, August 1997.

[2] R. Taton and C. Wilson, *Planetary Astronomy from the Renaissance to the Rise of Astrophysics*, Vol. 2A. Cambridge University Press, 1989.

[3] V. G. Szebehely, *Adventures in Celestial Mechanics, a First Course in the Theory of Orbits*. University of Texas Press, Austin, 1989.

[4] M. Hénon, "Sur les Orbites Interplanétaires qui Recontrent Deux Fois la Terre," *Bulletin Astronomique*, Vol. 3, 1968, pp. 377–402.

[5] D. L. Hitzl, "On the Perko Timing Condition for Second Species Orbits in the Restricted Problem," *Astronomy and Astrophysics*, Vol. 54, 1977, pp. 47–55.

[6] K. C. Howell, "Consecutive Collision Orbits in the Limiting Case μ=0 of the Elliptic Restricted Problem," *Celestial Mechanics*, Vol. 40, No. 3–4, 1987, pp. 393–407.

[7] K. C. Howell and S. M. Marsh, "A General Timing Condition for Consecutive Collision Orbits in the Limiting Case μ=0 of the Elliptic Restricted Problem," *Celestial Mechanics*, Vol. 52, 1991, pp. 167–194.

[8] R. W. Farquhar and D. W. Dunham, "A New Trajectory Concept for Exploring the Earth's Geomagnetic Tail," *Journal of Guidance and Control*, Vol. 4, March-April 1981, pp. 192–196.

[9] R. Farquhar, D. Muhonen, and L. Church, "Trajectories and Orbital Maneuvers for the ISEE–3/ICE Comet Mission," *Journal of the Astronautical Sciences*, Vol. 33, July-September 1985, pp. 235–254.

[10] P. Sharer, H. Franz, and D. Folta, "Wind Trajectory Design and Control," *CNES International Symposium on Space Dynamics*, Toulouse, France, June 1995.

[11] K. Uesugi, H. Matsuo, J. Kawaguchi, and T. Hayashi, "Japanese First Double Lunar Swingby Mission 'HITEN'," *Acta Astronautica*, Vol. 25, July 1991, pp. 347–355.

[12] N. Ishii and H. Matsuo, "Design Procedure of Accurate Orbits in a Multi-Body Frame with a Multiple Swingby," AAS Paper 93-655, *AAS/AIAA Astrodynamics Conference*, Victoria, British Columbia, Canada, August 1993.

[13] S. M. Marsh, "Sun-Synchronous Trajectory Design Using Consecutive Lunar Gravity Assists," M.S. Thesis, Purdue University, May 1988.

[14] D. A. Spencer, "Multiple Lunar Encounter Trajectory Design Using a Multi-Conic Approach," M.S. Thesis, Purdue University, December 1991.

[15] R. S. Wilson, "A Design Tool for Constructing Multiple Lunar Swingby Trajectories," M.S. Thesis, Purdue University, December 1993.

[16] S. W. Wilson, "A Pseudostate Theory for the Approximation for Three-Body Trajectories," AIAA Paper 70-1061, *AAS/AIAA Astrodynamics Conference*, Santa Barbara, California, August 1970.

[17] D. V. Byrnes and H. L. Hooper, "Multi-Conic: A Fast and Accurate Method of Computing Space Flight Trajectories," AIAA Paper 70-1062, *AAS/AIAA Astrodynamics Conference*, Santa Barbara, California, August 1970.

[18] L. A. D'Amario, "Minimum Impulse Three-Body Trajectories,". Ph.D. Dissertation, Massachusetts Institute of Technology, June 1973.

[19] H. J. Pernicka, "The Numerical Determination of Nominal Libration Point Trajectories and Development of a Station–Keeping Strategy,". Ph.D. Dissertation, Purdue University, May 1990.

[20] D. V. Byrnes, "Application of the Pseudostate Theory to the Three-Body Lambert Problem," *Journal of the Astronautical Sciences*, Vol. 37, July-September 1989, pp. 221–232.

[21] T. H. Sweetser, "Some Notes on Applying the One-Step Multiconic Method of Trajectory Propagation," *Journal of the Astronautical Sciences*, Vol. 37, July-September 1989, pp. 233–250.

[22] W. H. Goodyear, "A General Method for the Computation of Cartesian Coordinates and Partial Derivatives of the Two-Body Problem," NASA CR-522, Technical Report, September 1966.

[23] D. L. Hitzl, "Keplerian Transition Matrices for Elliptical Orbits," *Astronomy and Astrophysics*, Vol. 63, 1978, pp. 429–432.

[24] D. L. Richardson, "Analytic Construction of Periodic Orbits About the Collinear Points," *Celestial Mechanics*, Vol. 22, 1980, pp. 241–253.

[25] D. L. Richardson and N. D. Cary, "A Uniformly Valid Solution for Motion About the Interior Libration Point of the Perturbed Elliptic-Restricted Problem," AAS Paper 75-021, *AIAA/AAS Astrodynamics Specialists Conference*, Nassau, Bahamas, July 1975.

[26] R. W. Farquhar, "The Control and Use of Libration-Point Satellites," Goddard Space Flight Center, Technical Report, September 1970.

[27] K. C. Howell, "Three-Dimensional, Periodic, 'Halo' Orbits," *Celestial Mechanics*, Vol. 32, 1984, pp. 53–71.

[28] K. C. Howell, D. L. Mains, and B. T. Barden, "Transfer Trajectories From Earth Parking Orbits to Sun-Earth Halo Orbits," AAS Paper 94-160, *AIAA/AAS Spaceflight Mechanics Meeting*, Cocoa Beach, Florida, February 1994.

[29] K. C. Howell and H. J. Pernicka, "Numerical Determination of Lissajous Trajectories in the Restricted Three-Body Problem," *Celestial Mechanics*, Vol. 41, 1988, pp. 107–124.

[30] G. Gómez, A. Jorba, J. Masdemont, and C. Simó, "Final Report: Study Refinement of Semi-Analytical Halo Orbit Theory," ESOC Contract Report, Technical Report, April 1991.

[31] G. Gómez, A. Jorba, J. Masdemont, and C. Simó, "Study of the Transfer from the Earth to a Halo Orbit Around the Equilibrium Point L_1," Technical Report, December 1991.

[32] G. Gómez, A. Jorba, J. Masdemont, and C. Simó, "Moon's Influence on the Transfer from the Earth to a Halo Orbit Around L_1," Technical Report.

[33] B. T. Barden, "Using Stable Manifolds to Generate Transfers in the Circular Restricted Problem of Three Bodies," M.S. Thesis, Purdue University, December 1994.

[34] B. T. Barden, K. C. Howell, and M. W. Lo, "Application of Dynamical Systems Theory to Trajectory Design for a Libration Point Mission," *Journal of the Astronautical Sciences*, Vol. 45, No. 2, 1997.

[35] J. Guckenheimer and P. Holmes, *Nonlinear Oscillations, Dynamical Systems, and Bifurcations of Vector Fields.* Springer-Verlag, New York, 1983.

[36] S. Wiggins, *Introduction to Applied Nonlinear Dynamical Systems and Chaos.* Springer-Verlag, New York, 1990.

[37] T. S. Parker and L. O. Chua, *Practical Numerical Algorithms for Chaotic Systems*. Springer-Verlag, New York, 1989.

[38] S. M. Marsh and K. C. Howell, "Double Lunar Swingby Trajectory Design," *Proceedings of the AIAA/AAS Astrodynamics Conference*, Minneapolis, Minnesota, pp. 554–562, August 1988.

[39] R. S. Wilson and K. C. Howell, "A Design Concept for Multiple Lunar Swingby Trajectories," AIAA Paper 94-3718, *AIAA/AAS Astrodynamics Conference*, Scottsdale, Arizona, August 1994.

[40] K. C. Howell and R. S. Wilson, "Trajectory Design in the Sun-Earth-Moon System Using Multiple Lunar Gravity Assists," AIAA Paper 96-3642, *AIAA/AAS Astrodynamics Conference*, San Diego, California, August 1996.

[41] R. S. Wilson and K. C. Howell, "Trajectory Design in the Sun-Earth-Moon System Using Lunar Gravity Assists," *Journal of Spacecraft and Rockets*, Vol. 35, March-April 1998, pp. 191–198.

[42] L. A. D'Amario, D. V. Byrnes, L. L. Sackett, and R. H. Stanford, "Optimization of Multiple Flyby Trajectories," AAS Paper 79-162, *AAS/AIAA Astrodynamics Conference*, Provincetown, Massachusetts, June 1979.

[43] B. Barden. Purdue University. Private Communications, 1996-1998.

VITA

VITA

Mr. Wilson was born to Stan and Linda Wilson on July 10, 1969 in Charlotte, North Carolina. After also living in Athens, Greece and San Antonio, Texas, he moved with his parents and sister to Vincennes, Indiana in 1980. He was elected class president for both his junior and senior years in high school and graduated valedictorian in 1987. His love for physics, math, and all things related to space led him to Purdue University, where he received his Bachelor of Science in Aeronautical and Astronautical Engineering in May of 1991. Due primarily to the influence of Dr. Kathleen Howell, he entered graduate school at Purdue and began working on the multiple lunar swingby problem. He wrote a thesis entitled "A Design Tool for Constructing Multiple Lunar Swingby Trajectories" for which he received a Masters of Science in Aero/Astro Engineering in December of 1993. He then decided to continue on for a doctorate to more fully explore this vast area of research in the three and four body problems. In November 1996, he was married in Lafayette, Indiana to Kimberly Pettit, whom he met after he decided to stay for his doctorate. An internship at the Jet Propulsion Laboratory in the summer of 1997 developed into a full time position, and he will begin work at JPL in the fall of 1998. His work will be developing software based, in part, on his research here at Purdue, and he will also be supporting the trajectory design for the upcoming GENESIS mission.